Scanning probe microscopy studies of crystal surfaces

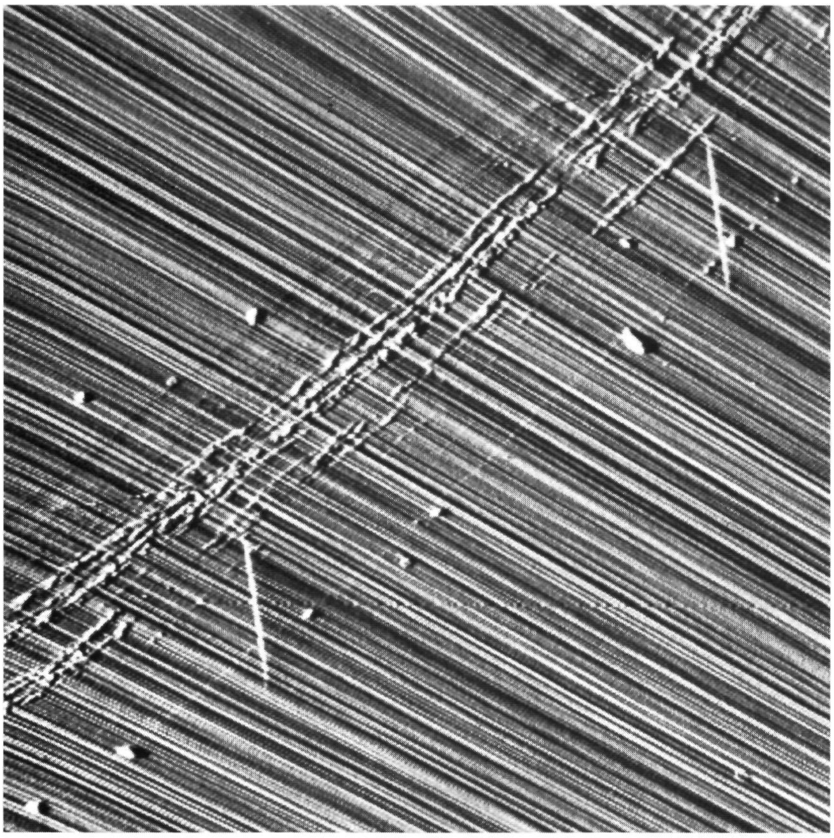

Marcos da Silva Couto

Scanning probe microscopy studies of crystal surfaces

CIP-DATA KONINKLIJKE BIBLIOTHEEK, DEN HAAG

Couto, Marcos da Silva

Scanning probe microscopy studies of crystal surfaces /
Marcos da Silva Couto. -[S.l. : s.n.]. - Ill.
Thesis Nijmegen. - With ref. - With summary in Dutch and Portuguese
ISBN 90-9007805-3
Subject headings: scanning tunnelling microscopy / atomic force microscopy / diamonds.

Scanning probe microscopy studies of crystal surfaces

een wetenschappelijke proeve op het gebied van
de Natuurwetenschappen

Proefschrift

ter verkrijging van de graad van doctor aan
de Katholieke Universiteit Nijmegen,
volgens besluit van het College van Decanen
in het openbaar te verdedigen op
dinsdag 10 januari 1995,
des namiddags te 1.30 uur precies

door

Marcos da Silva Couto

geboren op 10 mei 1966
te Santo Antônio do Monte
(Brazilië)

Promotor:	Prof. Dr. P. Bennema
Copromotor:	Dr. W.J.P. van Enckevort

I would like to thank all the people who collaborated in the making of this thesis, in particular: Piet Bennema, Willem van Enckevort, Hugo Meekes, and all co-authors of the papers which make up the various chapters presented herein.

I would also like to thank everyone who supported me through their friendship.

Aos amigos e familiares no Brasil um agradecimento todo especial pelo suporte durante esses quatro anos.

Finalmente eu agradeço à CAPES pelo suporte financeiro que tornou esta pesquisa possível.

This thesis was sponsored by Coordenação de Pessoal de Nível Superior (CAPES), Brazil, Process number 371/90-4

Parts of this thesis have been published in *Applied Surface Science* (Elsevier Science Publishers B.V.), *Journal of Applied Physics* (American Institute of Physics), *Philosophical Magazine B* (Taylor & Francis), *Journal of Hard Materials* (IOP Publishing Ltd.), *Journal of Physics D: Applied Physics* (IOP Publishing Ltd.) and *Industrial Diamond Review*. The author acknowledges the permission to reprint these.

Contents

Introduction

1. Crystals: their growth, transformation, preparation and observation

The interest in crystals is not new. Crystals in the form of precious and semi-precious stones have been and continue to be used in adornments such as jewellery. Besides jewellery, crystals are also present in areas as diverse as food – e.g. sugar, butter and table salt – and electronics – e.g. semiconductors used in a host of everyday applications such as television and radio. The major difference between the crystals used in the jewellery business and those used for technological applications is that the former are naturally occurring, whereas the latter are usually synthetic, that is, 'man-made'.

The primary reason why most crystals used in technological applications are synthetic is that a high degree of crystalline perfection and well defined chemical composition are essential in order to guarantee good electronic, optical, thermal, or mechanical properties.

In the past a vast amount of research has been carried out in order to achieve a better control of the crystallization processes (Hurle, ed., 1993, 1994). In order to accomplish this a good understanding of how crystals grow is essential (Bennema 1993). The method employed to grow crystals from various materials influence the shape and/or the quality of the product. If a crystal, for example, is grown from vapour or melt, its purity will be mainly determined by the purity of the starting material. If the growth proceeds from flux or solution the purity will also be determined by the components of the flux or solution that may be incorporated into the crystal.

It is not only the purity of the grown crystal that is affected by which solvent is used. Different impurities present in the solution will also affect the crystallization and may block the growth completely for not too high supersaturations. In addition, the shape of the crystal can also change drastically depending on the solvent. These phenomena are due to adsorption of these impurities onto the crystal surface during growth, hindering step advancement or changing the properties of the solid-fluid interface.

A phenomenon that is common to many crystalline materials is that they can undergo phase transitions in response to changes in the ambient conditions. Examples of such phase transitions are changes in the type of crystalline lattice as a function of temperature or the changes in the orientation of liquid-crystal molecules in response to changes in an electrical field. Some of these phase transitions are used to improve the quality of some product, for example, the hardening of steel. Others form the base of functioning of some devices, for example liquid-crystal displays. In many cases, however, phase transitions in a crystal will not improve its quality and can even destroy the crystal completely due to stresses generated during the transition.

All the crystals used in jewellery and virtually all the ones used in technologic applications undergo some kind of treatment after being mined or grown in order to reveal the beauty hidden in a natural precious stone or to get the shape that is required for a device. Among these treatments cutting and polishing are the most common. In order to cut or polish a crystal, a material harder than the crystal being worked on is used. This method works well for all crystals except diamond, which is the hardest material known. These carbon crystals are best cut and polished by other diamonds (Wilks and Wilks 1994).

An examination of the as-grown crystal and/or the final product is usually performed in order to either understand crystal growth better or to check for the quality obtained. For surface observation, optical microscopy is the most commonly used technique (van Enckevort 1984). Used in combination with polarized light, optical microscopy becomes sensitive to the crystal defect structure, lattice type and changes in crystallographic orientation.

In the past twelve years, sensitive techniques have been developed that are capable of giving images with extremely high resolution of a crystal surface (Binnig *et al.* 1982a, 1982b, Binnig and Rohrer 1983, Binnig *et al.* 1986). These techniques are known as scanning tunnelling microscopy (STM) and atomic force microscopy (AFM). Both of these techniques have the highest resolution in lateral and vertical directions, and are capable of giving atomic resolution on many materials. These are the main techniques used in this work and therefore will be discussed in more detail below.

2. Scanning tunnelling microscopy

In scanning tunnelling microscopy a difference in potential is applied between a sharp tip and a conducting specimen, the surface of which is to be imaged. The tip is then brought to a close proximity (a few angstrom) to the surface until a tunnelling current of typically one nano-ampere starts to flow. The tip is then scanned across the surface using elements made of piezoelectric ceramics (fig. 1). Conversely, the sample can be scanned under the tip in the same manner as described above. Usually a feedback system is used that moves the tip, or sample, in the direction perpendicular to the sample surface in order to keep a constant tunnelling current and, consequently, a constant distance between the tip and sample. The voltage necessary to stretch or shrink the piezoelectric element is used as a measure for the height of the surface features and with the known X-Y positions a three dimensional image is obtained. This scan mechanism is called 'constant current mode'. The tunnelling current is highly dependent on the distance between the tip and the surface (for a review on the theory of STM see Wiesendanger and Güntherodt 1993), which provides a high vertical resolution. Using a sharp tip images with very high lateral resolution can be obtained. Atomic resolution can be achieved for many materials, such as highly oriented pyrolytic graphite (HOPG), Si, GaAs and Au.

An alternative manner of obtaining a topographic image of the surface does not use the feedback system and the tip, or sample, are scanned without any corrections for the changes in distance between tip and sample. Due to the irregularities on the sample surface the distance between the surface and the tip, and thus the tunnelling current, changes during the scan. The changes in the tunnelling current are used as a measure for the height of the features on the surface and again a three dimensional image is obtained. This is called 'constant height mode'. This scanning procedure can only be applied to flat surfaces, since for rough surfaces the tip crashes on the sample. Since it is not necessary to control a feedback system, scanning in the constant height mode can be performed much faster (up to a few scans per second) than in the constant current mode. This enables relatively fast processes, such as the movement of steps on a growing crystal, to be detected.

STM measurements can be performed in many different environments. For samples that are susceptible to oxidation, or to changes on the surface due to reactions with gases, measurements can be performed in ultra-high vacuum. Measurements may also be performed in either non-conducting, or conducting, solutions. For conducting solutions, typically an almost completely isolated tip is used. The measuring temperatures may range anywhere from

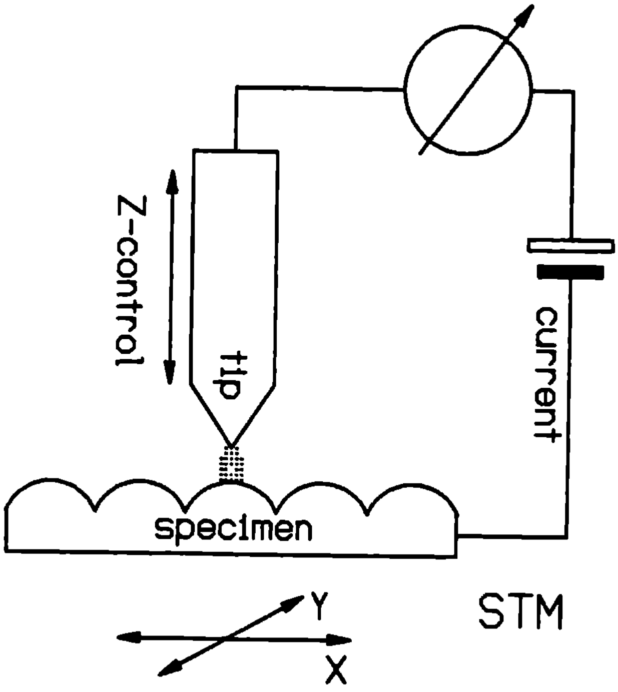

Fig. 1. Schematic of a scanning tunnelling microscope.

less than one Kelvin to about 800 K. These conditions allow for many experiments to be performed *in situ*, for example, crystal growth studies.

Although STM requires a conducting sample, many images could be successfully obtained from one to a few monolayers of nonconducting materials adsorbed on a conducting substrate. The mechanism of image formation for these layers is not completely understood but a few processes have been suggested that describe the tunnelling processes in these cases (Guckenberger *et al.* 1992).

Besides being highly dependent on the distance between tip and sample, the tunnelling current is also dependent on the surface local density of states (Wiesendanger and Güntherodt, eds., 1993). This makes the interpretation of the images obtained for materials that do not have a homogeneous distribution of the density of states more complicated, since the image obtained contains both topographic and electronic information. On the other hand, this dependence on the local density of states can be used to get some spectroscopic information of the surface being imaged. It is possible, for example, to make a distinction between gallium and arsenic atoms on a GaAs surface (Feenstra *et al.* 1987), or to observe how electronic states of individual atoms change when a chemical reaction takes place on a surface of silicon (Wolkow and Avouris 1988, Avouris and Wolkow 1989).

3. Atomic force microscopy

Contrary to STM, atomic force microscopy does not require a conducting sample. AFM uses a sharp tip attached to a cantilever spring that is also brought to a close proximity to the surface to be imaged. When the tip comes sufficiently close to the surface, some force acting between the surface and the tip attracts, or repels, the tip, thus bending the cantilever (Meyer and Heinzelmann 1992) (fig. 2). In order to detect this bending of the cantilever a few

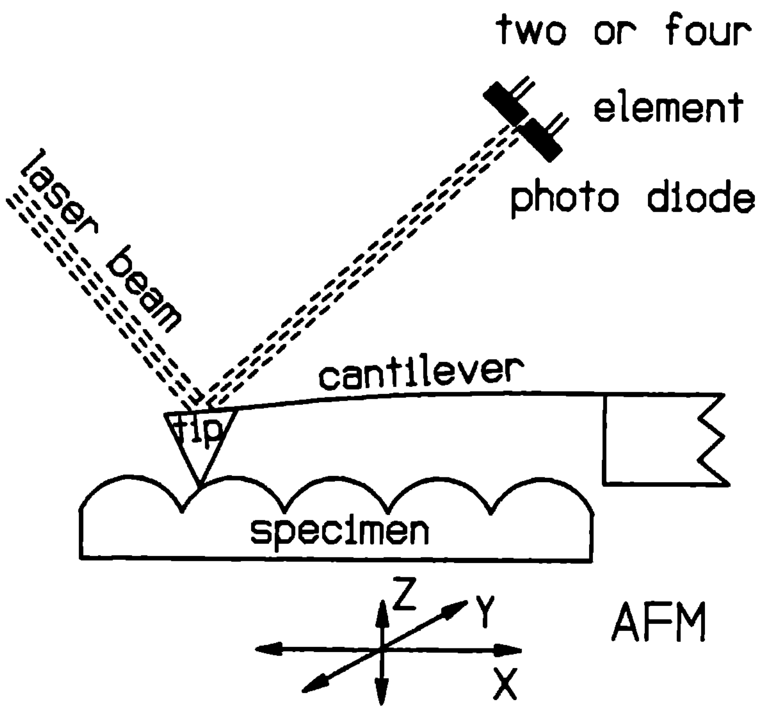

Fig. 2. Schematic view of an atomic force microscope: the amount of cantilever bending is a measure for the interaction force between the tip and the specimen surface.

techniques can be used.

In the first atomic force microscope a scanning tunnelling microscope was used to monitor the changes in distance between a fixed STM tip and the cantilever. Later, optical techniques, such as interferometry, were used to detect the movement of the cantilever. Measurements of changes in capacitance of a capacitor formed by the cantilever and another fixed plate can also be used. Presently most atomic force microscopes use laser beam deflection, that is, a laser beam shines on the cantilever and is reflected to a two or four quadrant photodetector. When the cantilever is bent the laser beam illuminates a different area on the detector and the movement of the cantilever can be monitored. Very low forces, in the order of 10^{-13} N, can be measured in this way. With a four quadrant detector the lateral bending of the cantilever can also be measured. This gives information on the frictional forces on the surface.

In atomic force microscopy there are three possible scan modes. The first one uses a feedback system in a similar fashion as described above for the STM. The only difference is that instead of a current, now it is the force between sample and tip that is kept constant. This scan mechanism is called 'constant force mode'.

In the second mode, the tip is scanned across the surface without the use of the feedback system. Due to the topographic features on the sample the force between surface and tip, and thus the deflection of the cantilever, varies during the scan. The photodetector monitors the changes in the position of the reflected laser beam resulting from the movement of the cantilever. Using this signal as a measure for height gives a three-dimensional image. This is called 'variable force mode'. A scan with variable force can be performed much faster than a scan with constant force.

For the third mode, the cantilever is brought to oscillate near its resonance frequency at a low amplitude. When the tip approaches the sample surface (without touching it) the force between sample and tip changes the effective spring constant of the cantilever, and consequently its resonance frequency. Monitoring the change in resonance frequency, or in oscillation amplitude, gives the information on the local height of the topographic features. This is called 'non-contact mode'. This scanning procedure is often not stable since if the tip penetrates the thin contamination layer which is common for many specimen surfaces it may be trapped inside it, ceasing to oscillate. The cantilever may also be brought to oscillate at a higher amplitude than in the procedure described above. The amplitude is set to such a value that the tip moves in and out through the contamination layer, just touching the sample surface: the so-called 'tapping mode'. The advantage of the latter two types of scans is that forces between the sample and tip can be reduced to values lower than the ones used for the first two scan modes described above. In addition, the frictional forces can be almost completely eliminated.

Like STM, AFM can also be used in air, vacuum, or solution. Due to water vapour in the atmosphere, samples measured in air normally are covered by a thin layer of adsorbed water. When the tip is brought close to the surface (within this moisture layer), capillary forces pull the tip towards the surface and the force between tip and sample is increased. For 'soft' samples this can be a problem since due to these large forces the tip can damage the surface during the scan. Imaging with the sample, tip, and cantilever immersed in some liquid eliminates the capillary force, thus enabling a scan with lower forces between sample and tip. For biological specimens, scanning in solution is also an advantage since samples such as cells can be kept alive during the scan (Häberle *et al.* 1991).

Contrary to STM, spectroscopic measurements have not been developed in combination with AFM. Measurements of the forces between sample and tip, as a function of the distance between them, can be performed for different points on the surface. This gives information on surface properties, such as elasticity and adhesion, with great spatial resolution. Monitoring the lateral bending of the cantilever during the scan gives information on frictional forces between surface and tip (McClelland and Glosli 1992).

4. Scope and summary

In this thesis scanning tunnelling microscopy and atomic force microscopy are primarily used to study crystal surfaces.

Part I (chapters 1 through 6) deals with the study of diamond polishing. In order to solve the problem of how material is removed from the diamond surface during polishing, many diamonds polished along different crystallographic orientations are studied. From the surface topography explanations for the polishing mechanisms along the crystallographic directions of difficult and easy material removal have been deduced.

In Part II (chapters 7 through 9) several types of crystals are studied *in situ* and *ex situ* using, not only STM and AFM, but also optical microscopy. Chapter 7 treats the problem of phase transitions of C_{70} crystals that affect the surface morphology. The transition from an f.c.c. to a rhombohedral structure is studied and an explanation is given for the domain structure observed on the $\{100\}$ and the $\{111\}$ faces.

Chapter 8 deals with the growth of $K_2Cr_2O_7$ crystals. *In situ* measurements are performed to study the effect of impurities on the growth process. *Ex situ* measurements using the AFM give a high resolution view of the shape of the steps, allowing for a comparison between different growth models.

Chapter 9 treats the problem of the adsorption of n-alkane molecules on graphite. A model for the ordered structure that is formed on the graphite surface is given. The effects of temperature on the ordering of the molecules are presented.

5. References

Avouris, Ph., and Wolkow, R., 1989, Phys. Rev. B, **39**, 5091.

Bennema, P., 1993, *Handbook of Crystal Growth*, Vol. 1, edited by Hurle, D. T. J., (Amsterdam: Elsevier Science Publisher B.V.) p. 477.

Binnig, G., Rohrer, H., Gerber, Ch., and Weibel, E., 1982a, Phys. Rev. Lett., **49**, 57.

Binnig, G., Rohrer, H., Gerber, Ch., and Weibel, E., 1982b, Apply. Phys. Lett., **40**, 178.

Binnig, G., Rohrer, 1983, Surf. Sci., **126**, 236.

Binnig, G., Quate, C. F., and Gerber, Ch., 1986, Phys. Rev. Lett., **56**, 930.

Feenstra, R. M., Stroscio, J. A., Tersoff, J., and Fein, A. P., 1987, Phys. Rev. Lett., **58**, 1192.

Guckenberger, R., Hartmann, T., Wiegräbe, W., and Baumeister, W., 1992, *Scanning Tunneling Microscopy II*, edited by Wiesendanger, R., and Güntherodt, H. -J. (Berlin Heidelberg: Springer-Verlag) p.99.

Häberle, W., Hörber, J. K. H., and Binnig, G., 1991, J. Vac. Sci. Technol. B, **9**, 1210.

Hurle, D. T. J., ed., 1993, *Handbook of Crystal Growth 1*, (Amsterdam: Elsevier Science Publisher B.V.).

Hurle, D. T. J., ed., 1994, *Handbook of Crystal Growth 2*, (Amsterdam: Elsevier Science Publisher B.V.).

McClelland, G. M., and Glosli, J. N., 1992, *Fundamentals of Friction: Macroscopic and Microscopic Processes*, edited by Singer, I. L., and Pollock, H. M., (Dordrecht: Kluwer Academic Publishers) p. 405.

Meyer, E., and Heinzelmann, H., 1992, *Scanning Tunneling Microscopy II*, edited by Wiesendanger, R., and Güntherodt, H. -J. (Berlin Heidelberg: Springer-Verlag) p.99.

van Enckevort, W. J. P., 1984, Progr. Cryst. Growth Charac., **9**, 1.

Wiesendanger, R., and Güntherodt, H. -J, eds., 1993, *Scanning Tunneling Microscopy III*, (Berlin Heidelberg: Springer-Verlag).

Wilks, J., and Wilks, E., 1994, *Properties and Applications of Diamond*, (Oxford: Butterworth-Heinemann).

Wolkow, R., and Avouris, Ph., 1988, Phys. Rev. Lett., **60**, 1049.

Part I

Diamond polishing

Chapter 1

Introduction

In ancient times diamonds were probably worn in their original, as-grown state. This made natural octahedrons and dodecahedrons of high symmetry much in demand. In the fourteenth century the first diamonds were polished to improve the regularity of the natural polyhedral forms. In later centuries this primitive shape developed into the modern standard brilliant and other cuts which exhibit the well-known sparkling effect. Although refined, the basic elements of the diamond polishing technique did not alter and remain based on the fact that the ultrahard diamond can only be polished at an acceptable rate by diamond. Nowadays diamond is polished by pressing a crystal against the surface of a rapidly rotating (about 50 m s^{-1}) cast-iron wheel, or scaife, of selected porosity. The scaife is charged with a mixture of diamond powder and oil and subsequently skimmed in order to press this mixture into the pores. The rate of material removal during polishing varies strongly with crystallographic orientation of the face being polished and with the direction of polish on that face. If the right crystallographic direction and orientation with respect to the scaife are selected, polishing rates of several micrometers per minute can be obtained. The anisotropy in material removal rate has long been known to diamond polishers, who explained this effect in terms of the 'grain' of a diamond. The directions of fast polishing are indicated as soft and the slow directions as hard. Until the third decade of this century diamond technology was based on 'art' rather than 'science'.

Following five centuries of empiricism, Tolkowsky (1920) carried out the first systematic measurements of diamond polishing rates, measuring the loss of weight as a function of time, polishing speed and crystal orientation. Later his results were confirmed and extended by Slawson and Kohn (1950), by Denning (1953, 1955, 1957) and by Wilks and Wilks (1959, 1972). Figure 1 shows the relation between the directions of slow material removal during polishing and the crystallographic orientation. From his experiments Tolkowsky concluded that material removal is a mechanical fracture process involving {111} cleavage of small octahedral and tetrahedral fragments and that the anisotropy of polishing was due to the orientation of the cleavage planes relative to the surface being polished. From this hypothesis which has been refined by Wilks and Wilks (1959, 1972), it follows that polished diamond surfaces should be rough on a nanometre scale with features delineated to some extent by {111} cleavage planes.

For a diamond stylus sliding on diamond the coefficient of friction is dependent on the crystallographic orientations of the polished face and the stylus as well as on the crystallographic direction of sliding. Seal (1958) showed for several diamond surfaces abraded with diamond powder that the orientations with the highest coefficient of friction coincide with those of the lowest grinding hardness. The correspondence between both phenomena prompted Seal to suggest that material removal during diamond polishing is a thermally activated pro-

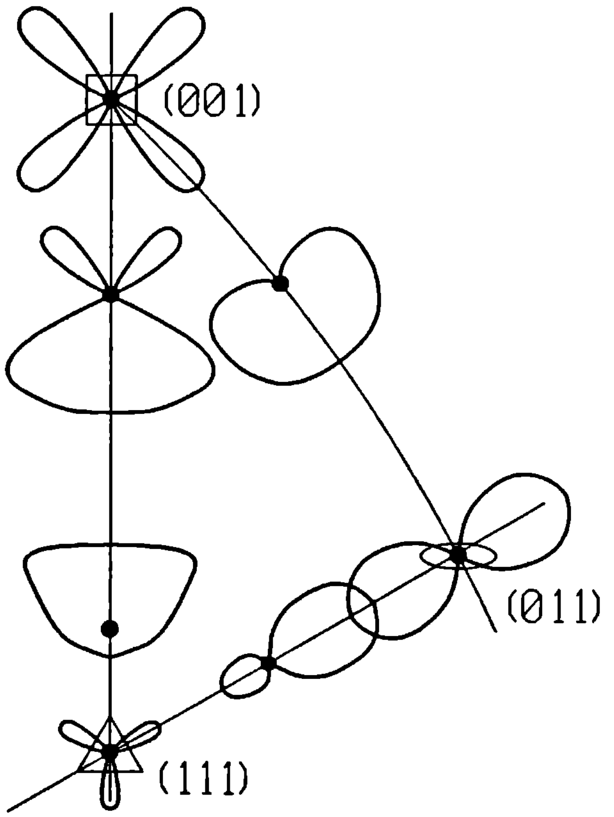

Fig. 1. Qualitative polar diagrams showing the directions of slow material removal during polishing as a function of crystal direction, imaged for several crystal faces on the stereographic projection of one asymmetric unit in the diamond point group m3m.

cess induced by the heat of friction generated during abrasion. In this hypothesis diamond 'vanishes' as graphite, CO or CO_2 and the diamond surface becomes smooth on a nanometre scale. However, this model conflicts with the observation that the rate of diamond removal depends linearly, rather than exponentially, on abrasion velocity (Tolkowsky 1920, Wilks and Wilks 1959, 1972). Moreover, it has been shown that the coefficient of friction between a diamond surface and a moving slider depends on the number of traverses (Seal 1981) and changes completely after some 25 passes.

In 1965 a third mechanism of diamond polishing was put forward. In this model Seal (1965, 1967) suggested that carbon atoms are removed singly or in small groups combined with surface species such as hydrogen thus forming hydrocarbon or other compounds. In such a process the statistical concepts of temperature and thermal activation become ill defined as only small groups of atoms are involved at any one location and the chemistry results from direct application of stress. This chemical hypothesis accounts for the anisotropy of polishing, its linearity with abrasion speed and the observed influence of ambient gases. According to this chemical model a polished diamond surface should also be smooth on a nanometre scale.

In the following three decades the problem of diamond polishing has been debated in several papers (Bowden and Tabor 1965, Wilks and Wilks 1979, 1991, 1992, Enomoto and Tabor 1981, Tabor and Field 1992), but the actual mechanism of material removal is not yet understood.

From experiments in which a diamond stylus slides at low speeds along a diamond surface it has been shown by reflection electron microscopy (REM) that, after single or multiple passes of the stylus, material can be removed from the diamond (Wang *et al.* 1991, Feng and Field 1992). It was observed that material removal can take place by three mechanisms, namely, at low pressures, atomic attrition (Seal 1965, 1967), at medium pressures and small stylus radius, 'plastic' grooving (Seal 1958, Wang *et al.* 1991) and, at high pressures, fracture (Seal 1958, Wang *et al.* 1991). Atomic attrition is material removal atom by atom, and one expects smooth surfaces or smooth grooves formed after many passes of the stylus. 'Plastic' grooving gives smooth grooves in one single pass of the stylus across the diamond surface. Fracture produces a rough structure or rough grooves in one or in multiple passes of the stylus.

One way to obtain information on the mechanism of diamond polishing is the careful examination of the polished surfaces. In the past this was done by using optical microscopy (Tolansky 1955), scanning electron microscopy (SEM) (Postek and Evans 1989), transmission electron microscopy (TEM) using a tungsten replica technique (Thornton and Wilks 1976) and by reflection electron microscopy (Seal 1958, Wang *et al.* 1991, Wang 1991, Tabor and Field 1992). These techniques showed that the surface presents polishing grooves, an overall surface roughness on a 5 nm scale (Seal and Menter 1953, Seal 1958, Thornton and Wilks 1976) and subsurface damage (Enomoto and Tabor 1981). Although these methods provided some essential information it was not possible to discriminate between hypotheses concerning material removal during diamond polishing.

Recently scanning probe microscopy has successfully been applied for the examination of the surface morphology of diamond crystallites grown from the gas phase (Turner *et al.* 1991, Tsumo *et al.* 1991).

In the attempt to find out what is the actual mechanism for material removal during diamond polishing in the soft directions, we used the techniques of scanning tunnelling microscopy (STM) and atomic force microscopy (AFM) to analyze features on the surfaces of polished diamond crystals.

Chapter 2

Scanning tunnelling microscopy of polished diamond surfaces[1]

M. S. Couto, W. J. P. van Enckevort

Department of Solid State Chemistry, University of Nijmegen, Faculty of Science, Toernooiveld, 6525 ED, Nijmegen, The Netherlands

B. Wichman,

Road and Hydraulic Engineering Division, Ministry of Transport, Public Works and Water Management, van der Burghweg 1, 2628 CS Delft, The Netherlands

M. Seal,

Sigillum B.V., Guido Gezellestraat 5, 1077 WN, Amsterdam, The Netherlands

Abstract

The morphology of surfaces polished on semiconducting diamonds has been investigated by scanning tunnelling microscopy. A {100} face polished in a direction of difficult abrasion is characterized by a hill and valley pattern. Cross-banded grooves, produced by a stick-slip process are found for the octahedral faces. When polished in a direction of easy abrasion, the {100} and {110} surfaces exhibit a pattern of superimposed, well-formed grooves, the surfaces of which are smooth down to a few nanometres.

---

[1] *Applied Surface Science **62** (1992) 263*

1. Introduction

In this chapter the technique of scanning tunnelling microscopy (STM) was used to study the surface topography of diamonds polished along the soft and hard directions. The aim of this study is to discover what are the mechanisms of polishing for different crystallographic planes along different crystallographic directions. The mechanisms of material removal by single or multiple passes of the abrading particles are discussed.

2. Experimental details

Scanning tunnelling microscopy (STM) needs electrically conducting specimens. Since the electrical resistance of natural, semiconducting type IIb (Collins and Lightowlers 1979) diamonds is too high, we resorted to heavily boron doped, high-pressure high-temperature synthetics. In such p-type crystals the distribution of the boron impurity is not uniform (Burns *et al.* 1990), so that only surfaces adjacent to volumes of maximal acceptor concentrations were examined. From infrared absorption spectroscopy (Burns *et al.* 1990) it followed that in these regions the concentration of uncompensated acceptor centres was about 10 atomic ppm.

From three crystals, plates and blocks with faces parallel to {100}, {110} and {111} were cut and polished. Polishing was carried out by the conventional method in which the specimen diamond is pressed against the surface of a cast-iron wheel charged with a mixture of diamond powder (particle diameter less than 15 μm) and oil, and rotating at high speed about a vertical axis. The polishing speed was 50 m s^{-1}. During polishing no *zoeten*, that is, lateral movement of the specimen, was applied. The (100) faces were polished along a direction of easy abrasion [010] or an abrasion-resistant direction, 15° from [011]. The (110) surfaces were polished along the easy [001] direction and the (111) face along approximatelly $[1\bar{1}0]$.

The quality of the polished surfaces is similar to that of standard brilliant facets, that is, mirror smooth. However, since no *zoeten* was applied a faint pattern of shallow polishing lines can be recognized by optical microscopy. The surfaces of the commercially available or 'home produced' optical quality diamond windows, which, among other, are used for surface reconstruction studies in ultra-high vacuum systems (Hamza *et al.* 1988, 1990), are abraded in essentially the same manner, except that finer powders are used. Since the nanometre scale morphology of a polished diamond face varies only slightly with the particle size of the powder used (Bailey and Seal 1956), the general features of 'optical quality' diamond surfaces are expected to be comparable to that of the present specimens.

Prior to STM the specimen surfaces were cleaned by boiling in an aqueous solution of detergent, followed by rinsing in distilled water and isopropyl alcohol. To verify the influence of adsorbed surface layers formed after cleaning, a fourth type IIb diamond was cleaved along {111} and subsequently treated in the same manner. Its surface, which, except for cleavage steps, should be atomically smooth served as a reference.

The STM instrument used was home-made and, except that the electrochemical cell was replaced by a conventional sample holder, identical to that described by Hottenhuis *et al.* (1988). The tips were prepared from 0.5 mm 90% Pt–10% Ir wire by mechanical cutting. The measurements were carried out under atmospheric conditions.

3. Results and discussion

Figure 1 shows a typical current-voltage curve recorded for the cleaved specimen. Similar curves were also found for the polished crystals. The observed diode behaviour is characteristic for a Schottky barrier at a metal–p-type semiconductor interface. Therefore a detectable tunnelling current could only be obtained for negative tip voltages. The selection of the optimal voltage was essential for obtaining good STM topographs. Too high a voltage (between -2.0 and -3.0 V) led to a dramatic decrease in lateral and vertical resolution, probably because a considerable area of the needle top was in direct contact with the surface. A voltage below -4.0 to -5.5 V produced images dominated by noise which must be attributed to effects other than simple tunnelling. The best images were obtained for voltages ranging from -3.0 to -5.0 V, depending on the dopant level of the crystals. All the topographs in this paper were produced in the constant current mode, keeping the current at 200 pA. Lower currents resulted in a loss of resolution and higher currents gave no essential improvement.

Scanning of the cleaved specimen crystal only revealed up to 16 nm cleavage steps as well as a number of perturbed regions. For the rest the surface was very smooth, although individual atoms could not be observed. Probably due to a preferential accumulation of adsorbed material at the step edges, the lowest cleavage steps on the topographs appeared as elevations of about 0.5 nm in height. From this it follows that height differences down to 0.5 nm can be detected. Further it was deduced from the various STM topographs, that the lateral resolution was limited to a few nanometres. The loss of resolution might be explained by the presence of an adsorbed surface layer of about 1 nm in thickness. Although in STM spatial changes in electrical properties are also imaged as height variations, in the present case of polished diamond surfaces the observed differences in height are far too large to be accounted for by this effect.

Figure 2 shows the surface structure of a (100) plate polished in a direction 15° from [011]. This is a direction of difficult abrasion (Tolkowsky 1920, Seal 1958, Wilks and Wilks 1959, 1972, Thornton and Wilks 1976). The very rough surface is dominated by a hill-and-

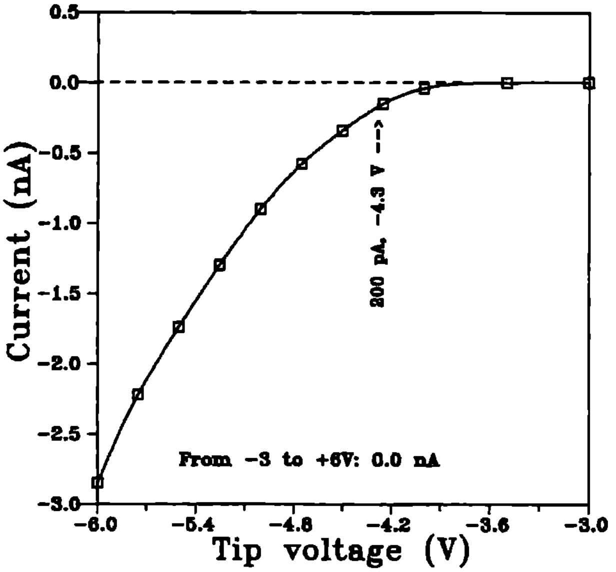

Fig. 1. Current-voltage curve measured for a fixed tip-surface separation on the cleaved type IIb diamond surface.

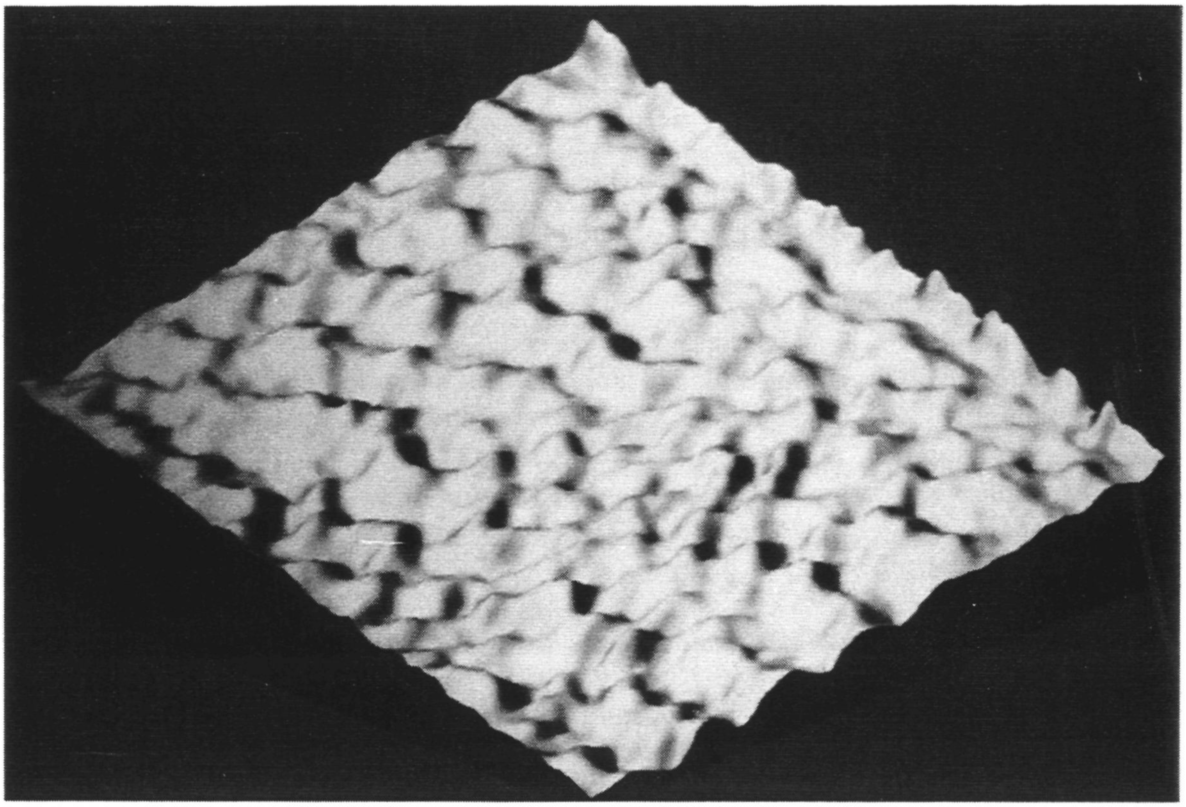

Fig. 2. STM image of a 500 nm × 500 nm region of a diamond (100) surface polished 15° from [011]. The surface is shaded with a light source shining from the left-hand side.

valley pattern. The average width of the features is 38 nm, their height is about 4 nm. In other words, the elevations are somewhat steep with an inclination of roughly 12°. Although somewhat larger, the structures look quite similar to the electron microscopic patterns as imaged by Thornton and Wilks (1976) for several polished diamond surfaces. Also irregular polishing grooves with fragmented side-walls were observed. The morphology of this crystal surface is indicative of a polishing mechanism involving fracture and chipping on a nanoscale.

A different pattern was found for the polished {111} surfaces (fig. 3). It consists of many cross-banded grooves which are parallel to the polishing lines as observed by optical microscopy. The channels are about 30 nm wide and 6 nm deep. The features are indicative of a stick-slip process during diamond polishing and look very similar to the fracture patterns which are produced when a hard, spherical indenter scratches a planar diamond surface (Seal 1958). The average height (about 4 nm) of the cross-bands is slightly less than the depth of the grooves. This strongly suggests that the grooves were formed during one single pass of a moving, abrading particle. From the polishing speed and separation between two successive cross-bands the stick-slip frequency was deduced to be approximately 1 GHz. In comparison with the abrading particles the grooves are very narrow. This means that the contact between a particle and the diamond surface is non-uniform and interaction only takes place via corners or asperities on the tops of the particles (Wang 1991). It seems that for abrasion of the resistant {111} faces polishing also proceeds via nanofracture and chipping.

Polishing in the soft directions (Tolkowsky 1920, Seal 1958, Wilks and Wilks 1959, 1972, Thornton and Wilks 1976) produces well formed grooves. Figure 4 gives the characteristic morphology of a (100) surface polished along [001]. Its structure can be considered as

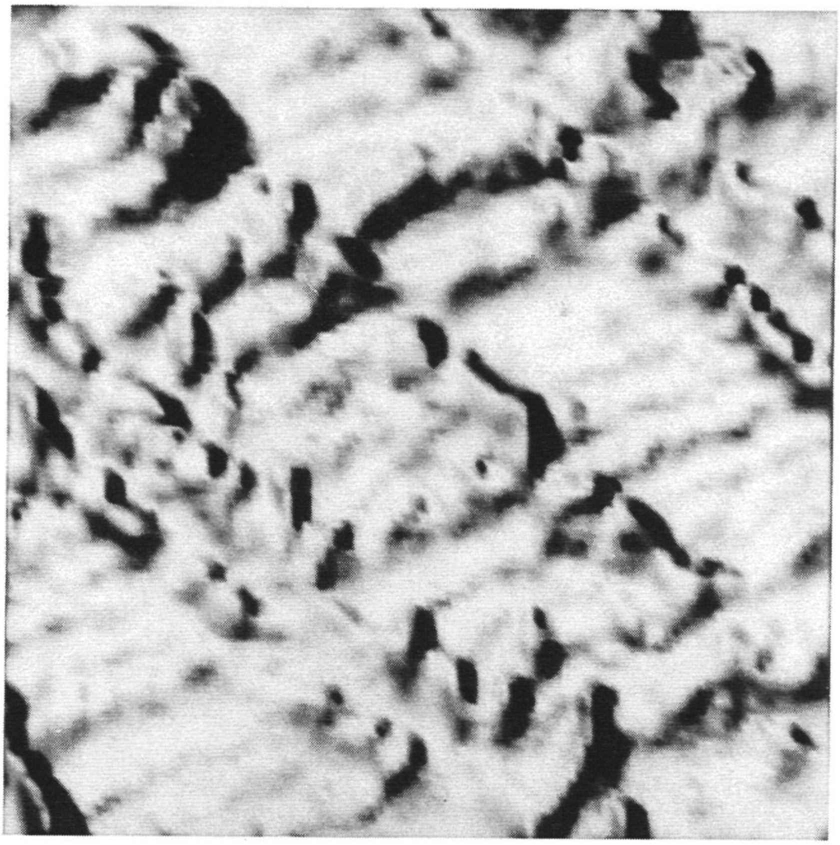

Fig. 3. STM grey-scale representation of a 400 nm × 400 nm region of a (111) surface polished along [1$\bar{1}$0]. The surface is shaded with a light source shining from the left-hand side.

a superposition of many grooves, which are 20 to 100 nm wide and 4 to 12 nm deep. The average slope of the side-walls is about 13°, which is somewhat steep. The structure of the (110) faces polished along the soft directions [001] looks very similar to the (100) face of fig. 4, except that the grooves can have larger dimensions, up to 32 nm in height and 200 nm in width. On {100} and {110} faces polished along their easy directions, the rounded groove surfaces exhibit a smoothness down to the resolution limit of a few nanometres. No evidence was found for the occurrence of ring cracks, micro-cleavage patterns or other fracture structures.

In interpreting the observed patterns of the grooves, it should be considered that the observed surface profile in fact is a convolution of the tip shape and the actual surface structure. This implies that the side walls of the grooves can be steeper than given above. The smoothness of the surface is not a tip shape effect since the resolution at the top of the grooves, where the effects from tip convolution are expected to be much less, is identical to that in the valleys. The application of different needles to the same specimen surface yielded the same results.

It seems that diamond polishing in the soft directions does not proceed via simple cleavage, chipping or micro-fracture. Also the grooves cannot result from thermal wear induced by the heat of friction. In that case the channels would be expected to broaden and to become shallower, because of simultaneous wear of the abrading diamond particles digging into the surface. Therefore an alternative explanation has to be found. From the literature it is known that smooth grooves in diamond can be formed in two distinct manners.

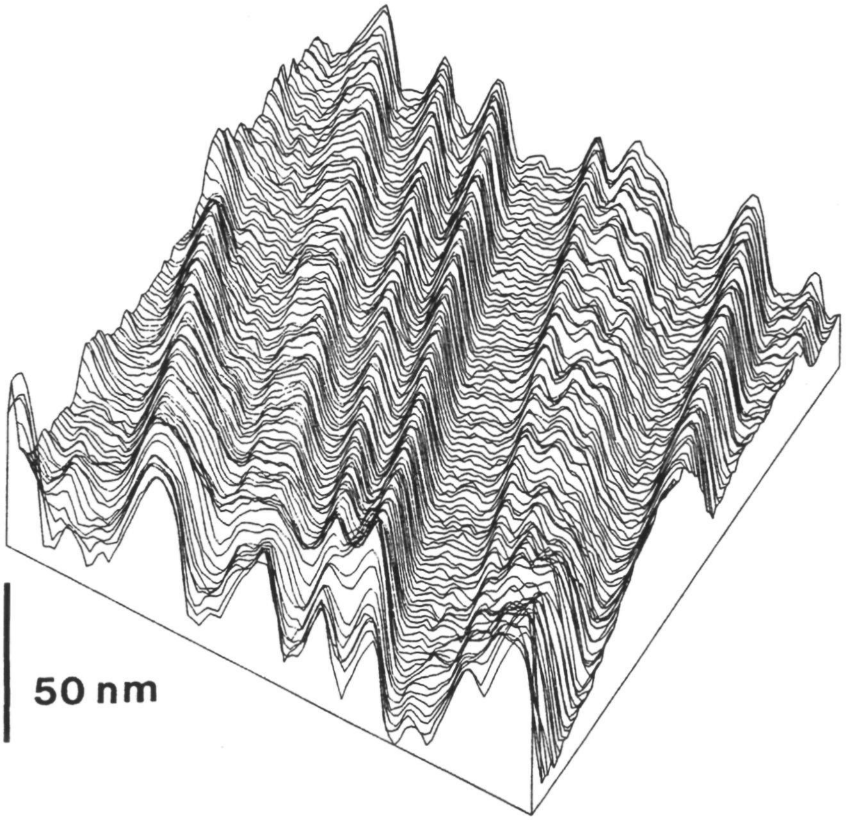

Fig. 4. STM image of a 500 nm × 500 nm region of a diamond (100) surface polished along [001].

(i) After a single pass of a sharp pointed sliding indenter at a supercritical load. In contrast to sliders with radii above about 30 μm, which cause the well known ring crack patterns, sharper sliders produce grooves free from cracking (Seal 1958, Seal 1967, Wang 1991, Wang *et al.* 1991). Wang *et al.* (1991) proposed that plastic deformation is here the underlying mechanism of groove formation. Seal (1967), however, suggested that the patterns are generated when the slider radius is sufficiently small that the critical stress required for crack formation exceeds the intrinsic strength of the diamond. Then grooves are formed by failure through disruption of interatomic bonds and disintegration of material (Roesler 1956). It is unlikely that plastic deformation plays a major role in diamond polishing, though Seal and Menter (1953) have suggested that some plastic deformation might be a consequence of polishing. Evidence against plastic deformation comes from TEM of some polished diamond cutting edges which revealed only a few (probably grown-in) dislocations, superimposed on a set of clear Pendellösing fringes.

(ii) After multiple passes of a sliding indenter at subcritical load (Seal 1965, 1967). Under such low pressure conditions no damage visible by optical microscopy or SEM could be detected after one or a few traverses. Repeated sliding over 10^3 to 10^6 passes, however, produced a clearly visible groove pattern. The average rate of material removal was considerably less than one atomic layer per traverse. This means that atoms or groups of atoms are removed statistically during sliding. The radicals produced in this way react with the ambient atmosphere and form organic substances. At higher temperatures these disintegrate into amorphous carbon. If the atom groups are more than say two nanometres across, then it is better to formulate the wear process in terms of nanofracture (Wilks and Wilks 1959, 1972, Thornton and Wilks 1976) rather than chemical attrition. REM of friction tracks produced at subcritical loads revealed a reorganization of the diamond surface on an atomic scale as well as some fracture (Hamza 1990).

The STM topographs of the diamond surfaces polished in the easy directions do not give information on whether the grooves are formed in a single pass or are a result of many passages by different abrading particles. No definite mechanism for material removal can be formulated in this case.

4. Conclusions

The present work has shown that different mechanisms are involved in polishing easy and difficult directions on diamond surfaces. Material removal in abrasion along the hard directions proceeds via fracture and chipping on a nanoscale. However, in the case of the soft directions no definitive mechanism for polishing can be given yet. In the coming research this question will be tackled by Monte Carlo simulations, STM of highly conductive (gas-phase grown) polished diamond surfaces and wear measurements at low sliding speeds.

5. Acknowledgements

The authors are grateful to Prof. Dr. P. Bennema and Prof. Dr. H. van Kempen for their interest in this work and to Dr. H. Meekes and Mr. J. W. Gerritsen for their help in setting up the STM facilities. In addition they are indebted to Mr. G. Pels and Mr. M. van den Heuvel for many stimulating discussions on diamond polishing. They wish to thank Dr. J.L. Hutchison for making TEM photographs.

One of the authors, M. S. Couto, wants to thank CAPES (Coordenação de Aperfeiçoamento de Pessoal de Nível Superior), Brazil, for a scholarship making this research possible.

Chapter 3

Nanostructures on polished diamond surfaces[1]

W. J. P. van Enckevort, M. S. Couto

Department of Solid State Chemistry, University of Nijmegen, Faculty of Science, Toernooiveld, 6525 ED, Nijmegen, The Netherlands

M. Seal,

Sigillum B.V., Guido Gezellestraat 5, 1077 WN, Amsterdam, The Netherlands

Abstract

The polished surfaces of several semiconducting diamonds have been examined by scanning tunnelling microscopy. It was found that the faces polished along a direction of difficult abrasion show a rough structure which indicates that material was removed by fracture and chipping on a nanometre scale. The faces polished along a direction of easy abrasion are covered by many, superimposed smooth grooves which are 20–100 nm wide and 2–12 nm deep. Possibly material was removed by ploughing by an abrading particle at supercritical load in one single pass, followed by the polishing action of numerous other particles at subcritical loads. From the present surface topographic study essential information on the process of diamond polishing has been obtained, but new questions have arisen too.

---

[1] *Industrial Diamond Review 53 (1994) 323*

1. Introduction

In order to obtain more information on the mechanisms of diamond polishing the techniques of scanning tunnelling microscopy (STM) and optical phase shifting interferometry (PSI) were applied to study diamond surfaces polished along the soft and hard directions. The effect of the application of *zoeten* and the possible mechanisms of material removal during polishing are discussed.

2. Experimental details

Since STM requires electrically conducting specimens, high-pressure high-temperature (HPHT) or chemical vapour deposition (CVD) grown synthetic diamonds with a large content of boron were used. The resistivity of the single crystals ranged from 10^2 Ωcm for the HPHT diamonds to 1 Ωcm for the CVD-grown diamonds. The tips for STM were prepared from 90% Pt–10% Ir wire by mechanical cutting. All the measurements were carried out under atmospheric conditions and in the constant current mode, keeping the tunnelling current at 200 pA.

For all the specimens polishing was carried out by the conventional method as described before, using diamond powder with a particle diameter less than 15 μm mixed with a small amount of (liquid) paraffin and a polishing speed of 50 m s^{-1}. The quality of the polished surfaces is similar to that of standard brilliant facets, that is, mirror smooth. Prior to STM the crystal surfaces were cleaned by three different methods, namely gently boiling in an aqueous solution of detergent, heating at 400°C in vacuum (10^{-3} Torr) and twenty minutes treatment with concentrated H_2SO_4. None of the cleaning procedures affected the surface structure as imaged by STM.

3. Results

3.1. Diamonds polished along a hard direction

Figure 1 shows the surface structure of a (100) plate polished in a direction 15° from [011]. This is a direction of difficult abrasion. The nanostructure of this surface is composed of a hill-and-valley pattern. The average width of the features is 40 nm and they are 4 nm deep. In some cases some rudimentary grooves with fragmented walls can be seen. A similar rough pattern was found for the hard {111} diamond surfaces which normally are avoided by diamond polishers. On these surfaces cross-banded grooves indicative of a stick-slip process during diamond polishing were found. They look very similar to the fracture patterns which are produced when a hard spherical indenter at maximal load scratches a planar diamond surface. In other cases 25 to 100 nm triangular fracture patterns were encountered, in accordance to the three-fold axis perpendicular to the {111} faces (fig. 2).

It is evident from all the STM topographs of the diamond surfaces which were polished along hard directions that polishing here proceeds via fracture and chipping on a nanometre scale. Material removal takes place in essentially the same way as proposed by Tolkowsky (1920) and Wilks and Wilks (1959, 1972): namely formation of cracks or cleavages followed by break-out of small diamond fragments.

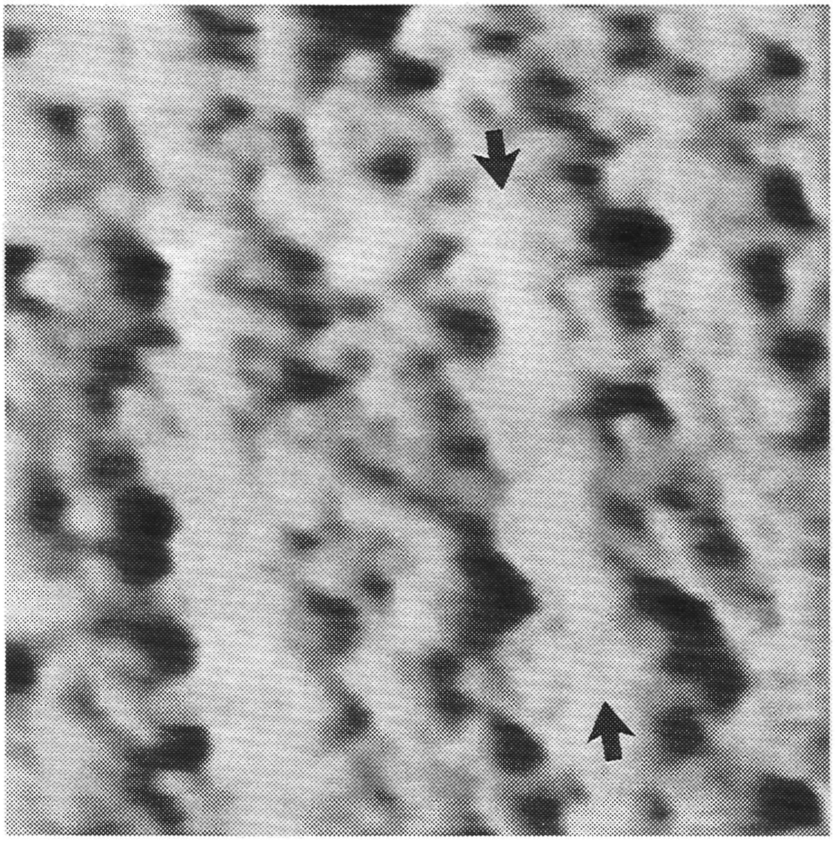

Fig. 1. STM image of the (100) surface of a HPHT-grown diamond polished along a (hard) direction 15° from [011]. The scan size is 925 nm × 925 nm. The arrows in this and several other STM topographs presented in this chapter indicate the direction of polishing.

3.2. Diamonds polished along a soft direction

In producing jewellery or high technology products from diamond the crystals are nearly always polished along the soft directions. Polishing along these directions is more economical, because the rate of material removal exceeds that in the hard directions by two or more orders of magnitude. Therefore special attention has been given to the surface morphology of (001) and (011) diamond plates polished along the soft directions [100].

Figures 3 and 4 show the typical surface structures of both (001) and (011) surfaces. Both surfaces can be considered as a superposition of many smooth grooves parallel to the direction of polish [100]. The features are 20 to 200 nm wide and 4 to 30 nm deep. The nanogrooves have walls sloping up to typically 5° to 20° with respect to the horizontal. The gaussian distribution of slopes at the side walls (Couto *et al.* 1994a (see chapter 4)) indicates that no preferred crystallographic orientation occurs. For the HPHT-grown diamonds the grooves are smooth down to the resolution limit of the STM. The CVD-grown diamonds show the outcrops of cleavage cracks parallel to {111} at some of the polishing grooves. This agrees with the occurrence of subsurface damage of polished diamond faces as was deduced from Rutherford He^+ backscattering spectroscopy (Haisma *et al.* 1992). In contrast to the hard directions no evidence was found for a break-out of Tolkowsky-type diamond fragments.

The grooves formed after polishing in the soft directions show two intriguing aspects.

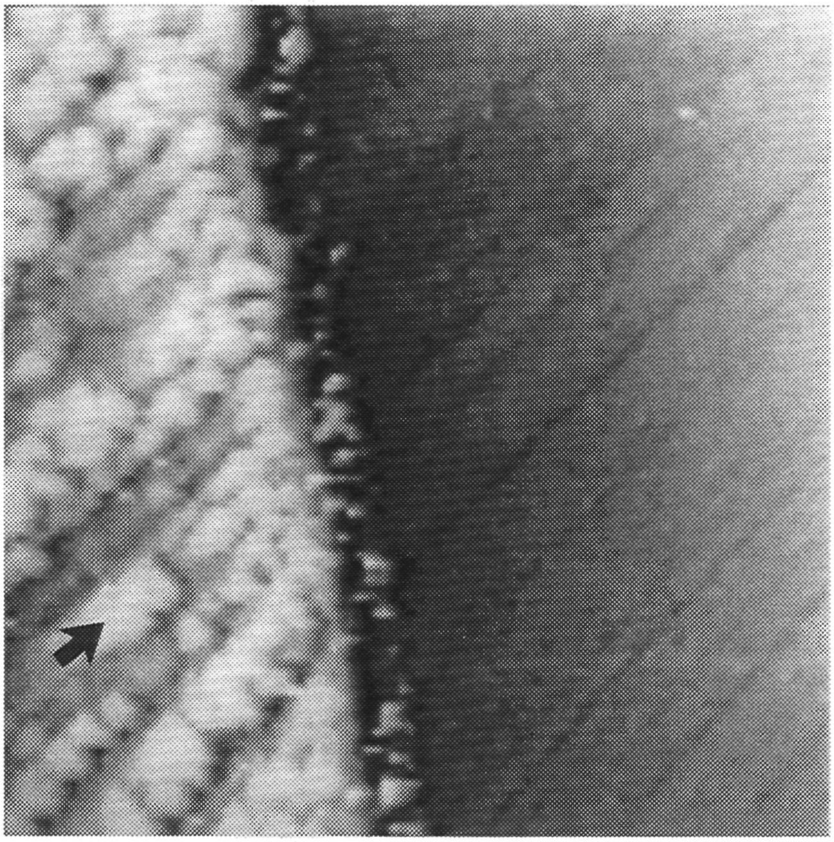

Fig. 2. STM image of a {111} diamond crystallite in a {110} surface of a CVD-grown diamond showing a triangular fracture pattern. The surrounding crystal shows a pattern of smooth grooves. The scan size is 1.1 μm × 1.1 μm.

First, in comparison to the size of the abrading diamond particles the width of the channels is two to three orders of magnitude smaller. This means that the contact between a particle and the diamond surface is not uniform and interaction only takes place via corners and asperities on the particles. Polishing can also proceed by interaction with small, loose particles which are broken off from the powder particles and form a slurry with the surface oil film. A second observation that poses questions is the fact that the shape of the grooves persists over distances exceeding the 20 μm scanning range of the STM used. Both depth and width do not alter. This implies that in contrast to the surface being polished the abrading particles show no simultaneous wear. If they did the channels would be expected to broaden and to become shallower.

3.3. Zoeten

The nanogrooves on diamond surfaces polished in the easy directions are very different from those seen by the standard ten times magnifying loupe used in the diamond trade or by an optical interference contrast microscope. The 'optical grooves' are 1 to 25 μm wide and have inclinations from one hundredth to a few tenths of a degree (fig. 5). To obtain very smooth facets, free from polishing lines, diamond workers generally apply *zoeten* (dutch for the verb 'to smooth'). This is a repeated, lateral movement of the workpiece during polishing.

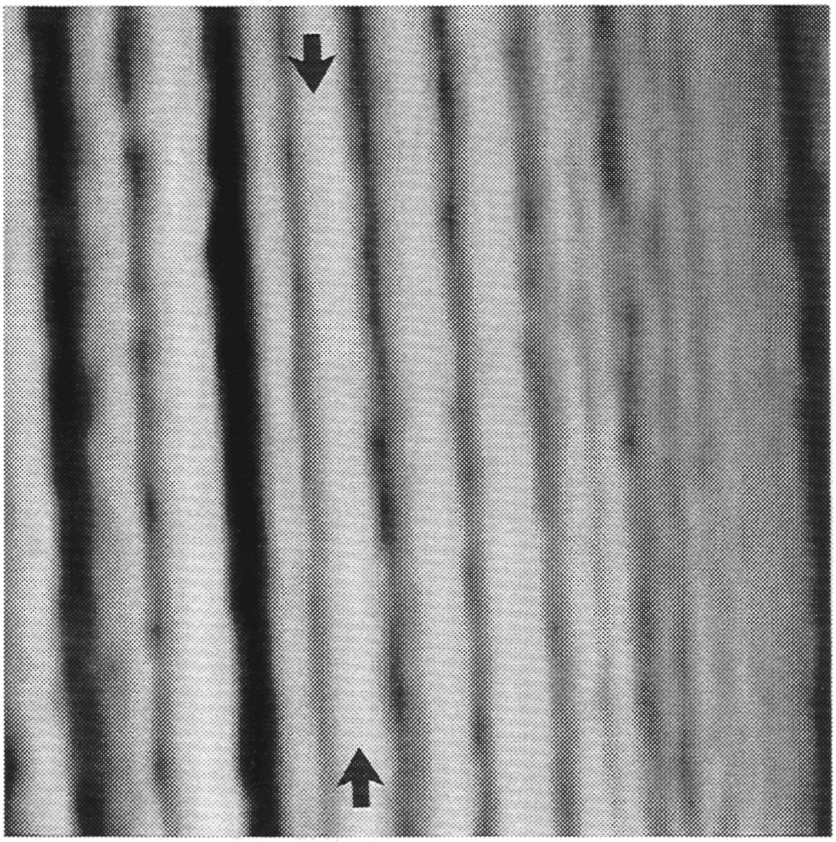

Fig. 3. STM image of a (100) face of a HPHT-grown diamond polished along the (soft) [001] direction showing well formed grooves. The scan size is 370 nm × 370 nm.

Zoeten was also applied to one of the CVD-grown crystals: optically the surface was smooth, but under the STM the surface was identical to that of the other, non-*zoeted*, crystals. Optical microscopy of a scaife surface that had already been used for polishing showed grooves that were comparable to those imaged on the non-*zoeted* crystals. This suggests that the optical grooves, which are in fact a superposition of numerous nanoscale grooves, are more or less a replication of the scaife structure. The smoothing effect of *zoeten* is explained by the fact that due to the lateral movement of the diamond being polished the replication of the groove pattern on the scaife to the workpiece is avoided (Grodzinski 1953). In contrast to the nanogrooves, the grooves on the diamond surfaces as imaged by optical microscopy do not give information on the actual polishing process.

4. Discussion

From the STM observations it follows that diamond polishing in the soft directions does not proceed via simple cleavage, chipping or microfracture. Therefore an alternative mechanism has to be searched for. In doing this one comes to the central problem: how are the nanogrooves in the soft directions formed? In essence there are two possible ways out.

(i) The grooves are formed by a multiple pass mechanism at subcritical load. Diamond on diamond sliding experiments (Seal 1965, 1967) have shown that under such low-pressure conditions no damage visible by optical microscopy or SEM can be seen after one or a few

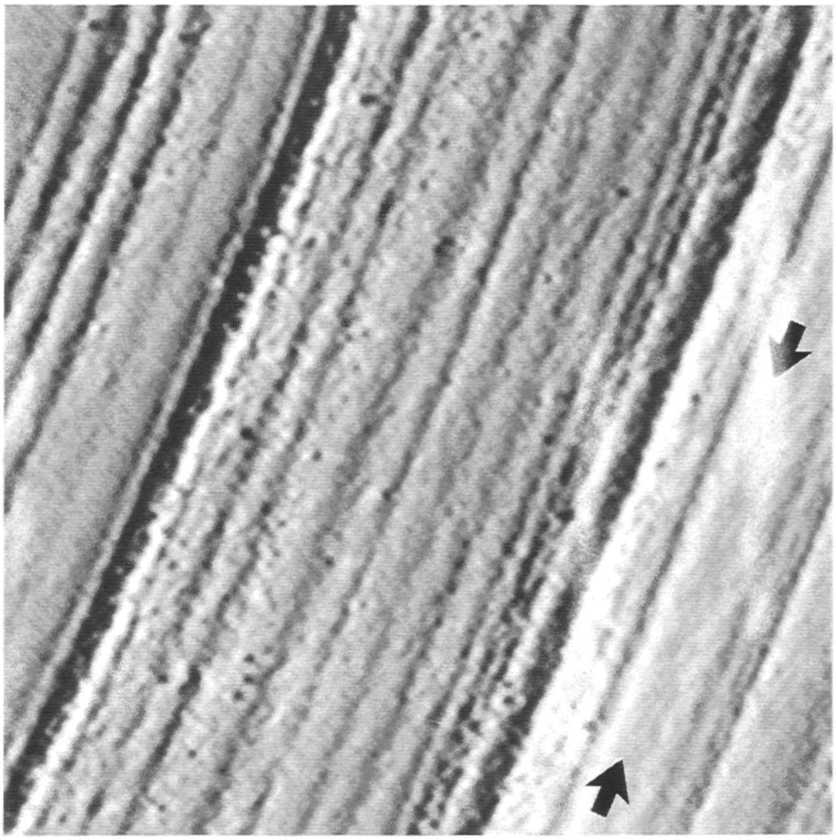

Fig. 4. STM image of a (110) face of a CVD-grown diamond polished along the (soft) direction [001]. The surface is shaded with a light source shining from the left-hand side.

passages. REM, however, has revealed a structural modification or damage of the upper atomic layers (Wang *et al.* 1991, Wang 1991, Tabor and Field 1992). Repeated sliding over 10^3 to 10^6 passes leads to a clearly visible groove pattern (Seal 1965, 1967, Tabor and Field 1992, Feng and Field 1992). The average rate of material removal is considerably less than one atomic layer per traverse. During this process a wax-like wear debris is formed, most of which consists of hydrocarbon. This means that atoms or groups of atoms are removed statistically, for instance by adhesion followed by plucking off, and subsequently react with the ambient atmosphere to form organic substances. If diamond polishing is governed by this mechanism, then the nanogrooves gradually build up after many passages of different powder particles. This implies that the asperities or nanoparticles must be constrained to follow the grooves by the skidding effects for low angle impacts on slopes, which follow from simple mechanical theory (Seal 1981). A movement of a diamond stylus influenced by the profile of the polishing lines on a diamond surface has indeed been observed for sliding speeds of 100 μm s^{-1} (Wang *et al.* 1991, Wang 1991). However it is quite dangerous to extrapolate this to the speeds of 50 m s^{-1} which occur during diamond polishing.

(ii) The grooves are formed by a single pass mechanism at supercritical load. As mentioned before, plastic grooving occurs when a sharply pointed diamond stylus slides on a diamond surface at contact pressures exceeding approximately 20 GPa (Seal 1958, Wang *et al.* 1991, Wang 1991, Tabor and Field 1992). REM showed that the channels, which are formed after a single pass, are smooth and do not change in shape over distances exceeding several tens of micrometers. The width of the grooves ranges from 2 to 50 μm. Since several

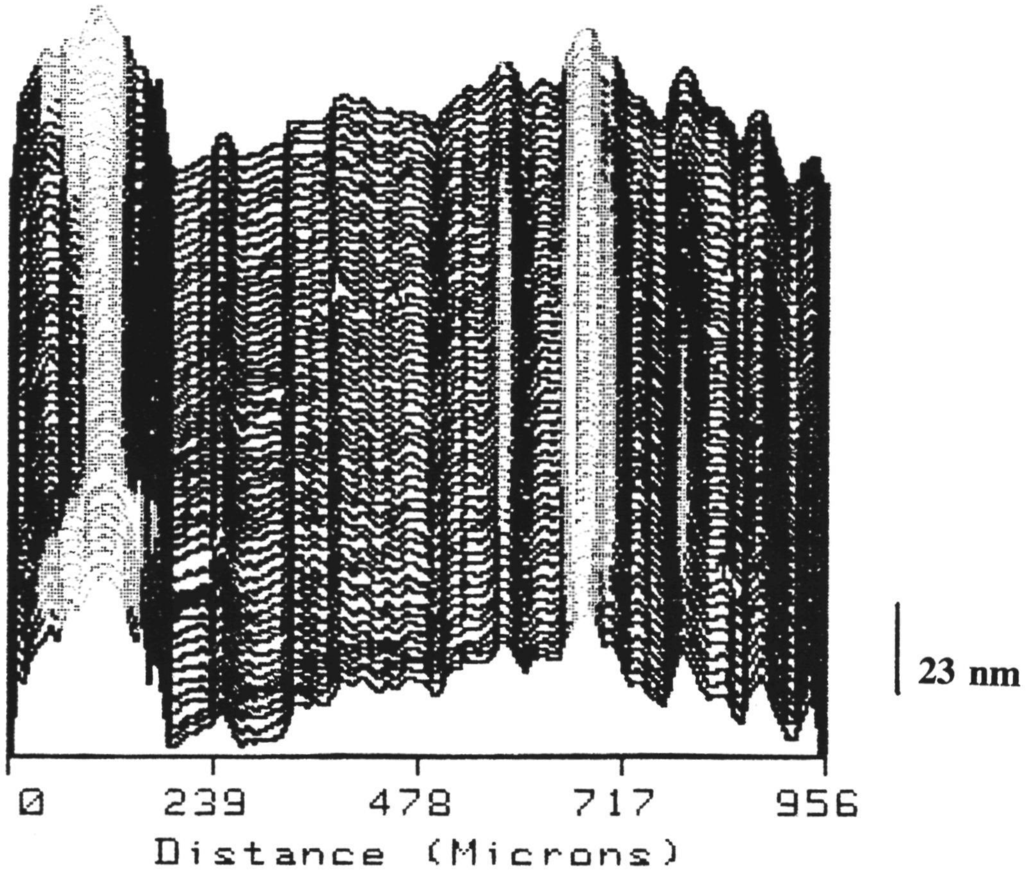

Fig. 5. Height profile of a (100) surface of a HPHT-grown diamond polished along the (soft) direction [001] obtained by an optical, phase shifting interferometry microscope.

parallel grooves are formed during one or a very few passes, in most cases they must have been produced by the asperities on top of the needle rather than by the needle apex itself. No marks of fracture were encountered. In short, the grooves formed by sliding at supercritical pressures appear quite similar to those imaged by STM on polished diamond surfaces.

The actual mechanism of plastic grooving is not clear. Wang (1991) and Wang *et al.* (1991) proposed that plastic deformation is the underlying cause. On the other hand, Seal (1967) suggested that the patterns are generated when the very local stresses exceed the intrinsic strength of diamond. Then the grooves are formed by failure through disruption of interatomic bonds and disintegration of material. Further one might speculate about a phase transition of carbon at the contact points of ultra-high pressures, followed by a transformation into the soft graphite after release of contact.

From the shape of the grooves as imaged by STM no conclusion can be drawn whether diamond polishing is dominated by a multiple or a single pass mechanism. Hints are obtained from some peculiarities on the surfaces.

First, many adjacent nanogrooves seem to occur in bands. This points to a single pass of an abrading particle topped with several asperities. Second, a few grooves suddenly begin or end on the surface. For the CVD grown diamonds smooth grooves 0.5 to 2 μm wide and a few hundred nanometres deep were found to emerge from diamond inclusions (fig. 6). The shape of these microgrooves does not differ from that of the nanogrooves. It is suggested that the larger channels are produced by a single pass of a diamond fragment fractured from the

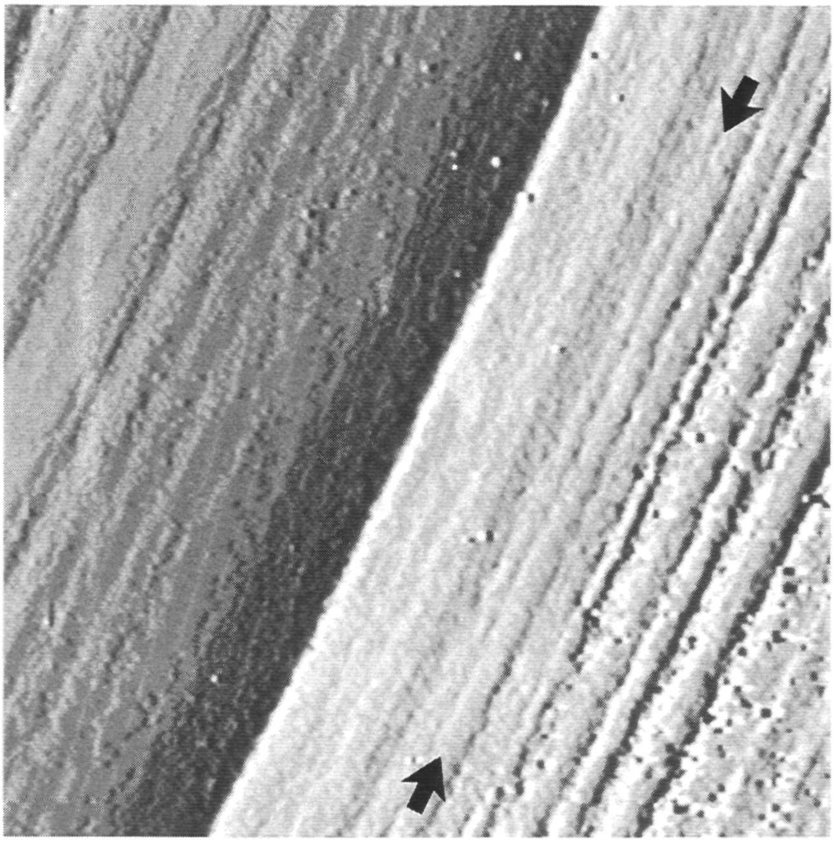

Fig. 6. STM image of an exceptionally broad polishing groove along the (soft) [001] direction on the (110) surface of a CVD grown diamond. The channel originates from a diamond inclusion that emerges at the crystal surface. The surface is shaded with a light source shining from the left-hand side.

inclusion. These and several other observations (Couto *et al.* 1994b (see also chapter 5)) are in favour of the single pass model for nanogroove formation, but a definite proof has still to be given.

The single pass hypothesis does not rule out additional, multiple pass material removal by particles at subcritical pressures. For instance the plastic grooves as imaged by Wang (1991) and Wang *et al.* (1991) exhibit sharp edges. The nanogrooves on polished diamond surfaces do not do so. Occasionally rough tracks together with the more common smooth grooves were observed on the surfaces abraded along soft directions. These observations suggest that the nanogrooves are formed by one single pass of a particle at a supercritical pressure followed by a polishing action of particles at subcritical pressures.

5. Conclusions

STM topography has provided a lot of information on the actual mechanism of material removal during diamond polishing. It was shown that abrasion along the hard directions proceeds via fracture and chipping on a nanometre scale. Material removal in the soft directions seems to take place by single pass grooving by diamond particles at supercritical loads followed by a polishing action by particles at subcritical loads. Unfortunately the enigma of diamond polishing is not yet completely solved: many questions remain.

What is the actual mechanism of 'plastic' grooving? What is the relative contribution of material removal by single pass grooving with respect to the subsequent multiple pass polishing? And finally, now that the Tolkowsky cleavage model must be abandoned for polishing along soft directions, how can the extreme dependence of polishing rate on crystal orientation be explained? There is a challenge for both experimentalists and theoreticians (Harrison *et al.* 1992). Diamond polishing is an ancient trade, but it still remains a source of new, unexpected science.

6. Acknowledgements

The authors are grateful to Dr. R. J. Caveney (De Beers Industrial Diamond Division) for providing heavily boron doped HPHT diamond specimens and to G. Janssen and W. Vollenberg for growing the homoepitaxial, boron doped CVD-grown diamond layers. Further they wish to thank the diamond workers at Drukker International B.V. for polishing the specimens.

M. S. Couto acknowledges CAPES (Coordenação de Aperfeiçoamento de Pessoal de Nível Superior), Brazil, for a scholarship making this research possible.

Chapter 4

Diamond polishing mechanisms: an investigation by scanning tunnelling microscopy[1]

M. S. Couto, W. J. P. van Enckevort

Department of Solid State Chemistry, University of Nijmegen, Faculty of Science, Toernooiveld, 6525 ED, Nijmegen, The Netherlands

M. Seal,

Sigillum B.V., Guido Gezellestraat 5, 1077 WN, Amsterdam, The Netherlands

Abstract

The morphology of the polished surfaces of semiconducting diamonds has been examined by scanning tunnelling microscopy. The faces polished along a direction of difficult abrasion show a rough structure which indicates that material was removed by fracture and chipping on a nanometre scale. The faces polished along a direction of easy abrasion are characterized by a superposition of many smooth grooves which are 20–100 nm wide and 2–12 nm deep. Cracks suggesting a stick-slip process were found. The smallest structures were 1 nm in size. The morphology of these surfaces indicates a process dominated by mechanical interactions of diamond on diamond. A mechanism is proposed which is based on adhesion, followed by plucking of fragments of the order of size of nanometres or smaller from the surfaces. Optical microscopy of the polishing scaife shows the presence of broad grooves and Raman spectroscopy indicates only the presence of diamond. Analyses of the black powder formed during polishing revealed iron in the form of carbides and oxides, diamond particles and probably amorphous carbon.

---

[1] *Philosophical Magazine B 69 (1994) 621*

1. Introduction

In the previous chapters it has been shown that diamond polishing in directions of difficult material removal proceeds via fracture. Such surfaces are characterized by cracks and a rough hill-and-valley pattern. On the other hand, during polishing in the 'fast' directions very smooth parallel grooves develop. It is not clear whether this pattern is formed after one single pass of a diamond particle at supercritical pressure or is the result of a multiple-pass mechanism involving chemical attrition or nanofracture.

In this chapter new results of scanning tunnelling microscopy (STM) studies on diamond polishing are presented. First, polishing along the directions of difficult abrasion is discussed. This is followed by a treatment of polishing along the easy directions. Then the results obtained from the characterization of the polishing wheel surface and the powder formed during polishing are presented. Finally we discuss the mechanisms of diamond polishing.

2. Experimental details

2.1. Specimen preparation

STM requires that the sample to be studied be electrically conducting. Since the electrical resistance of available natural type IIb semiconducting diamond is too high (for example Collins and Lightowlers (1979)), we used either high-boron-content synthetic diamonds grown by high-pressure high-temperature (HPHT) or chemical vapour deposition (CVD). In such p-type crystals the distribution of the boron impurity is not uniform (Burns *et al.* 1990), so that only surfaces adjacent to volumes of maximum accepter concentrations were examined. The resistivity of the specimens was about 10^2 Ωcm for the HPHT-grown diamonds and 0.1 - 1.0 Ωcm for the CVD-grown diamonds.

From the HPHT crystals, plates and blocks with faces parallel to {100}, {110} and {111} were cut and polished. The CVD-grown layers were obtained by the epitaxial deposition of diamond films on {110} substrates in a hot-filament low-pressure reactor. To produce p-type doping, boron compounds were added to the methane-hydrogen atmosphere. In this way, heavily boron-doped single-crystal diamond films of 5–20 μm thickness were produced (Janssen *et al.* 1992). The surfaces of these films were then polished. For all the specimens the polishing was carried out by the conventional method described above, using diamond powder with a particle diameter less than 15 μm mixed with a small amount of (liquid) paraffin at a polishing speed of 50 m s^{-1}. In order to obtain smoothing on a macroscopic scale, *zoeten* (Grodzinski 1953), that is, lateral movement of the specimen, was applied during the polishing of one of the CVD crystals. The (100) faces were polished along a direction of easy abrasion [010] or an abrasion-resistant direction, 15° from [011]. The (110) surfaces were polished along the easy [001] direction and the (111) face along approximately $[1\bar{1}0]$. The quality of the polished surfaces is similar to that of standard brilliant facets, that is, mirror smooth.

Prior to STM measurements the specimen surfaces were cleaned by boiling in an aqueous solution of detergent, followed by rinsing in distilled water and isopropanol. After one series of measurements with the CVD crystals one specimen was cleaned in concentrated H_2SO_4 for 20 min and the others were heated to 400°C in vacuum (10^{-3} Torr) for 20 min. A new series of measurements was then carried out in order to check for surface contamination effects.

2.2. Scanning tunnelling microscopy method

The scanning tunnelling microscope used was home made and identical with that described by Hottenhuis *et al.* (1988), except that the electrochemical cell was replaced by a conventional sample holder. The tips were prepared from 0.5 mm 90% Pt–10% Ir wire by mechanical cutting. The measurements were carried out using a negative tip voltage. For the HPHT specimens the tunnelling voltages used ranged from -3.0 to -5.0 V, depending on the dopant level of the crystal. Too negative a voltage (between -2.0 and -3.0 V) led to a dramatic decrease in lateral and vertical resolutions, probably because a considerable area of the needle apex was in direct contact with the surface. A voltage below between -4.0 and -5.5 V produced images dominated by noise. For the CVD specimens, due to the higher conductivity of the crystals, the tunnelling voltages used ranged from -0.5 to -1.0 V. All the measurements were carried out under atmospheric conditions and in the constant-current mode, keeping the current at 200 pA. Lower currents resulted in a loss of resolution and higher currents gave no improvement.

Before STM the polished surfaces were pre-examined by optical differential interference contrast microscopy and by phase-shifting interferometry (PSI) (Wyant *et al.* 1986, van Enckevort 1992).

2.3. Scaife and polishing powder

More information on the process of diamond polishing can be acquired by examination of the polishing scaife. In order to do this blocks of about 1 cm^3 were sawn from one scaife that had already been used for polishing. We used Raman spectroscopy, optical microscopy and SEM measurements to examine these surfaces.

During polishing a black powder is formed which is deposited on and around the scaife as well as on the holder used to press the diamond against the scaife. Analysis of this powder can bring some knowledge on chemical reactions that might occur during the polishing process. The powder was collected and examined by infrared absorption spectroscopy, Raman spectroscopy, X-ray powder diffraction, SEM and energy-dispersive X-ray analysis (EDXA).

3. Results

3.1. Current-voltage measurements in the scanning tunnelling microscope

In order to verify the implications of the difference in electrical conductivity of the HPHT-grown crystals and the CVD-grown crystals for their behaviour in the STM current-voltage (I-V) measurements were carried out on both kinds of specimen. Figure 1(*a*) shows a typical I-V curve for a HPHT diamond. The curve presents a diode behaviour which is characteristic for a Schottky barrier at a metal–p-type semiconductor interface. A tunnelling

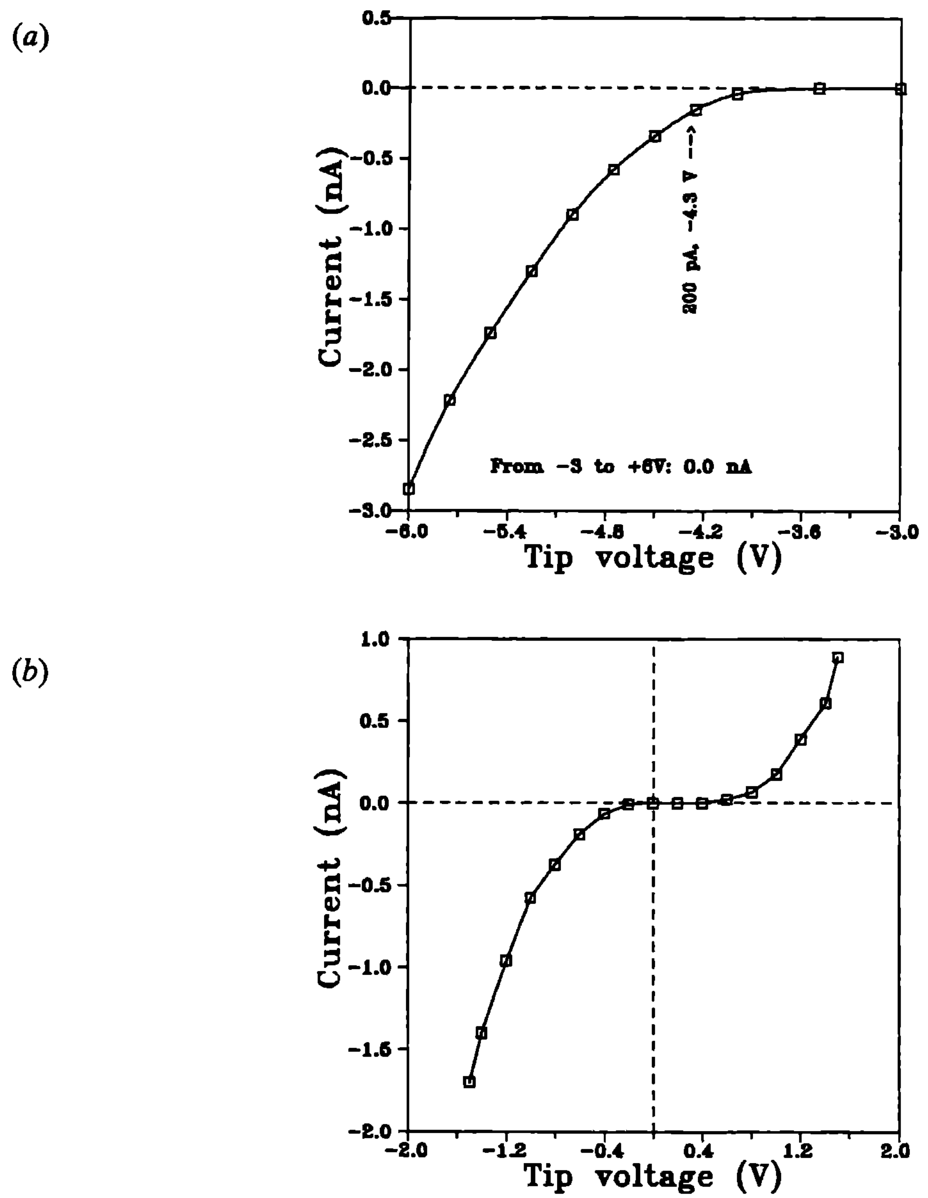

Fig. 1. Current-voltage curve for a fixed tip-surface separation on (*a*) HPHT-grown diamond showing a diode behaviour and (*b*) CVD-grown diamond where the diode behaviour is very much reduced, owing to the higher sample conductivity.

current could be detected only for negative tip voltages below approximately -3.0 V. For the most heavily doped HPHT crystals this threshold goes to -1.5 V. Figure 1(*b*) presents a typical I-V measurement for the CVD specimens. The diode behaviour was very much reduced. Owing to the higher conductivity the curve is almost symmetrical for negative and positive voltages, the absolute values of the currents being slightly less for positive voltages. An interval of about 0.5 V was observed around 0.0 V where no current could be detected. Because of the higher conductivity of the CVD-grown crystals a higher resolution could be obtained by STM. Also, measurements using a positive tip voltage could be performed. These measurements revealed exactly the same surface structures as for negative tip voltages. Therefore only the latter measurements are presented in this paper. Highly doped CVD-grown diamond has been used to manufacture good STM tips (Visser *et al.* 1992).

It was observed that for the HPHT diamonds a change in the height of the tunnelling tip of a few nanometres was necessary to produce a tenfold increase–decrease in the tunnelling current, while for the CVD diamonds a change of about 1 nm was sufficient to produce the same change in the tunnelling current. This can be attributed to either some electrical effect due to the poor conductivity of the HPHT diamonds or to the presence of some adsorbed layer of contaminants on the diamond surface. If the tip touching this layer is moved away from the surface the layer makes a connection between the tip and the crystal surface, maintaining some current flow between them. For the CVD diamonds a normal tunnelling process is observed and thus allows for a higher STM resolution down to atomic dimensions.

3.2. Crystals polished along a hard direction

It could be observed that the (100) plate polished along a direction 15° from [011] was rough on a nanometre scale, presenting two different types of surface structures. The first of these structures is shown in fig. 2(*a*) and is composed of a hill-and-valley pattern with an average width of 38 nm and a height of 4 nm, giving a slope of 12° for the side walls. Figure 2(*b*) shows the second type of structure. It can be seen that the surface exhibits some elongated, rough microstructures running along the direction of the polishing. The 'grooves' have an average width of 76 nm and a depth of 8 nm, giving a slope of 12°. Although somewhat larger, both structures look similar to the patterns observed by electron microscopy by Thornton and Wilks (1976).

The observed surface structure of the (111) face polished along $[1\bar{1}0]$ is different from that of the (100) face. As shown in fig. 3 it consists of a pattern of parallel polishing grooves superimposed on a second pattern of lines connecting two adjacent grooves at an angle of 90°. The polishing grooves are about 60 nm wide and 7 nm deep. The slope of the side walls is 12°. The distance between adjacent lines is approximately 20 nm and they are about 2 nm deep.

In some of the {110} polished faces of the CVD grown diamonds, several micrometre sized diamond crystallites were found, apparently each with {111} parallel to the {110} face of the host. Figure 4 shows part of one of these crystallites. Since the {111} face is more resistant to abrasion than the (110) face polished along [001], these {111} crystallite faces were higher than the surrounding surface after polishing. It can be seen that the {111} surface is rough and dominated by a triangular fracture pattern, indicative of the threefold symmetry of the [111] direction. Polishing grooves can be seen, several of which are continuous across the step dividing the two surfaces, but some are discontinuous.

The morphologies of the diamond surfaces which were polished along a hard direction are all indicative of a polishing mechanism involving fracture and chipping on a nanometre scale as will be discussed later.

3.3. Crystals polished along a soft direction

Figure 5(*a*) shows the surface morphology of a (100) face of a HPHT-grown diamond polished along the [001] direction. For this face very well formed grooves can be seen. The structure can be considered as being formed by the superposition of many grooves with

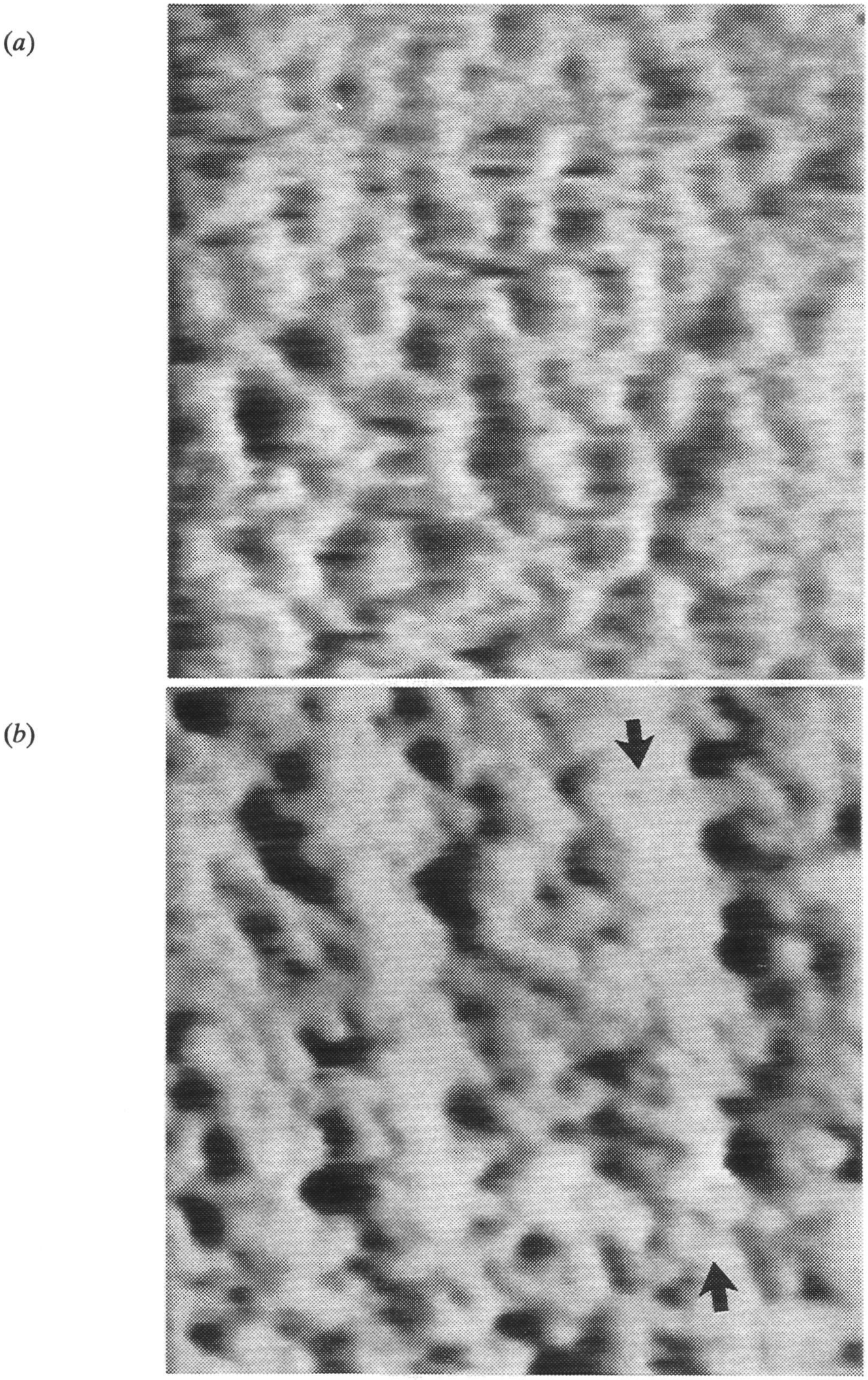

Fig. 2. STM image of the (100) face of a HPHT-grown diamond polished along a direction 15° from [011]: (*a*) the surface is composed of a hill-and-valley pattern; (*b*) the surface presents some elongated, rough micro-structures. The scan size is 440 nm × 440 nm in (*a*) and 925 nm × 925 nm in (*b*). The arrows in (*b*) and in the other STM photographs presented in this chapter indicate the direction of polishing.

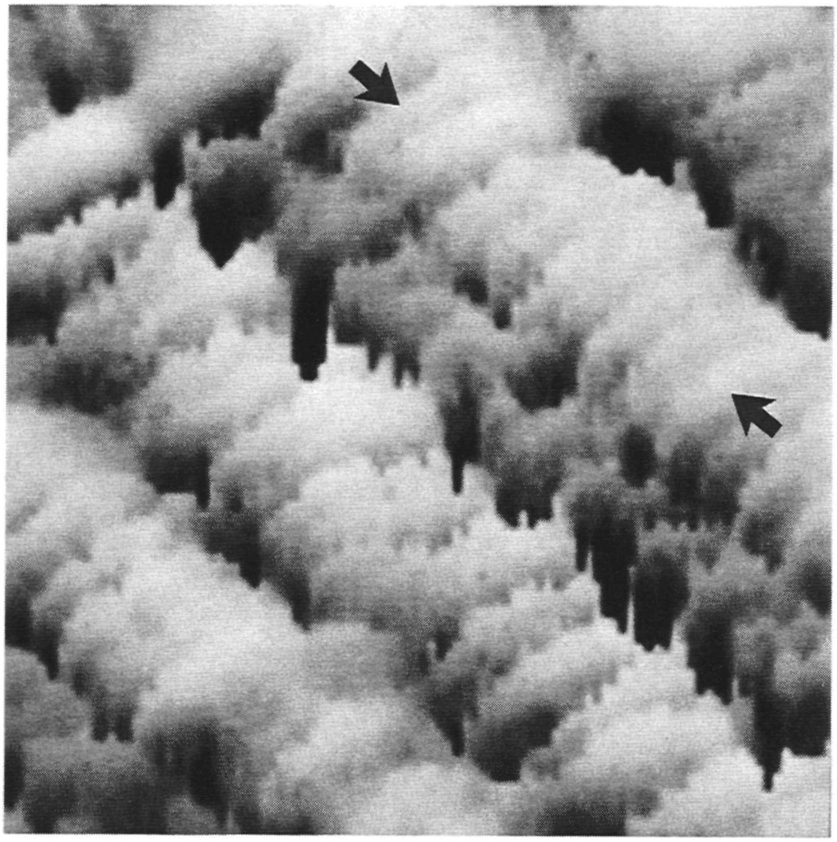

Fig. 3. STM image of the (111) face of a HPHT-grown diamond polished along $[1\bar{1}0]$ showing the polishing grooves and the superimposed pattern of crossed lines. The scan size is 370 nm × 370 nm.

widths ranging from 20 to 100 nm and depth ranging from 4 to 12 nm. For the (110) face polished along the [001] direction the structure found was very similar to that of the (100) face, except that the grooves could be up to 200 nm wide and 32 nm deep. For both surfaces of the polished HPHT-grown crystals the grooves are very smooth, down to the conductivity-limited resolution of the scanning tunnelling microscope (a few nanometres). No evidence for the formation of cracks or fracture structures was found. The cross-section of the individual grooves does not change in shape over distances exceeding several microns. The distribution of inclinations at the side walls is approximately Gaussian and no preferred (*hkl*) orientation was found (fig. 5(*b*)). It should be noted that these and the other groove patterns observed by STM and described below are quite different from the grooves which can frequently be seen on polished diamond surfaces by eye or by optical microscopy. Those typically are tens to hundreds of microns wide with side-wall slopes averaging one to a few minutes of arc.

Figure 6(*a*) shows the polished (110) surface of one of the CVD-grown crystals. At the low magnification used to make this picture, only the polishing grooves can be seen. The average width of the grooves is 30 nm and their depth is 4 nm, with a slope of 15°. It is interesting that many grooves are grouped in bands made up of several parallel individuals. A major difference between the CVD specimens and the HPHT specimens measured before is that now it is possible to see some polishing grooves that either stop or begin at some point of the surface. At higher magnifications it was possible to see a second pattern of lines running across the polishing grooves (see fig. 6(*b*)). As for the {111} faces, these lines appear like nanocracks caused by the abrading particles. It is also possible to see some very rough

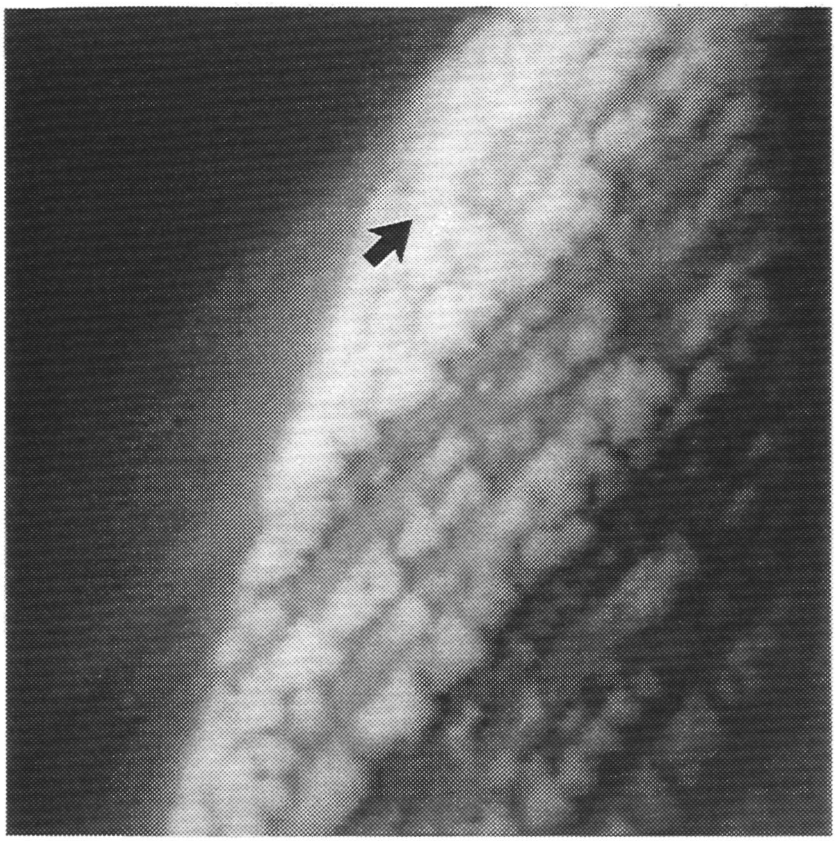

Fig. 4. STM image of a {111} diamond crystallite in a {110} CVD surface. The rough surface of the crystallite contrasts with the smooth surface of the surrounding crystal. The scan size is 1.1 μm × 1.1 μm.

areas in the centre of the picture in the neighbourhood of the smooth regions at the upper left-hand corner. No difference between the surface morphology of the specimens cleaned in the aqueous solution of detergent and those treated with concentrated H_2SO_4 was found.

For the diamond that was moved laterally during polishing the average width of the grooves was 30 nm and they were about 3 nm deep. These values are similar to those for the diamonds that were not moved. Cracks could still be seen on the surface. It is obvious that the macroscopic smoothing effect obtained by *zoeten* does not persist on a nanometre scale. Optical microscopy showed that on a micron scale the surface is smoother than the surface of the diamonds that were not moved during polishing. From this it follows that the surface obtained by *zoeten* is sufficient for optical purposes but another polishing method must be found if improvement of the polished surface in the nanometre region is needed.

After several measurements the diamonds were heated in vacuum in an attempt to remove a possible contaminant layer from the surface. A small improvement in the resolution and a slight decrease in noise level could be observed. However, the new measurements showed that the surface had the same structure as before, namely mainly showing smooth grooves, but with some roughly grooved regions with transverse cracks. In fig. 7 a detail of these cracks can be seen. The average distance between two cracks is 15 nm, the depth is about 1 nm and they have an angle of about 52° with respect to the direction of the grooves. Figure 8(*a*) shows another area covered by these transverse patterns. Here the cracks are perpendicular to the direction of the polishing grooves. The average separation is 15 nm, the depth is about 2 nm. A high-magnification STM topograph of this region (fig. 8(*b*)) showed

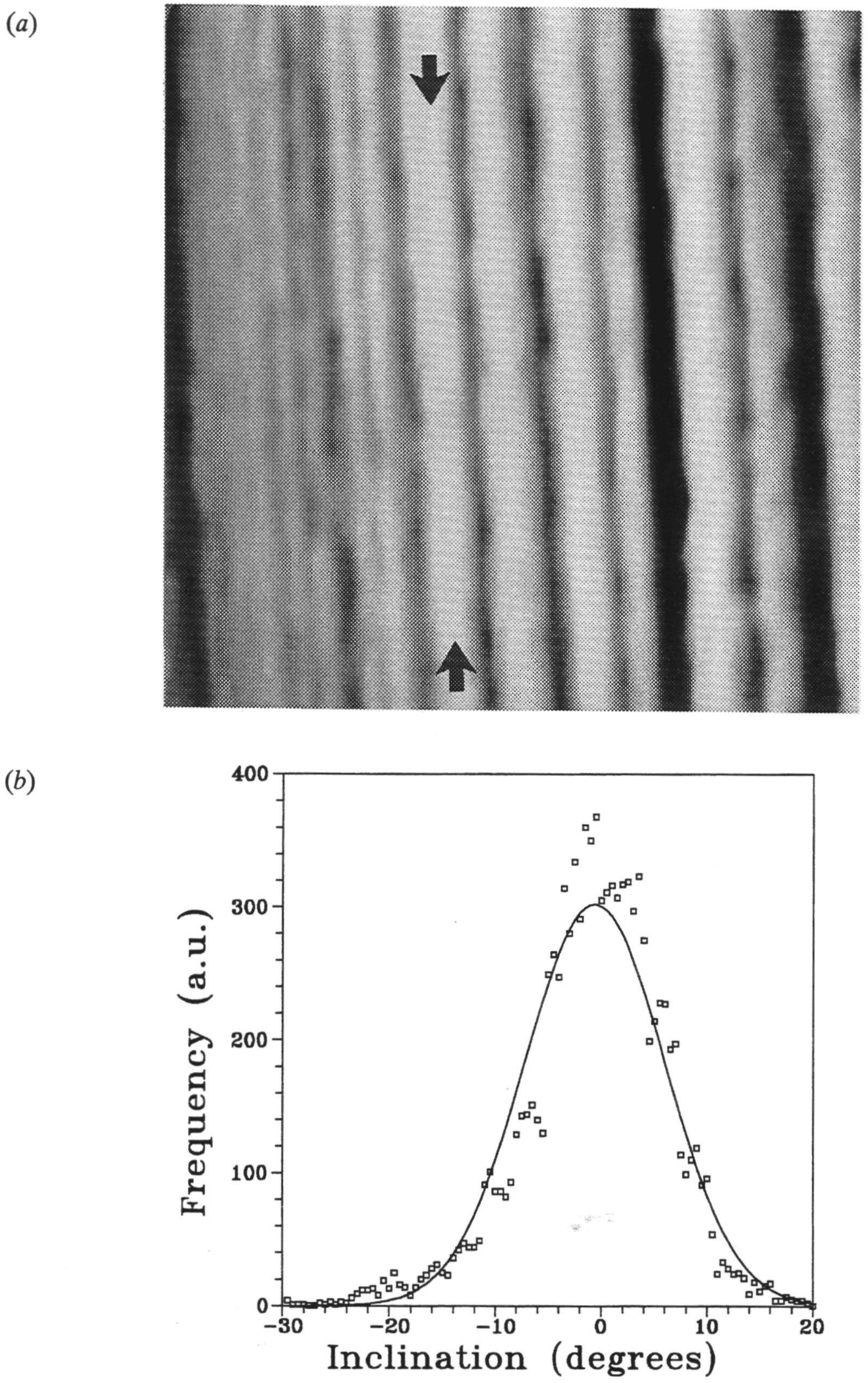

Fig. 5. (*a*) STM image of a (100) face of a HPHT-grown diamond polished along the [001] direction, showing well formed grooves. The scan size is 370 nm × 370 nm. (*b*) Histogram showing the distribution of slopes at the side walls of the grooves shown in (*a*) (a.u., arbitrary units).

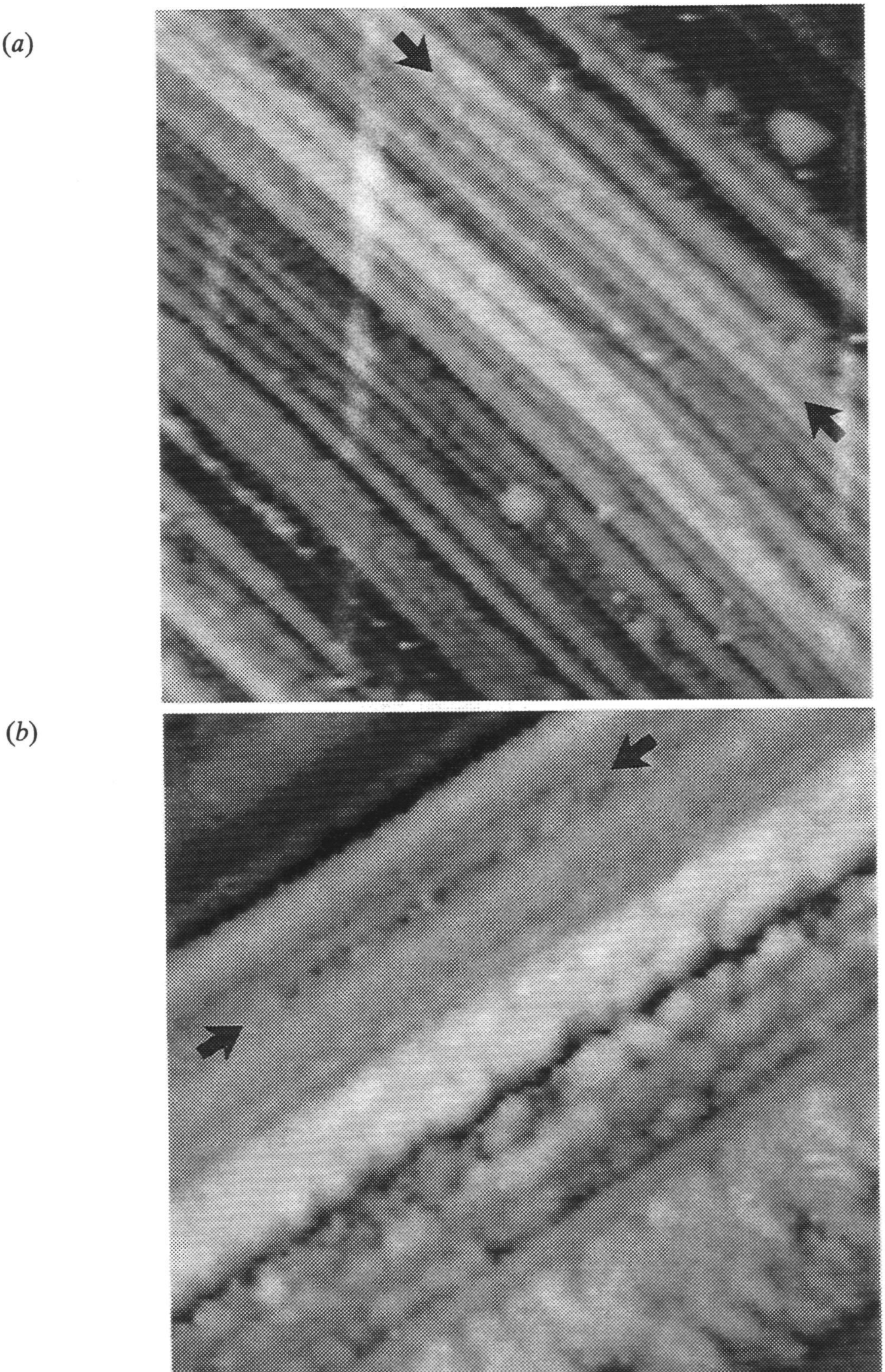

Fig. 6. STM image of a (110) face of a CVD-grown diamond polished along the [001] direction. In the lower right-hand corner of (*a*) the end–start of some polishing grooves can be seen. The scan size is 855 nm × 855 nm. In the lower right-hand corner of (*b*) a pattern of lines running across the polishing grooves can be seen. The scan size is 150 nm × 150 nm.

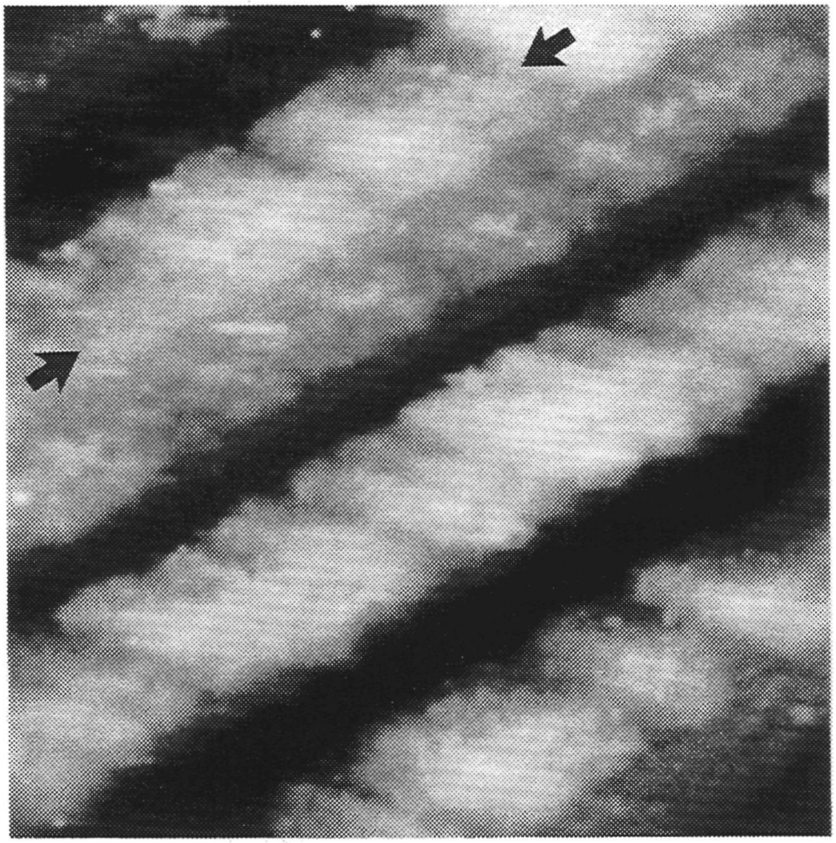

Fig. 7. STM image showing a detail of some cracks (inclined to the grooves) on the (110) face of a CVD diamond. The scan size is 171 nm × 171 nm.

that the cracks have some microstructure. The white spots, such as indicated by the arrow, are about 1.6 nm wide and 0.5 nm high and are the smallest structures that we could measure. Their strict ordering with respect to the polishing grooves suggests that they originated from the polishing process rather than from some contamination.

For the (110) faces polished along the [001] direction, the orientation of 90° for the cracks corresponds with the intersection line of one set of inclined {111} faces with the (110) plane. The orientation of about 52° for the cracks is close to the direction of the intersection line of a second set of perpendicular {111} faces with the (110) plane, which is 54.7°. The cracks are mostly localized to one band of grooves. Sometimes they extend to two or a few grooves. This indicates that they are not the outcrops of growth defects, like stacking faults or microtwins, which should extend to many grooves.

No individual atoms could be seen during the study even on the well conducting CVD samples. This is in contrast to several STM studies of as-grown CVD-grown diamond surfaces (Tsuno *et al.* 1991, Busmann *et al.* 1992, Maguire *et al.* 1992). It is suggested that as a result of the polishing process the surface is terminated by an ultra-thin disordered top layer. Maguire *et al.* (1992) also failed to achieve atomic resolution in their AFM studies of polished CVD diamond surfaces and attributed this in part to the water-absorbed properties of diamond surfaces.

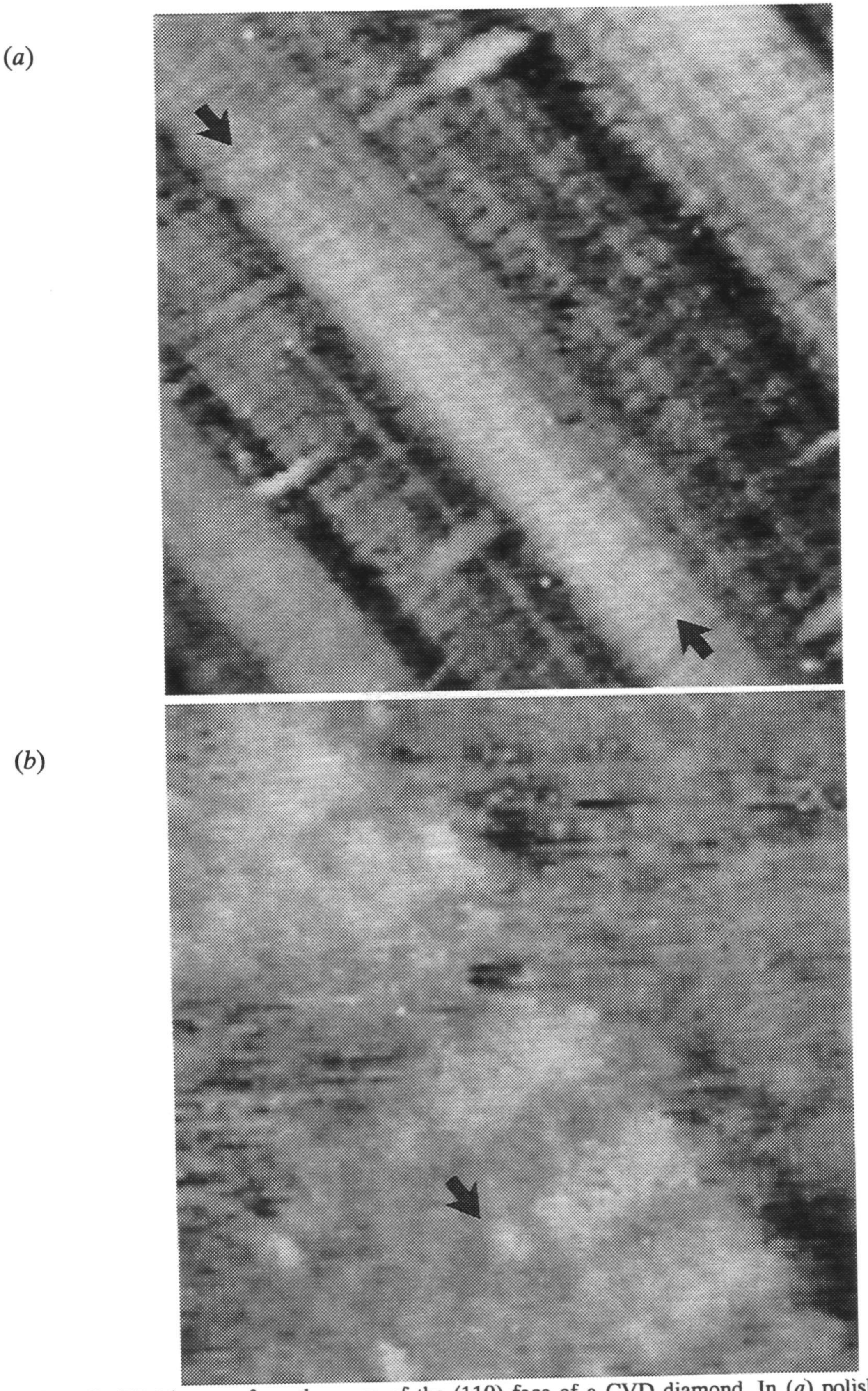

Fig. 8. STM image of another area of the (110) face of a CVD diamond. In (*a*) polishing grooves and cracks can be seen. The scan size is 428 nm × 428 nm. In (*b*) a detail of these cracks is shown. The scan size is 21 nm × 21 nm. The arrow indicates one of the smallest scale structures.

3.4. Scaife and polishing powder

Optical microscopy and SEM of the polishing scaife showed that the metal was plastically deformed by the diamond being polished. In addition, grooves were formed. The abrading diamond particles were pressed into the metal and the larger particles (greater than 2 μm) (fig. 9(*a*)) had a flat top, indicating that they were polished together with the workpiece. Raman spectroscopy indicated only the presence of diamond and provided little evidence for the existence of graphite or amorphous carbon. The grooves observed on the scaife were much broader (several microns) and less steep than the ones encountered by STM on the diamond surface. It is possible that the patterns are formed by plastic flow introduced by the polishing particles or by some chemical reaction of the iron of the scaife.

The grooved patterns on the scaife (fig. 9(*a*)) are comparable to those imaged on the diamond surfaces by optical microscopy and PSI (phase shifting interferometry) (fig. 9(*b*)). This suggests that these very shallow grooves, which in fact are a superposition of numerous nanometre scale grooves, are more or less a replication of the scaife structure. The smoothing effect of the *zoeten* is easily explained by the fact that, owing to the lateral movement of the diamond being polished, replication of the groove pattern on the scaife to the workpiece is avoided (Grodzinski 1953). The grooves on the diamond surfaces as imaged by optical microscopy do not give information on the actual polishing mechanism.

The black powder formed during polishing was collected and examined by SEM, EDXA, X-ray powder diffraction and by infrared and Raman spectroscopy. The SEM pictures revealed only an 'amorphous' substance containing thin plates. EDXA analysis of this material showed that the main component was iron. In addition, small amounts of sodium, chlorine, silicon and calcium were found. Here, it must be noted that our instrument could not detect elements lighter than sodium (such as carbon). Infrared spectroscopy showed two sharp C-H peaks near 2900 cm^{-1} and four broader peaks in the range from 1800 to 700 cm^{-1} (fig. 10). Comparison of the results found for the black powder and the results obtained for the paraffin used during polishing showed that the C-H peaks near 2900 cm^{-1} are due to this oil. The other peaks could not be identified. Raman spectroscopy using a wave number interval from 500 to 3700 cm^{-1} revealed a strong diamond peak at about 1330 cm^{-1} with a half-width of 9 cm^{-1}. This sharp peak was superimposed on a continuous background with very weak broad bands at 1600 and 2450 cm^{-1}. The band at 1600 cm^{-1} might be attributed to amorphous carbon (Huong 1991).

X-ray powder diffraction showed a sharp (111) diamond peak and two broad bands corresponding with $d_{hkl} = 0.49$ and 0.37 nm. The first of these bands was approximately three times more intense than the second and the widths of both corresponded with $\Delta d_{hkl} = 0.1$ nm. The identity of these bands is unknown, but the large width points to a very low crystallinity of the material.

The powder was heated in air to 750°C (at this temperature all the organic compounds should burn). After this treatment the powder became brownish but visual inspection of the material did not reveal any decrease in volume indicating that the amount of organic material is not too high. Further heating to 1000°C diminished the amount of powder to half. Inspection of the material under the microscope showed that the material was very porous, and Raman spectroscopy demonstrated that all the diamond had been burned.

From these analyses, we can conclude that the powder contains a considerable amount of iron (originating from the polishing scaife) in the form of carbides or oxides. The second main component comprises diamond particles from the polishing powder. Since the diamond peak of the X-ray powder diffractogram was very sharp, it does not originate from nanometre-

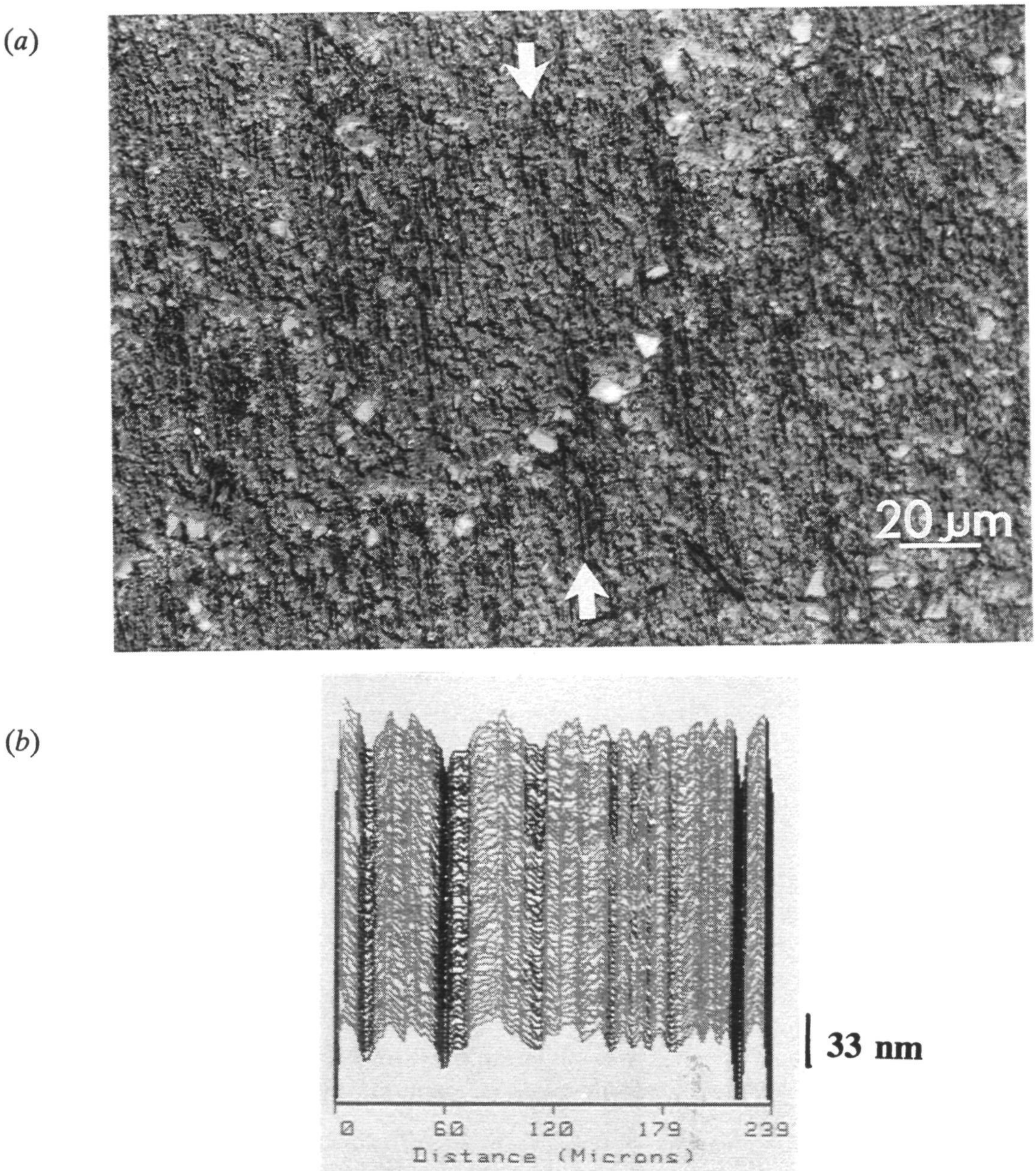

Fig. 9. (*a*) Optical microscope image of the polishing scaife, showing some particles of the polishing powder and grooves on the scaife surface. (*b*) PSI image of a (110) surface of a HPHT-grown diamond polished along [001].

sized diamond particles. The remaining material probably is amorphous carbon originating from the conversion of diamond or some paraffin oil used during the polishing.

4. Discussion

The surfaces that we examined had been polished by a conventional technique. Those which had been polished in hard directions show considerable cracking, whilst those polished in soft directions are for the most part covered with nanogrooves which are apparently fairly

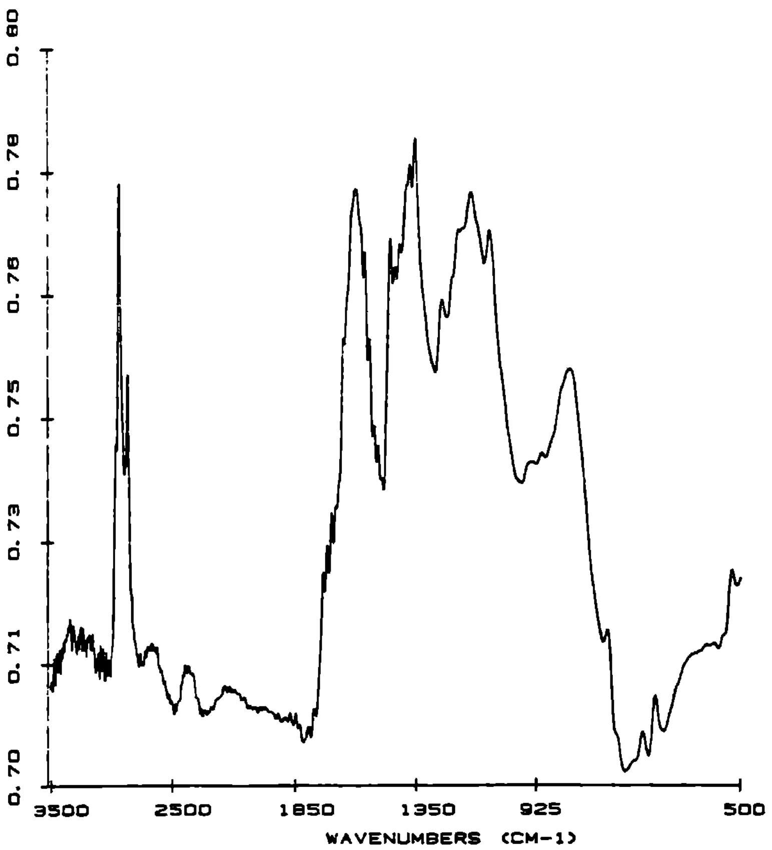

Fig. 10. IR spectroscopic measurements of the black powder formed during polishing.

smooth within, but which have walls sloping at angles of up to 20° or more to the horizontal (fig. 5(*b*)). STM images are known to be a convolution between the actual surface morphology and the shape of the scanning tip. The grooves may thus be deeper and have steeper walls than the values measured. They are not a tip artifact since the use of different tips on the same surface gave identical results.

The STM pictures have a direct bearing on theories of the mechanism of diamond friction and wear. It seems clear, for instance, that wear does not proceed by the removal of Tolkowsky-type cleavage fragments. There are indeed indications that these may form, but usually in the *hard* directions (fig. 4) and not the soft. Our STM pictures for (100) (figs. 2 and 5) show similarities to the block and groove structures depicted in figs. 10 and 11 of the paper by Wilks and Wilks (1972), but the orientations are reversed, [001] in place of [011] and vice versa. In addition, no preferred inclinations at the groove side walls corresponding with a low-index (*hkl*) plane were found. Our results are consistent with the ideas of Samuels and Wilks (1988) where they stated that '...it is the difference of surface topography produced by polishing in [100] and [110] directions that is responsible for the different abrasion rates'. Samuels and Wilks also suggested that it was likely '...that the polishing process has produced a structure even on the very fine 5 nm scale which tends to ease the passage of asperities sliding parallel to the direction of polish'. We confirm here the existence of that structure, and refer also to fig. 5 of the paper by Enomoto and Tabor (1981).

However, we favour the view, discounted by Samuels and Wilks, that adhesion plays an important role in the interaction of sliding diamonds. This idea is quite old and has been reviewed and developed by Tabor (1979). He combined adhesion and Coulomb surface roughness terms to explain the friction of diamond on diamond and its variation with crystal direction. More recently Tabor and Field (1992) have published a modified theory involving adhesion as one of several factors. Also Harrison *et al.* (1992) have published results of calculations using molecular dynamics simulations to model the interaction of diamond {111} surfaces on a nanoscale. They find that indentation can result in non-adhesive (elastic) or adhesive (plastic) interaction depending on the applied load and the number of surface free bonds. Adhesion can be accompanied by fracture and transfer of material. We suppose that such adhesion also occurs in the polishing process between diamond workpiece and powder particles, and that material is removed from the workpiece by fracture on a nanoscale, bond rupture or perhaps atom by atom. The size of the fragments is uncertain, but in the soft directions they can be no larger than the grooves which we observe (about 30 nm across) and are more likely to be of the order of size of the spots seen within the grooves (fig. 8(*b*)), namely about 1.6 nm across and 0.5 nm high. Such a fragment would contain some 200 carbon atoms if it retains the diamond structure, or fewer if composed of a less dense organic species. The very low crystallinity of the powder produced during polishing and the absence of nanometre-sized diamond particles in it, which should give a broad X-ray diffraction diamond peak, are consistent with the limited dimensions of the carbon fragments. If they are diamond at the moment of separation they subsequently react with the ambient iron or are transformed into amorphous carbon. The simulations published by Harrison *et al.* (1992) suggest that groups of 10 or more atoms can be transferred during nano-indentation.

We work therefore from the hypothesis that adhesion between the sliding surfaces occurs on a nanometre scale. Fragments are plucked from the workpiece. They are small but their exact size is unknown. They could be individual atoms, groups of atoms which form organic molecules in combination with other atoms from atmosphere or surface, or true diamond fragments containing up to perhaps a million carbon atoms for soft directions, or many more for hard directions. The anisotropy in wear rate must then relate to the ease of removing these fragments. One can devise theories based on the bonding of surface atoms (Kraus and Slawson 1939), for instance that {111} surfaces are hard because their atoms are in general bonded by three bonds to the layer below whereas, on unreconstructed {100} surfaces only two bonds are involved. Attempts to take this approach further involve too many assumptions and will not be elaborated here. Unknowns include fragment size, the nature of surface reconstruction, and the details of the random distribution of surface orientation within the nanogrooves (which may have orientations $\{h10\}$ where $h \geq 3$ on nominally {100} surfaces). It may be noted that the energy dissipated in friction is about 1000 times larger than the energy needed to vaporize the carbon atoms lost by wear (Seal, 1981).

We also emphasize the observation that nanoscale cracking occurs when diamond surfaces are polished in hard directions. The blocks bounded by these cracks must buttress each other and prevent further break-out of material. In the soft directions the nanogrooves may act as guides for small abrasive particles. Thus the structures appear to be self-propagating as suggested by Samuels and Wilks (1988). There is also a ready explanation of the friction results reported by Seal (1981). When diamond slides on diamond repeatedly along the same track with both surfaces oriented in their hard directions, the friction starts low and rises with repeated sliding. In the soft directions, it remains constant or falls slightly. Presumably the friction for sliding in the hard directions on both surfaces is low at first because the surfaces are smooth having been polished in soft directions, but rises after an initiation period as cracking develops. In the soft directions the friction may fall slightly as the softer surface wears to conform to the harder.

The question of how the self-propagating surface structures form in the first place needs attention. We have assumed above that the interaction is of diamond on diamond. This seems likely, though not proven. It could be that the polishing occurs through chemical interaction with the iron of the scaife and the function of the diamond powder is to harden the surface of the scaife and prevent the workpiece digging into it. We prefer the diamond-on-diamond explanation as the same anisotropy in wear is shown when polishing diamond on a scaife as when rubbing single-crystal diamond on single-crystal diamond in model experiments (Seal 1965). The anisotropy is also shown in the sawing of diamond with phosphor-bronze saws loaded with diamond powder. This is a much-used industrial technique and the affinity of iron for carbon cannot be a factor here.

In normal scaife preparation large numbers of diamond particles are dispersed on the scaife surface. It is common practice to use 0.1–1.0 carats (20–200 mg) of powder, the particle size varying from maybe 2 μm up to more than 20 μm. Theoretically 1 carat of 2 μm powder is sufficient to cover the iron surface as a virtually complete mono layer. This was verified by SEM. Actual loadings will be much less than this as much powder is lost in the process of working the scaife in. This can be concluded from the X-ray and Raman analysis of the black powder produced during polishing. Nevertheless any of the coaxial circular tracks on the rotating scaife surface is likely to intersect many particles. It may be that some of these are flatted (fig. 9(*a*)) because they are oriented in soft directions, and others are not. All are very large (at least as applied) in relation to the structures reported here. The nanogrooves are in fact some two to three orders of magnitude smaller than the nominal powder particle sizes.

During the process of polishing, the flattened particles in the scaife move over the diamond workpiece, although not necessarily in contact with it. It may be that the surfaces interact directly, and abrasion occurs by sliding of diamond flat on diamond flat. More probably, loose particles are involved and abrasion occurs by the sliding of hard corners of such particles on the softer diamond workpiece. It is still difficult to explain the nanogrooves, as asperities with included angles of 140° to nearly 180° are not particularly likely on otherwise flat or convex surfaces of powder particles some 100–1000 times larger. In our view, the most likely effect is that the powder particles are pushed into the iron, but fragments break off under the impacts and intense shear. This may be what is happening in the scaife conditioning which is common industrial practice (low-value diamonds are 'polished' on newly prepared scaifes until a good surface becomes attainable). A slurry of fine diamond fragments in the surface oil film would then result. Fine abrasive particles such as postulated above would be constrained to follow the nanogrooves by the skidding effects for small-angle impact on slopes, which follow from simple mechanical theory (Seal 1981).

It is not clear whether the abrading particle acts as a plough, leaving a furrow in one pass, or causes some incipient damage not immediately manifest, but which results in later loss of material after passage of other abrasive particles. Wang (1991) observed both kinds of damage using REM to observe the results of sliding a diamond needle on a diamond surface in one pass or repeatedly over the same track. We also observed different kinds of damage on the same surface. Figure 6(*b*) illustrates the occasional formation of cracks and blocks after abrasion in a soft direction together with the more common smooth grooves. We suppose, following Wang, that the rough tracks are caused by particles at critical pressures and the smooth grooves result from subcritical pressures, the former causing immediate damage and the latter incipient damage. An alternative explanation for the smooth grooves may be that they are formed by one single pass of a particle at a supercritical pressure followed by a polishing action of particles at subcritical pressures.

The idea of subcritical damage is attractive in explaining the lengths of the nanogrooves which otherwise present a problem in that they do not become shallower in the way one would expect if the abrading particles were wearing away. Fatigue failure is plausible in that fatigue failure on a larger scale is well known in diamond (Field (1992) and references cited therein). Typically on the macroscopic scale, approximately 1000 loadings are required to produce significant damage. The same may be happening on the near-atomic scale during abrasion, but the generally accepted mechanism of incomplete crack closure due to debris and imperfect matching after each cycle needs to be adapted to this scale. STM and AFM pictures of the surfaces of other crystals have been published which show varying degrees of displacement of surface atoms from their strict geometrical lattice positions. Perhaps energy is stored progressively in such displacements until break-out of an atom or fragment occurs. Subsurface damage was postulated by Enomoto and Tabor (1981) to explain the visibility in cathodoluminescence of friction tracks in their experiments. During the present STM study, outcrops of subsurface damage were identified as nanocracks inclined or perpendicular to the polishing grooves. Also Haisma *et al.* (1992) using Rutherford back scattering found subsurface damage amounting to 1.2×10^{17} displaced atoms cm^{-2} in the top 200 nm of a mechanically polished diamond.

It is not clear yet whether the grooves are formed by the ploughing action of one particle at supercritical pressure on a surface damaged by previous impacts or whether the grooves are gradually built up by the repeated passage of abrading particles at subcritical pressures.

5. Conclusions

The present work has shown that the polishing process of diamond is dominated by mechanical interactions. However, the removal of the diamond does not seem to proceed via the removal of Tolkowsky-type cleavage fragments. It was observed that the surfaces of the specimens polished along a hard direction are rough, sometimes showing the crystallographic symmetry of that face. This structure indicates that the polishing proceeds via fracture and chipping on a nanometre scale. The specimens polished along a soft direction are characterized by a pattern of numerous smooth (and some rough) parallel grooves. These tracks sometimes exhibit cracks which are aligned along the direction of the intersection of that face with the {111} planes. It is not clear how the grooves are formed but we suppose that they are introduced by particles interacting with the diamond at a subcritical pressure causing subsurface damage that leads to fatigue failure of the diamond. In this way the grooves gradually develop during the passage of numerous particles. An alternative explanation may be that some supercritical particles plough isolated, somewhat rough tracks in a surface already weakened by subsurface damage. These tracks may subsequently be smoothed by subcritical particles. In both cases we think that adhesion involving pulling off of material fragments plays an important role. The size of the particles removed from the diamond surface could not be measured directly but, from the sizes of the grooves and the structures therein, it is likely that they are a few nanometres across or less.

Our experiments have presented some new and interesting results but without full and unambiguous explanation. The key question remains: how are the nanogrooves in soft directions formed?

6. Acknowledgements

The authors are grateful to Dr. R. J. Caveney (De Beers Industrial Diamond Division) for providing two of the heavily boron-doped HPHT specimens and to G. Janssen and W. Vollenberg (University of Nijmegen) for growing the homoepitaxial boron-doped CVD diamond layers. Further they acknowledge Drukker International B.V. for polishing the specimens and for the use of some of their equipment.

One of the authors, M. S. Couto, wishes to thank CAPES (Coordenação de Aperfeiçoamento de Pessoal de Nível Superior), Brazil, for a scholarship making this research possible.

Chapter 5

On the mechanism of diamond polishing in the soft directions[1]

M. S. Couto, W. J. P. van Enckevort

Department of Solid State Chemistry, University of Nijmegen, Faculty of Science, Toernooiveld, 6525 ED, Nijmegen, The Netherlands

M. Seal,

Sigillum B.V., Guido Gezellestraat 5, 1077 WN, Amsterdam, The Netherlands

Abstract

The morphologies of polished, natural and chemical vapour deposited (CVD) diamond surfaces have been studied by scanning tunnelling microscopy and atomic force microscopy. The surfaces were each polished along the direction of easy abrasion and show the presence of numerous, superimposed grooves which are 35–220 nm wide. One of the CVD surfaces was just partially polished. Examination of the boundary between as-grown and polished parts revealed the presence of isolated smooth grooves. This observation indicates that diamond polishing involves the formation of nanogrooves, each in a single pass of a diamond abrading particle. We postulate that material removal occurs by direct rupture of atomic bonds under the influence of the ultrahigh pressures induced by the asperities on the tops of the abrading particles in contact with the surface. Many atoms must be affected in any cross section of the groove as the asperity passes. The absence of observable dislocations gives support to this mechanism. The conclusion that material removal results from a mechanical interaction between the abrading particles and the diamond surface is confirmed by the morphology of the polished surface of a natural diamond containing many 'naats' (micro twins).

---

[1] *Journal of Hard Materials 5 (1994) 31*

1. Introduction

For the directions of easy abrasion scanning tunnelling microscopy (STM) measurements have shown that the polished surface exhibits smooth grooves, often free from fracture. Therefore, for the soft directions, fracture of the diamond surface acting alone can be excluded and three possible mechanisms for material removal should be considered, namely (i) atomic attrition by multiple passes of abrading particles, (ii) grooving by a single pass of an abrading particle, (iii) grooving or fracture followed by polishing via atomic attrition.

In the attempt to find out what is the actual mechanism for material removal during diamond polishing in the soft directions, we used the techniques of atomic force microscopy (AFM) and STM to analyze features on the surfaces of polished diamond crystals.

2. Experimental details

2.1. Specimen preparation

We used three chemical vapour deposited (CVD) synthetic diamonds and one natural diamond. The CVD layers were obtained by homoepitaxial deposition of diamond films on {110} or {100} substrates from a CH_4/H_2 gas phase in a low-pressure hot-filament reactor (Janssen *et al.* 1992). In this way single-crystalline diamond films of 5–20 μm thickness were produced. To permit the use of STM, the two (110) specimens were doped with a high content of boron. To produce these type IIb diamonds, boron compounds were added into the methane-hydrogen atmosphere. The specific resistivity of the specimens was 0.1–1.0 Ωcm.

The surfaces of these films were then polished. The (100) face was polished along a direction of easy abrasion [010]. The (110) surfaces were polished along the easy [001] direction. For the (100) specimen only a part of the surface was polished, forming a bevelled edge. The angle between the polished and the as-grown surface was 0.9°. This bevelling was done in order that measurements could be carried out near the boundary between the polished and the as-grown surface. The polishing was carried out in a direction 45° to the direction of the boundary, with the polishing particles moving from the as-grown part to the bevelled edge. The sample is schematically presented in fig. 1.

The natural diamond was a pink Australian diamond and was polished with a face parallel to (110). The direction of the polishing was along [001]. By reflection interference contrast microscopy, many microtwins (naats) (Custers 1952) could be seen in the specimen surface running along the $[1\bar{1}2]$ and $[\bar{1}12]$ directions. The naats are grown-in features, which are parallel to the {111} faces. This was verified by focusing through the specimen by transmission optical microscopy.

For all the specimens the polishing was carried out by the conventional method described above, using diamond powder with a particle diameter less than 15 μm mixed with a small amount of (liquid) paraffin at a polishing speed of 50 m s^{-1}. The quality of the polished surfaces is similar to that of standard brilliant facets, that is, mirror smooth.

After polishing, the specimen surfaces were cleaned by boiling in an aqueous solution of detergent, followed by rinsing in distilled water and isopropanol. One of the specimens was heated to 400°C in vacuum (10^{-3} Torr) for twenty minutes. Immediately before the measurements the surface was cleaned again using isopropanol.

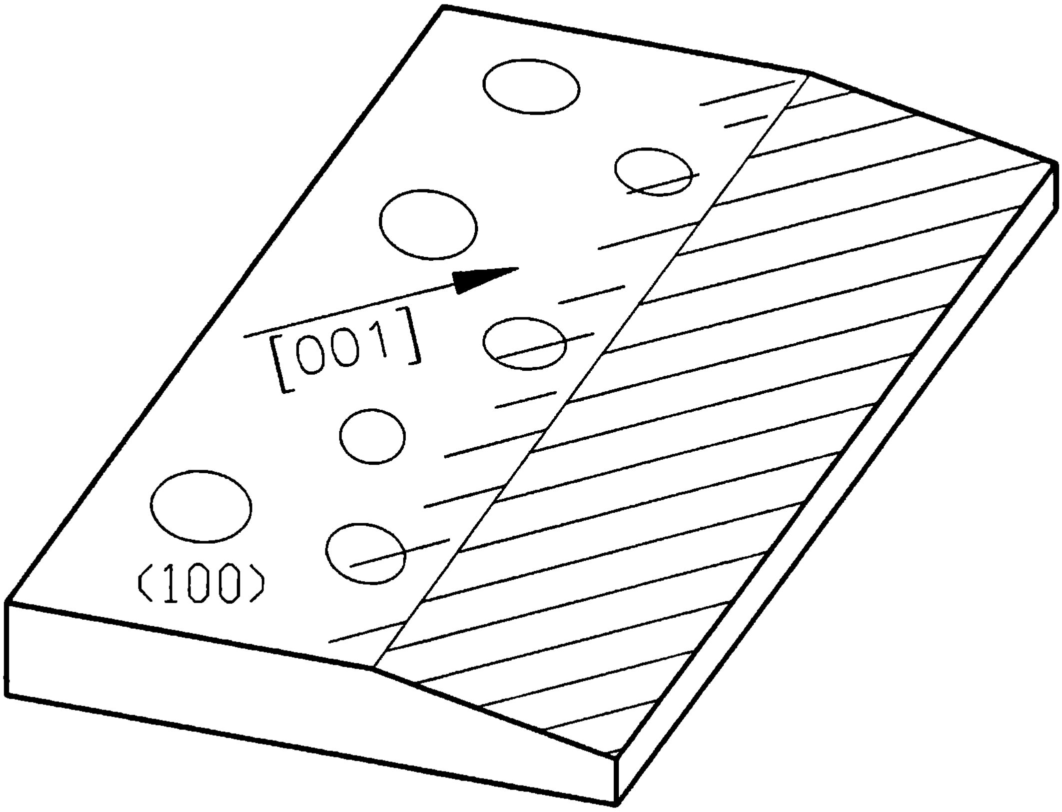

Fig. 1. Schematic representation of the bevelled (100) sample. The polished part is the right side. The arrow indicates the direction of movement of the abrading particles during polishing.

2.2. Scanning probe microscopy method

The equipment used for the AFM and STM measurements was a TopoMetrix TMX 2010. For the AFM measurements two different scanners, a tripod scanner with scan range of 150 μm and a tube scanner with scan range of 7.5 μm, were used. Silicon nitride cantilevers with two different types of tips were used. The first type was a pyramidal silicon nitride tip with a base of 4 μm and height of 4 μm. The second type was a 2 μm high diamond-like carbon rod with a base diameter of 0.15 μm. All the measurements were carried out under atmospheric conditions in the constant force mode.

Due to a larger tip radius and a larger top angle, the pyramidal tip gave results with less resolution than those obtained when the rod-like tip was used. For the former tip the grooves appeared to be less deep and less steep.

For the STM measurements the tips were prepared from 0.25 mm 90% Pt–10% Ir wire by mechanical cutting. The measurements were carried out using a negative tip voltage in the range from -0.5 to -1.0 V. Measurements using a positive tip voltage gave the same results. Only the measurements made using negative tip voltages are shown in this paper. All the measurements were carried out under atmospheric conditions in the constant current mode.

The resolution achieved by the AFM, using the rod like tip, was somewhat less than the resolution achieved by the STM. This could be due to the fact that, during the scan, the long and thin rod-like AFM tip can bend more than the stiffer STM tip.

Before the AFM and STM measurements the polished surfaces were pre-examined by optical differential interference contrast microscopy (DICM) and by phase shifting interferometry (PSI) (Wyant *et al.* 1986, van Enckevort 1992).

3. RESULTS

3.1. Bevelled (100) surface

For the bevelled (100) specimen the measurements were carried out on the as-grown surface near the boundary between the as-grown and the polished parts. In fig. 2(*a*) a part of the polished region can be seen on the right-hand side. On the as-grown surface many grooves can be seen near the boundary. Further away from the boundary, on the left-hand side, the number of grooves decreases. In fig. 2(*b*) the region closer to the boundary can be seen at higher magnification. The surface is not completely covered with grooves and the original CVD growth features, like hillocks, can be seen. Two types of hillocks are found, namely steep ones due to step nucleation from 3D diamond nuclei, and shallow ones probably due to spiral growth (van Enckevort *et al.* 1991, van Enckevort *et al.* 1994). The height of the shallow hillocks ranges from 4 to 30 nm, with inclinations ranging from 0.2° to 1.5°, with respect to the diamond (100) surface. Many of the grooves are not straight and their directions are scattered within a range of a few degrees with respect to the direction of polishing. The size of the grooves ranges from 35 to 220 nm in width and 0.3 to 3.0 nm in depth. Since the images obtained are a convolution of the real topography and the tip shape, the grooves can be somewhat deeper than stated above. The grooves are up to 40 μm long. All the grooves are found to follow the contour of the growth hillocks, keeping a constant depth. Grooves could be seen that suddenly start and/or end at some point of the surface (fig. 3(*a*)). Running along the sides of a part of the larger grooves an elevation can be observed (fig. 3(*b*)). Many others and most of the narrowest width grooves do not show this feature. Practically none of the grooves continues across the boundary into the polished part of the surface. On the as-grown surface there were many diamond crystallites standing above the level of the surface. As can be seen in fig. 4, grooves that meet one of these crystallites often undergo a change in direction, going around the crystallite. In some cases the grooves just stop at the crystallites.

Measurements were carried out on the as-grown surface far from the boundary with the polished part. No grooves could be found and only features due to the growth process were observed. All these features were exactly the same as the growth features that were observed between the grooves on the as-grown surface close to the boundary.

In only one case we found cracks within a groove. This groove is much broader (320 nm) and deeper (8 nm) than the other grooves (fig. 5). The other grooves appeared smooth in all cases.

Measurements carried out on the polished part of the specimen showed that the surface was covered by smooth parallel grooves, like the ones observed by STM on other samples (Couto *et al.* 1992, Couto *et al.* 1994a) (see previous chapters).

3.2. (110) surfaces

Several broad grooves could be observed on the surfaces of the (110) specimens. For one specimen these grooves traverse the diamond surface from one edge to the other (fig. 6). The grooves have widths ranging from 1.4 to 5.2 μm and depths ranging from 70 to 450 nm,

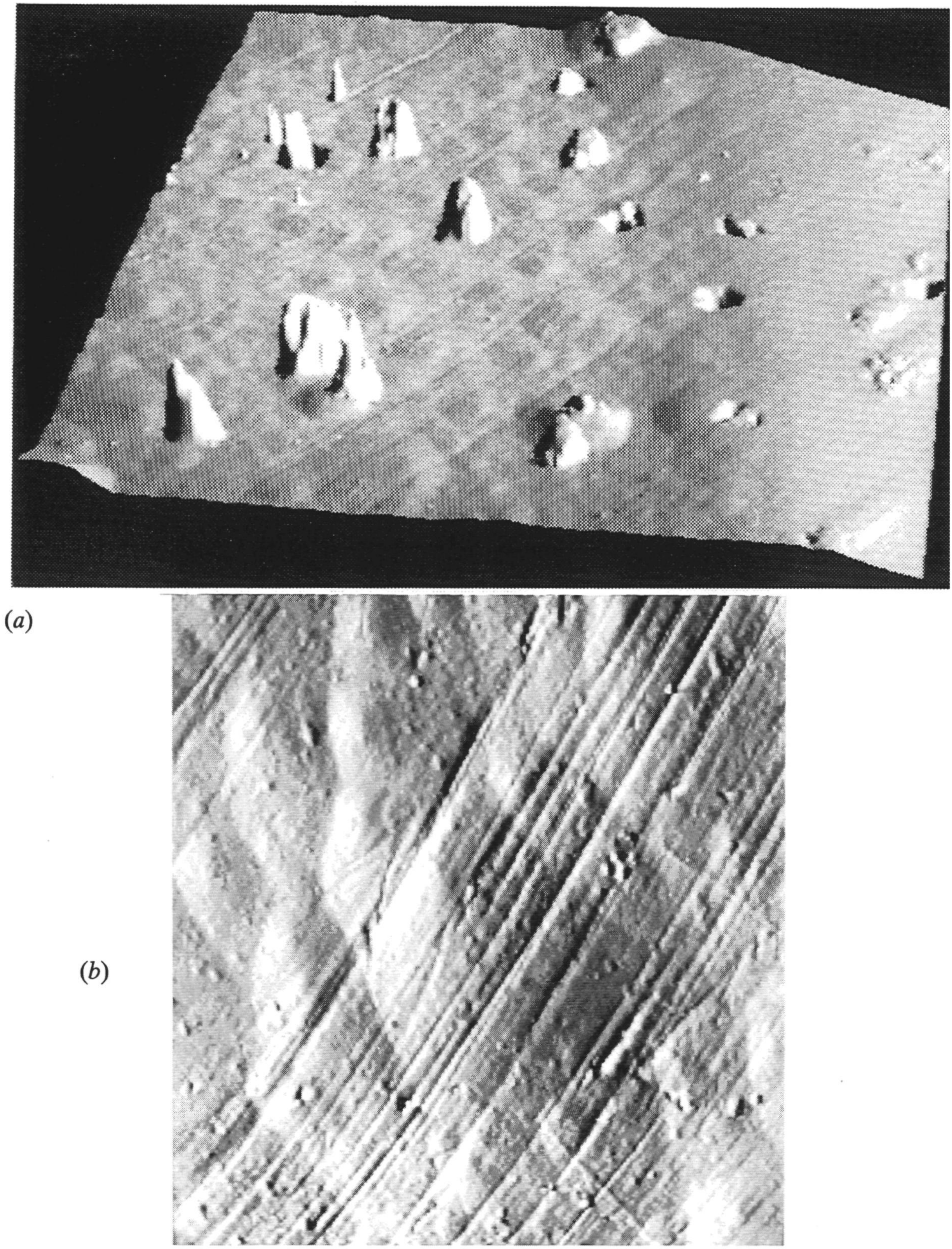

Fig. 2. AFM image of the bevelled (100) sample. (*a*) The boundary between the as-grown and the polished parts can be seen. The scan size is 46.5 μm × 46.5 μm. (*b*) On the as-grown part many grooves can be seen near the boundary, running across the growth hillocks. The scan size is 7.5 μm × 7.5 μm. Figure (*a*) is shaded with a light source shining from the right side. Figure (*b*) and all the others figures are shaded with a light source shining from the left side.

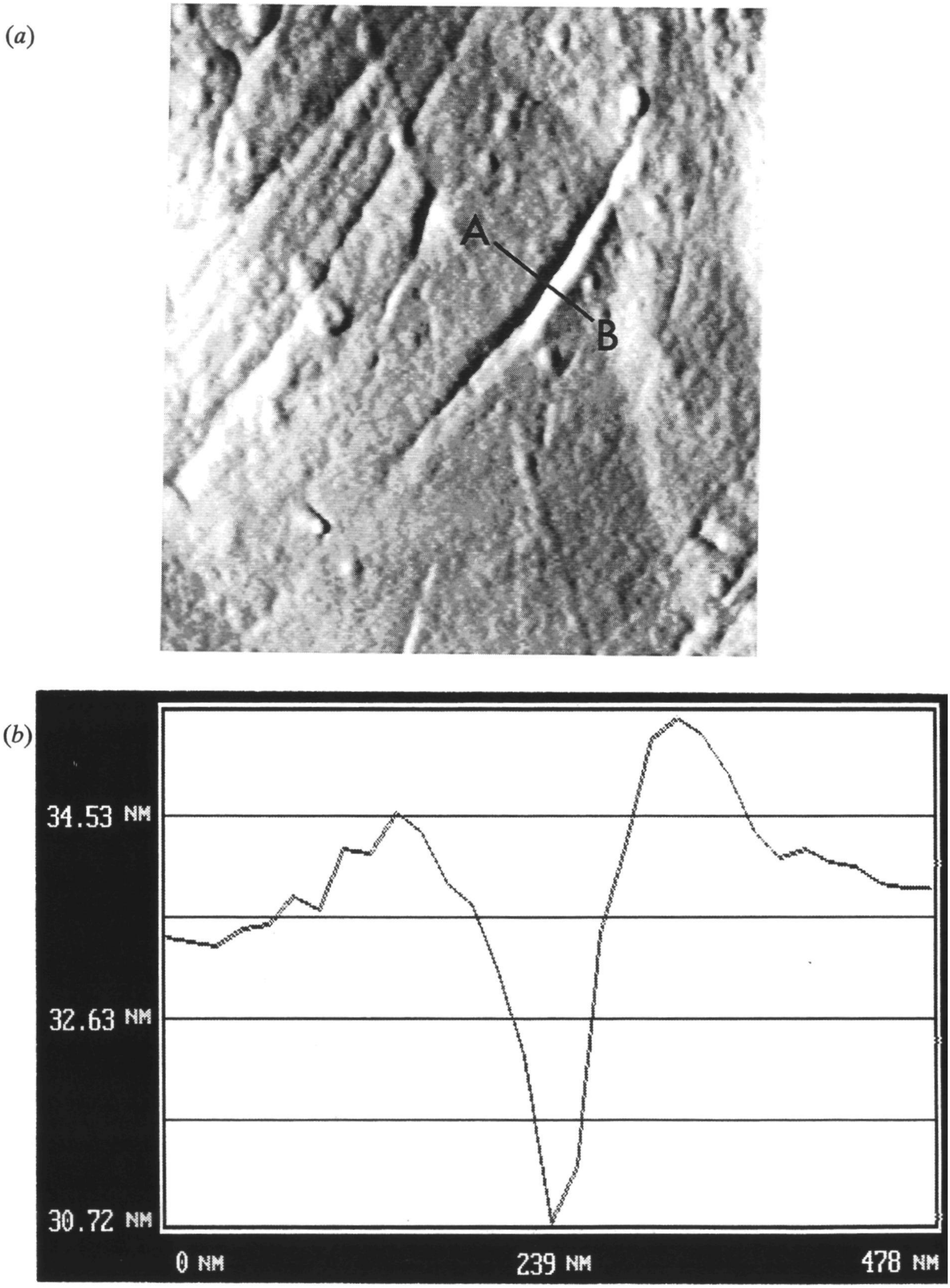

Fig. 3. AFM image of the as-grown part of the bevelled (100) sample. (*a*) Some of the grooves start and end at some point of the surface. The scan size is 2.9 μm × 2.9 μm. (*b*) Profile along the line AB showing that some of the grooves present an elevation running along their sides.

Fig. 4. AFM image of the as-grown part of the bevelled (100) sample. The direction of polishing was from the upper right-hand corner to the lower left-hand corner. On the lower part some grooves can be seen that either stop or go around a diamond crystallite. The scan size is 7.5 μm × 7.5 μm.

with side wall inclinations ranging from 1.7° to 15.0°. In another specimen a deep groove can be seen that originates from a hole in the surface and continues up to the edge of the diamond (fig. 7). Its width is 1.3 μm and its depth is 90 nm, with side wall inclinations of 8° and 20°. In all cases, small grooves can be seen on the bottoms of the deep grooves (fig. 8). No cracks could be observed.

3.3. Natural diamond

On this specimen naats and polishing grooves can be seen (figs. 9(*a*) and 9(*b*)). The naats are at angles of 34° or 49° with respect to the direction of the polishing grooves which is roughly [001]. The naats are harder than the surrounding diamond and manifest themselves as elevations on the surface, with widths ranging from 130 to 350 nm (fig. 9(*c*)). It can be seen from the AFM height profiles that the side of the naats that is facing the incoming abrading particles is steeper than the opposite side, with heights ranging from 2 to 15 nm.

Following the polishing grooves along the direction of advancement of the abrading particles, we can observe from the traces (fig. 9(*a*)) that the grooves are deep until they intersect a naat, then become shallow (about 0.3 nm) immediately after passage of this naat and become deeper (about 1.4 nm) until they meet the second naat. Only a few grooves were seen to continue on top of the broader naats but many could be seen that continued on the

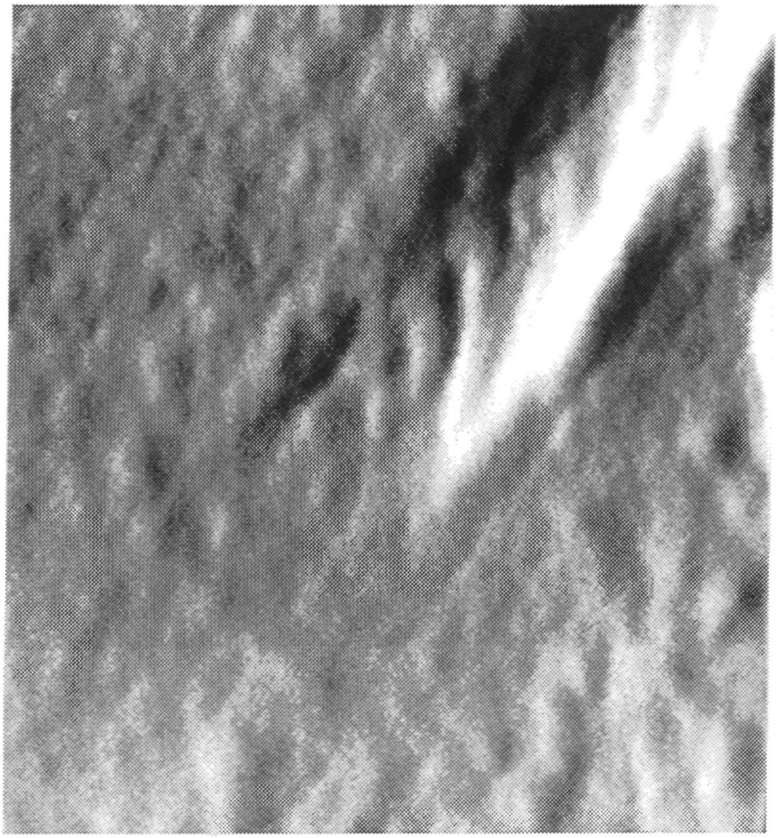

Fig. 5. AFM image of the as-grown part of the bevelled (100) sample. A broad and deep groove showing the presence of cracks can be seen on the upper right-hand corner. The groove stops in the centre of the image. The scan size is 1.3 μm × 1.3 μm.

other side of the naat. For the thinner naats the number of grooves that continued on top and on the other side of the naat is larger. No cracks could be seen on top of the naats, despite the fact that the polishing was close to a hard direction, as will be discussed in section 4.2.

It can also be seen that at the point where the abrading particles meet the naat they undergo a deviation on their direction, moving a small distance along the side of the naat before continuing their paths (fig. 10).

4. Discussion

4.1. Diamond polishing by single pass grooving

Many isolated grooves could be seen on the as-grown part near the boundary of polished–unpolished regions of the bevelled specimen. Since the growth features on the as-grown surface near and far from the boundary were identical, that is, the growth surface between the grooves is unaltered, it seems that the only process that is occurring near the boundary is the production of isolated grooves, without any effect on the surrounding surface. Since this part of the surface is not in direct contact with the scaife, the grooves must have been produced by large particles standing at most one micrometre above the surface of the scaife. Almost all the grooves were smooth. Only one groove showed the presence of cracks.

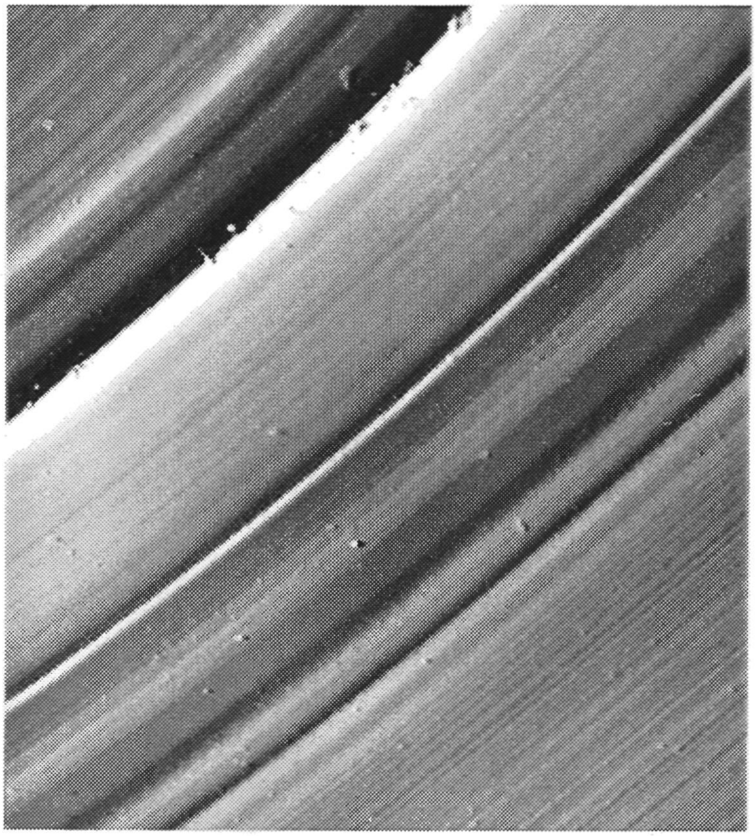

Fig. 6. AFM image of a (110) sample, showing the presence of some broad grooves. These grooves run across the sample from one side to the other. The scan size is 50 μm × 50 μm.

This groove was much broader and deeper than the others. It is known from sliding experiments that a broad and deep groove, produced by a high pressure of the sliding stylus, normally shows cracks (Seal 1958, Enomoto and Tabor 1981) but that the narrower ones are smooth (Seal 1958, Wang *et al.* 1991), in conformity with our observations.

From the three mechanisms that produce smooth grooves let us consider first the atom by atom removal of material. The formation of grooves by this mechanism implies that either one particle traverses the surface along the same track many times or that many particles traverse the surface along the same track. The latter possibility is not very likely since the existence of only isolated grooves on the as-grown part of the diamond would imply that there are preferred routes along the surface and that all the abrading particles are contacting the surface only along these routes. Many grooves could be seen that started and ended before they reached the boundary. The formation of these grooves by multiple passes of the same abrading particle is also unlikely since it involves the particles losing and regaining contact with the diamond surface at the same points several times. Moreover, the grooves are too narrow to be explained by this option. For a 50 nm wide groove and a scaife rotation of 50 turns sec^{-1} this means that the lateral translation rate must be less than 2.5 μm per second. Since the diamonds are slightly moved by hand during polishing, the actual stability must be much less than that required for multiple passes of the same particle on the same track. It is more likely that the grooves are formed in only one pass of the abrading particle. During the formation of the groove the particle may either break or be displaced on the polishing scaife, losing contact with the diamond surface and leaving behind grooves that suddenly terminate.

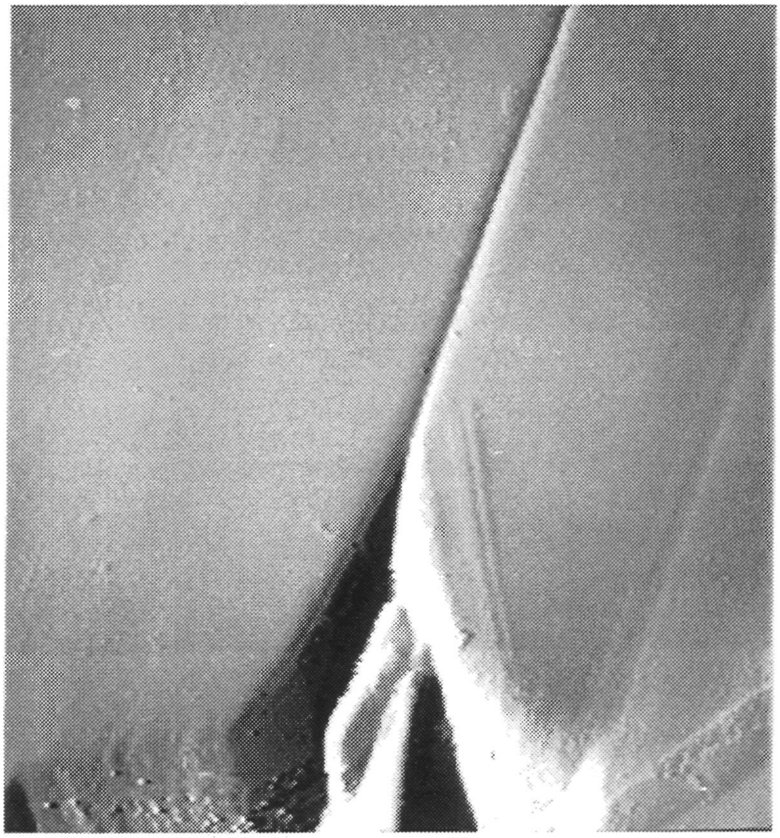

Fig. 7. STM image of a (110) sample. A deep groove can be seen that starts from a hole on the surface. The scan size is 20 μm × 20 μm.

Since the as-grown diamond surface between the grooves is unaffected, additional polishing and smoothing by atom by atom removal seems not to play an essential role and therefore cannot contribute to a smoothing of rough grooves. Since the production of smooth grooves by a mechanism involving fracture must also involve subsequent polishing via atom by atom removal of material, the only known mechanisms for groove formation and thus diamond polishing that are left are plastic flow or the direct removal of many atomic layers in a single pass of the abrading particle. Indication for plastic flow is the occurrence of elevations running along the sides of some of the larger grooves. In addition, plastic grooving as well as the direct rupture mechanism easily explain the linear dependence of polishing rate on scaife speed.

4.2. Diamond polishing as a mechanical process

It can clearly be seen that the movement of the abrading particles making the grooves is guided by the growth features. The grooves follow the profiles of the growth hillocks, keeping a constant depth, and when they meet some of the large diamond crystallites on the surface they change direction, going around the crystallite, or stop. The abrading particles behave as if they are connected to damped springs, being able to move up and down and from side to side. The absence of grooves continuing from the as-grown part, across the boundary, into the bevelled part is probably due to the fact that the part of the groove that is formed in

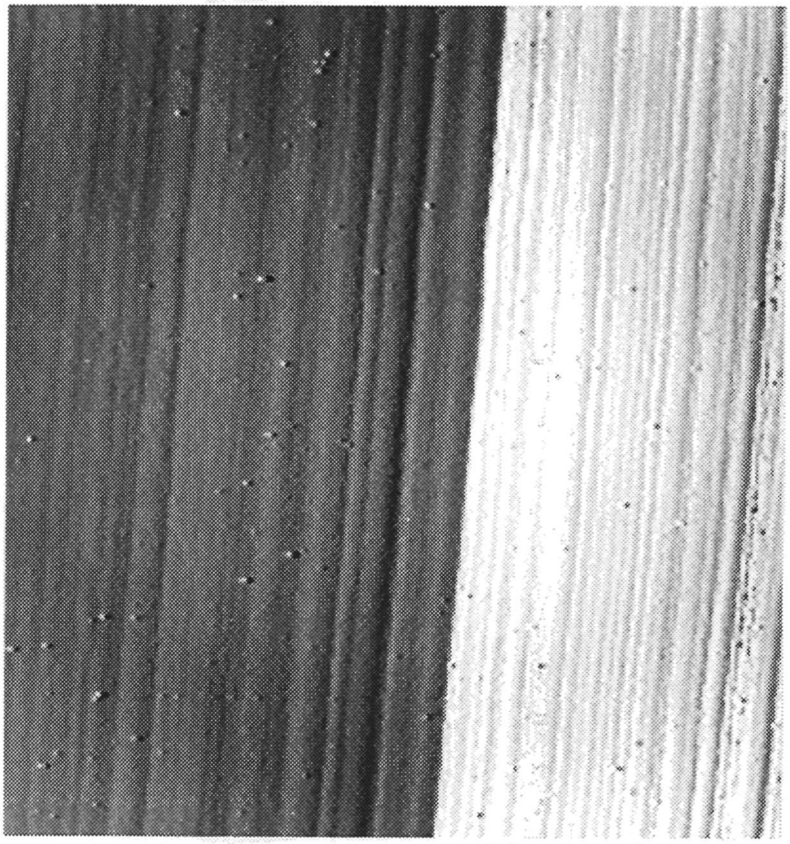

Fig. 8. STM image showing a detailed view of the bottom of the groove that can be seen on the upper left-hand corner of fig. 6. Smaller grooves can be seen on the bottom of the big groove. The scan size is 1.6 μm × 1.6 μm.

the polished region is polished away and replaced by other grooves of different sizes and/or at different positions, produced by other particles that are less protruding from the scaife.

The measurements on one of the (110) surfaces showed the presence of a very broad and deep groove starting at a hole in the centre of the diamond surface. Probably the hole was produced when a diamond crystallite, incorporated in a different orientation from the surrounding material during the growth process, broke away. This crystallite then scratched the diamond surface and produced the groove. Since the groove is only present in a part of the surface, namely from the hole to one of the edges, it must have been formed in only one pass of the diamond fragment. After the diamond crystallite had passed the diamond surface it was removed or displaced on the scaife and did not scratch the surface again during subsequent rotations. If such a large groove is produced by fracture, cracks are expected to occur. No cracks could be seen, but smaller, smooth, grooves were present on the bottom of the big groove. Probably these were formed by small asperities on the surface of the large particle. An alternative explanation for the smaller grooves is a further polishing of the big groove. Since the big groove found on the surface of the other (110) diamond traverses the surface from one edge to the other, it is not possible to say whether it was produced in one or in several passes of a large abrading particle. Small grooves were also present on the bottom of this big groove. It is not possible to say whether these grooves were produced by plastic flow or by fracture followed by a further polishing.

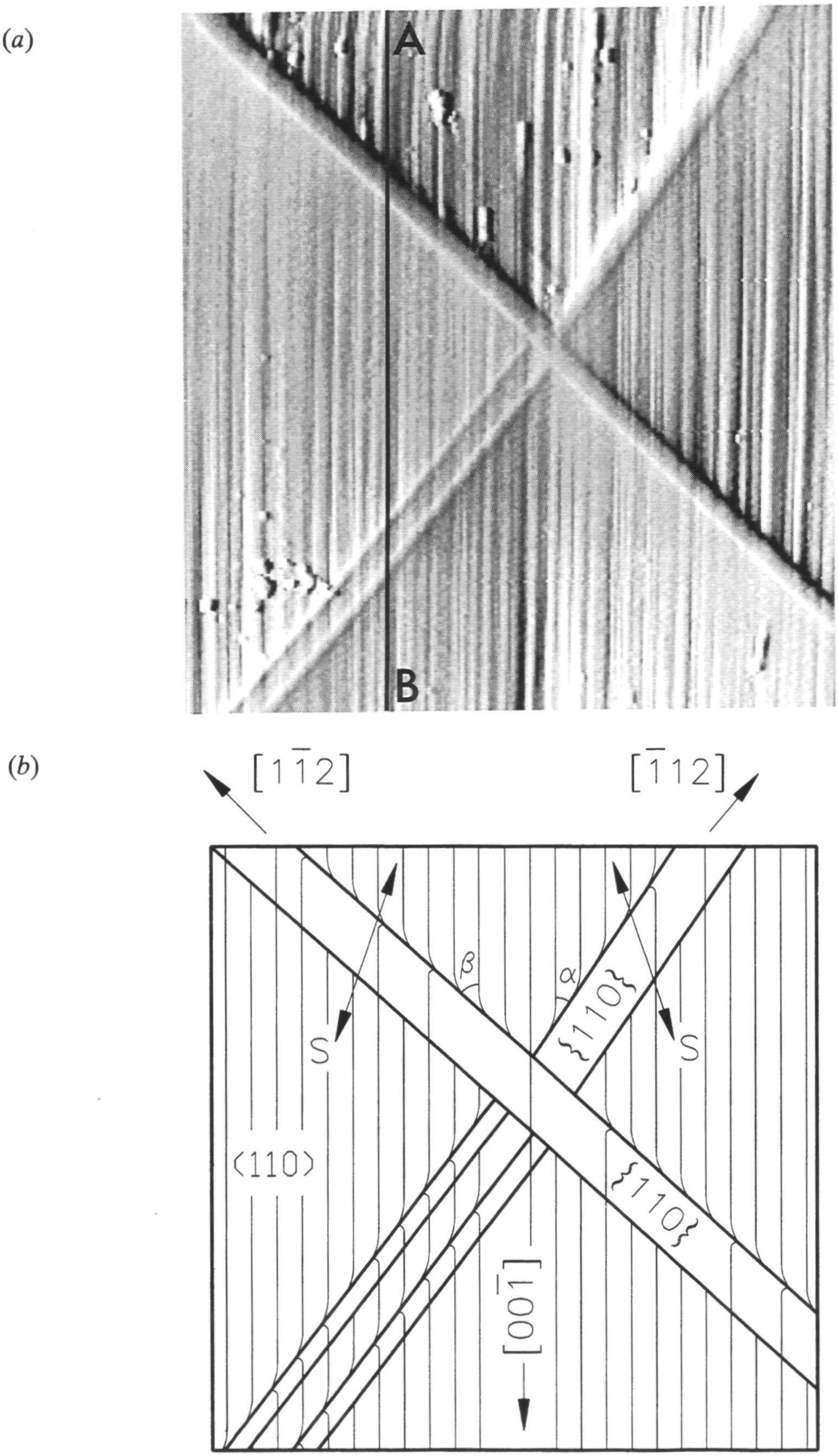

Fig. 9 (*a*)–(*b*). See next page for caption.

(*c*)

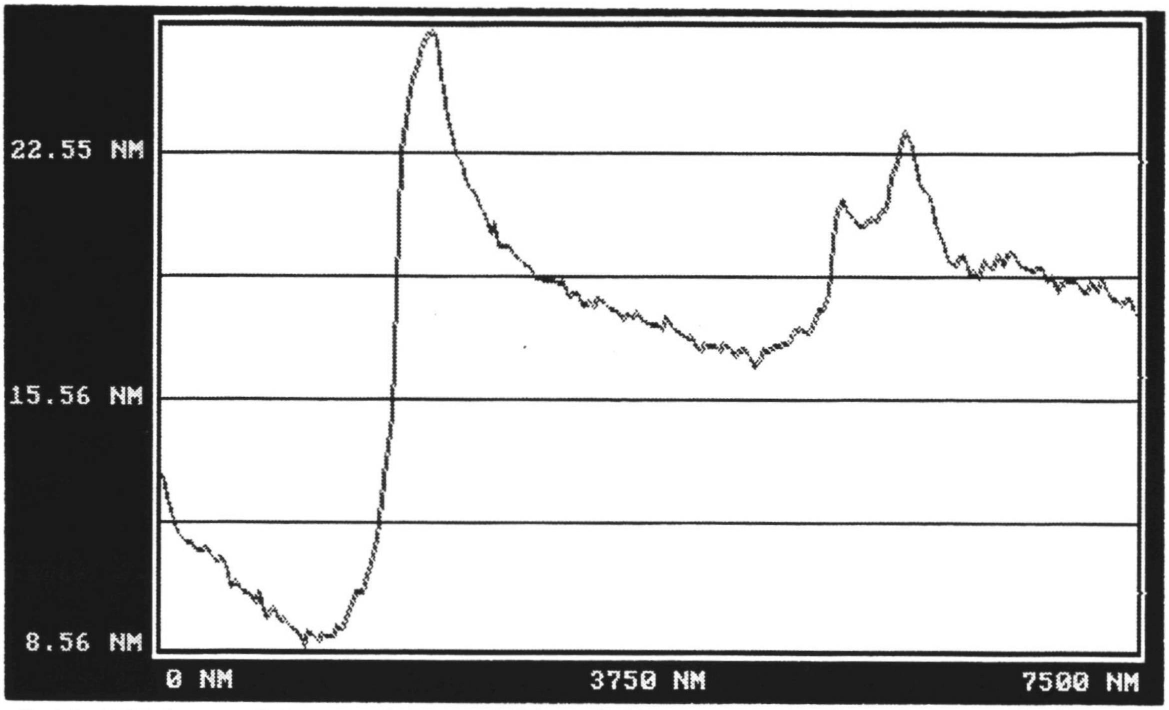

Fig. 9. (*a*) AFM image of the natural diamond. The polishing grooves run from the top to the bottom of the image. The lines running along the diagonals are the naats. The scan size is 7.5 μm × 7.5 μm. (*b*) Crystallographic orientations of the naats and polishing grooves. The angles between the naats and the polishing grooves are $\alpha = 34^\circ$ and $\beta = 49^\circ$. (*c*) Profile along the line AB on Figure 9(*a*).

From the measurements on the natural diamond we can see that the naats stand above the level of the (110) diamond surface. The surfaces on top of the naats also have a (110) orientation but the [001] directions make an angle of 109.5° with respect to those of the surrounding {110} surface. Due to this, when the surface of the diamond is polished along the [001] direction, that is the easy direction for polishing along this face, the surface on top of the naats is polished 19.5° from [100], that is a hard direction for polishing. The naats 'protect' that part of the surrounding surface which is close to the faults on the downstream side with respect to the movement of the abrading particles. For this part of the surface the effect of the polishing is decreased and the surface stands higher than the part that is further away from the naats. It seems that when the abrading particles pass the naat they are pushed downwards towards the scaife. Considering the line profile of fig. 9(*c*), one sees that the abrading particle moves 15 nm from the diamond surface to the top of the highest naat, corresponding to a horizontal movement of about 120 nm. With a polishing speed of 50 m s^{-1}, this displacement of the abrading particle takes place in about 2.5 ns. From Newton's laws for acceleration of mass this corresponds to a pressure of about 2×10^8 Pa for a cubic particle of 10 μm side. Since a real abrading particle is supported by the high-mass scaife and the surface interaction takes place via sharp corners and asperities producing contact areas with diameters of the order of the groove widths, the actual pressure acting on the diamond surface will be many orders of magnitude higher. Due to the short time involved in the displacement of the abrading particle, it is deformed only elastically at first and the abrading particle may return to substantially the original position after some time. Under the naat the pressure is larger. Most probably the contact areas between the abrading particles and the surface are also larger. These effects compensate for the higher hardness of the surface and the polishing of

Fig. 10. AFM image showing a detailed view of some of the points where the polishing grooves meet the naats. The direction of polishing is from the top to the bottom. Where the polishing grooves meet the naats they deviate to the right. The scan size is 1 μm × 1 μm.

the naats proceeds at the same rate as the polishing of the surrounding surface. When the abrading particles move from under the naat they gradually move upwards, producing grooves that become increasingly deeper and wider, until the deformations of the scaife and abrading particles are relaxed to the original state. As can be seen from Figure 9a the grooves recover their original widths and depths at a distance of about 5 μm from the naats. This corresponds to a recovery time of approximately 100 ns.

In summary, diamond polishing proceeds via a mechanical interaction between the abrading particles and the diamond surface. Due to the high pressures at the corners or asperities of the particles, grooves are produced in the diamond surfaces being polished. The abrading particle tips can be considered as moving as though they were suspended from vertical and horizontal springs. In this way the particle tips follow the features on the surface, with the result that variations in the directions and depths of the grooves occur. The validity of this mechanical spring model is beautifully demonstrated by the deflection of the polishing grooves where they intersect the naats (as shown in fig. 10 and schematized in fig. 9(*b*)).

4.3. Possible mechanisms of grooving

Since the grooves are formed in single passes of the abrading particles, the polishing rate (mm s^{-1}) can be expressed as:

$$R = fNDWSL\ ,$$

where N is the number of particles per square millimetre that are making contact with the diamond, D is the groove depth, W is the groove width, S is the number of revolutions of the scaife in one second and L is the distance travelled by the diamond in one revolution of the scaife. The factor f is the fraction of removed material:

$$f = \frac{V_r}{V_d + V_r},$$

with V_r and V_d the volumes of the removed and displaced diamond respectively. In essence this factor is equivalent to the Archard constant K, which is the probability factor for material removal when sliding surfaces contact each other (Archard 1953, 1961). In the case of wear involving repeated plastic deformation of interacting asperities typical values of K, and thus, f, range from 10^{-2} to 10^{-5} (Archard 1953, 1961, Karis and Novotny 1989). In this case the grooves are formed by *displacement of material* via plastic flow rather than by material removal. This plastic deformation involves the movement of dislocations. Alternatively, if f is close to one then the grooves are formed by *direct material removal*. Probably this occurs by rupture of numerous atomic bonds as a result of the ultra high pressures exerted by the asperities on top of the abrading particles on the diamond surface. It is known from early theories on plastic deformation not using the concept of dislocations that the shear stress necessary to produce breakage of atomic bonds must exceed about G/30, where G is the shear modulus for deformation in the direction of the applied stress (Frenkel 1926, Orowan 1940, Mackenzie 1949, Hull and Bacon 1984, Kittel 1971). Theoretical papers indicate that small radii indenters are capable of producing such a situation on brittle materials (Roesler 1956, Kendall 1978).

For the usual polishing procedure R is about 1.7×10^{-4} mm s^{-1}, L is about 600 mm and S is equal to 50 turns s^{-1}. In this work it was found that the average depth and width of the grooves were about 2.0×10^{-6} mm and 1.3×10^{-4} mm respectively. Using these values it is found that N = 22/f particles mm^{-2}. During polishing the pressure applied on the diamond is about 1 N mm^{-2}. If the abrading particles are considered as being cubes of 10 μm side, the pressure exerted on the diamond by each particle is about $(4 \times 10^8)/f$ Pa. In reality the abrading particles are not cubic, having many asperities on their surfaces. If it is considered that the real contact between the abrading particle and the diamond is due to an asperity with the shape of a truncated square pyramid with a top dimension equal to the groove width, the pressure exerted on the diamond surface is about $(3 \times 10^{12} f)$ Pa.

If $f \approx 1$, the pressure exerted on the diamond surface is about 3×10^{12} Pa. Since the critical shear stress necessary to produce simultaneous rupture of atomic bonds is about G/30 or 2×10^{10} Pa, it can be seen that the pressures exerted by the abrading particles are more than enough to produce grooves in the diamond surface. After passage of the particle stress release occurs and the disintegrated material recombines to softer forms of carbon, such as graphite (van Bouwelen *et al.* 1993) or reacts with ambient oxygen or surface hydrogen. In fact for $f \approx 1$ the contact pressures appear to be comparable with the 2000 GPa deduced for sliding experiments by Tabor and Field (1992) (their Figure 14.6). These impossibly high pressures could only be explained if it was assumed that the regions between the scratches bear the load elastically. We may make a similar assumption for the present case of diamond polishing, and also note that the 'impossible high' pressures provide an explanation of the transmission of disruptive effects through tens of atomic layers.

If $f = 10^{-2}$ to 10^{-5}, or material displacement determines groove formation, the contact pressures are considerably lower, namely 3×10^{10} to 3×10^{7} Pa. Except for the highest values pressures in this range are not sufficient for direct rupture of atomic bonds. However, if the temperature in the contact region exceeds about 1000K dislocations can be displaced by pressured in the middle of this regime (Brookes *et al.* 1990, Brookes 1992). Since elevated temperatures in the contact region are likely to occur due to heat produced by friction, it can be postulated that grooves could also be produced by plastic flow.

The key question that now arises is whether diamond polishing proceeds by direct material removal, that is $f \approx 1$, or via repeated displacement of material by plastic deformation, that is $f \ll 1$, with subsequent material removal. The first mechanism does not involve the production and movement of dislocations, whereas the second, $f \ll 1$, mechanism needs many *induced* dislocations. Grown-in dislocations occur far too infrequently to affect the polishing mechanism. From the present and previous AFM and STM studies of polished diamond surfaces no evidence was found for the occurrence of slip steps or slip bands, which are the fossils of dislocation movement. Moreover, only grown-in dislocations and nitrogen plateletes have been observed in polished knife edges by transmission electron microscopy (Couto *et al.* 1992 (see chapter 2)). A second characteristic of the $f \ll 1$ mechanism would be the displacement of diamond material, giving elevated rims along the grooves. These were only found for parts of the larger grooves on the as-grown part of the bevelled specimen. The volume of the displaced material was only 25% of the groove volume. Since these grooves were formed in only one pass of the abrading particle it is unlikely that the lack of displaced material along them is due to a subsequent removal of this material. For other large and all narrow grooves no elevated side walls were observed. Therefore a large amount of displaced material seems lacking. Thus most evidence supports the $f \approx 1$ mechanism for groove formation, and diamond polishing seems to proceed by direct rupture of many bonds leading to disintegration of the diamond material. It should be noted here that the shallowest grooves which we could detect were only 0.3 nm deep, and thus only two to three atomic layers are removed during passage of the abrading particle. This is a borderline case between the mechanism we suggest here and atomic attrition.

Diamond polishing by direct rupture of bonds as well as by multiple plastic deformation explains very well the linear dependence of material removal on scaife speed. The dependence on crystal orientation is not yet clear. If dislocations play a major role in the formation of grooves then the observed large difference in resistance to groove formation for the soft and hard directions (see fig. 10) can only be explained by an anisotropy of dislocation generation or mobility in the crystal. In view of the high symmetry of the diamond crystals and the occurrence of many symmetrically equivalent glide systems, such as 12 times the $<1\bar{1}0>/\{111\}$ system, a large anisotropy in plastic deformation seems unlikely.

If one considers the more probable case that $f \approx 1$ then a possible explanation for the anisotropy in wear rate is the relation between the direction of the atomic bonds on the crystal and the direction of polishing. In the theory of crystal growth a crystal such as diamond may be considered as a connected network of the so-called Periodic Bond Chains (PBC's) which are chains of atoms interconnected by strong bonds (Hartman and Perdok 1955, Hartman 1963, 1973). In the diamond lattice only one type of PBC occurs, namely the C/C\C/C\C zigzag carbon chains along the [110] directions. If the directions of the PBC's for a particular face are considered, one sees that for {100} and {110} the hardest directions of polishing are aligned along the PBC's and that the soft directions make an angle with respect to the PBC's (45° for {100} and 90° for {110}). In considering the anisotropy of polishing one should not only consider the bonding forces, but also the Born repulsion between atoms which can be extremely high for large compressions in the 'anharmonic' region. If one displaces a small group of atoms very far from their equilibrium position in a horizontal direction, the repulsion force by the atoms in front will be much more important than the force of attraction by the atoms in the rear. This means that removal of material involving the movement of atoms along the PBC's is difficult because the repulsive interaction of the atoms along a PBC is strong, with the atoms buttressing each other and preventing the breakage of the bonds. The movement of atoms at a significant angle to the PBC's is easier since the repulsive interaction of the atoms between different PBC's is weaker. To understand the anisotropy of diamond polishing in more detail computer modelling by molecular mechanics methods is required.

To attack the problem of the anisotropy during polishing, a new series of experiments is being set up. For these experiments an apparatus for scratching a diamond surface, with a diamond stylus, in a controlled way is being built. With this machine it will be possible to scratch the surface in different orientations and at different loads. Using the AFM or the STM to image the damage produced at the surface may give new insights on the problem of the anisotropy of diamond polishing.

5. Conclusion

Diamond polishing in soft directions proceeds via the formation of nanogrooves in the diamond surface. These are produced by asperities on the diamond abrasive particles, each in a single pass, in a process which is basically disruption of atomic bonds under the extremely high local pressures (though the near-atomic scale mechanism is still not clear). Observable cracking or plastic deformation in the sense of dislocation generation and movement are practically not involved. The dependence of abrasion rate on crystallographic orientation may well be related to the directions of periodic bond chains in the atomic lattice. Further theoretical analysis and detailed experiments are still needed to resolve the long-standing enigma of diamond polishing.

6. Acknowledgements

The authors acknowledge the help of Drukker International B.V. for polishing the specimens and for the use of some of their equipment. Further they wish to thank G. Janssen and W. Vollenberg for providing the CVD-grown diamond specimens.

One of the authors, M. S. Couto, wishes to thank CAPES (Coordenação de Aperfeiçoamento de Pessoal de Nível Superior), Brazil, for a scholarship making this research possible.

We thank one of the referees of this paper for a suggestion to interpret the results in terms of the Archard constant. This has, we believe, led to a much clearer exposition of our ideas.

Chapter 6

Friction tracks on diamond surfaces imaged by atomic force microscopy

M. S. Couto, W. J. P. van Enckevort

Department of Solid State Chemistry, University of Nijmegen, Faculty of Science, Toernooiveld, 6525 ED, Nijmegen, The Netherlands

M. Seal,

Sigillum B.V., Guido Gezellestraat 5, 1077 WN, Amsterdam, The Netherlands

Abstract

The friction tracks produced by spherical diamond styli sliding on a planar diamond face along a soft direction for polishing have been imaged by atomic force microscopy. The tracks produced by a single pass as well as by multiple passes of the stylus show the presence of many individual smooth grooves. Along the paths always some debris that was formed during the sliding process was found. The tracks produced at a high load on the stylus show the presence of ring cracks as well as grooves. The morphology of the grooves indicates that material is removed by the disruption of atomic bonds under high pressures. Implications for understanding the mechanism of diamond polishing are given.

1. Introduction

In the previous chapters the morphology of polishing grooves on diamond surfaces has been studied in detail. Although the mechanism of material removal during diamond polishing could be unravelled for the hard directions of polishing, for the soft directions a definitive explanation could not be given.

In this chapter the grooves produced by a diamond stylus sliding on a diamond surface are studied by atomic force microscopy (AFM). Since the parameters involved in this experiment (sliding direction and speed, stylus radius and load) can be better controlled than in the actual polishing process, a study of the tracks produced by the stylus gives valuable information on the process of groove formation during diamond polishing.

2. Experimental details

2.1. Specimen preparation

Synthetic diamonds grown by the high-pressure high-temperature method (HPHT) were used in the experiments. From the HPHT crystals, blocks of one to a few cubic millimetres with faces parallel to {100} and {110} were cut and polished. The polishing was carried out in a conventional manner, using a cast iron scaife, impregnated with diamond powder with a particle diameter less than 15 μm, mixed with liquid paraffin. The polishing speed was 50 m s^{-1}. Both surfaces were polished along their soft directions: [010] for the (100) surfaces and [001] for the (110) surfaces.

After polishing the diamonds were cleaned by boiling in an aqueous solution of detergent, followed by rinsing in distilled water and isopropanol. Before scratching the surfaces were cleaned again using isopropanol.

2.2. The scratching apparatus

The apparatus used to make the friction tracks on the diamond surfaces in a defined manner is shown schematically in fig. 1. An aluminium frame (F) suspended by a violin string (V) carries a diamond stylus (S) at one end. The screw (C) is used to tighten the violin string and the weight (W) is used to balance the aluminium frame. When balanced the sensitivity of the apparatus is 0.3 g. This is the additional weight placed over the stylus which is sufficient to cause rotation of the frame (F).

The diamond to be scratched is placed on a translator that can be moved, by a stepping motor, in a horizontal direction perpendicular to the string (V). The stepping motor is controlled by a computer. The load on the surface, the sliding direction and speed, and the number of traversals along one track can all be controlled. In each of the experiments the scratches were made on a (100) face along the [001] direction (perpendicular to the polishing grooves, which are parallel to [010]) using a sliding speed of 0.1 mm s^{-1}.

The diamond styli used for making the scratches are standard, spherical pick-up needles for record-players, with radius of curvature R of 12.5 ± 0.5 μm and 16.7 ± 0.5 μm. The profile of one of these styli, prior to use, is shown in fig. 2. The crystallographic orientations of the styli are not known. The diamond quality of the needles was verified by micro-

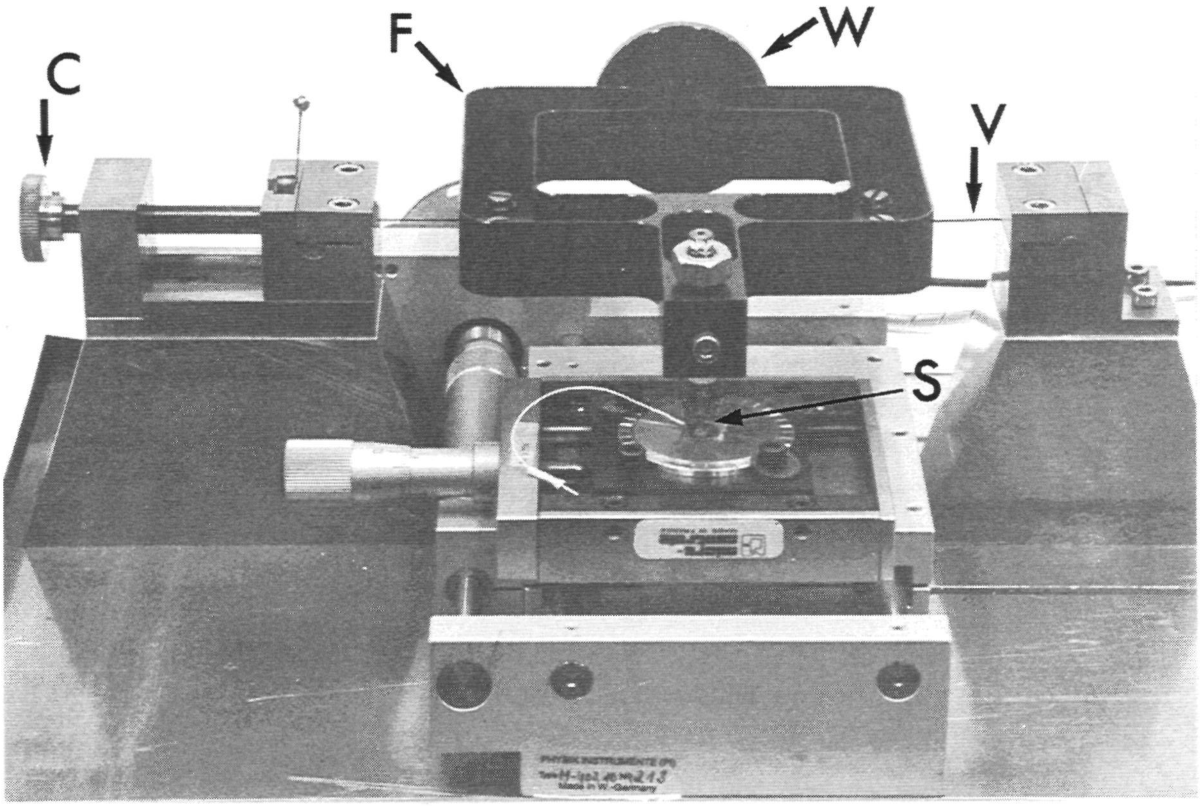

Fig. 1. Apparatus for making friction tracks on a diamond surface.

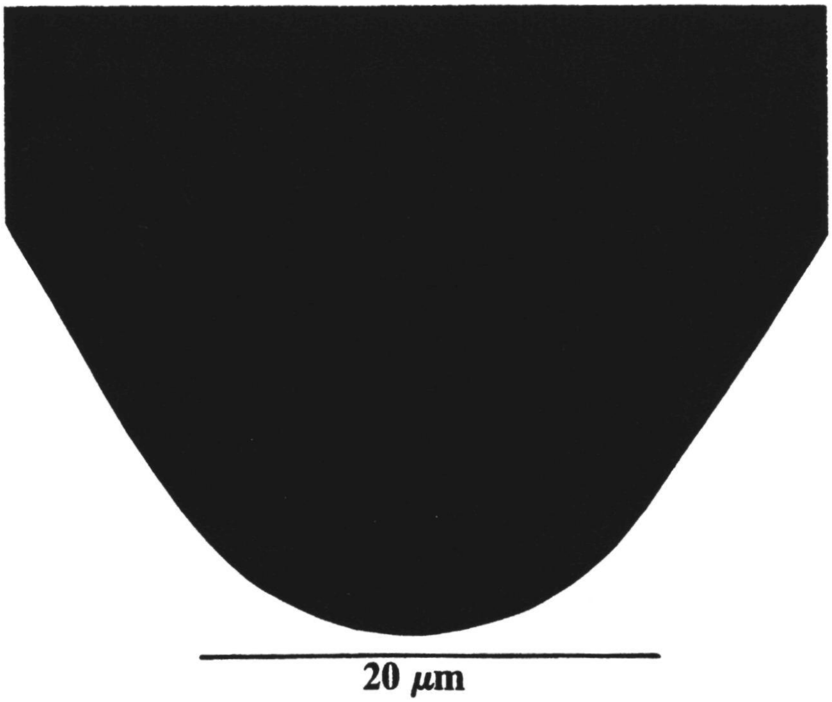

Fig. 2. Profile of a diamond stylus prior to its use (optical micrograph).

Raman spectroscopy.

2.3. Atomic force microscope

The AFM used was a TopoMetrix TMX 2010. For the measurements a tripod scanner with scan range of 75 μm was employed. The tips used were 2 μm high diamond-like carbon rods with a base diameter of 0.15 μm. The cantilevers were made of silicon nitride. All the measurements were carried out under atmospheric conditions in the constant force mode. After a series of measurements on each of the tracks after the sliding experiment, the surface was cleaned with isopropanol and the track was measured again.

3. Results

Figure 3(*a*) shows an image of a friction track produced by a single pass of a stylus with a radius of curvature of 12.5 μm. The load used was 16.5 g. The sliding direction is from the lower left corner to the upper right corner. The track has a width of 3.9 μm and is composed of many individual ridges and some grooves. Along the track some debris can be seen. A part of the debris particles are weakly attached to the surface and during the scan they can be displaced by the AFM tip. Figure 3(*b*) shows an image of the same area as in fig. 3(*a*) after cleaning the surface with isopropanol. The debris was completely removed and only grooves can be seen. Apparently some material in the grooves was removed during cleaning. A detail of the track is shown in fig. 3(*c*). The individual grooves are 30 nm to 255 nm wide and 0.4 nm to 1.2 nm deep.

Along the track shown in fig. 3 no cracks could be revealed. This is not the case for all the tracks produced by an equal pressure on the diamond surface. Fig. 4(*a*) shows a track produced by a stylus with a radius of curvature of 16.7 μm under a load of 28 g. Although this combination of stylus radius and load produce virtually the same tensile stress on the surface as for the track shown in fig. 3(*a*) (see table 1), cracks can be seen along the track. The sliding direction is from the upper right corner to the lower left corner. This track is 3.3 μm wide and is also composed of many individual grooves. A considerable amount of debris can be seen, specially in the central part of the track. Figure 4(*b*) shows a detail of the area covered by the track. The deepest groove that can be seen is 0.9 nm deep and 68 nm wide, which is somewhat shallower than the original polishing grooves.

Figure 5(*a*) shows another track formed by a single pass of a stylus with a radius of curvature of 12.5 μm. This time the load used was high, namely 63 g. A pattern of ring cracks running along the sliding direction (upper right corner to lower left corner) is clearly visible. Closer examination of the individual cracks shows that they are not circular, but are square with rounded corners. The edges of the squares are parallel to [011] and $[0\bar{1}1]$ on (100), which are the intersection lines of the four possible {111} planes with this (100) face. Some grooves can also be seen superimposed on the ring cracks. A detailed image of the area inside the cracks (fig. 5(*b*)) shows the presence of numerous grooves after cleaning. In average, the width of these grooves is 81 nm and their depth is 0.9 nm. Figure 5(*c*) shows a height profile along the line AB in fig. 5(*a*).

Figure 6(*a*) shows the track left after 4 passes of the stylus with a radius of curvature of 16.7 μm, under a load of 28 g. Some debris can be seen along the edges of the track. The

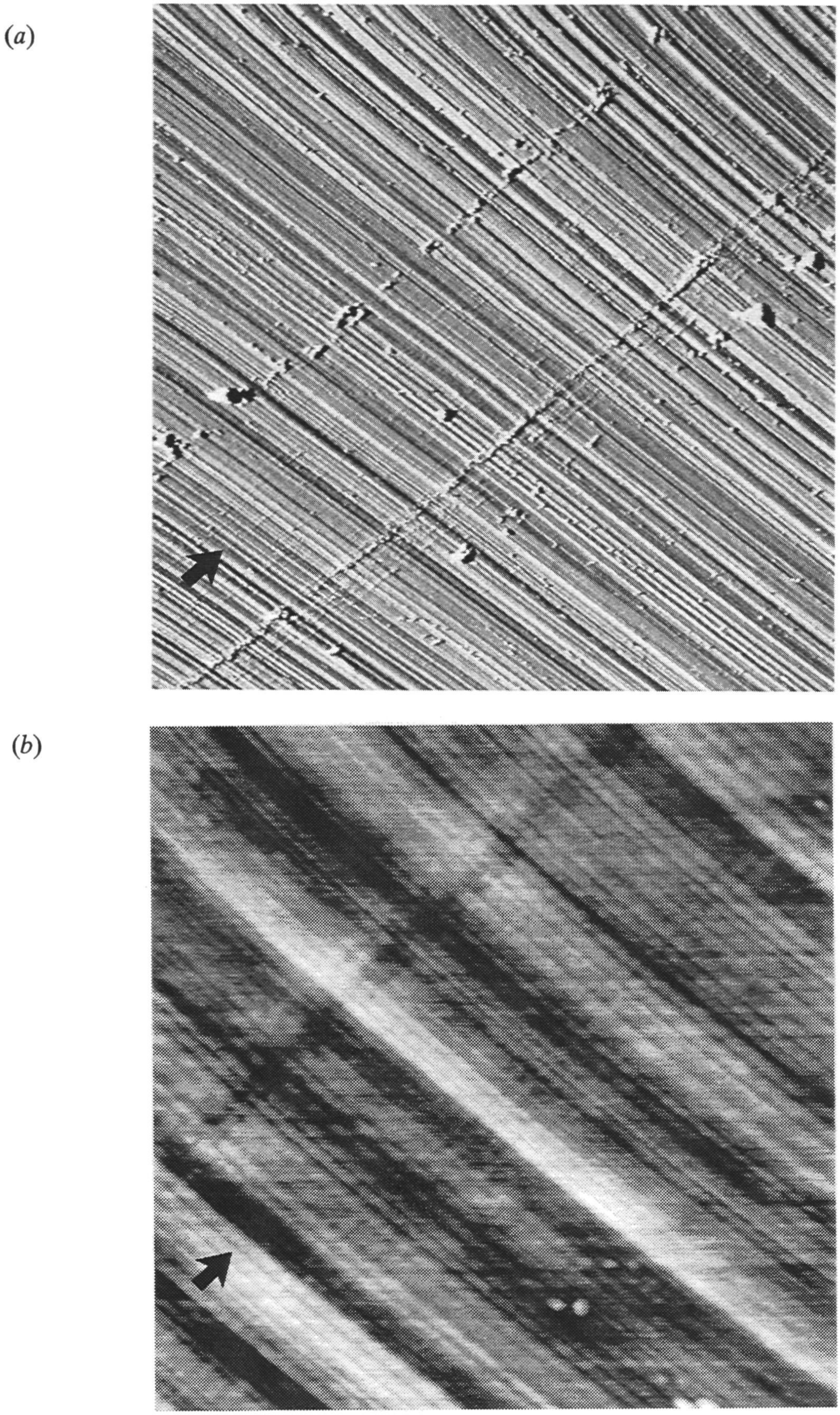

Fig. 3 (*a*)-(*b*). See next page for caption.

(*c*)

Fig 3. (*a*) Image of a friction track left by a single pass of the stylus with R = 12.5 μm under a load of 16.5 g. The scan size is 10 μm × 10 μm. The surface is shaded with a light source shining from the left-hand side. (*b*) Same area as shown in (*a*) after cleaning the surface with isopropanol. The scan size is 5 μm × 5 μm. (*c*) Detailed view of the upper part of the track shown in (*b*). The scan size is 2.5 μm × 2.5 μm. The arrows in this, and several other figures in this chapter, indicate the sliding direction.

same area of fig. 6(*a*) can be seen again in fig. 6(*b*) after cleaning the surface with isopropanol. The width of the track is 5.2 μm and it is again formed by many individual grooves. An image with higher magnification is shown in fig. 6(*c*). The width of the individual grooves is 51 nm and their depth is 0.4 nm, in average. The appearance of the grooves is very similar to the perpendicular ones produced during polishing

In fig. 7(*a*) a track is shown that was formed by 24 passes of the stylus with a radius of curvature of 12.5 μm under a load of 2 g. The amount of debris is large. Most of the particles are weakly attached to the surface and during the scans they are easily displaced by the AFM tip. The track covers a region 5.7 μm wide, and can be seen again in fig. 7(*b*) after cleaning of the surface with isopropanol. The area inside the track can be seen in greater detail in fig. 7(*c*). The largest groove is 467 nm wide and 1.8 nm deep.

Figure 8 shows the profile of the stylus shown in fig. 2 after it was used to produce several friction tracks. A close inspection of the tip of the stylus shows that the smooth profile shown in fig. 2 has changed into a ragged one.

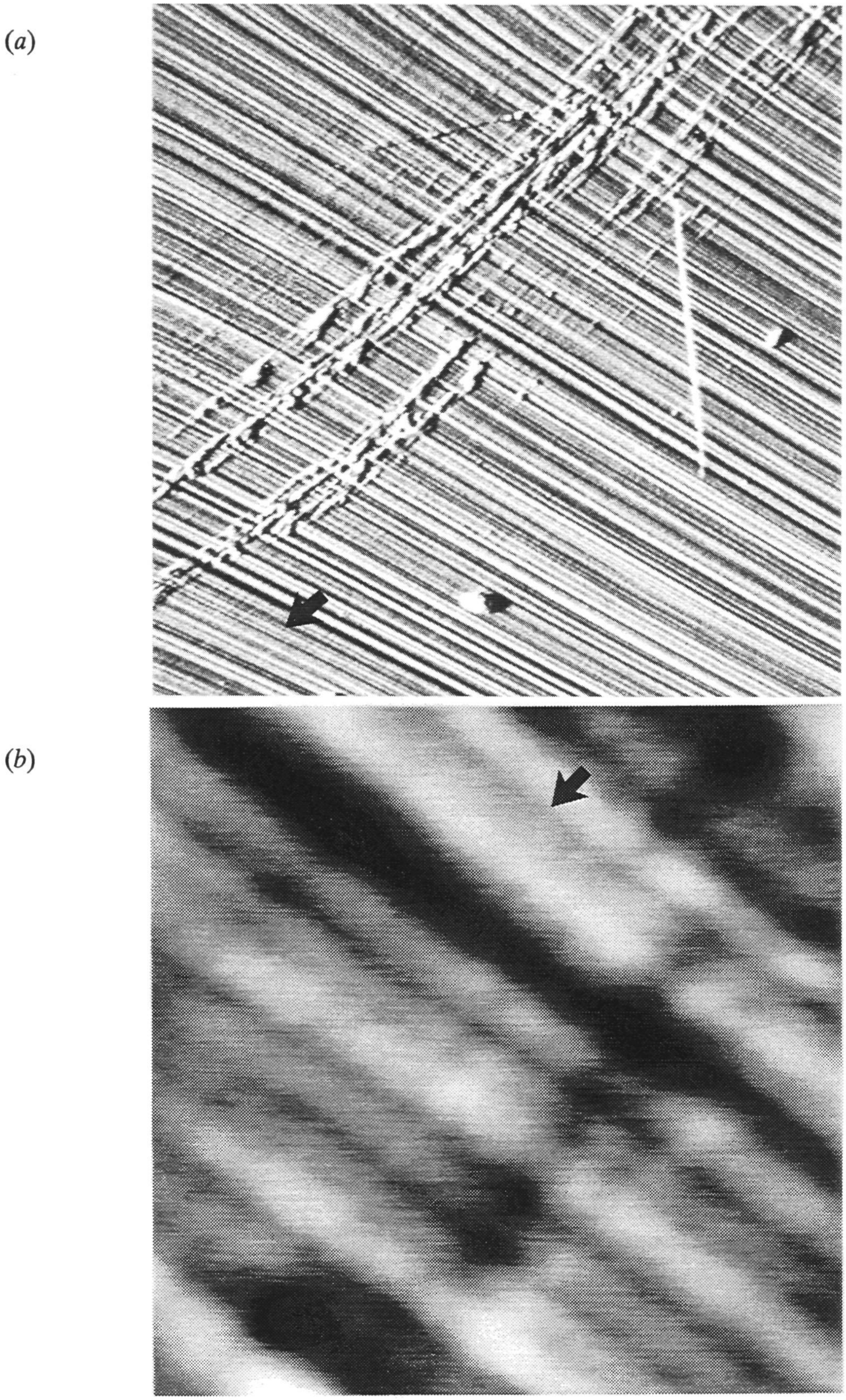

Fig. 4. (*a*) Friction track produced by a single pass of the stylus with R = 16.7 μm under a load of 27.9 g. The scan size is 5 μm × 5 μm. The surface is shaded from the left-hand side (*b*) Image showing a higher resolution scan of some of the grooves produced by the stylus. The scan size is 644 nm × 644 nm.

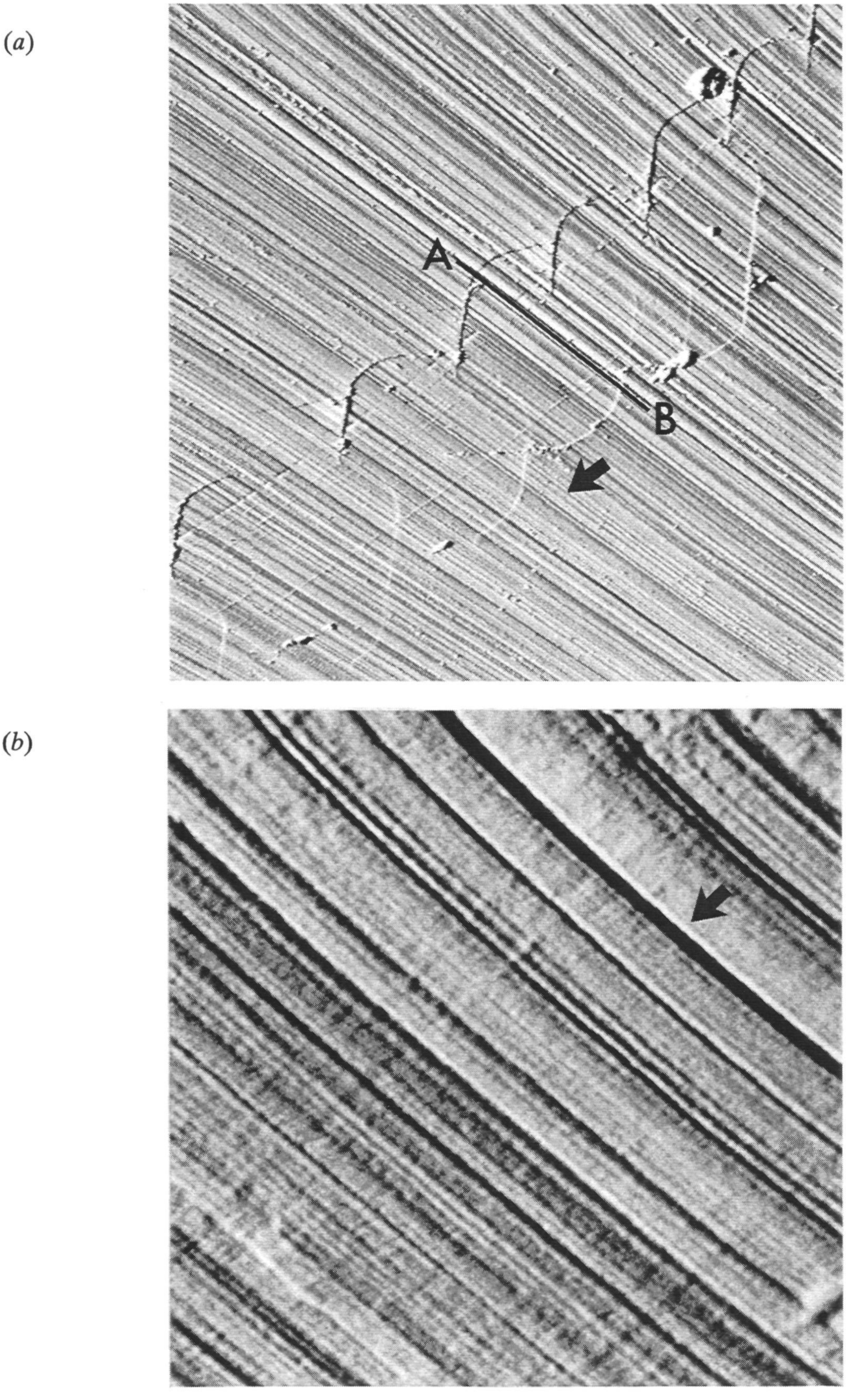

Fig. 5 (*a*)-(*b*). See next page for caption.

(*c*)

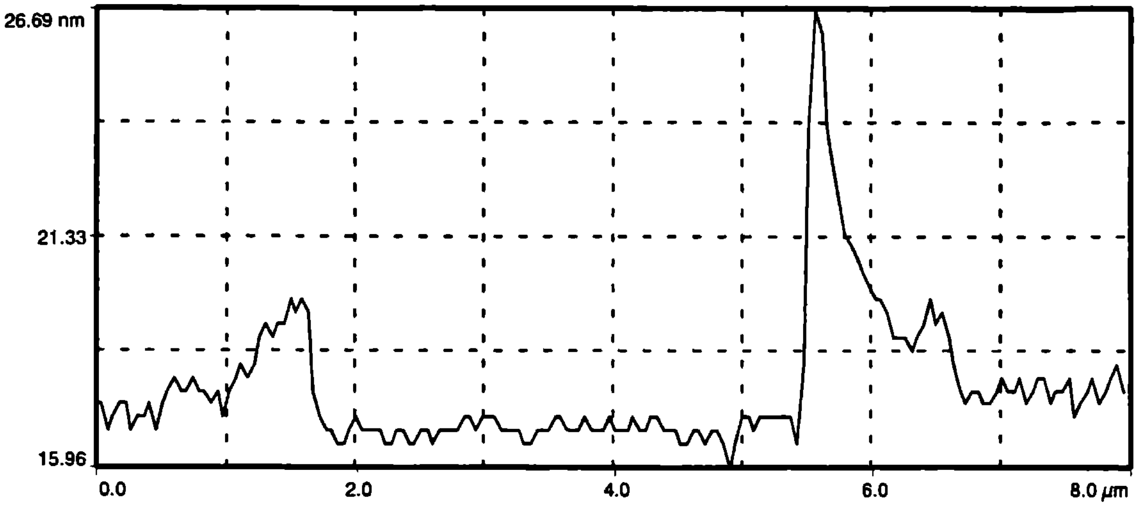

Fig. 5. (*a*) Ring cracks and grooves produced by a single pass of the stylus with $R = 12.5$ μm under a load of 63 g. The scan size is 15 μm × 15 μm. (*b*) Detail of the grooves inside one of the ring cracks after cleaning the surface with isopropanol. The scan size is 2.5 μm × 2.5 μm. (*c*) Profile along the line AB in (*a*). Both surfaces are shaded with a light source shining from the left-hand side.

4. Discussion

When a spherical indenter is pressed against a flat surface, both the indenter and the surface deform elastically and a circular area of contact is established between them. Two stress fields are generated: a compressive stress, with a maximum on the surface at the centre of the area of contact, and a tensile stress, with a maximum on the surface at the edge of the area of contact. The stress fields were calculated by Hertz for isotropic materials and are given by (Wilks and Wilks 1991):

$$p_{\mathrm{max}} = 1.5 p_{\mathrm{mean}} , \qquad (1)$$

where

$$p_{\mathrm{mean}} = P/\pi a^2 . \qquad (2)$$

p_{max} is the maximum compressive stress, P is the load on the indenter and a is the radius of the area of contact. When the indenter and the flat surface are of the same material the radius a of the contact area is given by:

$$a^3 = 1.5(1 - \upsilon^2)PR/E , \qquad (3)$$

where υ is the Poisson ratio, E is the Young modulus and R is the radius of the indenter. The maximum tensile stress is given by:

$$\sigma_{\mathrm{max}} = \tfrac{1}{2}(1 - 2\upsilon)p_{\mathrm{mean}} . \qquad (4)$$

When the load on the indenter is increased beyond the elastic regime two phenomena can occur: both surface and indenter deform plastically or they fracture. In diamonds, plastic

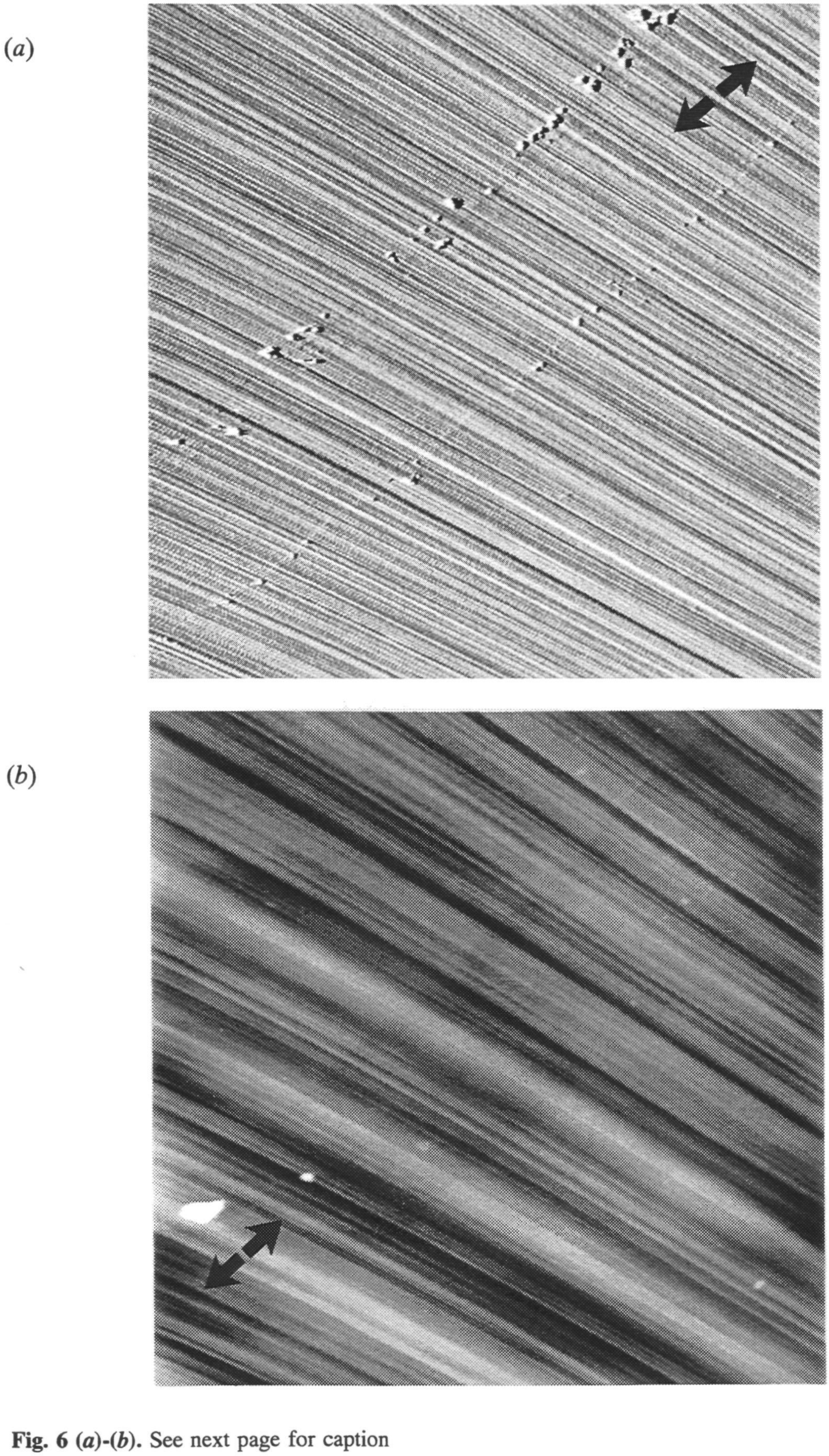

Fig. 6 (*a*)-(*b*). See next page for caption

(*c*)

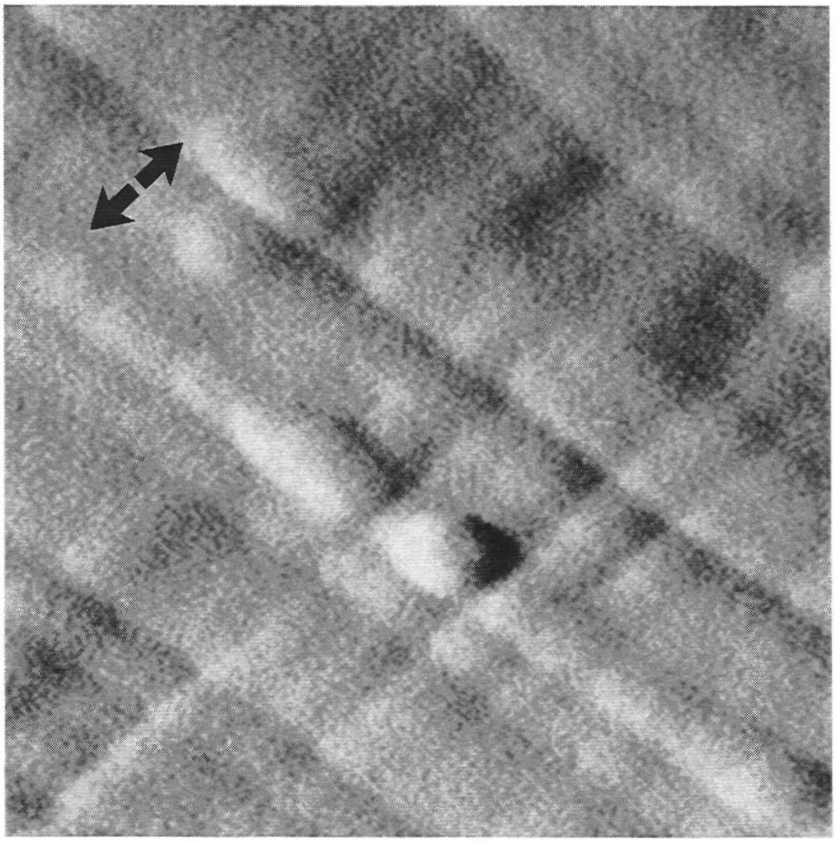

Fig. 6. (*a*) Image of a track produced by four passes of the stylus with R = 16.7 μm under a load of 28 g. The scan size is 20 μm × 20 μm. (*b*) Image of the same area shown in (*a*) after cleaning the surface with isopropanol. The scan size is 10 μm × 10 μm. (*c*) Higher resolution scan of individual grooves produced by the stylus. The scan size is 646 nm × 646 nm. (*a*) and (*c*) are shaded with a light source shining from the left-hand side.

flow is not expected to occur in an appreciable amount at room temperature. Normally when the load is increased, at a critical load a cone crack appears on the surface due to failure (fracture) of the diamond under the tensile stress. The cone crack penetrates into the material at a depth which is equivalent to the diameter of the contact area.

Equations (1) to (4) were developed for the case of materials under a static load. In the case of a sliding indenter the tensile stress on the surface at the back of the indenter is increased. This greatly decreases the critical load necessary for crack formation. The cracks in this case do not form closed circles (or polygons in the case of anisotropic materials) on the surface, but form arcs or open polygons (Hutchings 1992).

In the discussion on our experiments equations (1) to (4) will be used for the interpretation of the results. In view of the differences between the system studied by Hertz and the system treated in this paper, it should be realized that these equations are only approximately valid.

Since diamond is anisotropic, the values of υ and E are a function of the crystallographic directions. Fortunately, this anisotropy in elasticity is not large. If the values of $\upsilon = 0.07$ and E = 1050 GPa (Wang *et al.* 1991) are used, the values of a, p_{mean} and σ_{max} can be calculated for the indenters and loads used in this work. The results are shown in table 1.

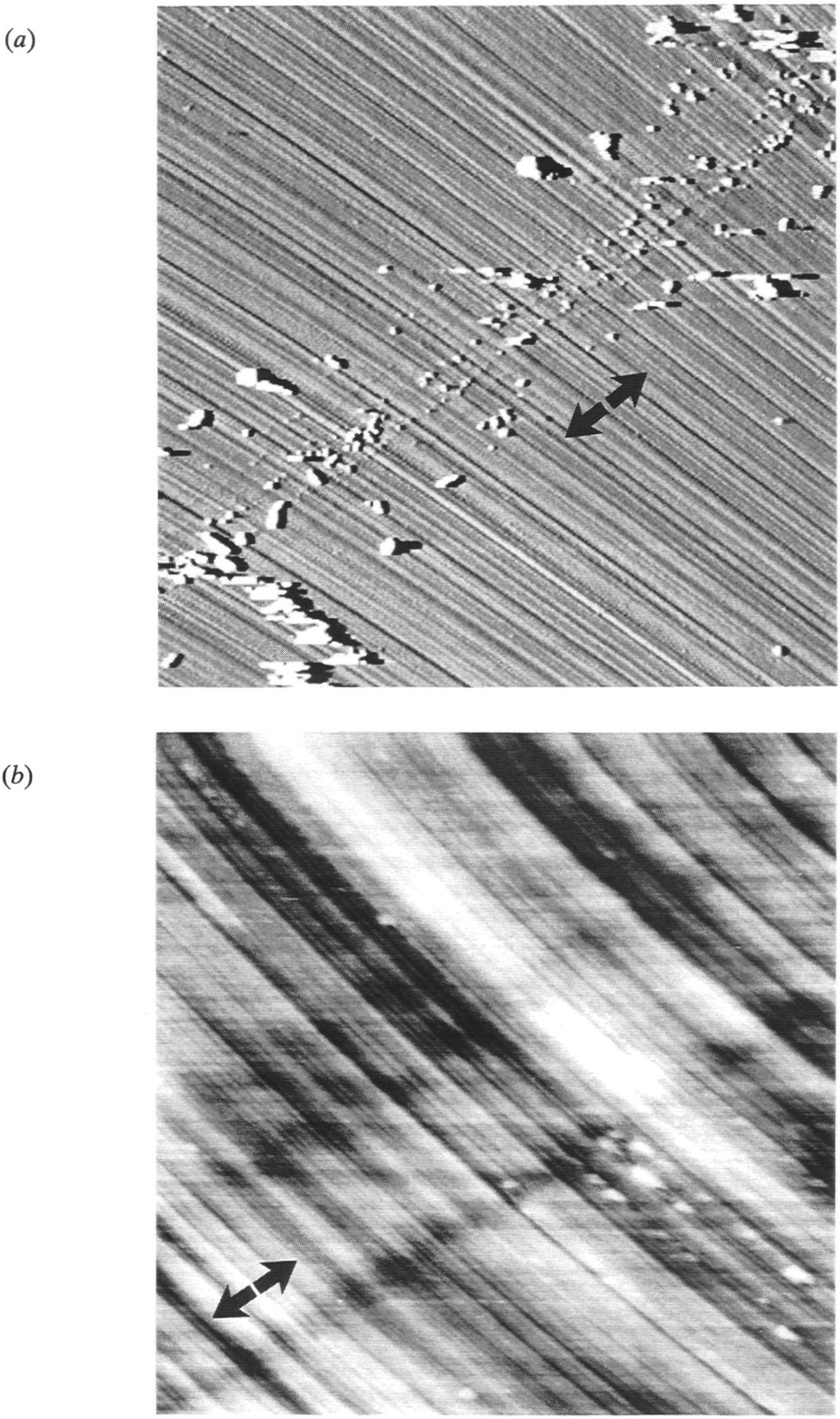

Fig. 7. (*a*)-(*b*). See next page for caption.

Fig. 7. (*a*) Friction track left after 24 passes of the stylus with R = 12.5 μm under a load of 2 g. The surface was shaded with a light source shining from the left-hand side. The scan size is 33 μm × 33 μm. (*b*) View of the same area shown in (*a*) after cleaning the surface with isopropanol. The scan size is 10 μm × 10 μm. (*c*) Higher resolution of the groove shown in the lower left corner of (*b*). The scan size is 2.5 μm × 2.5 μm.

Table 1. The values of a, p_{mean} and σ_{max} as calculated from equations (2) to (4) for the experimental set-up used in this work. The experimental values of a are given in the last column.

R (μm)	P (N)	a (μm)	p_{mean} (GPa)	σ_{max} (GPa)	a (μm) (experimental)
12.5	0.02	0.7	12.7	5.5	2.85 (24 passes)
	0.16	1.4	25.4	10.9	1.95
	0.62	2.2	39.9	17.1	2.40
16.7	0.27	1.9	24.9	10.7	1.65 2.60 (4 passes)

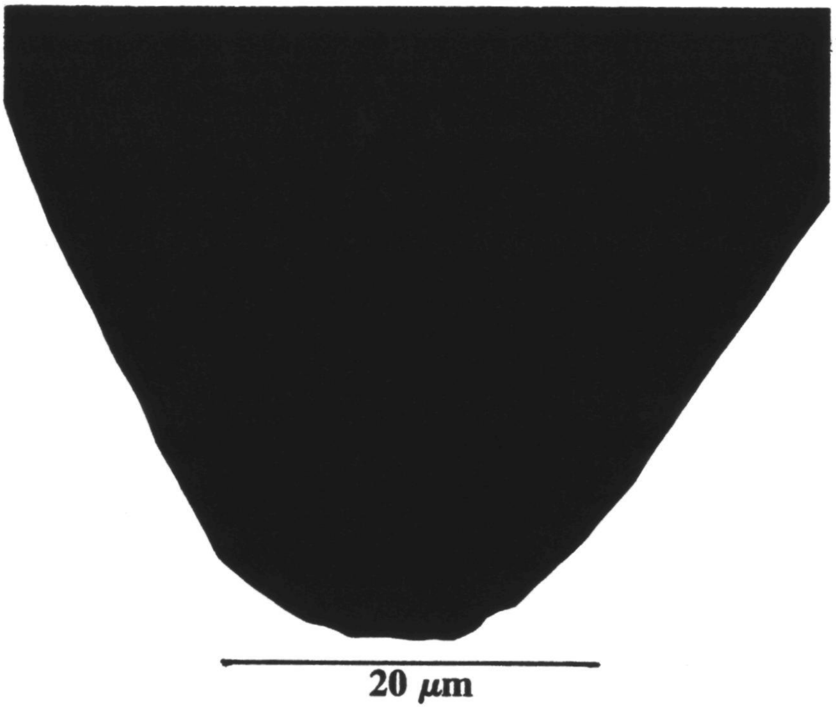

Fig. 8. Profile of the stylus shown in fig. 2 after it was used a few times (optical micrograph).

A comparison between the theoretical and experimental values of the contact radius a, given in table 1, shows that the tracks that were produced by one or four passes of the stylus have radii that are within a factor of 0.9 to 1.4 from the expected values. The track produced by 24 passes of the stylus is 4 times broader than expected. This might be due to the fact that the stylus became blunt during the experiment. The profile of the stylus shown in fig. 8 was obtained after that the track with 24 passes was produced. As mentioned above, the smooth profile of fig. 2 changed into the ragged profile of fig. 8 with $R = 13.0 \pm 0.5$ μm. However, this new value of R cannot account for the discrepancy between the sizes of the theoretical and observed contact areas. A more likely explanation is that the stylus did not follow exactly the same trajectory for the different passes.

All the tracks are composed of many individual grooves. This indicates that the contact between the stylus and the diamond surface was non-uniform and that the load was born by small asperities on the stylus. As a consequence, the local pressures exerted by the asperities might be much higher than the nominal values given for p_{mean} in table 1.

The debris observed along the tracks has been reported by several other authors (Seal 1965, Samuels and Wilks 1988, Feng and Field 1992, van Bouwelen *et al.* 1993). Analysis of the debris using electron energy loss spectroscopy (EELS), infrared spectroscopy and X-ray diffraction indicated that the debris has a structure intermediate between amorphous carbon and defect graphite (van Bouwelen *et al.* 1993) or that it is mainly hydrocarbon material (Seal 1965, Feng and Field 1992). In our work no analysis was made of the debris. From the AFM measurements it seems that the volume of debris is always larger than the volume of the grooves formed. It was also found that the interaction between the debris and the surface is non-uniform. Some of the particles can be easily displaced along the surface by the AFM tip, while other particles remain at the same position even after repeated scans.

Even though the tracks in figs. 3(a) and 4(a) were produced at the same calculated p_{mean}, the track in fig. 4(a) shows the presence of cracks. The orientations of the cracks agree with the directions of the intersections of the {111} planes with the (100) face and with the direction of the movement of the stylus. A close inspection of the tracks shown in both figures depicts that they are not oriented perpendicular to the polishing grooves. The track shown in fig. 3(*a*) makes an angle of 78.5° with the polishing grooves, while the angle for the track shown in fig. 4(*a*) is 71°. For the track shown in fig. 4(*a*) the stylus slid in a harder direction than that of fig. 3(*a*), because the misorientation of the former track from [001] is larger than that of the latter. Nevertheless a check on the diagram displayed in fig. 1 of chapter 1 shows that both these sliding directions are not very hard. Another possibility is that the actual p_{mean} is different for the two tracks. This could happen if the stylus used to produce the track shown in fig. 4(*a*) was not exactly spherical and had a local radius of curvature, at the point of contact, that was smaller than the nominal value of 16.7 μm. The experimental value of the contact area, as given in table 1 for the track shown in fig. 4(*a*), is smaller than the theoretical value expected for *a*.

The orientations of the cracks along the tracks shown in figs. 4(*a*) and 5(*a*) agree with the [011] and $[0\bar{1}1]$ orientations of the intersections of the {111} planes with the (100) face. This suggests that cracking mainly proceeds along {111}, which are the main cleavage planes for diamond. The profile along one of the ring cracks of fig. 5(*a*) shows that the region inside the ring is at a slightly lower level than the surface outside the crack. For this profile the average difference in height between the surfaces is 1.1 nm but in some other areas this value may be larger or smaller. Interesting is the fact that close to the crack the outer surface bends upwards, giving steps of 3.5 and 10 nm in height at the crack in fig. 5. The profile seems to agree with the results presented by Lawn and Komatsu (1966). Their explanation for the formation of the cracks is that the material fails under the tensile stress and that when the load is removed debris in the crack prevents it from closing completely.

The main result from our experiments is that in all the tracks, even in those obtained by a single pass of the stylus, numerous parallel, smooth grooves, free of cracks, can be observed. For the tracks produced by a single pass the grooves range from 30 nm to 260 nm in width and from 0.4 nm to 1.2 nm in depth. The track produced by 24 passes of the stylus has broader (470 nm) and deeper (1.8 nm) grooves.

Figure 6(*c*) shows that the grooves formed by the stylus are present on both the top and the bottom of the polishing grooves. This suggests that the asperities on top of the stylus follow the profile of the polishing grooves, moving up and down, during the sliding process. The fact that the grooves are smooth indicates that material removal did not proceed by cleavage of small fragments. It seems then, that the removal of material occurred through the disruption of atomic bonds under high local pressures, as suggested in chapter 5. Upon release of pressure the ruptured carbon may transform to graphite or react with ambient molecules to hydrocarbon materials, which leads to the production of debris.

Since the grooves formed by the stylus have the same appearance as the polishing grooves, we suggest that both are formed by the same process. From other experiments (Wilks and Wilks 1972) it is known that under given conditions the amount of material removed during diamond polishing only depends on the number of revolutions of the scaife, rather than on the polishing speed. Therefore the extremely large difference in sliding speed during the present experiments and that during diamond polishing does not exclude an identical mechanism for material removal.

5. Conclusion

The grooves formed by a diamond stylus sliding along a soft direction on a diamond surface are probably produced by disruption of atomic bonds under high pressures. The high pressures are generated due to the fact that only a limited number of asperities on the surface of the stylus bear most of the applied load. It is suggested that the grooves formed during diamond polishing along the soft directions are produced by the same mechanism.

References

Archard, J. F., 1953, J. Appl. Phys., **24**, 981.

Archard, J. F., 1961, J. Appl. Phys., **32**, 1420.

Bailey, A. I., and Seal, M., 1965, Ind. Diamond Rev., **16**, 145.

Bowden, F. P., and Tabor, D., 1965, *Physical Properties of Diamond*, edited by Berman, R. (Oxford: Clarendon Press) ch. 7.

Brookes, C. A., Brookes, E. J., Howes, V. R., Roberts, S. G., and Waddington, C. P., 1990, J. Hard Mater., **1**,3.

Brookes, C. A., 1992, *The Properties of Natural and Synthetic Diamond*, edited by Field, J. E. (London: Academic Press) p. 515.

Burns, R. C., Cvetkovick, V., Dodge, C. N., Evans, D. J. F., Rooney, M. T., Spear, P. M., and Welbourn, C. M., 1990, J. Cryst. Growth, **104**, 257.

Busmann, H. G., Zimmerman-Edling, W., Sprang, H., Güntherodt, H-J., Hertel, I. V., 1992, Diamond and Rel. Mat., accept for publication.

Collins, A. T., and Lightowlers, E. C., 1979, *The Properties of Diamond*, edited by Field, J. E. (London: Academic Press) p. 79.

Couto, M., van Enckevort, W. J. P., Wichman, B., and Seal, M., 1992, Appl. Surf. Sci., **62**, 263 (Chapter 2 of this thesis).

Couto, M. S., van Enckevort, W. J. P., and Seal, M., 1994a, Phil. Mag. B, **69**, 621 (Chapter 4 of this thesis).

Couto, M. S., van Enckevort, W. J. P., and Seal, M., 1994b, J. Hard Mater., **5**, 31 (Chapter 5 of this thesis).

Custers, J. F. H., 1952, Ind. Diamond Rev., **12**, 130.

Denning, R. M., 1953, Am. Miner., **38**, 108.

Denning, R. M., 1955, Am. Miner., **40**, 186.

Denning, R. M., 1957, Am. Miner., **42**, 362.

Enomoto, Y., and Tabor, D., 1981, Proc. R. Soc. London A, **373**, 405.

Feng, Z., and Field, J. E., 1992, J. Phys. D: Appl. Phys., **25**, A33.

Field, J. E., 1992, *The Properties of Natural and Synthetic Diamond*, edited by Field, J. E., (London: Academic Press Limited) p. 473.

Frenkel, J., 1926, Zeit. Phys., **37**, 572.

Grodzinski, P., 1953, *Diamond Technology*, (NAG Press, London) p.178

Haisma, J., van der Kruis, F. J. H. M., Spierings, B. A. C. M., Oomen, J. M., and Fey, F. M. J. G., 1992, Precision Engineering, **14**, 20.

Hamza, A. V., Kubiak, G. D., and Stulen, R. H., 1988, Surf. Sci., **206**, L833.

Hamza, A. V., Kubiak, G. D., and Stulen, R. H., 1990, Surf. Sci., **237**, 35.

Harrison, J. A., White, C. T., Colton, R. J., and Brenner, D. W., 1992, Surf. Sci., **271**, 57.

Hartman, P., and Perdok, W. G., 1955, Acta Cryst., **8**, 49, 521, 525.

Hartman, P., 1963, Z. Krist., **119**, 65.

Hartman, P., 1973, *Crystal Growth: an Introduction*, edited by Hartman, P. (Amsterdam: North-Holland) p. 367.

Hottenhuis, M. H. J., Mickers, M. A. H., Gerritsen, J. W., and van der Eerden, J. P., 1988, Surf. Sci., **206**, 259.

Hull, D., and Bacon, D. J., 1984, *Introduction to Dislocations*, (Oxford: Pergamon Press) p.16.

Huong, P. V., 1991, Diamond and Related Materials, **1**, 33.

Hutchings, I. M., 1992, *Tribology: Friction and Wear of Engineering Materials*, (London: Edward Arnold).

Janssen, G., van Enckevort, W. J. P., Vollenberg, W., and Giling, L. J., 1992, Diamond and Rel. Mat., **1**, 789.

Karis, T. E., and Novotny, V. J., 1989, J. Appl. Phys., **66**, 2706.

Kendall, K., 1978, Proc. R. Soc. Lond. A, **361**, 245.

Kittel, C., 1971, *Introduction to Solid State Physics*, (New York: John Wiley & Sons, Inc.) p. 133.

Kraus, E. H., and Slawson, C. B., 1939, Am. Mineral., **24**, 661.

Lawn, B. R., and Komatsu, H., 1966, Phil. Mag., **14**, 689.

Mackenzie, J. K., 1949, Thesis, University of Bristol.

Maguire, H. G., Kamo, M., Lang, H. P., Güntherodt, H. -J., 1992, Appl. Surf. Sci., **60/61**, 301.

Orowan, E., 1940, Proc. Phys. Soc., **52**, 8.

Postek, M. T., and Evans, C. J., 1989, Scanning Microsc., **3**, 435.

Roesler, F. C., 1956, Proc. Phys. Soc., **B69**, 55.

Samuels, B., and Wilks, J., 1988, J. Mater. Sci., **23**, 2846.

Seal. M., and Menter. J. W., 1953, Phil. Mag., **44**, 1408.

Seal, M., 1958, Proc. R. Soc. London A, **248**, 379.

Seal, M., 1965, Ind. Diamond Rev., **25**, 111

Seal, M., 1967, *The Science and Technology of Industrial Diamonds, Vol. I, Science*, edited by Burls, J. (London: Industrial Diamond Information Bureau) p. 145.

Seal, M., 1981, Phil. Mag. A, **43**, 587.

Slawson, C. B., and Kohn, J. A., 1950, Ind. Diamond Rev., **10**, 168.

Tabor, D., 1979, *The Properties of Diamond*, edited by Field, J . E., (London: Academic Press) pp. 325-350.

Tabor, D., Field, J. E., 1992, *The Properties of Natural and Synthetic Diamond*, edited by Field, J. E., (London: Academic Press Limited) p. 545.

Thornton, A. G., and Wilks, J., 1976, J. Phys. D.: Appl. Phys., **9**, 27.

Tolansky, S., 1955, *The Microstructures of Diamond Surfaces* (London: NAG) pp. 58.

Tolkowsky, M., 1920, Ph.D. Thesis, University of London.

Tsuno, T., Imai, T., Nishibayashi, Y., Hamada, K., Fujimori, N., 1991, Jpn. J. Appl. Phys., **30**, 1063.

Turner, K. F., LeGrice, Y. M., Stoner, B. R., Glass, J. T., and Nemanich, R. J., 1991, J. Vac Sci. Techn., **B9**, 914.

van Bouwelen, F. M., Brown, L. M., Field, J. E., 1993, Poster at the Diamond Films'93, 4th European Conference on Diamond, Diamond-like and Related Materials, Albufeira, Portugal.

van Enckevort, W. J. P., Janssen, G., Vollenberg, W., Chermin, M., Giling, H. J., and Seal, M., 1991, Surface and Coatings Technology, **47**, 39.

van Enckevort, W. J. P., 1992, J. Cryst. Growth, **119**, 177.

van Enckevort, W. J. P., Janssen, G., Vollenberg, W., Chermin, M., Giling, H. J., 1994, J. Cryst. Growth, accepted.

Visser, E. P., Gerritsen, J. W., van Enckevort, W. J. P., and van Kempen, H., 1992, Appl. Phys. Lett., **60**, 3232.

Wang, Z. L., Feng, Z., and Field, J. E., 1991, Phil. Mag., **63**, 1275.

Wang, Z. L., 1991, J. Electron Microsc. Tech., **17**, 231.

Wilks, E. M., and Wilks, J., 1959, Phil. Mag., **4**, 158.

Wilks, E. M., and Wilks, J., 1972, J. Phys. D.: Appl. Phys., **5**, 1902.

Wilks, J., and Wilks, E. M., 1979, *The Properties of Diamond*, edited by Field, J. E. (London: Academic) ch. 11.

Wilks, J., and Wilks, E., 1991, *Properties and Applications of Diamond*, (Oxford: Butterworth-Heinemann), p. 251.

Wilks, J., and Wilks, E., 1992, *The Properties of Natural and Synthetic Diamond*, edited by Field, J. E., (London: Academic Press Limited) p.573.

Wyant, J. C., Koliopoulos, C. L., Bushan, B., and Basila, D., 1986, Trans. ASME J. Tribology, **108**, 1.

Part II

Crystal growth studies

Chapter 7

Optical and Atomic Force Microscopy studies of rhombohedral domains in C_{70} crystals[1]

M. A. Verheijen, M. S. Couto, K. W. M. Koutstaal and W. J. P. van Enckevort

Department of Solid State Chemistry, University of Nijmegen, Faculty of Science, Toernooiveld, 6525 ED, Nijmegen, The Netherlands

Abstract

The phase transition of the f.c.c. structure towards the trigonal structure on the {100} and {111} surfaces of C_{70} crystals has been studied *in situ* with the help of optical reflection microscopy. Extensive *ex situ* studies of domain patterns on both types of surfaces have been performed using both optical and atomic force microscopy. A detailed interpretation of the domain patterns is given. An additional phase transition was observed *in situ* at 303 K.

---

[1] *Philosophical Magazine, submitted*

1. Introduction

The crystal structure of C_{70} has been the subject of extensive studies. Upon growth from the vapour phase both h.c.p. and f.c.c. crystals have been obtained (Vaughan *et al.* 1991, Verheijen *et al.* 1992, van Tendeloo *et al.* 1993). At high temperatures the molecules in both structures are orientationally disordered. Upon cooling the rotation of the molecules freezes in two steps. In the intermediate phase the molecules are all aligned with their long axes parallel to each other and rotation only occurs around this long axis. At low temperatures rotation is completely frozen in and an ordered structure results. For the h.c.p. grown crystals thus an orthorhombic structure is formed (Nelissen *et al.* 1993, van Smaalen *et al.* 1994, Agterberg and Walker 1993) via an intermediate hexagonal phase having $P6_3/mmc$ symmetry with a c/a ratio of 1.82 instead of the ideal value of 1.63.

Cooling down f.c.c. C_{70} crystals results in a rhombohedral distortion of the cubic lattice. The deformation of the cubic unit cell can be considered as a stretching of this cell along one of the four body diagonals (the <111> directions), the C_{70} molecules having their long axis parallel to this body diagonal. This results in four different rhombohedral domains. Each f.c.c. unit cell with a = 14.943Å thus transforms into one of the four different rhombohedral cells in the (trigonal) space group $R\bar{3}m$ with a = 14.96Å and α = 85.7° (Vaughan *et al.* 1993, Christides *et al.* 1993). At low temperatures the rhombohedral structure transforms into a monoclinic structure in which the molecules do not rotate. The temperatures at which the phase transitions of both h.c.p. and f.c.c. grown C_{70} crystals take place depend strongly on the purity of the material (McGhie *et al.* 1994). For example, the transition of f.c.c. to rhombohedral occurs at 361 K, 318 K and 307 K for C_{60} contents of 0%, 1.2% and 1.9% respectively. Therefore the room temperature structure of f.c.c. grown C_{70} is determined by its purity.

Although a great amount of studies have been carried out on the solid state properties of the fullerenes, little has been published about the crystal growth itself. In previous papers, optical microscopy studies of the surfaces of f.c.c. C_{60} crystals grown from the vapour phase were presented (Verheijen *et al.* 1993, Verheijen *et al.* 1994). Much could be learned about the growth process via the observation of growth steps, several kinds of step sources, dislocations, epitaxial dendrites and morphological instabilities at the step edges. Also post growth processes such as surface fracture and dislocation glide have been studied.

In this paper we will present surface studies of f.c.c. grown C_{70} crystals. As was mentioned above, the room temperature structure of these crystals depends on the purity of the material. This enables us to study the surfaces of both the f.c.c. and the rhombohedral crystals at room temperature conditions. In this study attention is focused on the surface morphology of the rhombohedral crystals and on the phase transition rhombohedral to f.c.c. and vice versa. Furthermore, the occurrence of a low temperature transition of the rhombohedral structure towards a possible monoclinic one is studied. The surface structures of the different phases are studied *ex situ* at room temperature using Atomic Force Microscopy (AFM), Differential Interference Contrast Microscopy (DICM) and Reflection Polarization Microscopy (RPM), while the phase transitions are studied *in situ* by optical reflection microscopy.

2. Experimental

As a starting material for crystal growth either 90% or 99.9% pure C_{70} was used. The growth procedure has been described in detail elsewhere (Verheijen *et al.* 1993). As a result crystals with either a h.c.p. or a f.c.c. morphology were obtained. However, during cooling down to room temperature the crystals grown from the pure material all undergo a phase transition. The crystal structure of the h.c.p. crystals transforms into the deformed h.c.p. structure, which causes fracture of the crystals and does not allow for surface studies. The structure of the f.c.c. grown crystals becomes rhombohedrally distorted resulting in crystals made up of the four types of domains. The surfaces of these crystals show many domain walls, the largest of which are just visible by eye. On the other hand, the crystals grown from the 90% pure material all remain in the high temperature phases and thus have smooth faces. In this study we focused our attention on the domain structure of the {111} and the {100} surfaces of the f.c.c. grown crystals. In order to be able to directly compare the results obtained by the different surface topographic methods, all the techniques were applied on each one of the {111} and the {100} faces. The reproducibility of our observations was verified on several other crystals. To minimize contamination and oxidation effects the quartz tubes containing the crystals were opened just before beginning the optical and AFM studies.

For the DICM and the RPM studies a Reichert MeF II optical microscope was used in combination with normal and high contrast photography. DICM is a differential, phase sensitive technique by which inclinations down to 0.05° can be detected (van Enckevort 1984). With the help of RPM the surface symmetry can be determined from bireflectance measurements. To avoid cracking of the surfaces due to the heat introduced by illumination, low level light intensities were used in combination with a green transmission filter.

In order to study the phase transition *in situ* a single crystal of about 1 mm^3 was placed in a thermostated vessel under a continuous nitrogen flow. The vessel was placed under an optical reflection microscope provided with a video camera. The experiment could be followed on a monitor and was recorded on videotape. Both bright field reflection microscopy and DICM were used to study the surfaces. The temperature, which ranged from 298 K to 363 K during the experiments, was measured with the help of a Pt/PtRh10% thermocouple.

The AFM used was a TopoMetrix TMX 2010. Two different scanners with scan ranges of 75 μm and 7.5 μm respectively, together with silicon nitride cantilevers and pyramidal silicon nitride tips, were used. All measurements were carried out under atmospheric conditions in the constant force mode. Forces ranging from 10^{-9}N to 10^{-8}N were used.

3. Results

In this study the two different types of faces occurring on the crystals have been examined in detail. For convenience, the faces of both the f.c.c. and the rhombohedral phase will be indicated by the Miller indices representative for the high temperature f.c.c. structure, that is, {111} and {100}. As the phenomena on both faces show large differences the observations will be described seperately for all techniques used.

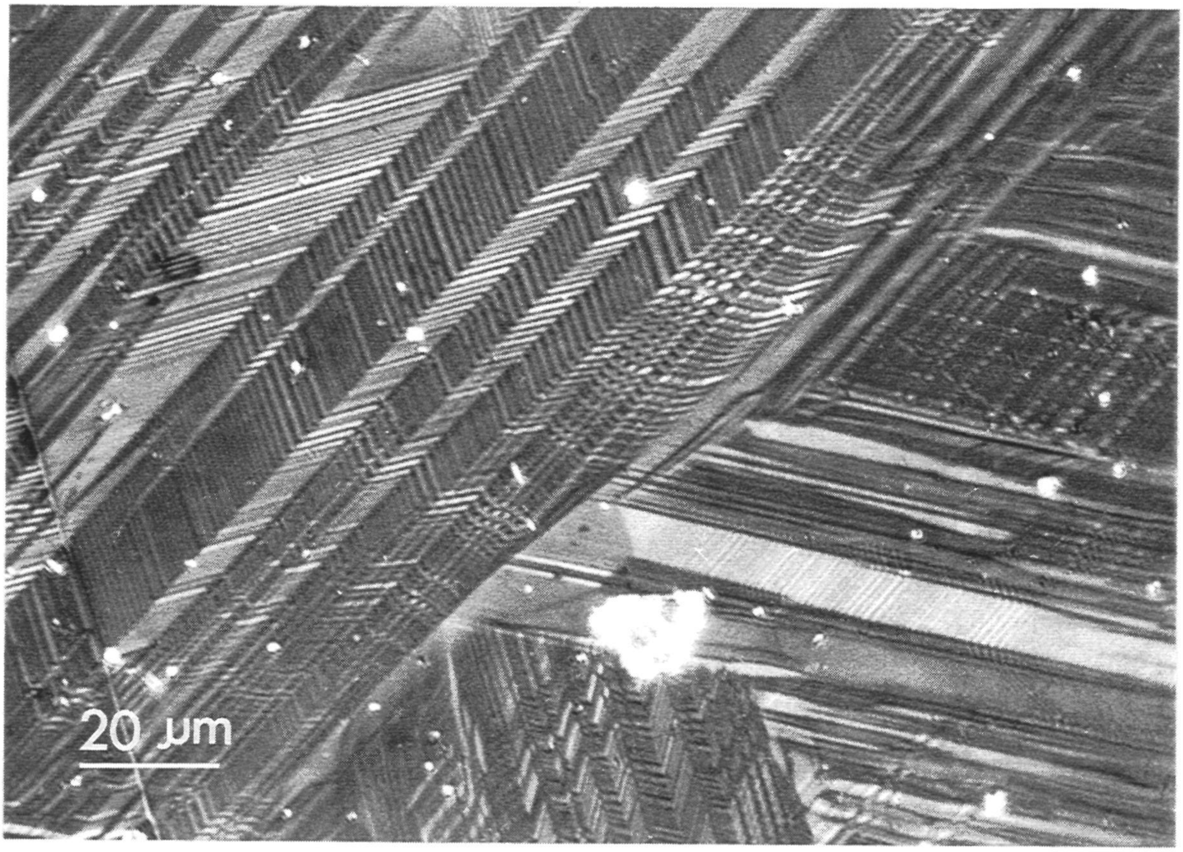

Fig. 1. DICM image of a {111} surface displaying a pattern of rhombohedral domains.

3.1. DICM studies

The surfaces of 99.9% pure C_{70} crystals were studied with DICM. In fig. 1 a DICM image of a {111} face is shown. The pattern of lines and regions with different inclinations that can be seen is characteristic for the domain structure that is introduced by the transition from the f.c.c. to the trigonal phase. In this pattern two types of domain walls can be recognized. The first type of domain wall is a long interrupted line running in one of the three $/1\bar{1}0/$ directions on the (111) face (type I). Here /uvw/ is defined as the vector [uvw] and its symmetrical equivalents in a given plane (hkl). On both sides of each line of type I shorter lines are present that represent a different type of domain boundary as will be shown below. One set of these lines runs approximately in one of the $/\bar{2}11/$ directions (type IIa) whereas the other set is approximately parallel to one of the $/1\bar{1}0/$ directions (type IIb). In this way a type I line accompanied by a set of type IIa and IIb lines forms a 'feather pattern'. A schematic drawing of this morphology is given in fig. 2. As is indicated in this figure two patterns of domain walls occur which are mirror images ($F_{\alpha\beta}$ and $F_{\beta\alpha}$) in the two-dimensional point group 3m of the {111} face in the high temperature f.c.c. structure. These feathers mostly occur in groups of the same pattern, which is either $F_{\alpha\beta}$ or $F_{\beta\alpha}$. In these groups all the parallel type I lines point in one of the three $/1\bar{1}0/$ directions. In the regions where two groups meet either one of the sets of lines stops or, in a few cases, a crossing of the feathers can be observed.

In fig. 3(*a*) a DICM image of the {100} face is presented. The domain pattern on this surface consists of lines parallel to the /010/ directions. The domain walls are relatively long

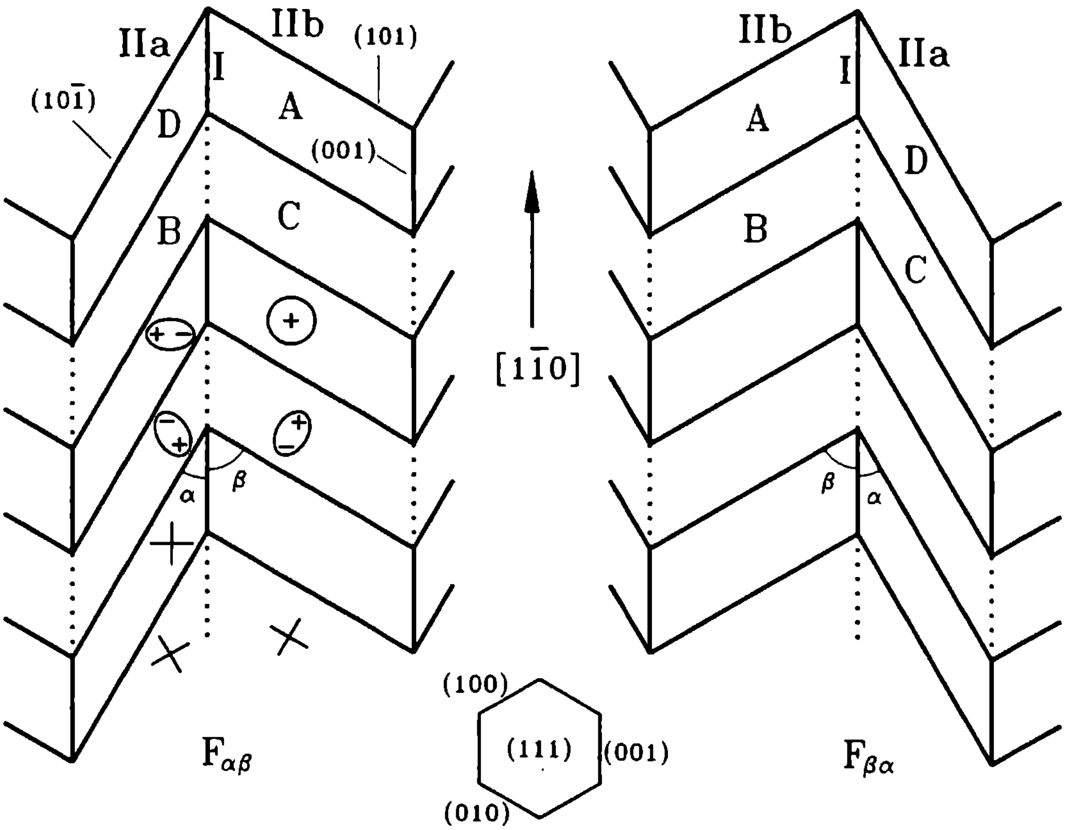

Fig. 2. Schematic drawing of rhombohedral domain feather patterns $F_{\alpha\beta}$ and $F_{\beta\alpha}$ on {111} with indication of domain types A, B, C and D, domain wall types I:(001), IIa:(10$\bar{1}$) and IIb:(101) and angles α and β. For the feather pattern $F_{\alpha\beta}$ for each domain the main axes of the intersections of the indicatrices as well as the orientations of the C_{70} molecules are given (the + and - signs indicate the orientation of the long axis). A, B, C and D represent rhombohedral domains having their unique axis in the [111], [$\bar{1}$11], [1$\bar{1}$1] and [11$\bar{1}$] directions respectively. The dashed lines represent domain walls that can only be observed by RPM.

in comparison to the size of the crystal surface, indicating a preferential orientation of the domain growth during the phase transition. Even at the highest magnifications details of several patterns are hardly resolved on the {100} faces. Large parts seem to be flat indicating either unresolved structures with a high density of domain walls or regions that did not undergo the phase transition and thus still are f.c.c..

On several other {100} faces feather patterns were observed (see fig. 3(*b*)). The shape of these feathers differs from those observed on the {111} faces. The main stems and the side branches of the former feathers run in the /010/ and the /01$\bar{1}$/ directions respectively. A schematic drawing of this morphology is presented in fig. 4.

When the edge connecting a {111} and a {100} face was studied it could be seen that the type I boundaries on the {111} face (running in the /1$\bar{1}$0/ directions) proceeded as domain boundaries on the {100} face. As the latter lines run in the /010/ directions it can be concluded that the type I boundaries on {111} and the /010/ boundaries on {100} are caused by a domain wall parallel to a {001} face.

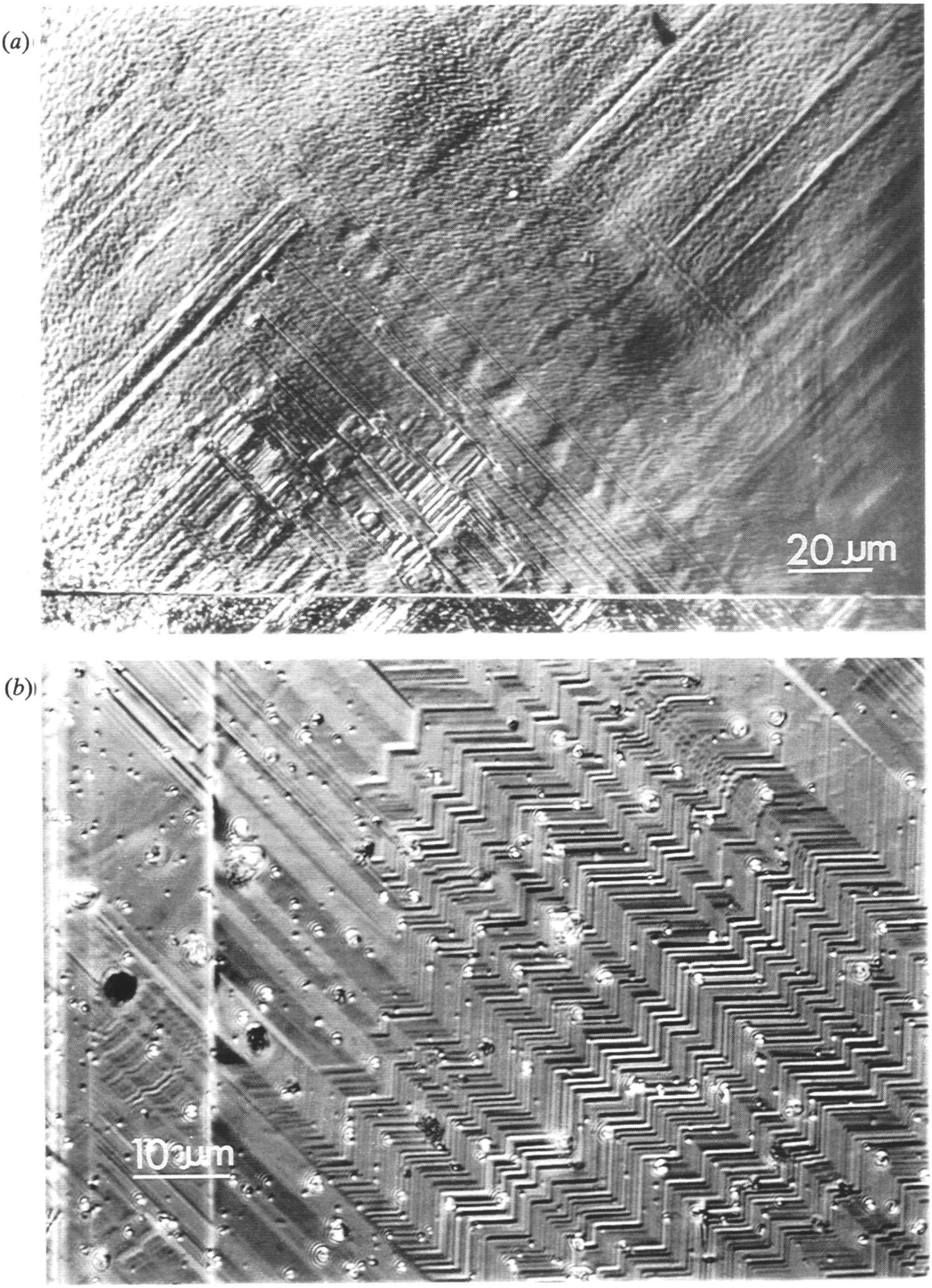

Fig. 3. (*a*) Pattern of rhombohedral domains on a {100} face (DICM). (*b*) feather patterns on the {100} face (DICM).

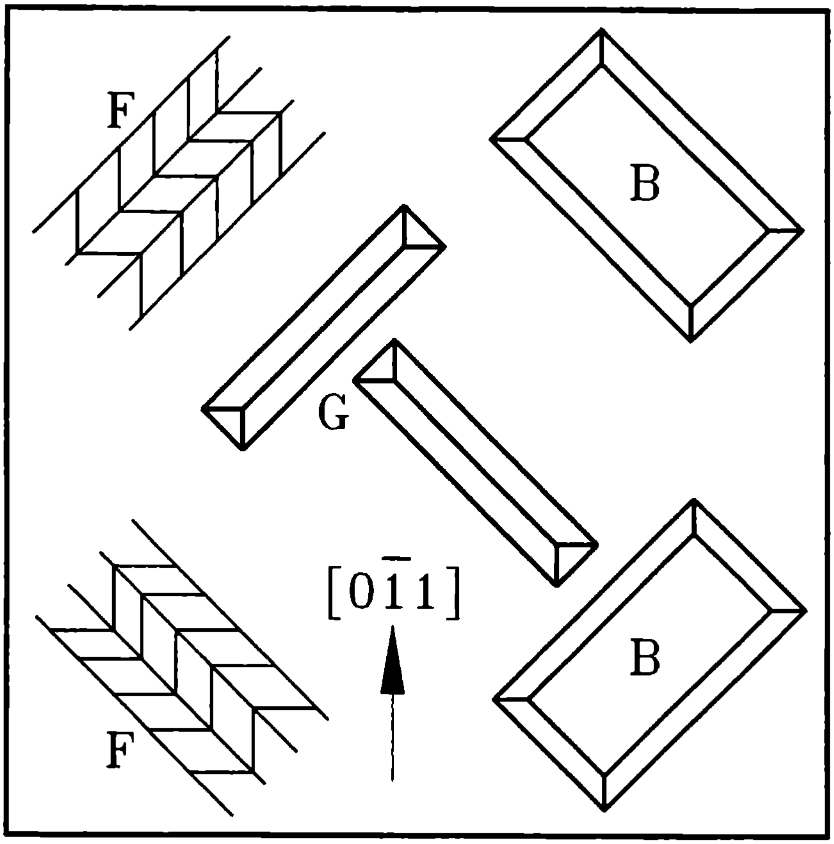

Fig. 4. Schematic drawing of domain patterns on {100} showing feathers (F), grooves (G) and a basin (B).

3.2. *In situ* studies of the phase transitions

3.2.1. The phase transition between the f.c.c. and the trigonal structures

The phase transition of the f.c.c. towards the trigonal structure of a 99.9% pure C_{70} crystal was studied *in situ*. Two series of experiments were carried out, one concerning a {111} surface, the other a {100} surface. One of the faces was oriented perpendicularly to the direction of the incident light of the microscope used. The temperature was subsequently raised from room temperature with a heating rate of 8 K/min. At approximately 353 K the phase transition took place. The domains vanished and a flat surface resulted. When the crystal was cooled down, again a domain structure was formed. The formation of the domains could be observed on the entire surface. This temperature cycle was repeated several times in order to study the phase transition in more detail. Heating rates ranging from 0.5 to 8 K/min were applied. The temperature at which the transition was monitored varied from 352 K to 355 K. In each cycle the domain structure vanished upon heating and a new domain pattern was formed upon cooling, showing that the phase transition is a reversible process. This was observed for both the {111} and the {100} face. In fig. 5 the result of a temperature cycle for the {111} face is shown. Figures 5(*a*), 5(*b*) and 5(*c*) show the surface morphology as was observed at room temperature at the beginning of the cycle, at 363 K and at room temperature at the end of the cycle respectively. Figure 5(*c*) displays a pattern of domain walls, which is different from the pattern that was present before the phase transition (fig. 5(*a*)). For both {111} and {100} faces the pattern of domain lines is not reproduced exactly

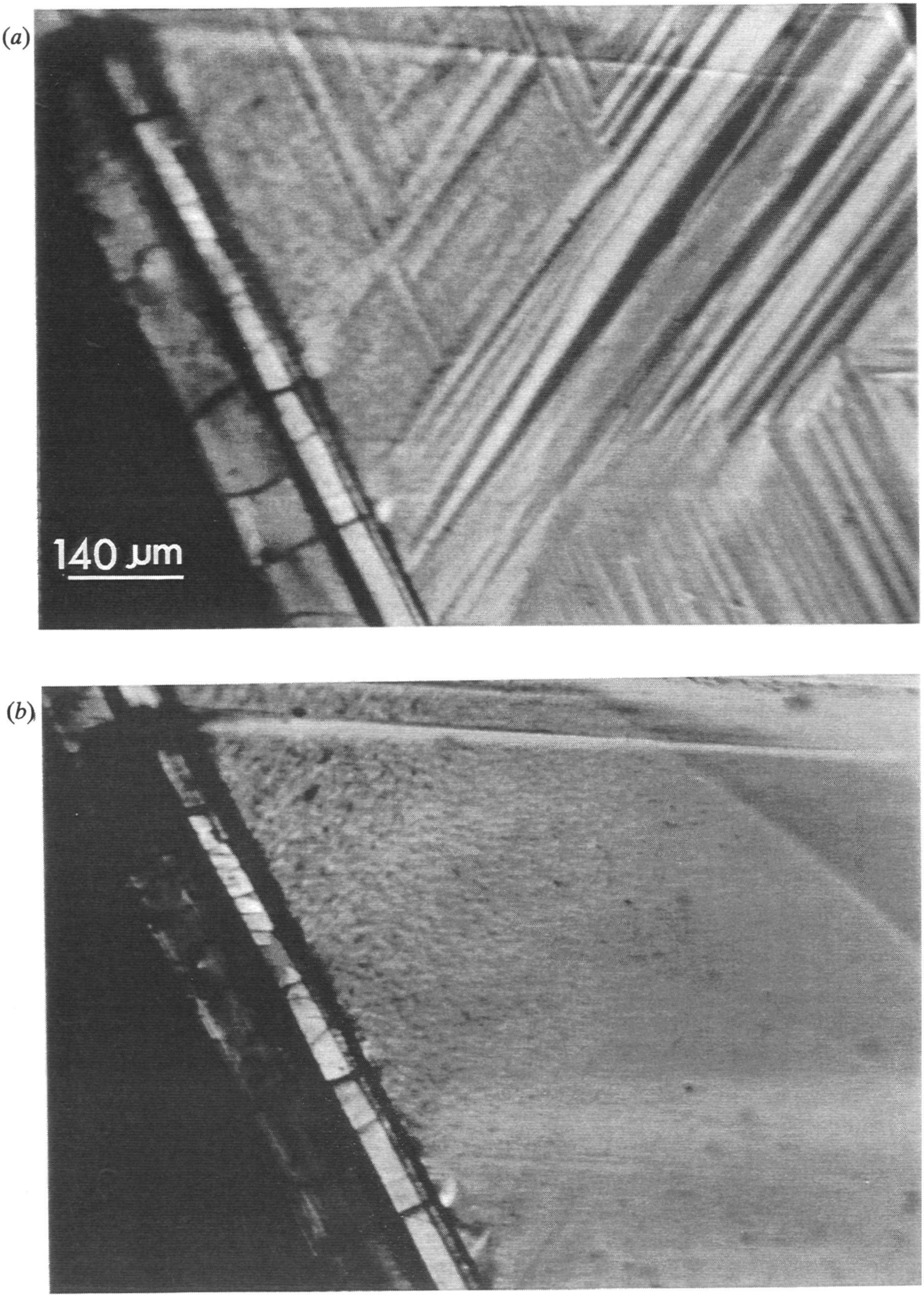

Fig. 5 (*a*)-(*b*). See next page for caption.

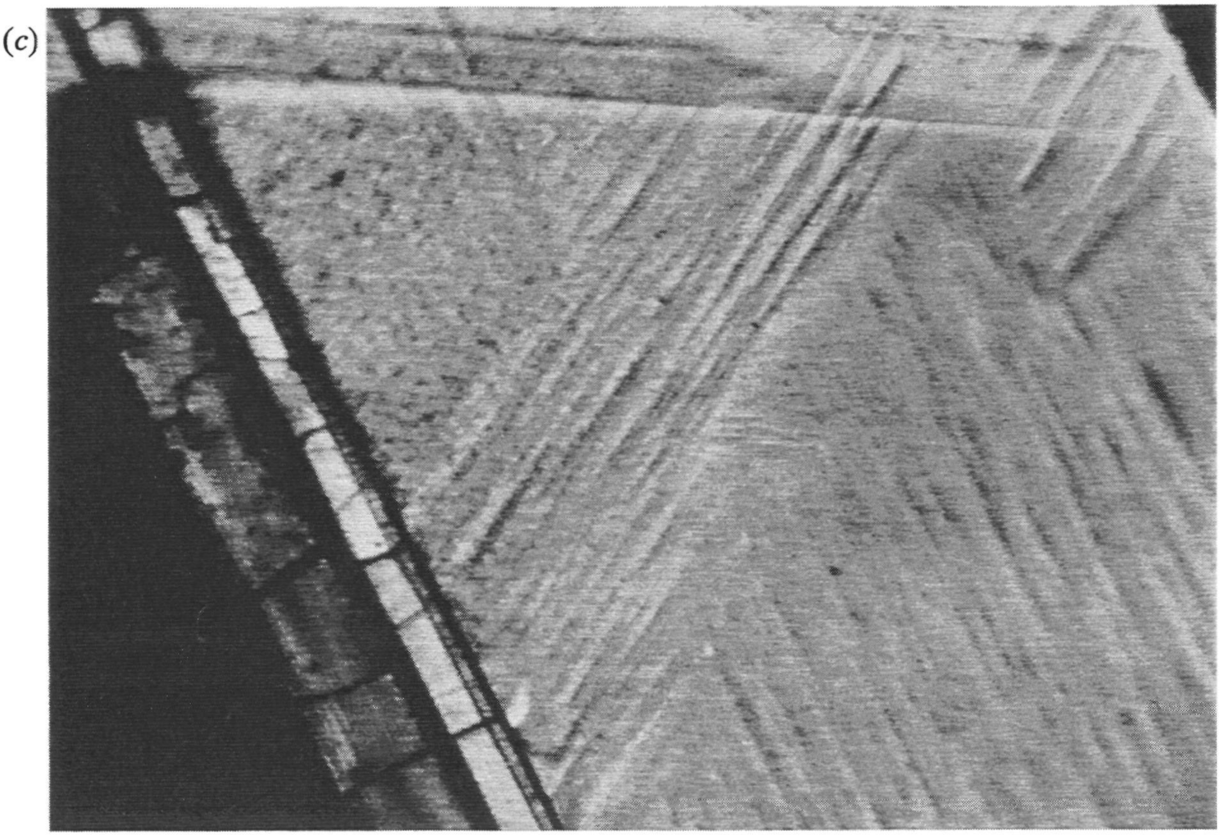

Fig. 5. Morphology of a {111} surface during a heating cycle: (*a*) at 300 K (before heating); (*b*) at 363 K; (*c*) at 300 K (after cooling).

after a temperature cycle, but in most cases the general distributions of preferential orientations of the domain walls persisted. From our observations no definite conclusions about the exact location and the identity of the nucleation sites can be drawn. It is not clear whether domain growth starts at the surface or in the bulk of the crystal and at what type of defect.

Upon studying the phase transition in more detail, several phenomena were observed on both types of faces. The domains disappeared and appeared in groups. For the {111} face such a group of domains consists of one domain wall of type I having on one side a set of type IIa lines and on the other side a set of type IIb lines, that is, one feather. For the {100} face such a formed group consists either of a feather or of two neighbouring domains with their length directions parallel to each other. Upon heating these domain groups mostly transformed as a whole into the f.c.c. structure, that is, within the time resolution of our video equipment these groups disappeared instantaneously. In some cases this transition occurred in several stages. In this case, a domain group shrunk stepwise in its length direction. This suggests that in this situation the rhombohedral phase is metastable and that the domains are temporarily stabilized by pinning points. During this phase transition in a few cases also some decrease in the width of the domain group could be observed.

In case of the phase transition from f.c.c. towards rhombohedral, phenomena that are similar to those occurring during the heating stage were observed for both the {111} and the {100} faces. Most of the domain groups appeared instantaneously. Some grew stepwise, mainly in the length direction of the group. No characteristic features could be identified as the possible nucleation sites of the domains. No changes in the domain patterns were observed on either of the faces within 15 minutes after the phase transition.

In order to investigate the mobility of the domain walls, a crystal that had been studied in detail with DICM was placed in a quartz tube that was subsequently pumped down to 10^{-5} Torr, sealed off and stored in a furnace at 333 K. After 21 days the tube was reopened and the crystal was again studied with DICM. No changes in the patterns of the domain structure could be observed on either of the faces. We therefore conclude that Ostwald ripening (Kern *et al.* 1979) of the domains does not play an essential role, that is, no growth of large domains at the cost of smaller domains due to interface energy minimization takes place.

Comparing the shape of the domains before and after several temperature cycles a significant decrease in domain size was observed. This points to an increase in the number of nucleation sites. This can be due to a faster cooling rate in the last cycles resulting in the formation of a larger number of nuclei. It might also be possible that after each cycle non-vanishing defects are formed, which may act as points for new domain nucleation. Detailed studies are necessary to obtain a definite explanation for this phenomenon.

3.2.2. The phase transition at 303 K

During the present DICM and RPM studies a second phase transition was observed *in situ* at 303 ± 2 K. This phase transition could be initiated by changing the intensity of the microscope light incident on the surface, or by heating or cooling the crystal with the help of a Peltier element. By the absorption of light in the surface layers of the crystal the temperature at the surface is increased. The heat introduced by the incident light raises the temperature maximally 6 K, as no phase transition could be introduced at crystal temperatures below 297 K. Upon reducing the temperature below 303 K the patterns of rhombohedral domain walls remained unchanged on both the {100} and the {111} faces, but additional domains superimposed on the rhombohedral domains appeared on both types of faces. With the help of RPM the appearance of bright regions moving fast over the surface could be monitored. Increasing the temperature reversed the process, that is, the superimposed domains moved in the opposite direction and subsequently disappeared. By means of slight changes in temperature the movement of the domain walls could be controlled and the motion of the walls could be stopped and reversed at any place on the surface.

DICM studies showed the formation of an extra structure on the surface. Domains having a surface orientation slightly different from the tilts in the feather patterns appeared, moved and were subsequently pinned. On the {111} faces the extra domain lines are connecting two rhombohedral domain lines of type I and make an angle of 80° - 85° with the type I lines (see fig. 6(*a*)). When the extra lines cross a type I line they change direction, whereas no changes in direction are observed at the crossings with the type II lines. Figure 6(*b*) shows the extra domain patterns on the {100} faces. On these surfaces at least two types of domain lines were found. These sets of lines make angles of approximately 45° and 80° with the main stems of the feathers (only the latter ones are visible in fig. 6(*b*)). Several individual domain walls running in other directions were monitored (e.g. parallel to the stems).

Upon further cooling to 268 K no changes were observed on the surfaces, although the phase transition of the trigonal structure towards the monoclinic structure has been reported to occur at 282 K (McGhie *et al.* 1994) or 295 K (Vaughan *et al.* 1993).

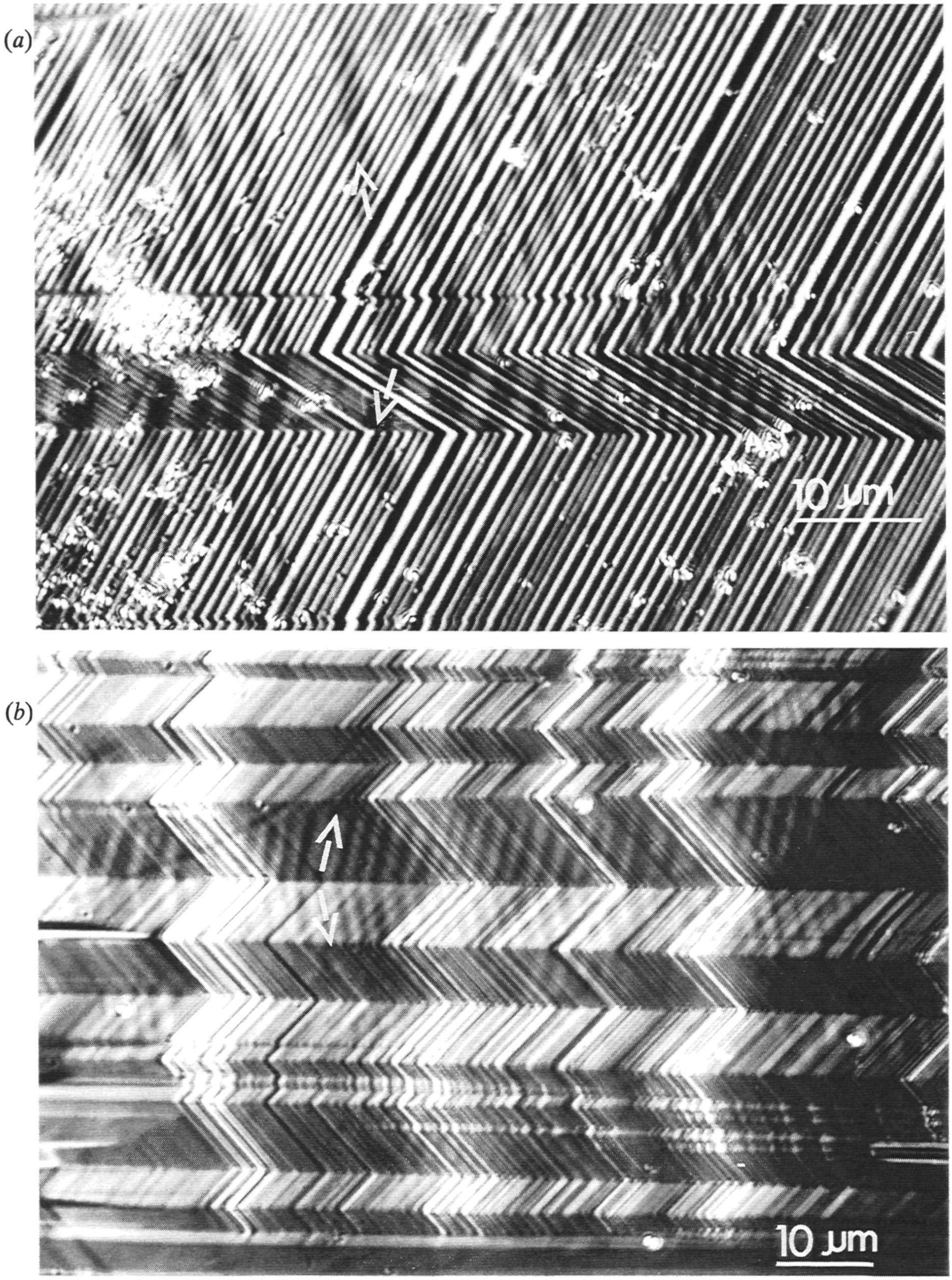

Fig. 6. DICM pictures showing the extra domains below 303 K on (*a*) a {111} face and (*b*) a {100} face. The domains manifest themselves as an alternating sequence of darker and brighter regions within each rhombohedral domain. The extra domain walls proceed across the type II domain lines and run parallel to the arrows indicated in the figure.

3.3. AFM studies

3.3.1. The {111} faces

Figure 7(*a*) shows a representative {111} surface topograph of a 90% pure C_{70} crystal as imaged by AFM. Low steps as well as step bunching are visible on this surface. The absence of domain lines indicates that this crystal has an f.c.c. crystal structure.

AFM images of a {111} face of a 99.9% pure C_{70} crystal are shown in figs. 7(*b*) and 7(*c*). The domain walls of type I are clearly visible in these pictures. They appear as lines running from the top left to the bottom right. Closer inspection of these figures shows that these domain walls seem to be an interrupted sequence of smaller domain walls. Three different inclinations can be recognized, which indicates the presence of at least three different domain types on this part of the surface. The interrupted type I lines separate two kinds of domains and the type II lines separate these domains from another type of domain. Figure 2 shows a schematic drawing of this domain pattern, in which the three different inclinations are indicated with A, B/C and D for the $F_{\alpha\beta}$ feather. The dashed lines in this figure represent domain walls that have been observed by RPM as will be presented in section 3.4.1. These walls can not be seen with AFM as the inclinations for the B and C domains are identical for this type of feather on the (111) face.

The type II domain walls in each feather are connected with those of the neighbouring parallel feathers. Thus, in the direction perpendicular to the length direction of the feathers zigzag rows having either an alternating sequence of type A and D domains or of type B and C domains can be observed.

The differences in the orientations of the four domains were determined by measuring the difference in the inclinations of two domains along a line perpendicular to the domain wall separating these domains. For the boundaries of type I, IIa and IIb orientational differences of respectively 6.4 ± 0.8°, 5.7 ± 0.3° and 3.6 ± 0.3° were found for the $F_{\alpha\beta}$ feathers and respectively 8 ± 1°, 6.8 ± 0.3° and 3.8 ± 0.6° for the $F_{\beta\alpha}$ feathers.

Also the angles between the different domain walls as projected on the {111} surface were measured. The average values of the angles α (between line type I and IIa) and β (between line type I and IIb) were determined to be 31 ± 2° and 68 ± 2° for the $F_{\alpha\beta}$ feathers and 32 ± 2° and 66 ± 4° for the $F_{\beta\alpha}$ feathers respectively. These values may deviate slightly from the real ones due to the drift in the AFM.

The sizes of the domains as shown in figs. 7(*b*) and 7(*c*) are not totally representative for the entire surface. In some regions a very fine structure of domains was present, resulting in a face which looked flat under the optical microscope. By AFM this pattern displayed the same morphology as presented in fig. 2, but on a sub-micrometer scale. Larger domain structures could also be observed. In some parts of the surface no domain structures could be seen down to the resolution of the AFM (about 10 nm).

In fig. 7(*d*) another area on the same {111} surface is shown. This area is divided in two symmetrically equivalent surfaces by a $/1\bar{1}0/$ boundary which is formed by the intersection of an even number of parallel twin planes with the growth face. None of the domains crosses the twin boundary. Domain growth across this boundary seems to be impossible. In the left part of the figure two different groups of feathers meet each other. The boundary between these two groups forms a zigzag pattern that follows the orientations of the domain walls of the two types of feathers. Some of the domain walls seem to proceed into the neighbouring group of domains.

In most of the AFM pictures many rounded particles can be seen. These particles are

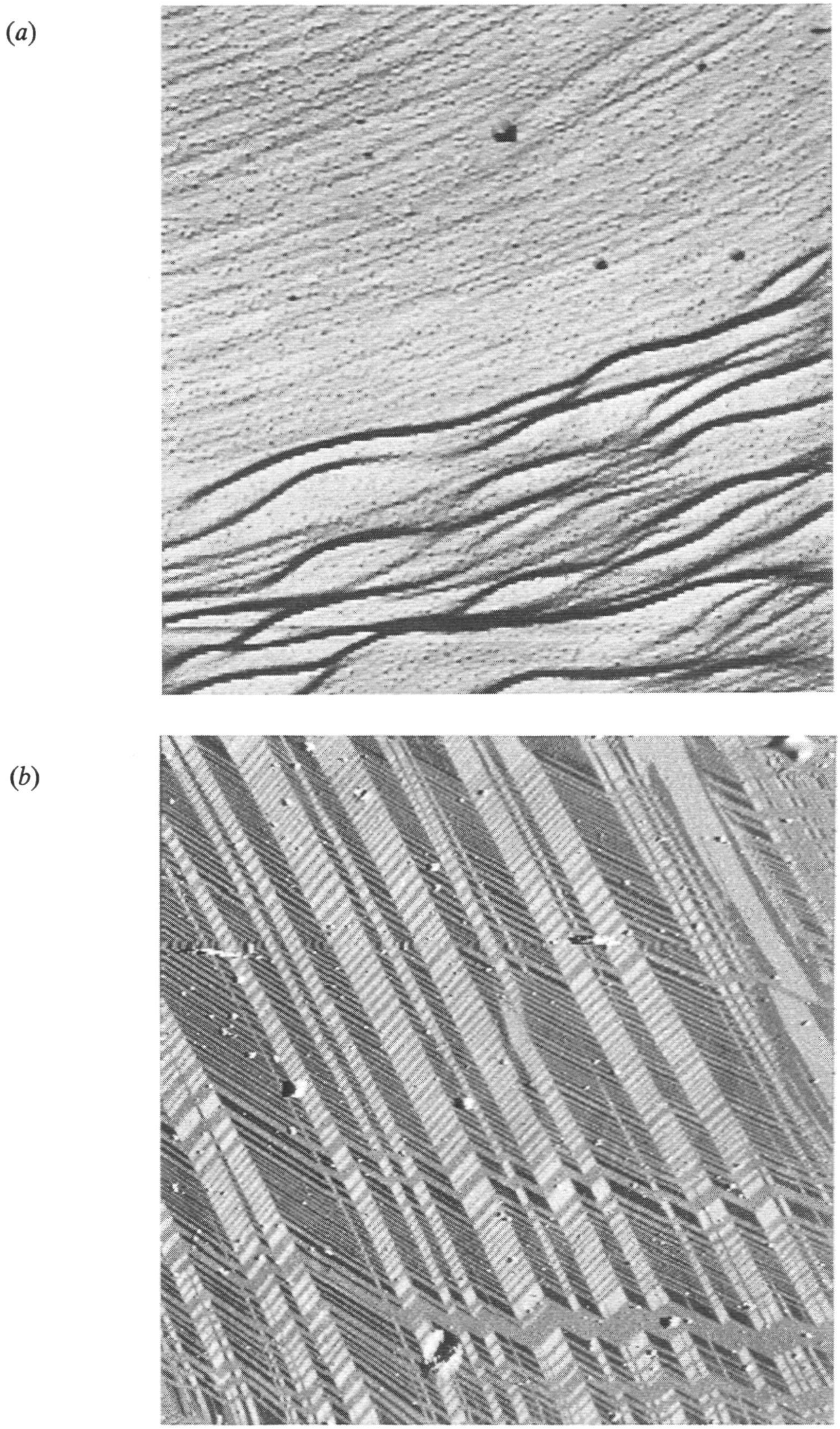

Fig. 7 (*a*)-(*b*). See page 105 for caption.

(*c*)

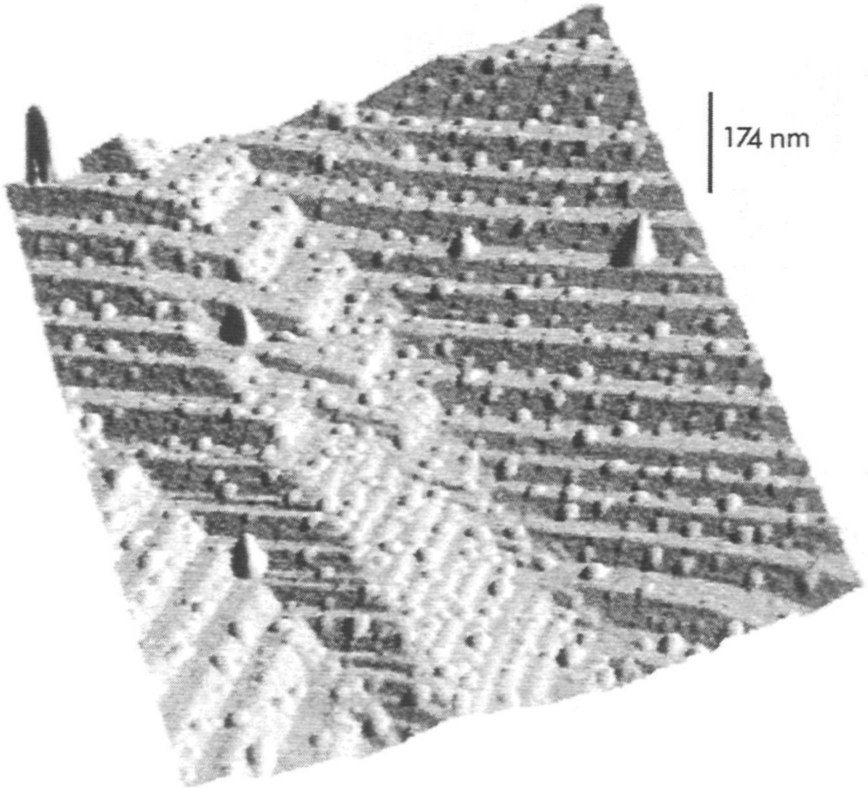

Fig. 7(*c*). See page 105 for caption.

attached loosely to the surface. During scanning they can quite easily be displaced by the AFM tip. This indicates that the interaction between these particles and the underlying surface is weak and, therefore, these particles probably consist of a compound different from C_{70}. An interesting observation is that these particles are all lying in parallel rows that do not follow the underlying domain pattern. In fact these particles are attached to the edges of the growth steps present on these surfaces. The fact that the particles decorate the steps indicates that the nucleation and growth of these particles occurred after cessation of the growth of the C_{70} crystal itself. As no domain walls are decorated, the nucleation must have taken place at a temperature above the f.c.c. to rhombohedral phase transition.

Although the exact nature of the impurities is still unknown we suggest that they either might be introduced in the growth tube at the time the quartz is melted locally to isolate the C_{70} or that they might be present in the growth tube as some carbon compound due to a partial decomposition of the C_{70}.

3.3.2. The {100} faces

In this section only the morphology of the {100} faces of 99.9% pure C_{70} crystals is described. In fig. 8(*a*) an AFM picture of a {100} face of a pure crystal is shown. Characteristic for this surface are the domain walls running in the /010/ directions separating domains elongated in these directions. Most of the surface parts corresponding with separate domains are tilted away a few degrees from the original orientation of the f.c.c. {100} face. Tilts have been found corresponding with the four different orientations $(1\delta 0)$, $(1\bar{\delta}0)$, (10δ) and $(10\bar{\delta})$

(*d*)

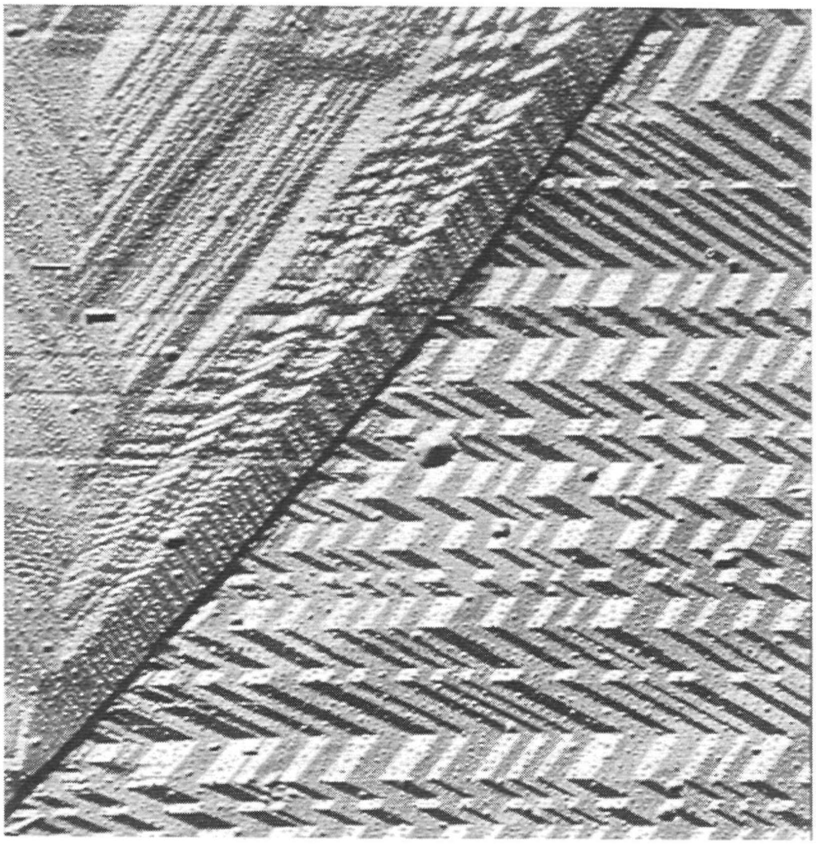

Fig. 7. AFM topographs of {111} surfaces of C_{70} crystals; (a) f.c.c. crystal of 90% purity. The scan size is 40 μm × 40 μm. (b) Overview of rhombohedral crystal of 99.9% purity. The scan size is 50 μm × 50 μm. (c) Detail of the same surface as shown in (b). The scan size is 8 μm × 8 μm. (d) Detail of the same face as shown in b) with twin boundary running from the bottom left to the top right of the figure. The scan size is 20 μm × 20 μm (*a*) and (*d*) are shaded from the upper left corner. (*b*) is shaded from the left-hand side and (*c*) from the right-hand side.

on (100) with $\delta \ll 1$. However, some regions appear to have conserved the original orientation. The combination of all these domains results in a complex surface pattern displaying 'basin' like structures and 'grooves'.

A detail of such a basin is given in fig. 8(*b*). Here a flat {100} area is bounded by the four different {1δ0} domains all tilted in a different direction and thus forming the side walls of the basin. The question now arises whether the bottom of the basin is really molecularly flat and corresponds with untransformed f.c.c. material or consists of numerous unresolved submicrometre domains. Detailed AFM scans were carried out on several of these regions. In part of the regions a pattern of narrow parallel domains was found. However, in other regions no fine structure could be identified. The latter surface areas thus either have the original orientation of the untransformed f.c.c. {100} face or consist of a dense pattern of nanometre sized tilted rhombohedral domains that could not be resolved during the scans.

For all domains that form the side walls of the basins the inclination with respect to the original {100} orientation was determined. Inclinations ranging from 3° to 5° were found.

In fig. 8(*c*) a pattern of grooves running in the /010/ directions is shown, which seems to be made up of an alternation of two types of domains. Also in the large domains a fine structure of domain walls can be observed. The tilt of the domains with respect to the original

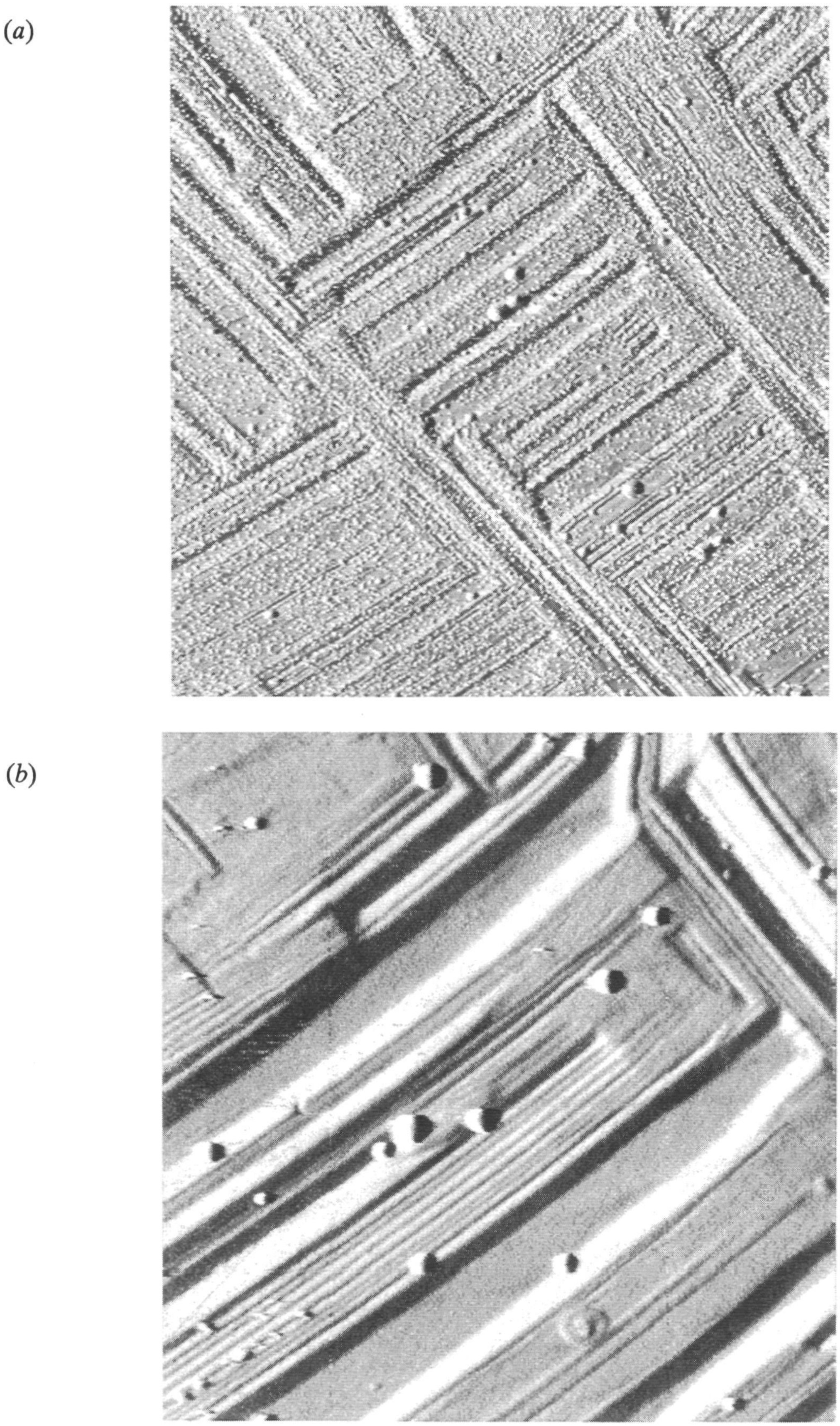

Fig. 8 (*a*)-(*b*). See next page for caption.

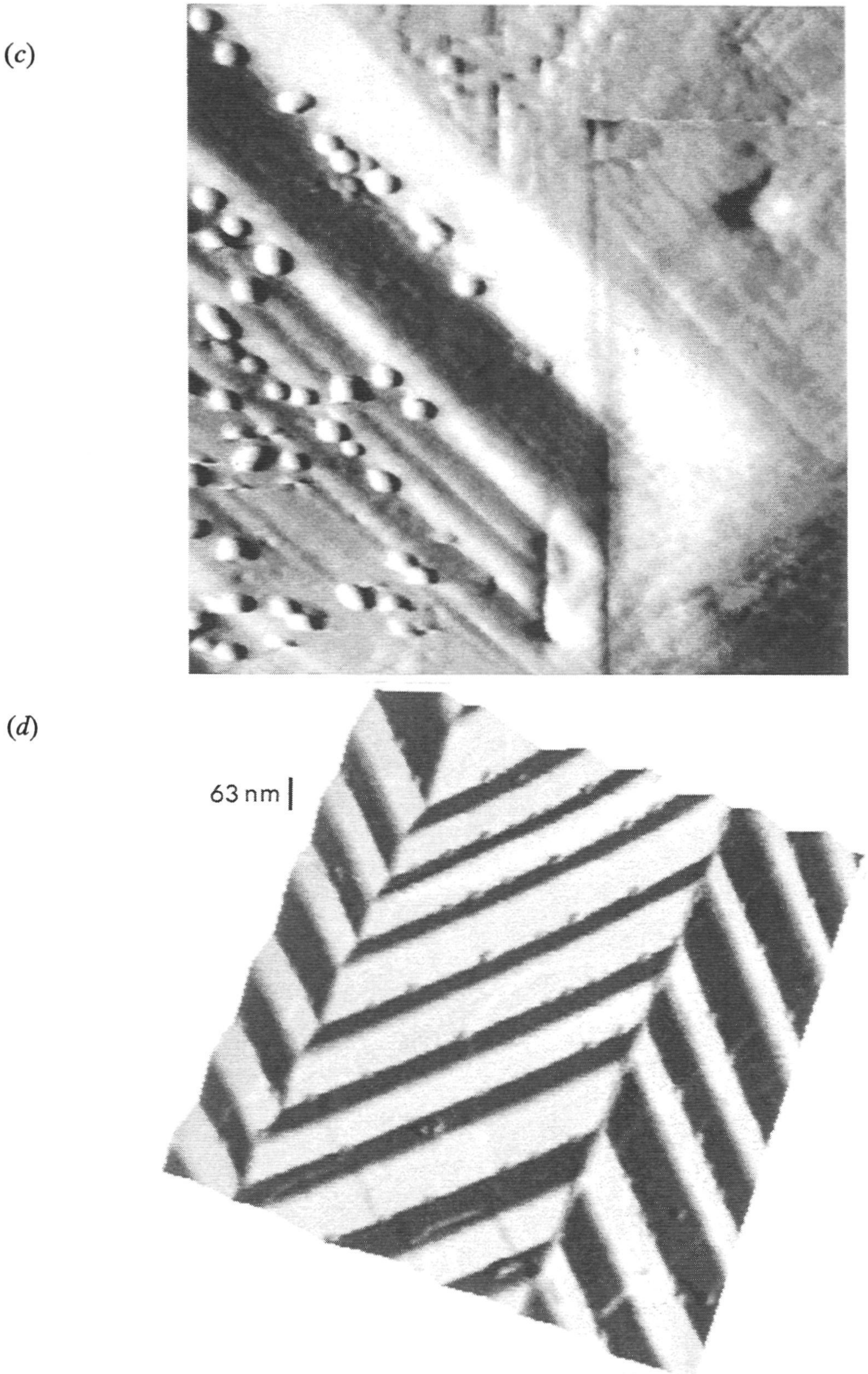

Fig. 8. AFM images of domain patterns on the {100} surfaces. (*a*) A general view. The scan size is 50 μm × 50 μm. (*b*) Arrangement of domains forming a so-called 'basin'. The scan size is 22 μm × 22 μm. (*c*) Patterns of grooves formed by an alternating sequence of two types of domains. The scan size is 7 μm × 7 μm. (*d*) Feather patterns. The scan size is 5 μm × 5 μm. (*a*) to (*c*) are shaded from the left-hand side. (*d*) is shaded from the right-hand side.

f.c.c. {100} orientation was found to be 4 ± 1°.

As was already mentioned in section 3.1 also on the {100} faces feather patterns were observed. In fig. 8(*d*) such a feather pattern is shown. The feathers are composed of main stems and side branches running in the /010/ and /011/ directions respectively. No basins have been observed in this region. Also for the feather patterns the differences in surface orientations between adjacent domains were measured. For two domains separated by a /010/ line an orientational difference of 8 ± 1° was found, whereas for domains bounded by a /011/ line a difference of 11 ± 1° was observed.

3.4. Reflection polarization microscopy studies

In order to identify the crystallographic orientations of the different domains outcropping at the surfaces reflection polarization microscopy was used. The surfaces, which were oriented perpendicularly to the direction of the incident beam of light, were examined with crossed polarizers by careful observation of local intensity changes upon rotating the samples around their surface normal. As the orientation of the surface with respect to the polarization direction of the incident light beam changes during rotation, the changes in intensity provide information on the anisotropy in reflection. If this anisotropy is determined by bireflectance, extinction will occur when the polarization direction of the incident light is parallel to one of the two perpendicular principal axes of the elliptical intersection of the optical indicatrix with the surface.

3.4.1. The {111} faces

Several {111} faces from both 90% and 99.9% pure C_{70} crystals were studied under crossed polarizers. The {111} faces of the 90% pure crystals remained dark upon rotation around the surface normal indicating an isotropic reflectivity. This agrees with the optically isotropic nature of the f.c.c. crystals that did not undergo the phase transition during cooling down.

On the contrary, on the {111} faces of the 99.9% pure rhombohedral crystals anisotropy of the reflectivity could be observed. In fig. 9 a representative RPM picture of a part of a {111} face is shown. The feather-like pattern of type $F_{\alpha\beta}$ as observed in the DICM and the AFM measurements is again clearly visible. Four different types of domains can be observed here.

When the orientation of the sample is rotated with respect to the polarizer one of the domains remains dark in all orientations (type A), whereas the other domains show a minimum in the intensity of the reflected light every 90°. Type D domains are dark when the polarization of the incident light beam is parallel or perpendicular to the type I lines and the type B and C domains are dark when the polarization is rotated 60° and 30° clockwise respectively with respect to the former orientations. In fig. 2 the principal axes of the intersections of the indicatrices are indicated for the domains present in this feather-like structure.

On the {111} faces the feathers point in three different directions, related by a threefold symmetry. Since each feather $F_{\alpha\beta}$ has a mirror equivalent $F_{\beta\alpha}$, six arrangements can be observed on this kind of surfaces. In all feather patterns four types of domains occur. The domains of type B, C and D are symmetry related by rotations of 120°.

For all domains the orientation of the C_{70} molecules within these domains can now be

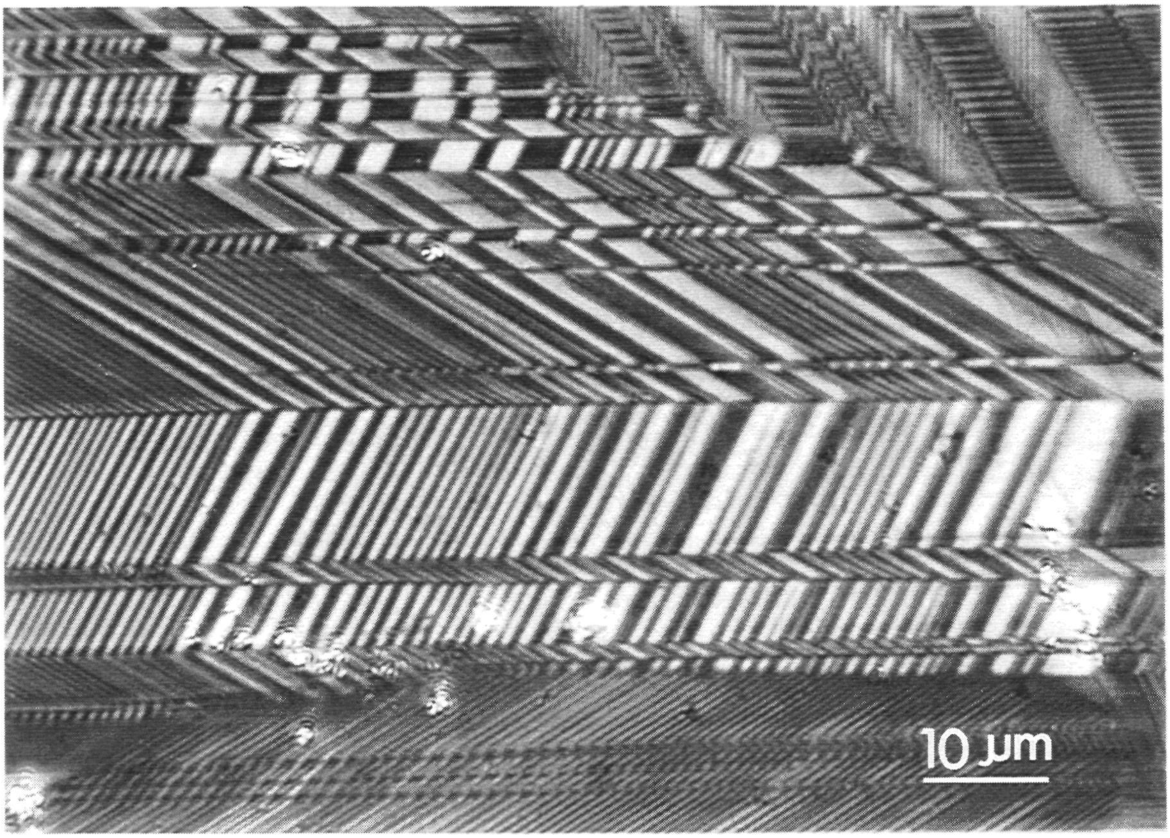

Fig. 9. RPM image of a {111} surface under crossed polarizers displaying four types of domains within a feather.

determined. For domains of type A the section of the indicatrix is circular. This implies either that the indicatrix is spherical because of cubic symmetry or that the unique axis of the indicatrix of a rhombohedral domain is oriented perpendicular to the (111) surface. In the former case the molecules are orientationally disordered. In the latter case they are pointing with their long axis along the unique axis of the trigonal unit cell, that is, along the surface normal of the (111) face. A rhombohedral domain has an indicatrix with its unique axis pointing in one of the <111> directions. For domains of types B, C,and D one of the principal axes of the section of the indicatrix is a projection of the unique axis on the surface. For the type B domain the projection of the unique axis is pointing in the $[\bar{2}11]$ direction. Thus, the C_{70} molecules within this domain all have their long axis parallel to the $[\bar{1}11]$ direction. In a similar way it can be deduced that the molecules in the domains of type C and D have their long axis parallel to the $[1\bar{1}1]$ and $[11\bar{1}]$ directions respectively. In fig. 2 the orientations of the C_{70} molecules in the different domains of a feather are shown.

RPM studies of several other {111} faces showed that both the $F_{\alpha\beta}$ and the $F_{\beta\alpha}$ feathers occur. For both types of feathers only one arrangement of domains was found, namely the ones presented in fig. 2. In table 1 the results of the RPM studies are presented. Indicated are the angles between the type I domain lines and one of the principal axes of the domains as deduced from the orientations of extinction. Theoretically these angles should all be either 0°, 30° or 60° for the D, C and B domains respectively. However, deviations from these values are found that cannot totally be explained by the error margins. We suggest that these deviations are caused by lattice deformations and form birefringence (see section 3.4.2).

Table 1: Angles between the type I domain lines and one of the principal axes of the intersection of the indicatrices with (111) for the different domains on the {111} surface in the different feather patterns observed. Clockwise rotations from the type I lines are given. The error margin is ± 4°.

type of feather	B	C	D
$F_{\alpha\beta}$	66°	28°	0°
$F_{\beta\alpha}$	62° 63° 65° 64°	25° 26° 24° 19°	6° 8° 0° 3°

The angles α and β as measured on the RPM photographs are 33 ± 2° and 62 ± 2° respectively.

3.4.2. The {100} faces

The {100} faces of rhombohedral C_{70} crystals also showed a position dependent anisotropy in the reflectivity upon rotation of the crystal surface under crossed polarizers. Large parts of the surface remained dark during rotation. For the other parts of the surface extinction could be observed every 90°. The minima in the intensity of the reflected light were observed when the polarization direction of the incident light was parallel to one of the four /011/ directions on (100). In fig. 10 a RPM picture is shown in which the polarization direction is parallel to the [010] direction. In this orientation the intensity of the reflected light is maximal for the regions with an anisotropic reflectivity. Many domains show up as bright lines being elongated along one of the /010/ directions. From these observations it cannot be concluded whether all the bright regions consist of only one type of domain displaying extinction every 90° or of more types of domains all having the principal axes of the (100) section of their indicatrix lying parallel. However, we know from the AFM studies that, apart from the regions exactly parallel to {100}, four types of domains occur on this surface. This implies that the bright regions in fig. 10 consist of four types of domains that all must have the same extinction directions, that is, the directions of the principal axes of the (100) sections of the indicatrices must be identical for the four different rhombohedral domains. For all domains the unique axis of the indicatrix is parallel to one of the <111> directions. The projections of these unique axes on the (100) face are pointing in the four /011/ directions. Therefore, for every domain the principal axes are also pointing in the /011/ directions and thus the four types of domains all have the same extinction directions as observed in the RPM studies.

The fact that some regions remain dark upon rotation can have two reasons. First, the reflectivity of these regions might be isotropic, indicating that these regions still have the f.c.c. structure and did not undergo the phase transition during cooling down. Second, these regions may consist of a very dense structure of microdomains, their dimensions being below the resolution of optical microscopy. The latter possibility is supported by the observation of

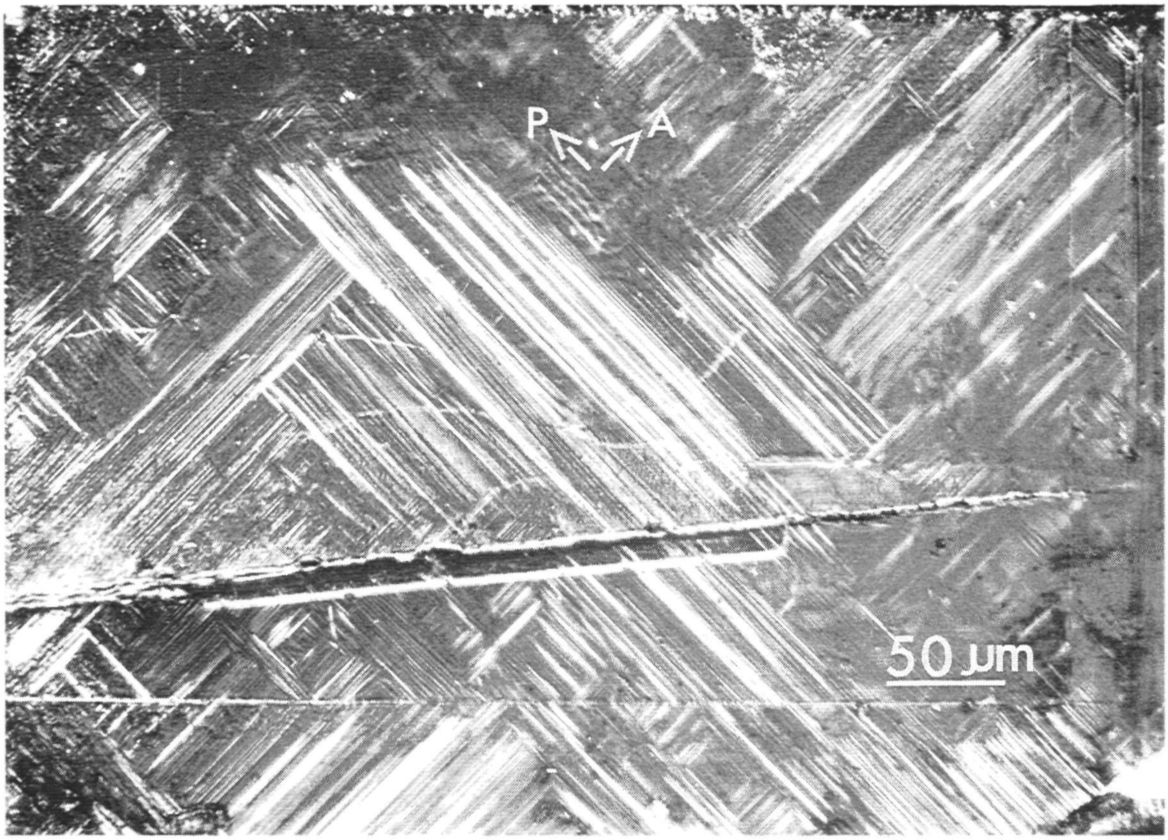

Fig. 10. RPM picture of a {100} face under crossed polarizers. The direction of the incident polarized light (P) is rotated 45° with respect to the main axes of the {100} intersection of the indicatrices of the rhombohedral domains.

pseudo-domains, the so-called 'puzzle game domains' (Schmid *et al.* 1988, Rabe *et al.* 1990) as shown in fig. 11. In areas with puzzle game domains a dense structure of domain walls parallel to /010/ is present. A group of parallel, elongated domain walls with submicrometre spacing introduces a pseudo-symmetry with pseudo mirror planes being parallel and perpendicular to the /010/ directions, that is, making an angle of 45° with the extinction directions of the domains. Due to form birefringence inside each of these puzzle domains, an anisotropic reflectivity occurs that is characterized by a difference in reflectivity for light with its polarization parallel and perpendicular to the domain walls. When linearly polarized light is incident on this bireflecting domain wall structure and the polarization direction is making an angle of 45° with the /010/ length directions of the adjacent domain walls (that is, parallel to the extinction directions of the domains itself) this light becomes slightly elliptically polarized upon reflection and in addition is rotated over a small angle. As a result, maximal contrast is obtained for the puzzle domains when the crossed polarizers are parallel to /0$\bar{1}$1/ on (100) and are slightly uncrossed. In case of fig. 11(*a*) and 11(*b*) the analyzer is rotated +2° and -2° respectively with respect to the crossed position, which leads to reversal of the image contrast. Within each puzzle domain often a dense pattern of parallel domain walls can just be discerned at the highest magnifications.

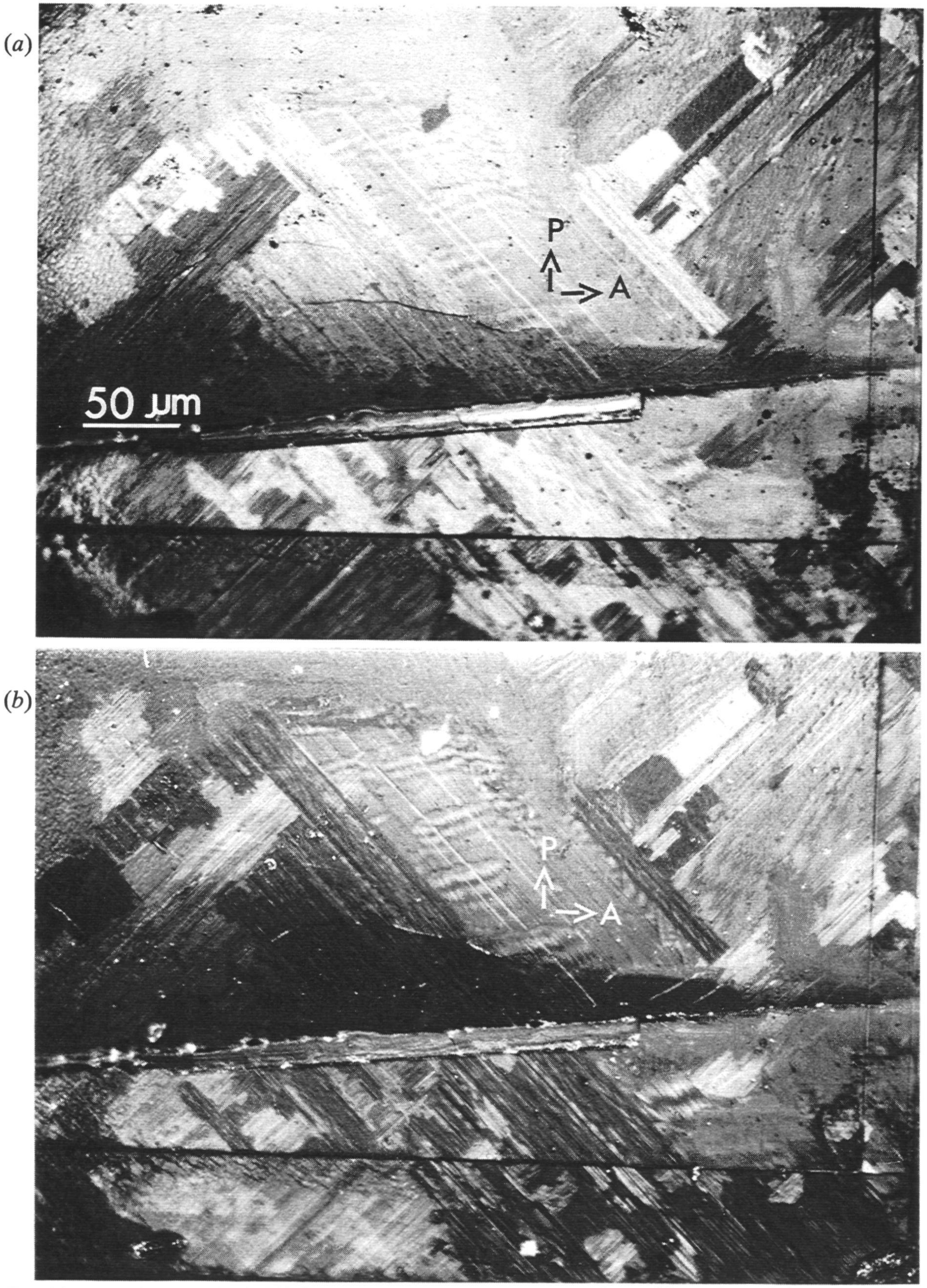

Fig. 11. RPM pictures of a {100} face under slightly uncrossed polarizers. (*a*) Analyzer (A) uncrossed over +2°; (*b*) uncrossed over -2°. The polarization direction of the incident light (P) is parallel to one of the main axes of the section of the indicatrices of the rhombohedral domains.

4. General discussion and conclusions

4.1. The formation of rhombohedral domains

As was mentioned in section 3.2, *in situ* studies of the phase transition showed that both on the {100} and the {111} faces the domains appeared and disappeared in groups. On the {111} surfaces growth of the domains occurred along the length direction of the feathers. On the {100} faces domain growth can also occur along feathers. On both types of surfaces the feather patterns consist of four different types of domains implying an alternating creation of two sets of domains. Such a regularity in the arrangement of the domains has already been described for the domain patterns on surfaces of, for example, $Pb_3(PO_4)_2$ (Torres *et al.* 1980), $KFe(MoO_4)_2$ and $KIn(WO_4)_2$ (Otko *et al.* 1983) crystals and is explained by a reduction of the internal stress by means of an alternation of opposite inclinations.

Although the feathers on one single surface were not formed at the same time the domain walls of parallel, adjacent feathers on both types of surfaces of the C_{70} crystals were connected. This implies either that the shape of a newly formed feather is determined by the shape of a neighbouring feather or that domain wall movement occurs after formation of the domain pattern. The second possibility seems unlikely, since during the present study never a moving boundary was observed. Both mechanisms suggest that the resulting pattern is formed by a reduction of internal stress.

As the phase transition is initiated in the crystal at more than one site, several types of feathers can be observed on one single surface. From our observations it could not be determined whether the phase transition is nucleated in the bulk or at the surface.

On both types of surfaces the domain walls manifest themselves as lines running in several directions. In order to assign orientations of domain walls to these lines, the domain walls that are allowed in this system have to be determined. Following the assumption that a change in length, due to spontaneous strain, of any infinitesimal vector contained in a domain wall is equal in the two adjacent domains, all possible domain walls can be determined (Fousek and Janovec 1969). For the phase transition of m3m to $\bar{3}$m the walls that are predicted (Aizu 1970, Sapriel 1975) are listed in table 2.

4.2. The domain patterns on the {100} faces

Using table 2 the orientations of the different domains of the feather patterns on the {100} surfaces can be deduced. As is shown in fig. 4, feathers running in two directions have been observed on the (100) face. These two feathers are symmetry related by the fourfold axis. Each symmetrically unique feather allows for two different assignments of domains and domain walls to their pattern, as is schematized in fig. 12. There are no other possibilities. The pattern presented in fig. 12(*b*) can be rejected for two reasons. First, as was mentioned in section 3.1, the type I lines on the {111} faces proceed as the main stems of the feathers on the {100} faces. Thus, these lines are the outcrops of {001} domain walls. Only in fig. 12(*a*) the main stems of the feathers are formed by these domain walls. Second, from the analysis of the AFM images it follows that the difference in orientation between two domains being separated by the line corresponding with the main stem of a feather is 8 ± 1° (see section 3.3.2). Calculations show that this difference is 4.3° for a $(1\bar{1}0)$, (110), (101) or $(10\bar{1})$ domain wall, whereas it is 8.5° in case of a (010) or a (001) domain wall (see table 2). The

Table 2: Orientations of domain walls between two adjacent domains that are indicated by the direction of their unique axes. The calculated orientational differences of the (111) and (100) surfaces of these domains along a line perpendicular to the intersection line of the domain wall and these (111) and (100) surfaces are also given.

unique axes of neighbouring domains	allowed domain walls	orientational differences	
		on (111)	on (100)
A: [111] and B: [$\bar{1}11$]	(100) (011)	8.2° 4.4°	- 12.5°
A: [111] and C: [$1\bar{1}1$]	(010) (101)	8.2° 4.4°	8.5° 4.3°
A: [111] and D: [$11\bar{1}$]	(001) (110)	8.2° 4.4°	8.5° 4.3°
C: [$1\bar{1}1$] and B: [$\bar{1}11$]	(001) ($1\bar{1}0$)	0° 6.1°	8.5° 4.3°
D: [$11\bar{1}$] and B: [$\bar{1}11$]	(010) ($10\bar{1}$)	0° 6.1°	8.5° 4.3°
C: [$1\bar{1}1$] and D: [$11\bar{1}$]	(100) ($01\bar{1}$)	0° 6.1°	- 12.5°

calculated orientational difference between two domains separated by a line forming the side branch of a feather is 12.5° for both patterns presented in fig. 12, which is in accordance with the angle of 11 ± 1° that was measured by AFM.

In the same way as above it can be deduced that the domains in the groove patterns parallel to [001] on the (100) face are B and D or A and C domains separated by (010) walls and those in the grooves parallel to [010] on the same face are A and D or B and C domains separated by (001) walls.

For the basin-like structures on the {100} faces no final explanation could be found. The orientational differences between the bottom of the basin and its side walls as determined by AFM measurements are approximately half as large as those for the boundaries between two tilted domains. This can be due to the fact that the bottom of the basin has kept the original orientation of the f.c.c. {100} face, and thus still has the f.c.c. structure, or consists of a very dense structure of nanodomains (the spacing between two adjacent walls must be smaller than 10 nm in this case). The question whether some parts of the crystal still have the f.c.c. structure is not yet solved. At this moment high resolution TEM measurements are being performed on these crystals in order to study their microstructure (Bernaerts 1995).

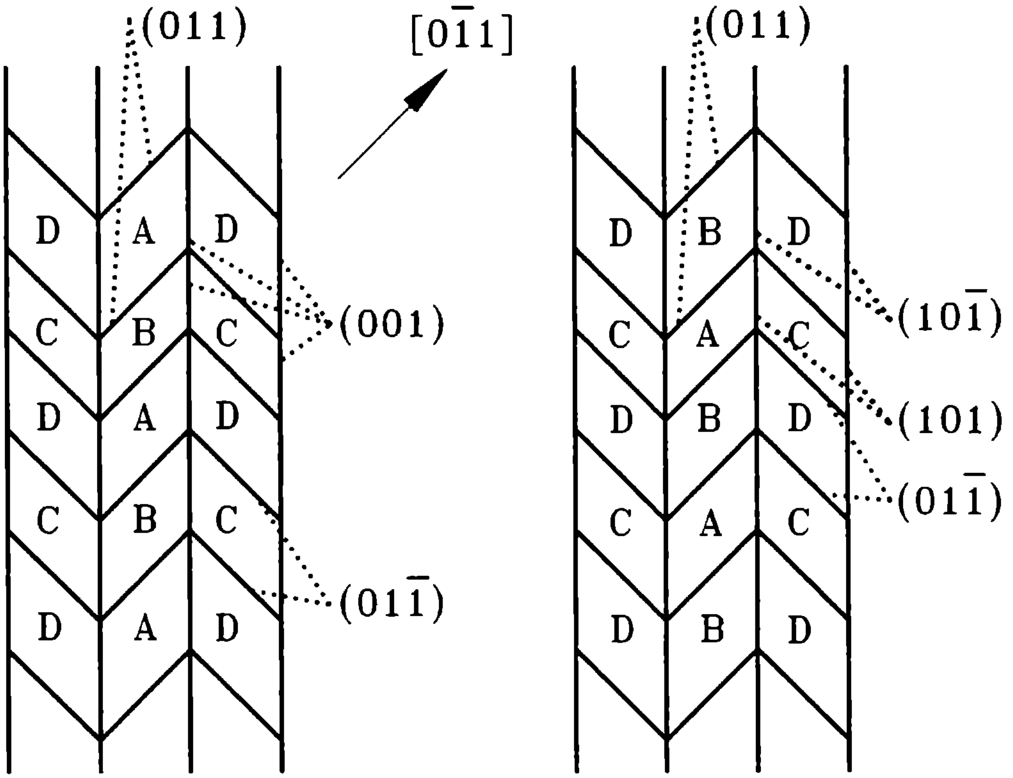

(a) (b)

Fig. 12. Assignment of domains and domain walls to the feather patterns on the (100) face. Using the criterion of allowed domain walls two possible arrangements, (*a*) and (*b*), can be derived. Confrontation with the results of DICM and AFM measurements rejects possibility (*b*). A, B, C and D represent rhombohedral domains having their unique axis in the [111], $[\bar{1}11]$, $[1\bar{1}1]$ and $[11\bar{1}]$ directions respectively.

4.3. The domain patterns on the {111} faces

Using table 2 domain walls can be assigned to all the lines that are present in the $F_{\alpha\beta}$ and $F_{\beta\alpha}$ feathers. For the $F_{\alpha\beta}$ feathers in fig. 2 the type IIa lines are the manifestation of $(10\bar{1})$ domain walls, the type I lines are either due to (001) or (110) domain walls and the type IIb lines are the result of either (101) or (010) domain walls.

It can also be derived from table 2 that for each type of feather only one arrangement of domains is possible, namely the one that is observed in the RPM measurements (see fig. 2). Thus, an interrupted type I line as observed with DICM and AFM is in fact an uninterrupted line composed of domain walls between A and D and between B and C domains. Comparing the orientational differences along the type I lines as determined in the AFM measurements (see section 3.3.1) with the calculated values (see table 2) it can be concluded that the type I lines are the manifestation of (001) domain walls at the (111) surface. This agrees with the same conclusion in section 3.1, which was deduced from the fact that the type I lines on the {111} faces proceed as the main stems of feathers on the {100} faces. The domain wall between the B and C domains as indicated by a dashed line in fig. 2 can not be observed with DICM and AFM because B and C domains that are separated by a (001) domain wall have the same inclination on the (111) surface. Similarly, it can be concluded that the type IIb lines are due to (101) domain walls.

The $F_{\alpha\beta}$ and $F_{\beta\alpha}$ feathers are related by the {001} mirror plane, that is present in both the cubic and the trigonal structure. This can be concluded from the fact that the angles α and β as well as the orientational differences of the domains at the boundaries of type I, IIa and IIb are identical for both types of feathers and that the arrangements of the domains within the two types of feathers are related by the {001} mirror plane.

4.4. The phase transition at 303 K

The exact nature of the phase transition at 303 K and the extra domain lines occurring below this temperature are still unknown. No hysteresis could be observed in the temperature of the phase transition as slight temperature changes around the transition temperature are sufficient to move the extra domain lines. Thus far, for f.c.c. grown crystals only two phase transitions have been reported. At 361 K the rhombohedral lattice transforms into the high temperature f.c.c. lattice and all domain patterns disappear. Cooling the crystal below 282 K results in a phase transition towards a monoclinic structure. At this phase transition the symmetry reduction is expected to introduce extra domain walls. However, we observe a second phase transition at a temperature that is 21 K higher. In the temperature region between 303 K and 268 K no phase transition was observed during these RPM and DICM studies. This suggests that the 303 K phase transition is the one between the monoclinic and the trigonal structure. Detailed studies of the crystal structure below 303 K are in progress.

The fact that the extra domain walls have not been observed during the AFM measurements can be explained by a local heating of the crystal surfaces during the scans by the solid state laser in the AFM equipment.

5. Acknowledgements

One of the authors, M. A. Verheijen, gratefully acknowledges the financial support of the Netherlands Organization for Scientific Research (NWO/SON). M. S. Couto wishes to thank CAPES (Coordenação de Aperfeiçoamento de Pessoal Nível Superior), Brazil, for a scholarship making this research possible. We are very grateful to H. Meekes for fruitful discussions and to I. Holleman and G. Meijer for synthesizing, purifying and characterizing the C_{70} powder.

6. References

Agterberg, D. F., and Walker, M. B., 1993, Phys. Rev. B, **48**, 5630.
Aizu, K., 1970, J. Phys. Soc. Jpn, **28**, 706.
Bernaerts, D. *et al.*, 1995, work in progress.
Christides, C., Thomas, I. M., Dennis, T. J. S., and Prassides, K., 1993, Europhys. Lett., **22**, 611.
Fousek, J., and Janovec, V., 1969, J. Appl. Phys, **40**, 135.
Kern. R., Le Lay, G., and Metois, J. J., 1979, *Current Topics in Materials Science*, Volume 3, edited by Kaldis, E. (Amsterdam: North-Holland Publishing Company), p. 277.
McGhie, A. R., Fischer, J. E., Stephens, P. W., Cappelletti, R. L., Neumann, D. A., Mueller,

W. H., Mohn, H., and ter Meer, H. -U., 1994, Phys. Rev. B, **49**, 12614.

Nelissen, B. J., van Loosdrecht, P. H. M., Verheijen, M. A., van der Avoird, A., and Meijer, G., 1993, Chem. Phys. Lett., **207**, 343.

Otko, A. I., Nesterenko, N. M., Krainyuk, G. G., and Nosenko, A. E., 1983, Ferroelectrics, **48**, 143.

Rabe, H., Rivera, J. -P., Schmid, H., Chaminade, J. -P., and Nganga, L., 1990, Mat. Sci. Eng. B, **5**, 243.

Sapriel, J., 1975, Phys. Rev B, **12**, 5128.

Schmid, H., Burkhardt, E., Walker, E., Brixel, W., Clin, M., Rivera, J. -P., Jorda, J. -L., François, M., and Yvon, K., 1988, Z. Phys. B, **72**, 305.

Torres, J., Ayroles, R., Roucau, C., and Takana, M., 1980, Ferroelectrics, **29**, 63.

van Enckevort, W. J. P., 1984, Prog. Crystal Growth and Charact., **9**, 1.

van Smaalen, S., Petricek, V., de Boer, J. L., Dusek, M., Verheijen, M. A., and Meijer, G., 1994, Chem. Phys. Lett, **223**, 323.

van Tendeloo, G., Amelinckx, S., de Boer, J. L., van Smaalen, S., Verheijen, M. A., Meekes H., and Meijer, G., 1993, Europhys. Lett., **21**, 329.

Vaughan, G. B. M., Heiney, P. A., Fischer, J. E., Luzzi, D. E., Ricketts-Foot, D. A., McGhie, A. R., Hui, Y. -W., Smith, A. L., Cox, D. E., Romanow, W. J., Allen, B. H., Coustel, N., McCauley, Jr., J. P., and Smith III, A. B., 1991, Science, **254**, 1350.

Vaughan, G. B. M., Heiney, P. A., Cox, D. E., Fischer, J. E., McGhie, A. R., Smith, A. L., Strongin, R. M., Cichy, M. A., and Smith III, A. B., 1993, Chem. Phys. Lett., **178**, 599.

Verheijen, M. A., Meekes, H., Meijer, G., Raas, E., and Bennema, P., 1992, Chem. Phys. Lett., **191**, 339.

Verheijen, M. A., van Enckevort, W. J. P., and Meijer, G., 1993, Chem. Phys. Lett., **216**, 72.

Verheijen, M. A., van Enckevort, W. J. P., Meijer, G., de Boer, J. L., van Smaalen, S., Petricek, V., and Dusek, M., 1994, *Proceedings of the IWEPNM 1994*, (Heidelberg: Springer Verlag).

Chapter 8

Behaviour of steps on the (001) face of $K_2Cr_2O_7$ crystals[1]

A. J. Derksen, W. J. P. van Enckevort and M. S. Couto

Department of Solid State Chemistry, University of Nijmegen, Faculty of Science, Toernooiveld, 6525 ED, Nijmegen, The Netherlands

Abstract

The behaviour of [100] steps, originating from spiral centres, on the (001) face of potassium bichromate ($K_2Cr_2O_7$, KBC) crystals growing from aqueous solutions has been studied by *in situ* and *ex situ* optical microscopy as well as by *ex situ* atomic force microscopy (AFM). After considerations concerning the centrosymmetry of KBC, the (001) and $(00\bar{1})$ faces are discriminated and a general view of the (001) surface morphology is given. The bunching, blocking and velocity of the [100] steps as a function of the supersaturation have been measured and are discussed in terms of models for step propagation influenced by time dependent impurity adsorption. Blocking is observed for both growth and dissolution at super (under) saturations below a critical value. By AFM steps of half, one and several unit cells in height are measured. For the supersaturation region where blocking occurs cusps are found in the steps, which correspond with the sites of the impurities that act as pinning points hindering step propagation. Bunching of lower steps to macrosteps and a proportional dependence of the mutual separation of these steps on their distance from the growth centre is found for supersaturations above the critical value for blocking.

---

[1] *Journal of Physics D: Applied Physics, to be published*

1. Introduction

The theory of Cabrera and Vermileya (1958) describes the blocking of steps below a critical supersaturation σ_{cr} due to impurity adsorption. In this model the steps are halted by immobile impurities that act as 'pinning points'. Above σ_{cr} the steps 'squeeze' themselves trough these pinning points and the step velocity, v, is given by:

$$v = v_\infty (1 - 2r_c/d)^{1/2}, \text{ for } d \geq 2r_c \text{ and} \qquad (1)$$
$$v = 0, \text{ for } d \leq 2r_c,$$

where v_∞ is the step velocity in the absence of impurities, r_c the radius of the critical two-dimensional nucleus and d is the distance between the impurity stoppers. The onset of step growth, that is, $v = 0 \rightarrow v > 0$, occurs at $\sigma_{cr} = 2\Omega\gamma_0/dkT$, which is the supersaturation where $2r_c = d$. Here γ_0 is the edge free energy per unit step height, k is the Boltzman constant, Ω is the volume of a growth unit and T is the temperature in K. Equation (1) can be rewritten in terms of supersaturation σ, using $v_\infty \propto \Delta\mu'/kT$ and $r_c = \Omega\gamma_0/kT\sigma = \gamma_0/\Delta\mu'$:

$$v = g(\sigma(\sigma-\sigma_{cr}))^{1/2}, \text{ for } \sigma > \sigma_{cr} \text{ and} \qquad (2)$$
$$v = 0, \text{ for } \sigma \leq \sigma_{cr},$$

Here g is a normalization constant and $\Delta\mu'$ is a driving force per unit volume which is defined as the difference in thermodynamic potential $\Delta\mu = \mu_s - \mu_f$ between the solid and the solute phase divided by the volume of a growth unit or $\Delta\mu' = \Delta\mu/\Omega$.

The theory above was later extended by van der Eerden and Müller-Krumbhaar (1986) who described the occurrence of bunching of lower steps to macrosteps for $d > 2r_c$. They assumed that the concentration of adsorbed impurities is not constant but is a time dependent function. In their model, each time when a step passes, it leaves a clean surface behind, which is contaminated slowly as new impurities adsorb on it. When the time interval until the next step passes is short, this second step will encounter only a few adsorbed impurities in front of it and these will hardly hamper this step. However, when the next step passes only after a long time, it will meet many adsorbed impurities and these will slow down the step. This gives a decrease in step advancement velocity for increasing step separations. Starting from a row of equidistant steps and introducing small perturbations in their mutual distances, the more widely separated steps lag behind and will be overtaken by the faster advancing ones with smaller distances. This leads to piling up of fast steps with the slow ones and macrosteps separated by large terraces develop. Using perturbation theory and computer simulations van der Eerden and Müller-Krumbhaar derived that the macrostep height and the spacing increase logarithmically with time.

After that paper, several other theoretical articles were published that also treated bunching phenomena (Vlachos and Jensen 1992, Potapenko 1993, Kardel and Weeks 1993, Chernov *et al.* 1993), but experiments on this subject remain scarce. It is known that crystals can have a 'dead zone' for growth on a certain facet for $\sigma < \sigma_{cr}$; examples are KDP {100} (Chernov and Rashkovich 1987), CdI_2 {001} (Onuma *et al.* 1992), KAP {010} (Jetten *et al.* 1983, Hottenhuis and Lucasius 1988) and lysozyme crystals (tetragonal form) {101} and {110} (Durbin and Feher 1986). However, apart from the observation that this phenomenon occurs, it has not been subjected to systematic research. The phenomenon of step bunching, related to the occurrence of the 'dead zone', was also described in a few cases (for example on KAP (van Enckevort and Jetten 1982)) but, except for the above mentioned theoretical paper by van der Eerden and Müller-Krumbhaar (1986), no connection was made with time dependent impurity adsorption.

During our *in situ* surface studies of the growth of potassium bichromate ($K_2Cr_2O_7$, KBC) crystals we also observed the above mentioned phenomena: a non-growth zone and, above σ_{cr}, the formation of bunching patterns. This prompted us to investigate these phenomena in more detail.

In our studies the behaviour of the [100] steps on the (001) face of KBC was monitored as a function of the supersaturation σ. The sources of these [100] steps were spirals which have already been observed *ex situ* by Szurgot and Sangwal (1982) and by Rak and Sangwal (1983). However, *in situ* experiments with the use of phase sensitive optical microscopy (van Enckevort 1984) allow to see the real time advancement of steps and, therefore, time dependent phenomena. Both growth and dissolution experiments were carried out, but more emphasis was placed on growth. In this article besides *in situ* also *ex situ* optical microscopy and *ex situ* atomic force microscopy (AFM) observations were done and a comparison with the relevant models in literature was made.

2. Experimental

2.1. Specimen preparation

KBC was chosen because it is an ideal model compound for experimental studies on crystal growth. The crystals are easily obtained by crystallization from aqueous solution and have a rich morphology. Moreover, they are suitable for *in situ* studies because of their high index of refraction which gives a high reflectivity when immersed in solution, and a large c-axis, which gives high steps on (001). Finally, due to a low wetting, the crystals can be separated from the solution without deteriorating the original growth patterns too much.

Aqueous KBC solutions were prepared using KBC (Merck, p.a.) and demineralized/deionized water.

The KBC crystals used as seeds for the *in situ* experiments varied in size from 1 × 2 × 2 mm to 3 × 4 × 8 mm and were grown, at room temperature, by slow evaporation and self-nucleation. As will be discussed in section 3.1 always the (001) face of the KBC crystals was used for the *in situ* and *ex situ* experiments.

2.2. In situ experiments

The *in situ* experiments were carried out in a double walled growth cell using a waterbath thermostat for temperature control, as schematized in Jetten *et al.* 1983. The growth cell contained about 40 cm^3 of solution and was covered by an optical window. During the *in situ* experiments the solution was not stirred.

The temperature was measured (using a thermocouple and a Pt-100 resistor) with an accuracy of about 0.02°C. This was also the temperature stability of the growth system. The equilibrium temperatures used varied between 23 and 26 °C.

During the *in situ* experiments the crystal surfaces were observed by optical microscopy, using oblique illumination with the aperture diaphragm closed as much as possible and placed slightly eccentrically with respect to the optical axis. This provides an enhanced image contrast (van Enckevort 1984). An objective lens specially corrected for observations through a thick liquid layer was used (Tsukamoto and Sunagawa 1985). The images were recorded with the help of a highly sensitive video camera, an analog differentiator and contrast enhancer, to reduce the disturbing influence of long range intensity variations of the background, a video-recorder (S-VHS) and a monitor. The lowest steps that can be observed with this kind of experimental set-up are 3 to 5 nm in height (Jetten *et al.* 1983). The step velocities and spacings were measured, after calibration, from the monitor screen.

The relative super (under) saturation of the nutrient phase was varied by varying the temperature of the growth cell which contains a solution of a fixed, known, concentration. The relative supersaturation was calculated from the temperature dependence of the KBC solubility in water, given by the relations (Szewczyk *et al.* 1985):

$$x = 681.292 \exp(-3349.62/T) \text{ for } T < 315 \text{ K}, \qquad (3)$$
$$x = 138.409 \exp(-2847.36/T) \text{ for } T > 315 \text{ K},$$

in which x is the mole fraction of KBC and T the temperature in K.

Because the activity coefficient for saturated aqueous KBC solutions is close to unity (0.980 (Robinson and Stokes (1955))) the following approximation was made for the driving force of crystal growth:

$$\Delta\mu/kT \approx \sigma = (c - c_{eq})/c_{eq}, \qquad (4)$$

where $\Delta\mu$ is the difference in chemical potential between solution and solid, c the actual concentration and c_{eq} the equilibrium concentration. Due to inaccuracies in the preparation of the solutions and measurements of the temperature the standard deviation of the supersaturation values was about 0.2%.

2.3. Ex situ observations

For the *ex situ* observations KBC crystals were used which were removed from the *in situ* growth cell and then quickly dried with a paper tissue. The benefit of this method is that the crystals are separated from a solution with a well defined supersaturation and, by drying, the shut off effect (van Enckevort 1984) is minimized. The resemblance of the image obtained by *ex situ* optical microscopy and the *in situ* image prior to specimen removal was used as a criterion for an 'artefact-free' separation of the crystal from its mother liquor.

For the *ex situ* observations Nomarski interference contrast and phase contrast optical microscopy were used (van Enckevort 1984). Both methods are capable of detecting step heights down to molecular-height with a lateral resolution down to approximately 0.5μm. For some of the *ex situ* observations also atomic force microscopy (AFM) was used. The microscope was a TopoMetrix TMX2010. Two scanners were used, namely a tripod scanner with a scan range of 150 μm and a tube scanner with a scan range of 7.5 μm. The tip was a diamond-like carbon rod of about 2.5 μm in length with a radius of curvature of about 10 nm. All the measurements were made at atmospheric conditions using constant force.

3. General features

3.1. Point group considerations

It has been reported that KBC crystals have a smooth, fast growing (001) face while the opposite, slowly growing ($00\bar{1}$) face is rough (Wagner and Follner 1981, Schubnikov 1911, 1931). This and the fact that sometimes faces (hkl) developed without the corresponding opposite faces ($\bar{h}\bar{k}\bar{l}$) led to a discussion about the space group to which the triclinic KBC belongs, P1 or $P\bar{1}$ (Schubnikov 1911, 1931, Stedehouder and Terpstra 1930). The structure determinations by X-ray diffraction seemed to have left no uncertainty with regard to the centrosymmetric space group $P\bar{1}$ (Podisko 1954, Brandon and Brown 1968, Kuzmin *et al.* 1969). The occurrence of left and right-handed crystals (Stedehouder and Terpstra 1930), which is discussed in terms of enantiomorphism (Podisko 1954, Podisko and Schubnikov 1955, Brandon and Brown 1968, Kuzmin *et al.* 1969, Sangwal *et al.* 1986), and the difference between the morphology of the (001) and the ($00\bar{1}$) faces, however, favoured P1. Twinning of the triclinic KBC with a metastable monoclinic β-phase was proposed to explain the observed hypomorphology (Kozlova *et al.* 1977, 1978).

In order to discriminate whether a {001} face is a (001) or a ($00\bar{1}$) face, some KBC crystals were cleaved along the {001} plane and subsequently placed in the *in situ* growth cell with its respective cleaved faces on top. In this manner we were able to see clear differences in growth features on these faces as shown in fig. 1. These pictures show for the ($00\bar{1}$) faces rectangular spirals and for the (001) faces half-rounded or six-fold sided spirals with a straight step parallel to the a-axis. On the ($00\bar{1}$) faces the spirals vanished after some time at a constant supersaturation of about 4% and a block-like structure appeared, but during the same growth experiments the spirals on the (001) faces did not vanish. Similar growth features have also been reported by Szurgot and Sangwal (1982) and Rak and Sangwal (1983) by *ex situ* surface topography of KBC. In defining a face as (001) and ($00\bar{1}$) we follow the convention given by the above authors who treated the crystals as non-centrosymmetric, though they did not mention this explicitly.

The hypomorphology of KBC cannot be explained in terms of twinning (Kozlova *et al.* 1977, 1978, Kozlova *et al.* 1979) since for the four cleavage experiments the cleavage plane would have to match exactly with the twinning plane. This is highly improbable. Judging from the topographs of Lefaucheux *et al.* (1984), X-ray diffraction topography does not reveal any image contrast due to a twinning of a monoclinic phase on a triclinic crystal. If present, such a contrast would readily be identifiable by the Lang method. In addition we were able to observe clear differences in growth features on the (010) and ($0\bar{1}0$) side faces (to be described elsewhere), which rules out the explanation in terms of twinning on the ($00\bar{1}$) face, since in that case only the {001} faces are different.

The above observation strongly indicates that KBC crystals are non-centrosymmetric and hence the point group is P1 instead of $P\bar{1}$. Therefore it seems that the space group determination by X-ray diffraction must be reconsidered. Further research on the pseudosymmetry of KBC will be carried out using ellipsometry, X-ray diffraction and sphere growth experiments.

By considering the shape of the spirals that appeared on the {001} faces we were always able to ensure that the (001) faces rather than the ($00\bar{1}$) faces were involved during the experiments described below. The actual structural differences between both opposite faces are not known, because the non-centrosymmetric properties of the KBC structure need

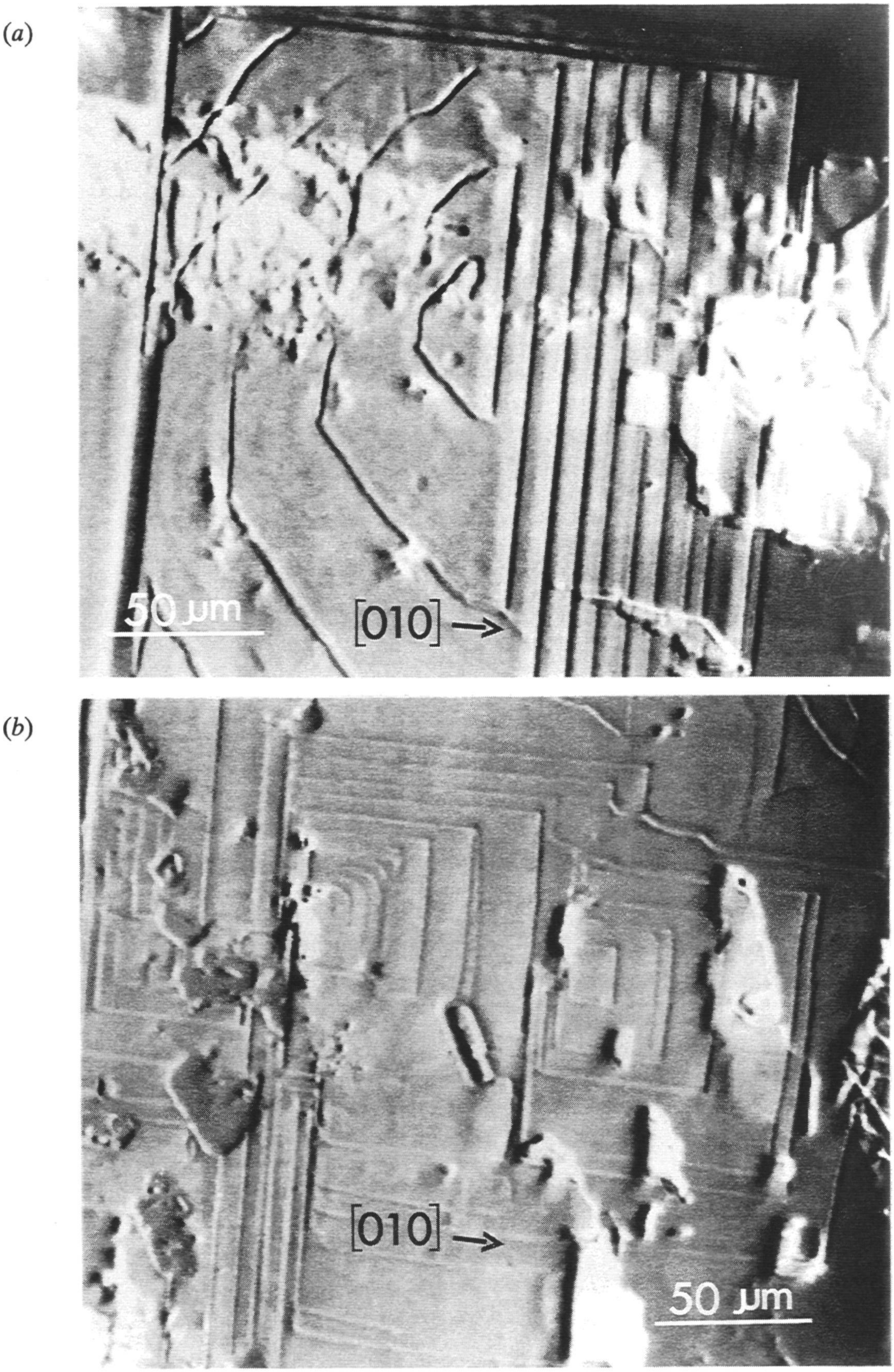

Fig. 1. Shapes of growth spirals on the {001} faces of KBC observed in situ shortly after insertion of the crystals into the growth cell, $\sigma = 3.1\%$. (*a*) (001) face; (*b*) $(00\bar{1})$ face. The scale bar is 100 μm.

to be determined. Moreover, when this asymmetry is known, then the absolute configuration of the structure needs to be established.

3.2. Surface micromorphology of the (001) faces

On the (001) faces of KBC crystals we observed two types of growth spirals and one type of etch pit. The general forms of these growth and etch patterns are sketched in fig. 2. In this figure it is also demonstrated that the straight [100] steps with step normal ≈ [010] are of the same type for both the growth spiral and the etch pit.

As can be seen from this figure the shape of the growth spiral at supersaturations exceeding 2.4%, is roughly the inverse of the etch pit shape. Both features are facetted with steps parallel to [100], [$\bar{1}$00], [$\bar{1}\bar{1}$0], [$\bar{1}$10], [010] and [0$\bar{1}$0] directions. However, the growth spirals at supersaturations below 2.4%, have a different, half-rounded, shape. This half-rounded shape was sometimes also observed for growth spirals at supersaturations exceeding 2.4%, but a growth spiral that has the inverse form of the etch pit, was never observed at supersaturations below 2.4%.

Because it is more convenient to measure on a straight step than on a lumpy, half rounded step, during the experiments described in this paper only the straight steps parallel to the **a**-axis with step normal ≈ [010] (see fig. 2) are considered. To allow for a comparison between dissolution and growth measurements, in the case of dissolution always the steps parallel to the **a**-axis of the etch pits were recorded that have the same approximately [010] step normal as the [100] steps for growth.

4. Advancement and blocking of [100] steps

Due to the fact that the straight [100] steps, as defined in section 3.2, do not have a significant curvature, and that during the *in situ* studies sometimes 'macro' kinks were seen moving quickly along the [100] steps, it can be concluded that the integration of growth units at the kink positions of these steps is rate limiting in step advancement. In addition, the density of kink sites at the step must be low. This follows from a theoretical study of step curvature far from a spiral centre as a function of surface/volume diffusion and kink density which will be published elsewhere (van Enckevort 1994).

4.1. Kinetics of the [100] steps

In fig. 3 the advancement velocity of the [100] steps on the (001) surface of KBC crystals in the [010] direction is given as a function of the supersaturation. In this graph the [100] steps have a positive velocity in the [010] direction for growth and a negative velocity for dissolution (that is, they advance in the opposite direction [0$\bar{1}$0]). In each growth experiment the advancement velocities were measured from high towards lower supersaturations in order to minimize time dependent effects.

In fig. 3 we distinguish a supersaturation region of etching, an interval without growth or etching, the so-called 'dead' region, and a region of growth. In contrast to growth, a blocking of steps for dissolution has, as far as we know, not yet been reported elsewhere. The

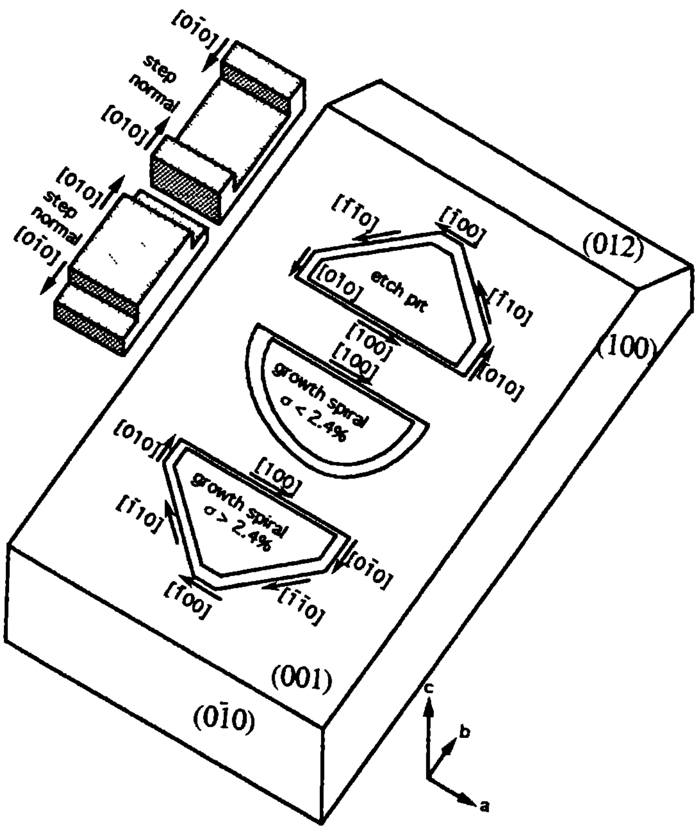

Fig. 2. Schematic representation of the spiral and etch pit morphologies on the (001) face of KBC.

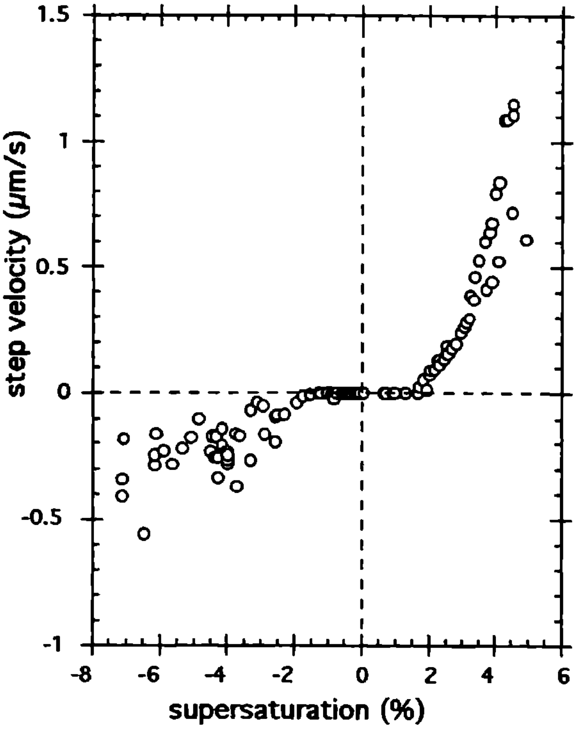

Fig. 3. Influence of the driving force of crystallization on step kinetics: [100] step velocity on the (001) face of KBC as a function of relative supersaturation σ.

'dead' region occurs for supersaturations between -1.6% and +1.7%. The value of -1.6% is, within the measuring error, equal to the critical supersaturation for growth. On the other hand for the etching region mass transport in the non-stirred cell hampers accurate measurements which gives a large scatter in the data. This also happens (although to a lesser amount) in the growth region above 3.4% supersaturation. The scatter of the data for $\sigma > 3.4\%$ is also due to the sharp increase of step velocity for increasing supersaturation. Therefore a small error in σ gives a large error in step velocity.

The occurrence and the width of the 'dead' region depends on the time that the surface is exposed to the solution at $\sigma < \sigma_{cr}$. This was shown by the following experiments:

i) If the supersaturation is rapidly increased starting from the etching region then growth occurs at supersaturations above 0% and below σ_{cr}. But after some period in this supersaturation interval the advancement of steps halts and growth only starts again when $\sigma > \sigma_{cr}$.

ii) If the supersaturation is decreased starting from the growth region then if the 'dead' region is entered and the supersaturation is subsequently increased above σ_{cr}, the steps remain blocked and the supersaturation needs to be further increased before growth is observed. The longer the period that the KBC crystal remains in the 'dead' region the more the supersaturation needs to exceed the σ_{cr} value before any growth occurs. The growth on a 'dead' surface starts at discrete areas from which a macrostep emerges that covers the blocked surface. In a similar way, as reported for {010} potassium hydrogen phthalate, on top of this fresh growth layer steps are mobile again (Jetten *et al.* 1983). The two above mentioned time dependent phenomena are visualized in fig. 4.

iii) Further evidence for this time dependence of step blocking was obtained by a cleavage experiment. A freshly cleaved crystal (therefore with a clean surface) showed, after placing in a KBC solution just above σ_{cr}, immediate growth on the entire (001) surface. On the other hand, on the as-grown surfaces of a non-cleaved crystal, growth starts, after placing in a KBC solution just above σ_{cr}, in only a few areas. Then by the propagation of macrosteps the old 'dead' surface is slowly covered with a 'new' surface on which spiral growth is observed. Freshly cleaved crystals also showed, after placing in the cell, immediate and, for a short period, continued growth at $\sigma \approx 1.0\%$ which is below the critical supersaturation. This critical supersaturation was determined, using other crystals, by decreasing the supersaturation from the growth region until no step advancement was observed anymore.

The above described time dependence of the blocking of steps indicates a slow adsorption of impurities on the crystal surface, where the degree of coverage increases with time. This explains the immediate growth on the cleaved surfaces, which are free from adsorbed impurities. On the as-grown surfaces impurities have been adsorbed and therefore growth only starts with difficulty.

Several attempts were made to ascertain the identity of the impurities that caused the above mentioned 'dead' zone. Small amounts of deliberately added Na_2S (an alien 2^- anion), $Na_2S_2O_3$ (a reducing agent), $CrCl_3$ (a 3^+ cation), Na_2SO_4 (an alien 2^- anion) and dipotassiumtartrate (a bidentate anion) showed no influence on the growth behaviour of KBC. The first two compounds caused some reduction of the bichromate ions in the solution and therefore some small precipitates appeared on the crystal surface. Similar particles on the crystal surface were also observed after the addition of AgCl and $BaCl_2$, because precipitates of $Ag_2Cr_2O_7$ and $BaCr_2O_7$ were formed, but no influence on the growth behaviour of KBC was seen. Upon the addition of $Pb(NO_3)_2$ (Pb^{2+} forms a precipitate with the bichromate ion) the shape of the growth spirals changed from half-rounded to triangular.

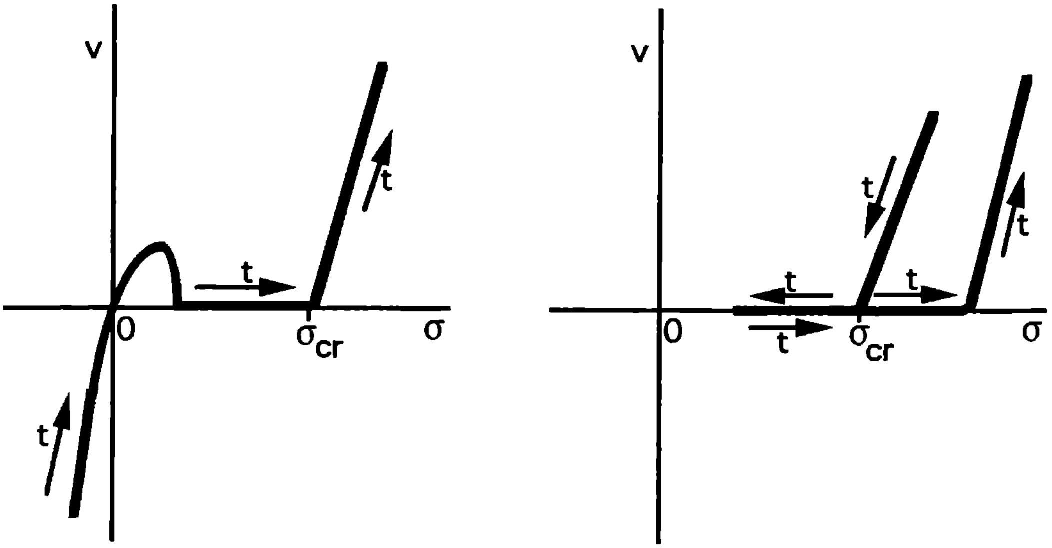

Fig. 4. Schematic representation showing the influence of time, *t*, on the blocking of [100] steps on the (001) face of KBC: (*a*) Fast rise in supersaturation starting from an undersaturated solution; (*b*) Lowering of supersaturation from growth region into the 'dead' region, followed by a rise back into the growth region. The time *t* is in the order of tens of minutes.

Besides the possibility that the impurities which cause the blocking are alien compounds in the p.a. quality KBC material, also intrinsic impurities (for example dimers, clusters, ions at wrong sites or decomposition products) may cause the above mentioned effect.

4.2. Surface topography

4.2.1. Optical microscopy

When a crystal is inserted into the growth cell and $\sigma > \sigma_{cr}$, then only after a while growth is observed at some few areas. The edges of these newly formed areas advance slowly over the old, impurity covered, crystal surface. However, the steps originating from the small spirals on these newly formed areas move much faster and accumulate at the edges of the new areas, which become higher. Islands of new crystal surface, bounded by macrosteps expand over the old blocked crystal surface until it is completely covered (fig. 5).

Because the old and polluted (001) crystal surface is covered by these increasingly higher macrosteps solution inclusions are easily formed via the step overhang mechanism, since growth units are more easily transported towards the upper part of the moving step than towards the lower part. A similar observation was also made for {010} KAP (Jetten *et al.* 1983). This formation of inclusions is undesirable because it troubles the observation of the crystal surface above it, due to internal light reflection. In order to minimize the formation of inclusions, the crystals are slightly etched by a wet paper tissue, to clean the surface, before they are inserted into the growth cell. This avoids excessive blocking of crystal growth.

Upon lowering the supersaturation from the growth region to the 'dead' region, the originally straight steps become irregular and lumpy in shape as is shown in fig. 6. This was also observed in the 'dead' region on KAP (Jetten *et al.* 1983).

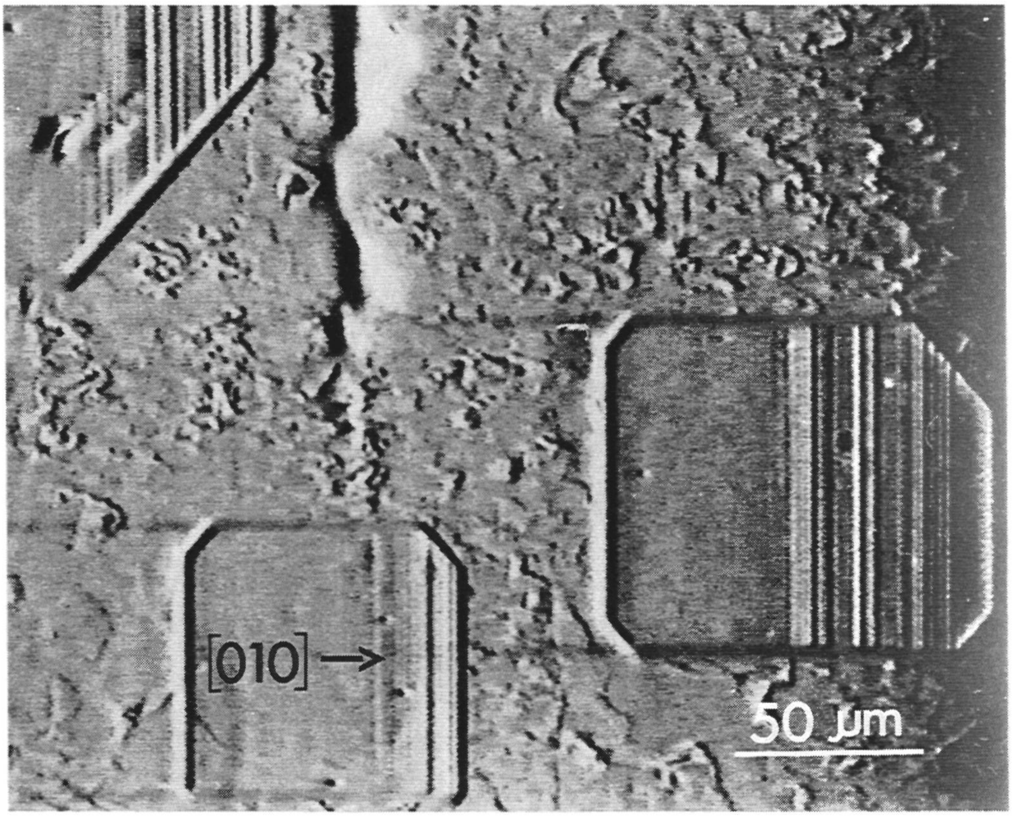

Fig. 5. (001) KBC surface showing 'islands' of new surface areas formed on the 'old' and blocked surface (in situ micrograph). The scale bar is 100 μm.

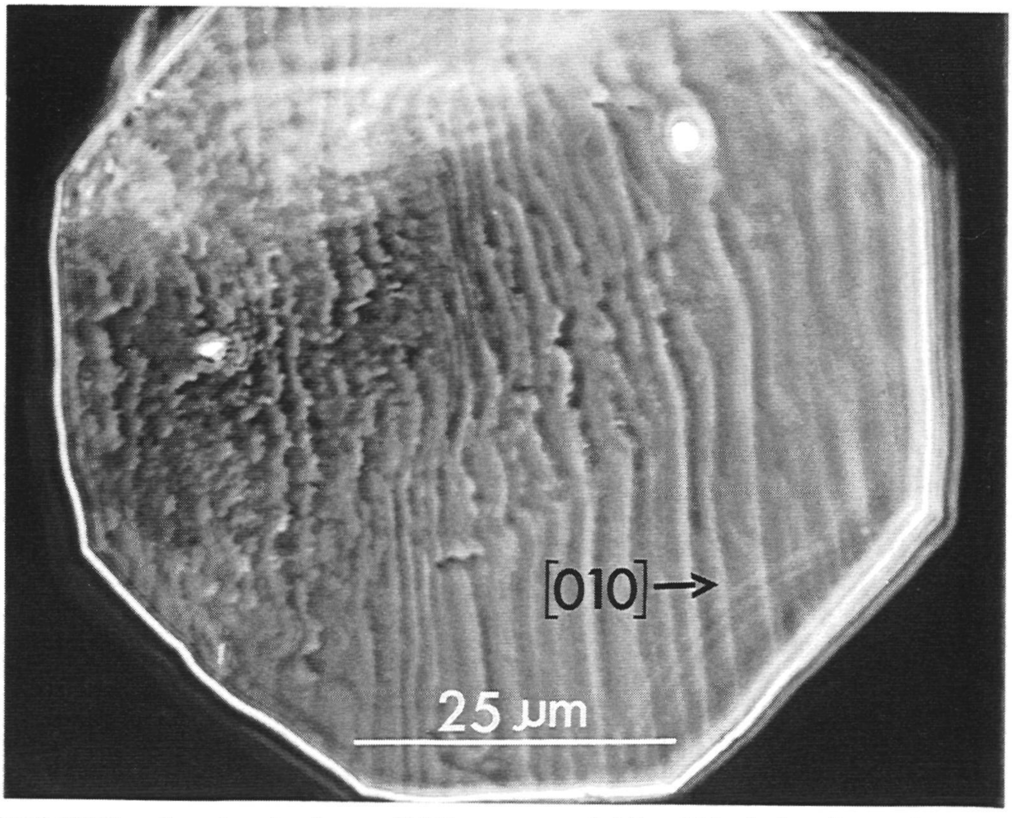

Fig. 6. (001) KBC surface showing lumpy [100] steps on an 'old' and blocked surface, prior to overgrowth, at $\sigma = 3.9\%$ (ex situ DICM). The scale bar is 25 μm.

4.2.2. Atomic force microscopy

On the (001) face of a KBC crystal, grown at a supersaturation much higher than σ_{cr}, [100] steps of single unit cell height (1.3 nm) well aligned parallel to the **a**-axis were observed by AFM (fig. 7(*a*)). In some cases these steps were a little higher (1.5, 2 or 3 times the unit cell height) or half the unit cell height. The steps can be lower than the unit cell height because the crystallographic unit cell of KBC consists of four formula units arranged in two somewhat different layers , d_{002}, of two formula units each. So the steps of half unit cell high are made up of only one of the two layers, d_{002}, in the unit cell.

Also the (001) face of a KBC crystal that stayed for some time in the 'dead' region (at a positive supersaturation) after growth at $\sigma > \sigma_{cr}$, was examined by AFM. fig. 7(*b*) shows that on the terraces between the steps that originate from screw dislocations, plateaus are present. The plateaus are half or one unit cell in height. This indicates that below σ_{cr}, where growth by the spiral mechanism is no longer possible, two-dimensional nucleation occurs between the halted steps. Therefore for $0 < \sigma < \sigma_{cr}$ growth on the [001] face of KBC crystals only proceeds by the slow two-dimensional nucleation process and therefore growth is extremely slow.

Figure 7(*c*) shows a close-up of a step of unit cell height on the crystal that stayed at $\sigma < \sigma_{cr}$. The steps are not straight, but show a cusped structure. The distance between the pinning points, which represent the impurity sites, in these steps is about 0.2 μm. In this AFM topograph (or at any further magnification) we were not able to detect the particles that acted as the pinning points, which should be present in these cusps. During the present studies the maximal lateral resolution obtained by AFM was a few nanometres. No atomic resolution was achieved on the (001) surfaces of the KBC crystals. From this it follows that the impurity particles are less than a few nanometres in diameter.

4.3. Density of pinning points

From simple thermodynamics it can be deduced that the radius r_c, of the two-dimensional critical nucleus is given by (Cabrera and Vermileya 1958):

$$r_c = \gamma_o / \Delta\mu', \qquad (5)$$

where γ_o is the edge free energy per unit step height (assuming that the edge free energy is the same as the surface energy γ_o) and $\Delta\mu'$ is the difference in the chemical potential per unit volume of solid. From relation (1) it follows that at the supersaturation in fig. 3 where growth just starts, the distance between the impurity stoppers should be twice the radius of the two-dimensional critical nucleus. For γ_o a typical value is 0.15 J/m^2, which was estimated from an empirical relationship between surface free energy and solubility of crystals (Sangwal 1987). From the density (Brandon and Brown 1968) and $\sigma_{cr} = 1.7\%$, a value of 3.8×10^5 J/m^3 for $\Delta\mu'$ is obtained. Using equation (5) it follows that the average distance between the impurity stoppers must be 0.8 μm. The measurements by AFM showed a distance of about 0.2 μm between the cusps in the steps, which is in the same order of magnitude as the calculated value. Since the crystal was grown at a supersaturation $\sigma < \sigma_{cr}$ and from the fact that here impurity adsorption is a time dependent phenomenon, it is expected that the surface density of adsorbed impurities is much larger than for a crystal grown at $\sigma = \sigma_{cr}$.

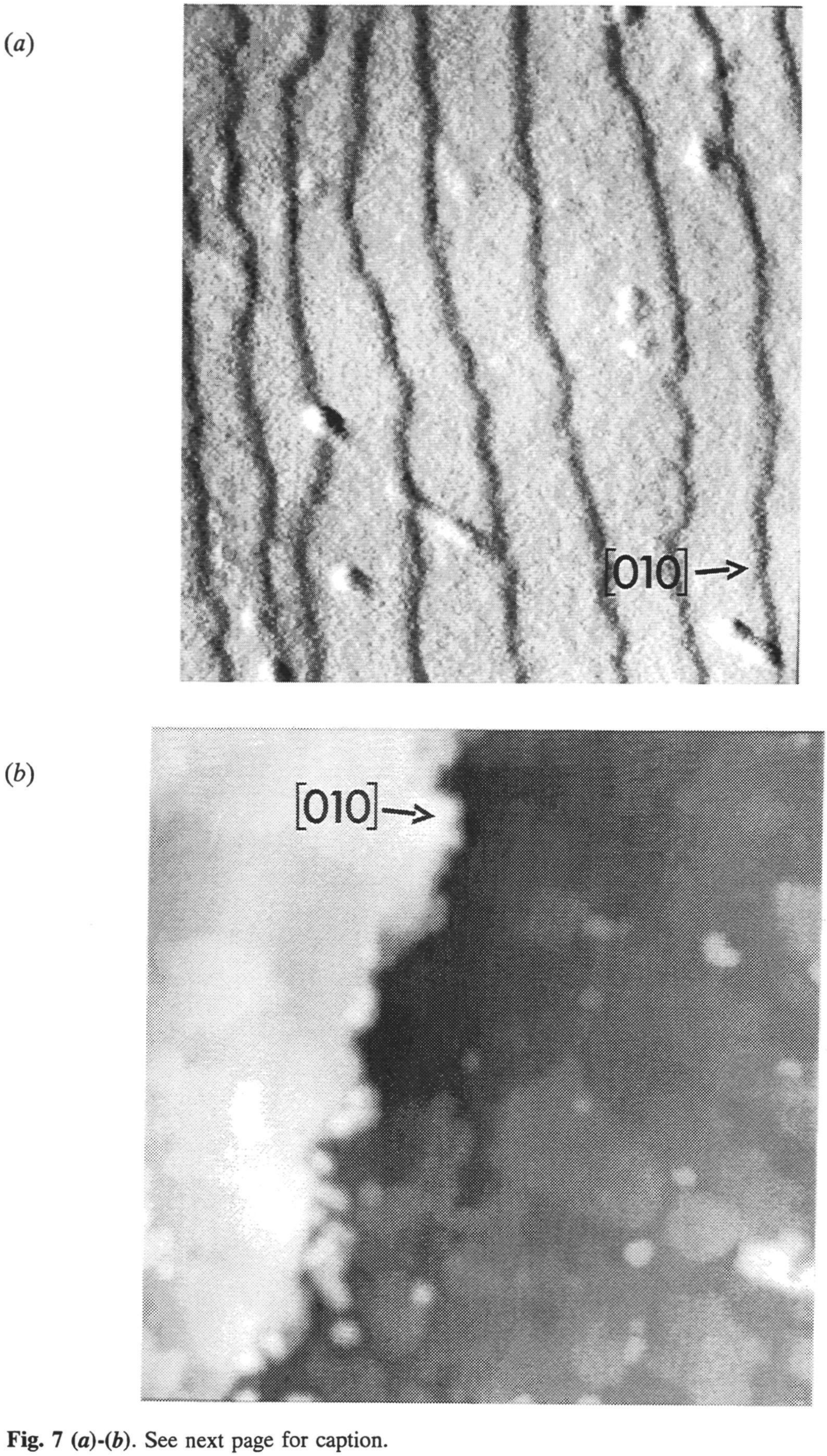

Fig. 7 (*a*)-(*b*). See next page for caption.

(*c*)

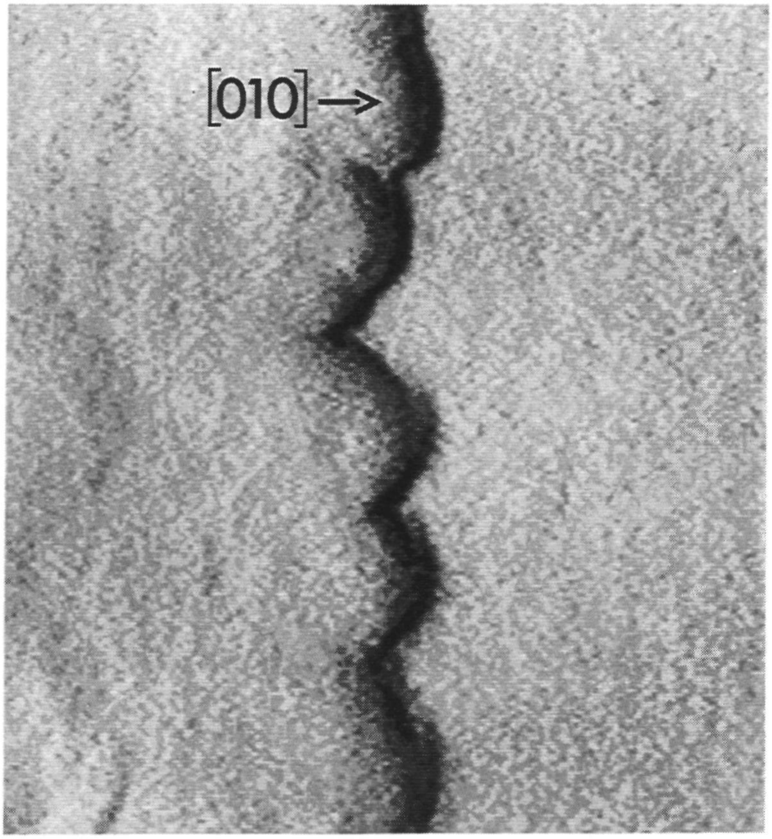

Fig. 7. (001) KBC surface as measured by atomic force microscopy: (*a*) [100] steps of unit cell height, $\sigma = 6.5\%$. The scan size is 2 μm × 2 μm; (*b*) plateaus of half and one unit cell in height between [100] steps, $\sigma = 1.0\%$. The scan size is 2.5 μm × 2.5 μm; (*c*) cusps in [100] steps, $\sigma = 1.0\%$. The scan size is 750 nm × 750 nm. (*a*) and (*c*) are shaded with a light source shining from the left-hand side.

4.4. Discussion

In fig. 8 the step velocities for $\sigma > \sigma_{cr}$ are fitted with equation (2) derived by Cabrera and Vermileya (1958), who used a model in which the moving steps form circular cusps between the impurity stoppers before the steps pass these impurities. Also a fit was made with equation (6) from Potapenko (1993). In this model the moving steps only form arches adjacent to the impurity stoppers and between these arches the steps are straight. Potapenko derived for the mean velocity of the, on average, rectilinear step:

$$v = b\sigma\{1+\frac{\ln(1-\zeta^{-2})}{2\zeta}+\frac{\arctan[(\zeta^2-1)^{-1/2}]}{\zeta(\zeta^2-1)^{1/2}}\}^{-1} \quad , \tag{6}$$

where $\zeta = \sigma/\sigma_{cr}$ and b is a normalization constant. Near the percolation threshold at $\sigma \rightarrow \sigma_{cr}$ he obtained the expression:

$$v \sim 2^{3/2}\pi^{-1}b(\sigma_{cr}(\sigma - \sigma_{cr}))^{1/2}, \tag{7}$$

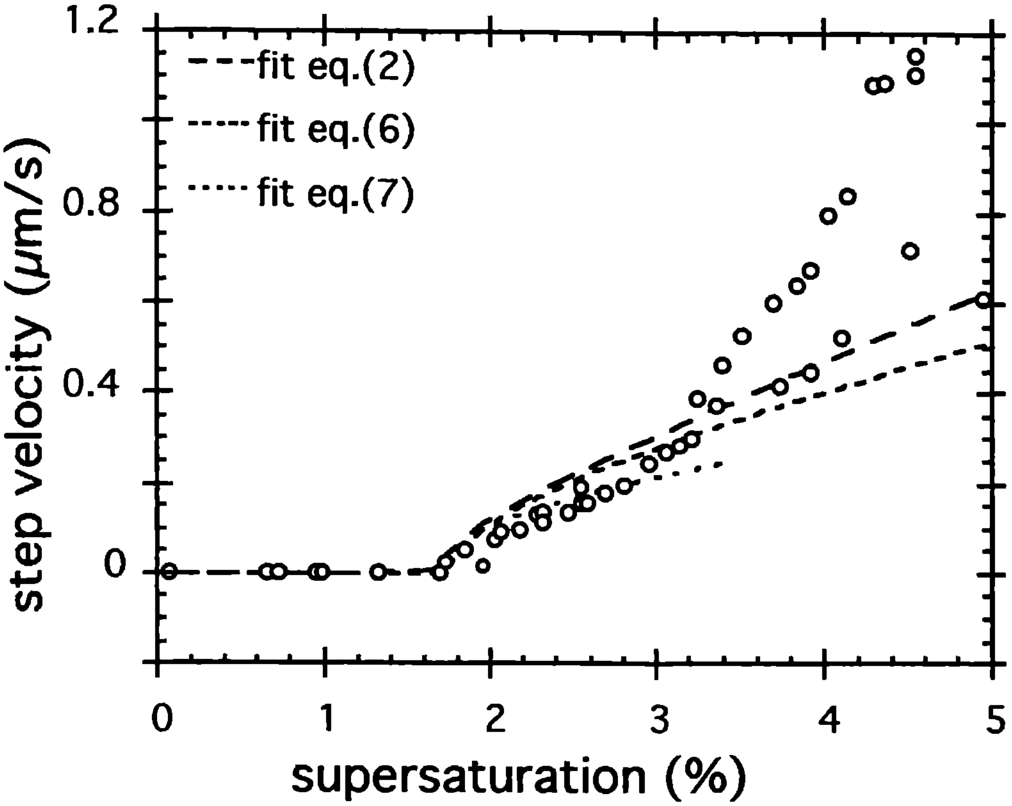

Fig. 8. Measured [100] step velocity, on the (001) face of KBC, as a function of the relative supersaturation σ. The experimental points are fitted with equations (2), (6) and (7).

which coincides with equation (2) in the vicinity of the critical supersaturation. We can see that for low step velocities the fits with (2), (6) and (7) are fairly good, except that in contrast to the experiments the theoretical curves show a second order derivative $d^2v/d\sigma^2 < 0$. At higher supersaturations the fitting curves give step velocities far too low in comparison with the experimental data. This is rather unexpected because in a non-stirred system mass transport should tend to make the observed step velocities lower than those predicted by the models. On the other hand the supply of impurities is also reduced. It is expected that at higher supersaturations the step velocities would asymptotically go to the velocities in the absence of any impurities, that is, a linear $v(\sigma)$ function going through the origin, but this is not observed. In the above mentioned models for step advancement the time dependence of impurity adsorption is not considered. If time dependent impurity adsorption is taken into account the situation is somewhat different and could perhaps explain the positive second order derivative of the plot in fig. 3.

5. Bunching of steps

5.1. Observations

For supersaturations $1.7\% < \sigma < 6.1\%$ the advancement of the [100] steps originating from small spirals is accompanied by the development of macrostep patterns. Close to the centre of the spirals the steps are low and closely spaced and, therefore often not individually

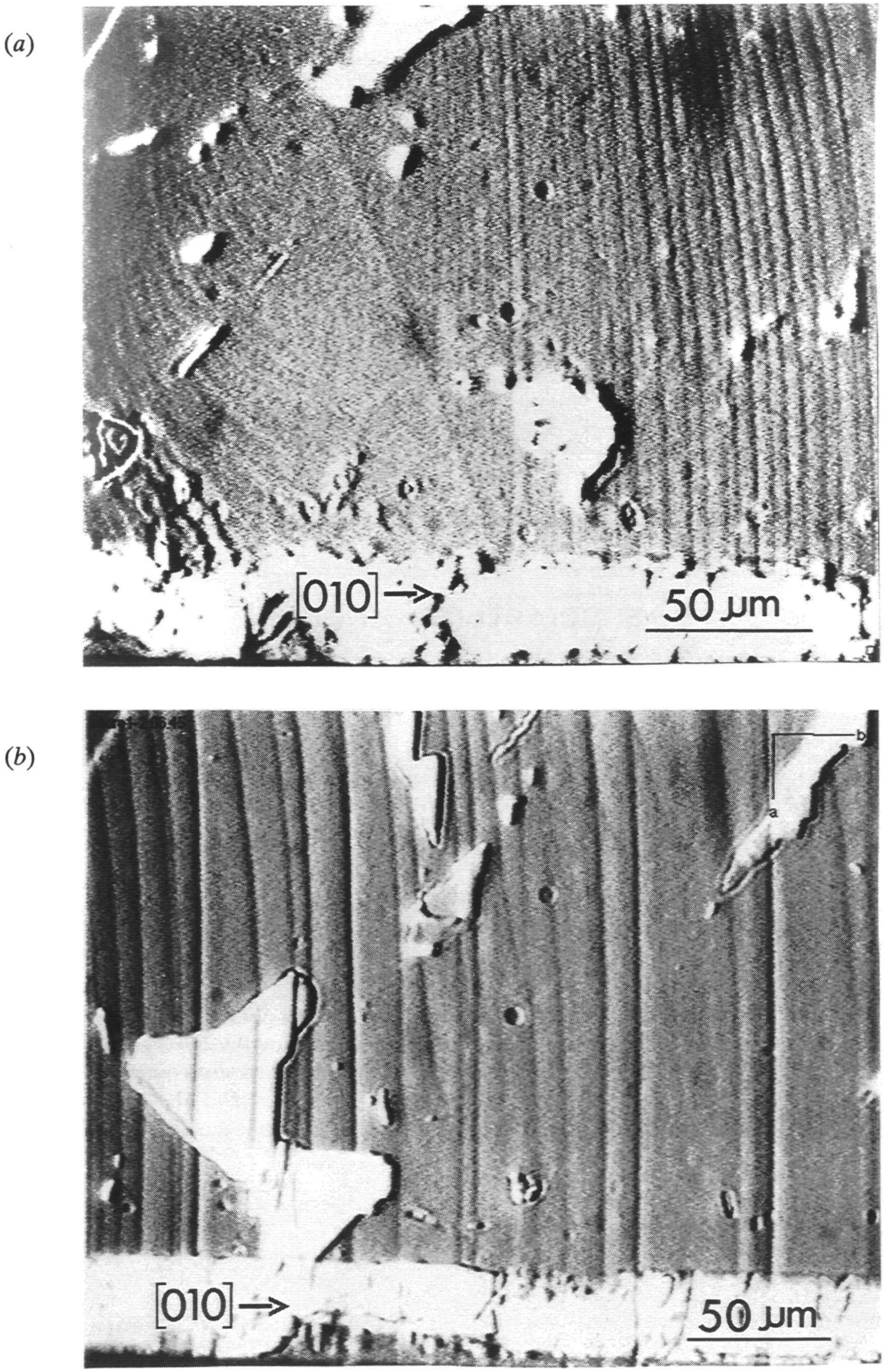

Fig. 9 (*a*)-(*b*). See next page for caption.

(*c*)

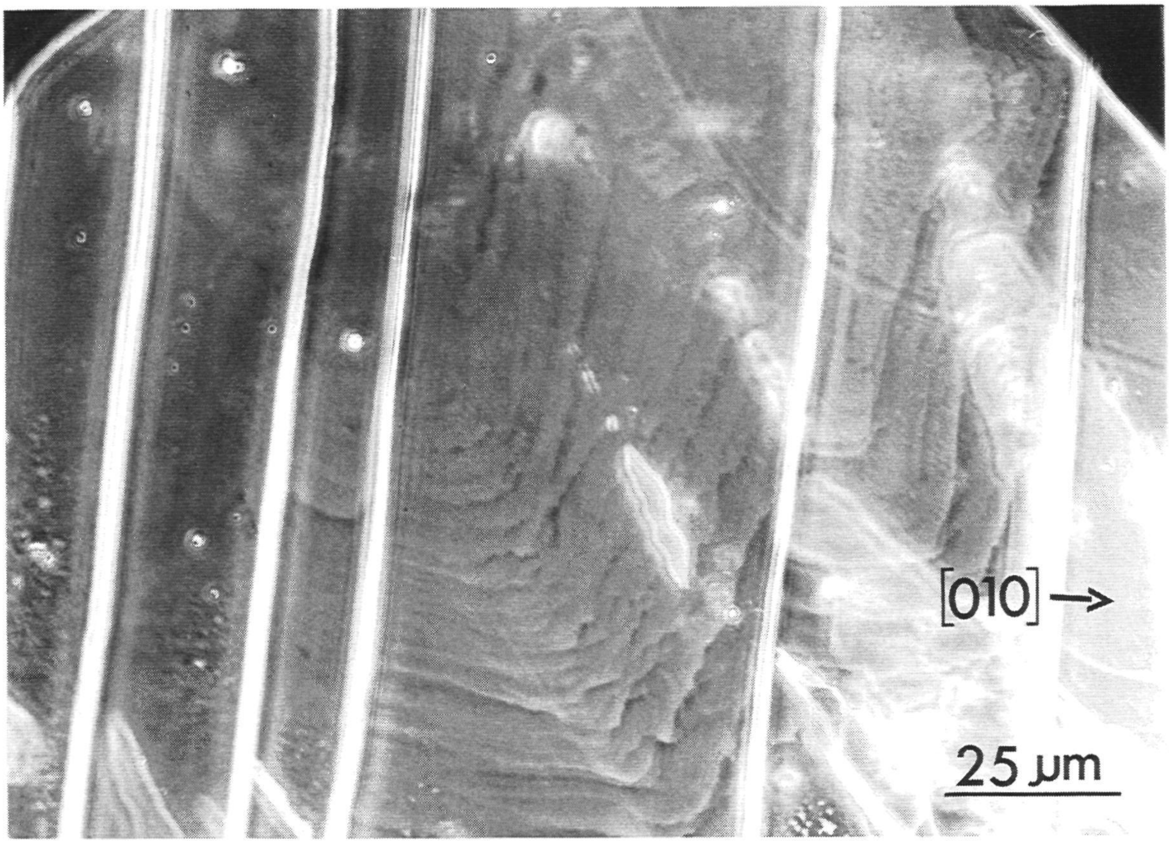

Fig. 9. In situ micrographs showing an increased spacing between adjacent [100] steps on the KBC (001) surface for increasing distances from the spiral centre: (*a*) spiral centre, $\sigma = 4.9\%$; (*b*) approximately 600 μm away from the spiral centre of (*a*) at the same supersaturation; The scale bar is 100 μm. (*c*) Spiral hillock emitting low steps, between widely spaced [100] macrosteps which are far away from their growth centre (ex situ DICM); The scale bar is 50 μm.

observable by optical microscopy. For increasing distances from the growth centre the height and the mutual separation of the macrosteps increase. Figures 9(*a*) and 9(*b*) show typical examples of steps close to the spiral centre and far away respectively. The development of macrosteps takes place over distances in the order of 1 mm, where they reach heights exceeding hundreds of nanometres.

The advancement velocities of the low, near the spiral centre, and high, far away from the centre, [100] steps do not differ very much: the highest steps move at about 0.9 to 0.95 times the velocity of the lowest steps. This is due to an increased time of impurity adsorption on the wide terraces in front of these higher steps. For the extremely high steps (> several μm) the step velocity is much lower, but their ledges, in fact, are facets.

As can be seen in fig. 9(*c*) in a few cases small spirals are observed between high and widely spaced macrosteps. These small spirals constantly renew the crystal surface, so less impurities are adsorbed on the surface when the high steps move over these areas. Therefore the macrostep velocity must be higher on these renewed terraces than on terraces free from small spirals.

A means of measuring bunching is to plot the spacing between steps versus the distance of these steps from the spiral centre. In figs. 10(*a*) and 10(*b*) two of these plots are shown for different values of the supersaturation. The data points were obtained from recor-

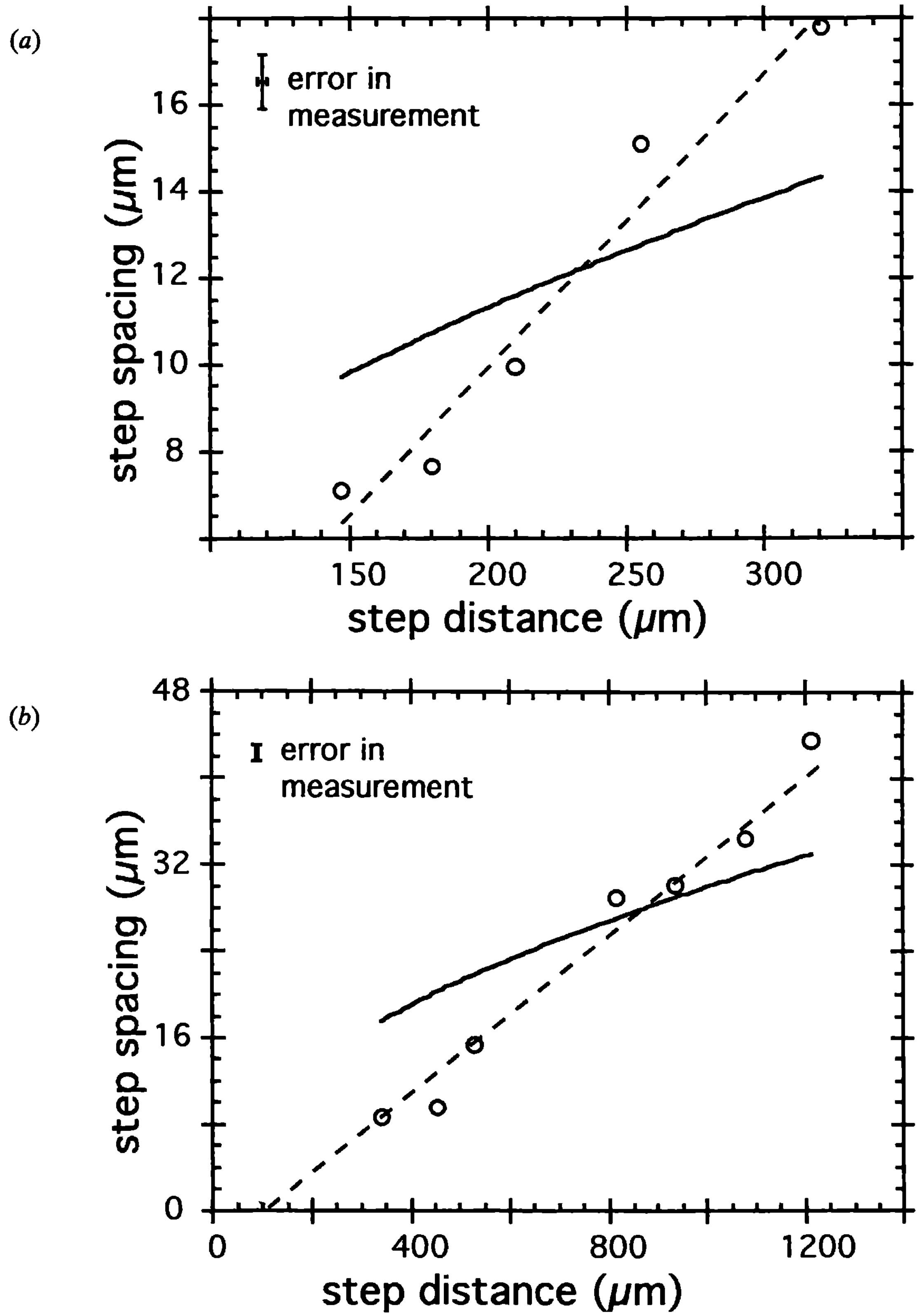

Fig. 10. Plots showing the linear relation between the distance, vt, from the spiral centre and the spacing, $v\tau$, between the [100] steps on the KBC (001) surface. (*a*) $\sigma = 3.2\%$; (*b*) $\sigma = 5.8\%$. The experimental points are fitted with a linear, $v\tau = avt + b$, and a square root, $v\tau = a(vt)^{1/2}$, dependence, which are indicated by the dashed and the solid lines respectively.

ded *in situ* experiments and were measured directly from the monitor screen. In all cases a linear dependence, roughly going through the origin, between the step spacing and the distance from the spiral centre (correlation coefficient $R \approx 0.95$), was found. So the step spacing is proportional to the distance from the spiral centre.

As a measure for the order of bunching, the slope of the linear relation as given in fig. 10 is chosen. If this value increases the order of bunching increases, that is, the bunching starts closer to the spiral centre. If this value equals zero, then no bunching is observed. In fig. 11 the slope values are plotted as a function of the supersaturation. From these data it can be derived that if $\sigma \approx \sigma_{cr}$, then only little macrostep formation occurs. In a large area, for σ up to 6.1%, a large, but seemingly independent of supersaturation, order of bunching is observed. In this supersaturation regime the order parameter shows a considerable scattering. This is due to differences in the configuration of the dislocation bundle at the centre of the different growth spirals recorded, rather than to errors in the measurement of step velocities and supersaturations. For $\sigma > 6.1\%$ the occurrence of bunching ceases. This can readily be seen by slowly increasing the supersaturation while observing the bunching patterns *in situ*. At 6.1% and above newly generated steps do not show any visible bunching and very smooth hillocks with very low steps develop. This easily detectable phenomenon allows for an accurate determination of the σ-value of this transition. The transition from bunching to non-bunching is fairly sharp, but it is not clear whether this is an abrupt 'phase transition', such as is suggested from chaos theory models (Kardel and Weeks 1993).

5.2. Discussion

The observed proportionality of the spacing between steps with the distance from the spiral centre and hence with time (the step velocity is within 10% constant for all distances from the spiral centre) is unexpected. The current models for step bunching give different relations. The kinematic wave theory formulated by Chernov (1961), gives a step spacing, aside from a small constant, proportional to $t^{1/2}$. The time dependent impurity adsorption model by van der Eerden and Müller-Krumbhaar (1986) gives a step spacing as a function of time, according to:

$$\lambda\tau = \theta \ln (t/t_0) \text{ for } t \gg t_0, \qquad (8)$$

where $\lambda = \kappa/\bar{n}$. Here $\bar{n}$ is the equilibrium density of adsorbed impurities, κ the adsorption flux (number of impurities arriving per unit time on a unit area), τ the time interval between the passage of two successive steps along a fixed position at the crystal surface, θ a normalization factor, t the time since the considered step was emitted from the spiral centre and t_0 the time after which bunching sets in for the steps. For the present spiral hillocks with almost constant step velocities the step spacing ($\propto v\tau$) is proportional to τ and the distance from the spiral centre ($\propto vt$) is proportional to t.

For 14 sets of spirals and supersaturations the step spacing versus the distance from the spiral centre has been fitted with the linear, the $t^{1/2}$ and the logarithmic relationships. The linear fits gave the best fitting-results, with a correlation coefficient $R \approx 0.95$. These curves go closely through the origin (see fig. 10). An attempt to fit with a $t^{1/2}$ relation gave poor results, so this model must be disregarded. Using relation (8), by fitting the step spacing with $\ln(t)$ gave somewhat poorer results ($R \approx 0.85$) than the proportional relation.

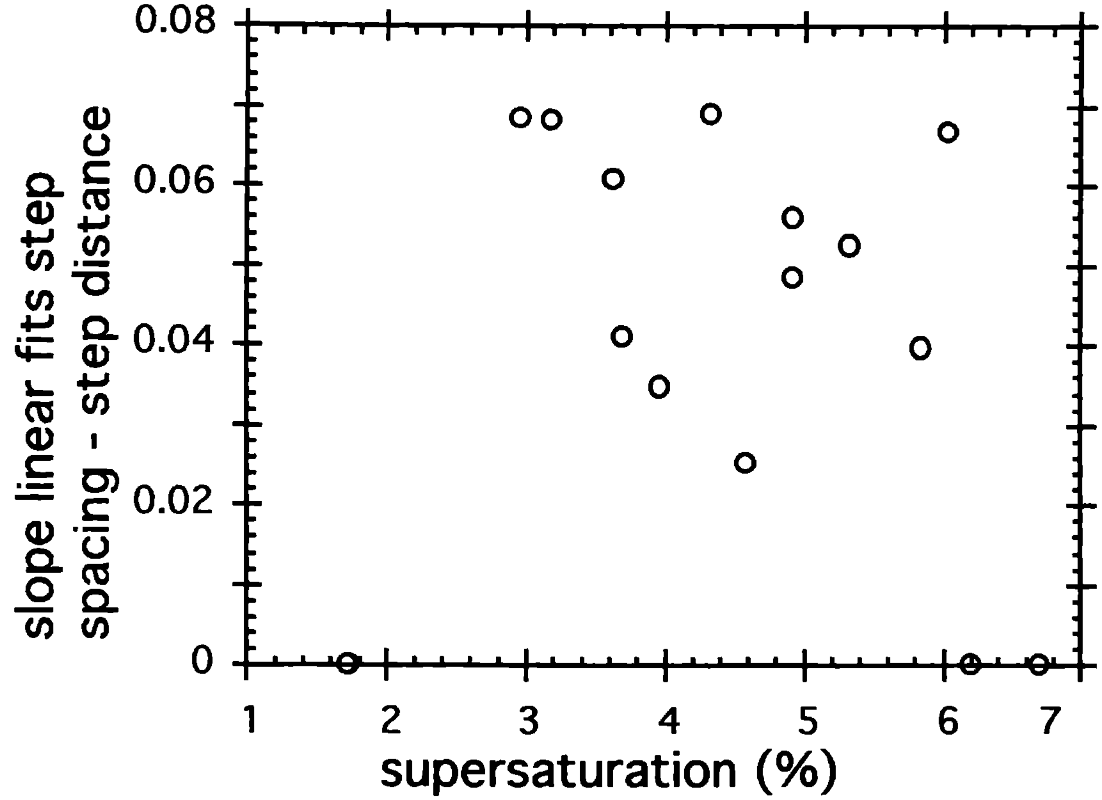

Fig. 11. The slopes of the linear fits in plots of the type as given in fig. 10, which give a measure for the tendency of bunching, as a function of the relative supersaturation σ.

The interesting observation that at $\sigma \approx \sigma_{cr}$ almost no bunching of steps occurs is in agreement with the model by van der Eerden and Müller-Krumbhaar (1986), in which for smaller supersaturations the time constant for bunch-formation increases according to:

$$\lambda t_0 \sim \exp[\{0.7 \ln(r_c \bar{n})\}\, d(t = 0)\lambda/v_\infty], \tag{9}$$

where $d(t = 0)$ is the initial spacing near the spiral centre of the almost equidistant monomolecular step sequence. Here, one must realise that r_c and $d(t = 0)$ are inversely proportional to the driving force $\Delta\mu$ and v_∞ is proportional to $\Delta\mu$. In this case a more or less steady state equilibrium impurity concentration is attained during the long time passage of two adjacent, slowly advancing, steps. In fact we have a linear *R-p* curve, type III, as described by van der Putte *et al.* (1978), where the step velocity does not depend on the spacing between steps. Using the kinematic wave theory it can be shown that in this case no bunching should occur, which agrees with the observations.

The present investigation of bunching phenomena on (001) KBC shows that the models for bunching developed so far do not accurately describe the results obtained. The reasons for the proportional relation between the step spacing and distance from the growth centre as well as the sudden termination of step bunching at $\sigma \approx \sigma_{cr}$ and $\sigma > 6.1\%$, are not clear. Probably the one-dimensional model by van der Eerden and Müller-Krumbhaar is too simple to describe the actual process in a precise, quantitative manner. Therefore more detailed models are needed. At this moment, Monte Carlo simulations of two dimensional step patterns in the presence of impurities are being carried out in our group.

6. Conclusions

In this article, experimental data obtained by *in situ* and *ex situ* optical microscopy and *ex situ* AFM measurements on the (001) face of KBC are presented.

A general view of the micromorphology was given and data on the blocking and velocities of the [100] steps were presented as a function of the supersaturation. It was shown that the shapes of the growth spirals on the (001) and $(00\bar{1})$ faces are clearly different. This proves that KBC crystals crystallize in a non-centrosymmetric space group. For both growth and etching a 'dead' zone was observed, with a critical supersaturation $|\sigma_{cr}|$ for blocking of 1.7%. The phenomena related to the blocking of growth steps in the supersaturation interval from $-\sigma_{cr}$ to slightly above σ_{cr} depended strongly on the previous history of the (001) growth face. This indicates that the adsorption of the impurities causing the 'dead' zone is not immediate but proceeds relatively slowly.

By AFM, [100] steps half, one or a few unit cells high were observed. For crystals grown in the 'dead' zone the steps showed cusps. The observations confirm the model by Cabrera and Vermileya (1958), but the identity of the impurities remains unclear.

For supersaturations $1.7\% < \sigma < 6.1\%$, the lower [100] steps, originating from small spirals, accumulated at some distance from the growth centres and formed bunching and macrostep patterns. In contrast to the model by van der Eerden and Müller-Krumbhaar (1986), which predicts a logarithmic dependence, the spacing between the (macro)steps was found to be proportional with the distance from the spiral centre. The order of bunching, defined as the slope of each linear plot of the step spacing versus the step distance, had for several supersaturations roughly the same value, except for $\sigma \approx \sigma_{cr}$ and for $\sigma > 6.1\%$, where bunching was strongly reduced or vanished almost completely, respectively.

7. Acknowledgements

The authors acknowledge Prof Dr P. Bennema and Prof Dr J. P. van der Eerden for their stimulating interest in the present work. One of us, M. S. Couto, wishes to thank CAPES (Coordenação de Aperfeiçoamento de Pessoal de Nível Superior), Brazil, for a scholarship making this research possible.

8. References

Brandon, J. K., Brown, I. D., 1968, Can. J. Chem., **46**, 933.

Cabrera, N., Vermileya, D. A., 1958, *Growth and Perfection of Crystals* (New York: Wiley), p. 393.

Chernov, A. A., 1961, Sov. Phys. Usp., **4**, 116.

Chernov, A. A., Rashkovich, L. N., 1987, J. Cryst. Growth, **84**, 389.

Chernov, A. A., Coriell, S. R., Murray, B. T., 1993, J. Cryst. Growth, **132**, 405.

Durbin, S. D., Feher, G., 1986, J. Cryst. Growth, **76**, 583.

Hottenhuis, M. H. J., Lucasius, C. B., 1988, J. Cryst. Growth, **91**, 623.

Jetten, L. A. M. J., van der Hoek, B., van Enckevort, W. J. P., 1983, J. Cryst. Growth, **62**, 603.

Kardel, D. K., Weeks, J. D., 1993, Physica D, **66**, 78.

Kozlova, O. G., Geraskina, G. P., Belov, N. V., 1977, Sov. Phys. Dokl., **22**, 462.

Kozlova, O. G., Geraskina, G. P., Belov, N. V., 1978, Sov. Phys. Dokl., **23**, 300.

Kozlova, O. G., Kharitonov, Yu A., Belov, N. V., 1979, Sov. Phys. Dokl., **24**, 509.

Kuzmin, E. A., Iljukhin, V. V., Kharitonov, Yu A., Belov, N. V., 1969 Kristall Techn., **4**, 441.

Lefaucheux, L., Robert, M. C., Sangwal, K., 1984, J. Cryst. Growth, **67**, 541.

Onuma, K., Tsukamoto, K., Sunagawa, I., 1992, Microgravity Sci. Technol., **2**, 62.

Podisko, V. S., 1954, Tr. Inst. Krist. Akad. Nauk SSR, **9**, 327.

Podisko, V. S., Schubnikov, A. V., 1955, Tr. Inst. Krist. Akad. Nauk SSR, **11**, 212.

Potapenko, S. Yu, 1993, J. Cryst. Growth, **133**, 147.

Rak, M., Sangwal, K., 1983, J. Cryst. Growth, **65**, 494.

Robinson, R. A., Stokes, R. H., 1955, *Electrolytic Solutions* (London: Butterworths), p. 490.

Sangwal, K., Szurgot, M., Szczepaniak, M., 1986, J. Cryst. Growth, **79**, 185.

Sangwal, K., 1987, *Etching of crystals* (Amsterdam: North-Holland), p. 209.

Schubnikov, A., 1911, Z. Krist., **50**, 19.

Schubnikov, A., 1931, Z. Krist., **76**, 469.

Stedehouder, P. L., Terpstra, P., 1930, Physica, **10**, 113.

Szewczyk, J., Sokołowski, W., Sangwal, K., 1985, J. Chem. Eng. Data, **30**, 243.

Szurgot, M., Sangwal, K., 1982, Cryst. Res. Technol., **17**, 1337.

Tsukamoto, K., Sunagawa, I., 1985, J. Cryst. Growth, **71**, 183.

van der Eerden, J. P., Müller-Krumbhaar, H., 1986, Electrochim. Acta, **15**, 1007.

van der Putte, P., van Enckevort, W. J. P., Giling, L. J., Bloem, J., 1978, J. Cryst. Growth, **43**, 659.

van Enckevort, W. J. P., Jetten, L. A. M. J., 1982, J. Cryst. Growth, **60**, 275.

van Enckevort, W. J. P., 1984, Prog. Cryst. Growth Charact., **9**, 1.

van Enckevort, W. J. P., 1994, to be published.

Vlachos, D. G., Jensen, K. F., 1992, Surf. Sci., **262**, 359.

Wagner, W., Follner, H., 1981, J. Cryst. Growth, **54**, 541.

Chapter 9

Scanning tunnelling microscopy studies on n-alkane molecules adsorbed on graphite[1]

M. S. Couto, X. Y. Liu, H. Meekes, and P. Bennema

Department of Solid State Chemistry, University of Nijmegen, Faculty of Science, Toernooiveld, 6525 ED, Nijmegen, The Netherlands

Abstract

The adsorption of n-alkanes on graphite has been studied by scanning tunnelling microscopy. These molecules can form very well ordered layers on the graphite surface. The results suggest that a transition from an ordered to a disordered state of the molecules occurs as a function of temperature. A model for the structure of the adsorbed layer and a possible explanation for the temperature effects are given.

---

[1] *Journal of Applied Physics 75 (1994) 627*

1. Introduction

Studies of odd-numbered n-alkane crystals in n-hexane solution have shown a first order roughening transition occurring at the {110} faces of these crystals (Liu and Bennema 1992). It was suggested that the unusual first order character of this transition is due to changes in the motional state of the crystal molecules at the interface crystal-solution. Above a critical temperature the surface molecules of the crystal start to rotate around their molecular axes. This makes the energy difference between the surface molecules of the crystal and the solution molecules very small, which causes the collapse of the edge free energy, leading to the roughening of the crystal faces.

Recently there have been reports on scanning tunnelling microscopy (STM) studies of n-alkane molecules adsorbed on the surface of highly oriented pyrolytic graphite (HOPG) (McGonigal *et al.* 1990, McGonigal *et al.* 1991, Rabe and Buchholz 1991a, 1991b), showing that these molecules can form ordered arrays with the molecules parallel to the surface of the HOPG. In this letter we report on the use of the technique of STM to give some evidence of the effect of temperature on n-alkanes adsorbed on a HOPG surface.

2. Experimental details

The systems studied were the n-alkanes ranging from 17 to 27 carbon atoms. The samples were prepared taking advantage of the fact that in a solution of different n-alkanes in contact with graphite, the n-alkane with higher number of carbon atoms adsorb preferentially to the other ones (Groszek 1970). The solution consisted of the n-alkane of interest dissolved in n-dodecane as a saturated solution at room temperature. A small amount of this solution was then applied to a freshly cleaved HOPG surface. The measurements were realized at a temperature of 21°C unless specified differently.

The STM was home-built and is similar to that described by Hottenhuis *et al.* (1988). For our experiments the electrochemical cell on the lower part of the STM was replaced by a small teflon cell containing the HOPG and the solution. The tips used were mechanically sharpened 90% Pt–10% Ir wires with a diameter of 0.5 mm. The tunnelling voltage was 0.5 V (sample positive) and the tunnelling current was 200 pA. Lower voltages resulted in a decrease of resolution for the molecules, bringing the HOPG atoms into resolution. Higher voltages resulted in an increase in noise level. All the images were taken in constant current mode. Normally several attempts were necessary before we could observe the ordered layers. This can be explained by the fact that the ordered n-alkane molecules do not cover the HOPG surface entirely but form islands separated by a distance larger than the scan range of our STM (1 μm), making it difficult to locate them. With our STM it was impossible to find the exact location of the C atoms with respect to the graphite lattice, due to drift. It nevertheless was relatively easy to observe that the molecules are aligned along the crystallographic axes of the graphite unit cell.

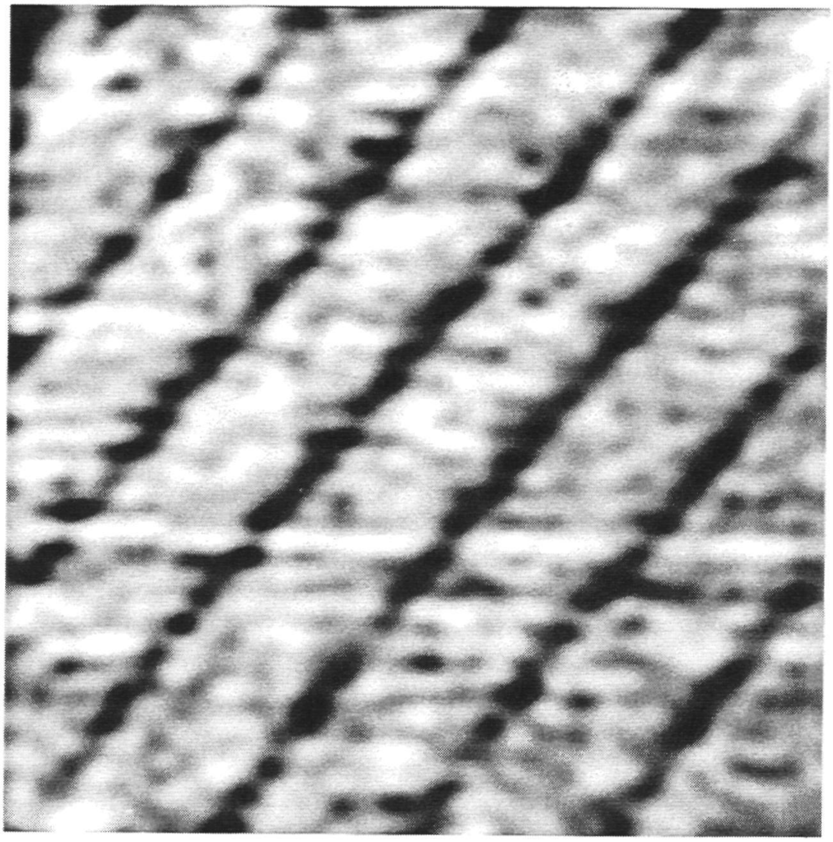

Fig. 1. STM atmospheric image of n-$C_{19}H_{40}$ molecules adsorbed on HOPG. The molecules are adsorbed parallel to the HOPG surface. The scan area is 12.5 nm × 12.4 nm.

3. Results and discussion

For the solutions of n-alkanes ranging from 17 to 22 carbon atoms we could not observe any ordered layer on the HOPG surface. An explanation for this is that at the temperature of 21°C the molecules are too mobile on the surface. This either makes an ordering of the molecules impossible or makes it easier for the tip to push the molecules away during the scan, disturbing the ordered layer.

Experiments with n-$C_{19}H_{40}$, however, showed that after leaving the solution in contact with the HOPG for one month an ordered layer could be imaged after removing the solution and cleaving the HOPG. During this time some n-$C_{19}H_{40}$ could diffuse in between the graphite layers and adsorb in some areas. Figure 1 shows a STM image obtained for this material. The horizontal lines running across the rows are not the alkane molecules, they are just noise occurred during the scan. High resolution scans on this material show that the molecules are very well ordered in rows, with their long axis perpendicular to the direction of these rows and parallel to the HOPG surface. These ordered layers extended without defects for more than 50 nm × 50 nm. The measured distance between two molecules in a row is 0.42 nm and the distance between two rows is 2.24 nm.

Figure 2 shows a STM image of adsorbed n-$C_{23}H_{48}$ obtained in solution. This n-alkane presents the same degree of ordering as observed for n-$C_{19}H_{40}$. It can be seen that across the rows the molecules are shifted vertically by half of the distance between two molecules in a row. The distance between two molecules is 0.40 nm and the width of the rows is 2.57 nm.

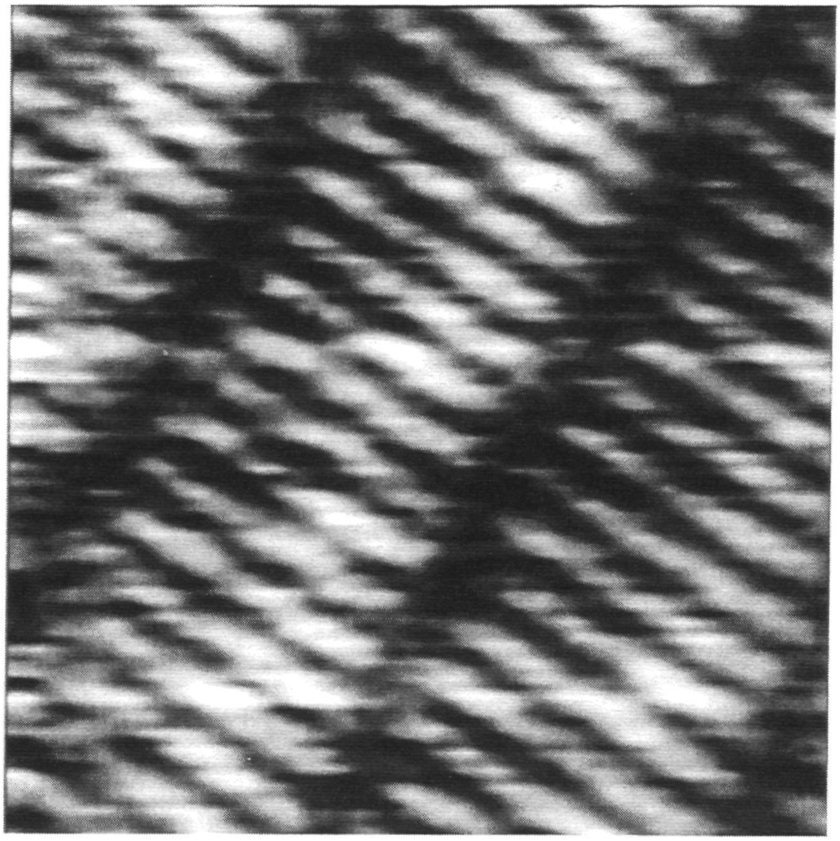

Fig. 2. STM solution image of n-$C_{23}H_{48}$ molecules. The shift of the molecules across the rows can be seen. The scan area is 6.3 nm × 5.5 nm.

Figure 3 shows another region of the same sample were we can see the boundary between an ordered region and a region were no molecular ordering could be imaged. For this region either there are no adsorbed molecules or the molecules are adsorbed perpendicular to the surface, making the imaging process more difficult. The horizontal lines crossing the rows of molecules on the ordered region are just noise occurred during the scan.

n-$C_{27}H_{56}$ also showed the same ordering as observed for the materials above. For this material it was found that in a region of a step on the HOPG surface the direction of the rows of molecules on the lower terrace is rotated 120° in relation to the direction of the rows on the upper terrace. The measured molecular distance is 0.38 nm and the width of the rows is 3.27 nm. Figure 4 shows a high magnification of some n-$C_{27}H_{56}$ molecules. For this material it was possible to achieve resolution of the individual CH_2 groups.

Figure 5 shows two proposed models for the adsorbed layer. In fig. 5(*a*) the plane of the carbon atoms in the molecule is perpendicular to the HOPG surface and in fig. 5(*b*) it is parallel. Both structures are different from the crystallographic planes of the bulk of the n-alkane crystal. For the molecules adsorbed in the way shown in fig. 5(*a*) the higher CH_2 groups will be imaged differently and the molecule will appear as a series of clearest dots which number is half of that of the carbon atoms in the molecule. For both orientations the molecules should be compressed by a small amount along their long axis to let the length of 0.251 nm of the C/C\C zigzag match with the length of 0.246 nm between the centre of two adjacent hexagons on the HOPG surface (Groszek 1970). For n-$C_{23}H_{48}$ all the measurements showed the molecules oriented in the way shown in fig. 5(*a*). This can be seen on the video

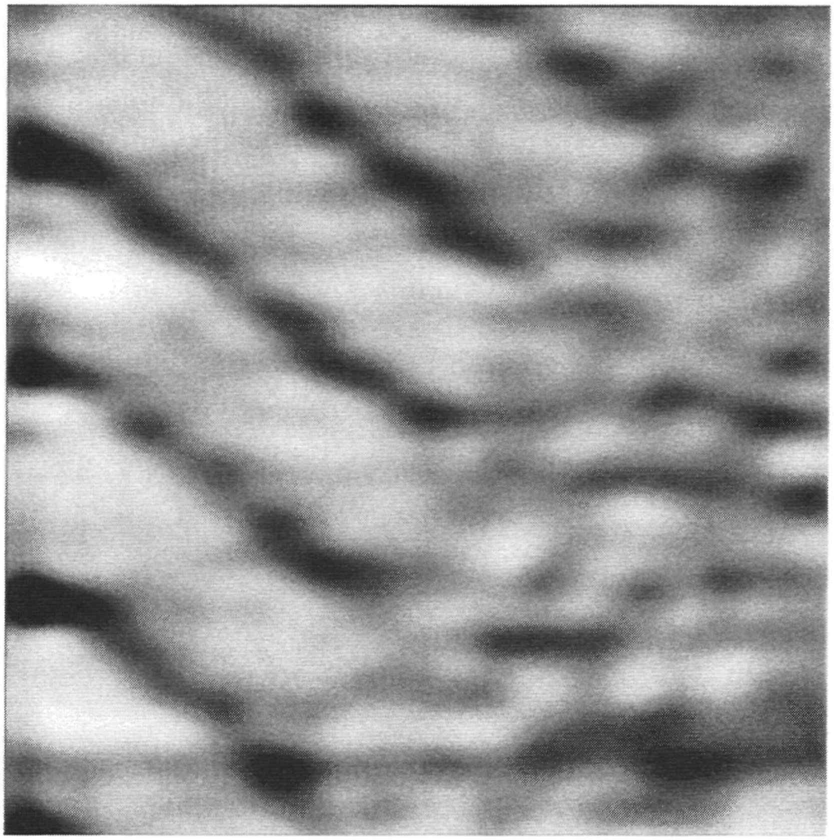

Fig. 3. n-$C_{23}H_{48}$ solution at a domain boundary. No resolution was achieved in the right side of this area. The image size is 12.5 nm × 11.1 nm.

screen but unfortunately is difficult to observe in fig. 2. For n-$C_{19}H_{40}$ and n-$C_{27}H_{56}$ both orientations were found in different areas of the same sample. The measured intermolecular distances of n-$C_{19}H_{40}$ and n-$C_{27}H_{56}$ agree very well with the expected molecular length of 2.26 nm and 3.26 nm respectively. The length of n-$C_{23}H_{48}$ was measured as being 0.19 nm shorter than expected. We attribute this to a temperature effect. At the temperature which the measurements were realized the formation of defects, like kinks, in n-alkane molecules can be favoured (Sumpter *et al.* 1992), shortening the molecules. An indication for this can be found in fig. 2, where the molecules in a row seem to have slightly different lengths.

Another attempt was made to image n-$C_{23}H_{48}$ and n-$C_{24}H_{50}$ at a temperature of 28°C. None of these compounds could be imaged at this temperature. Calorimetric measurements (Brown *et al.* 1975) on even n-alkanes with n ranging from 10 to 20 carbon atoms indicated the presence of ordered layers at the interface between a graphitised carbon surface and the liquid n-alkanes at temperatures close to the melting point of the n-alkanes. Experiments using differential refractometry by Bown (1973) indicate that for the systems n-C_5H_{12} + n-$C_{10}H_{22}$/graphon and n-C_6H_{14} + n-$C_{16}H_{34}$/graphon there are still molecules adsorbed on the graphon surface at a temperature of 28°C. This suggests, as mentioned before, that for our systems at some temperature between 21°C and 28°C the molecules, although still adsorbed, become so mobile on the HOPG surface that during the scan the STM tip pushes the molecules away and no resolution is achieved.

The imaging mechanism for the adsorbates is not completely understood. Mechanisms like resonant tunnelling and modulation of the working function of the substrate by the adsor-

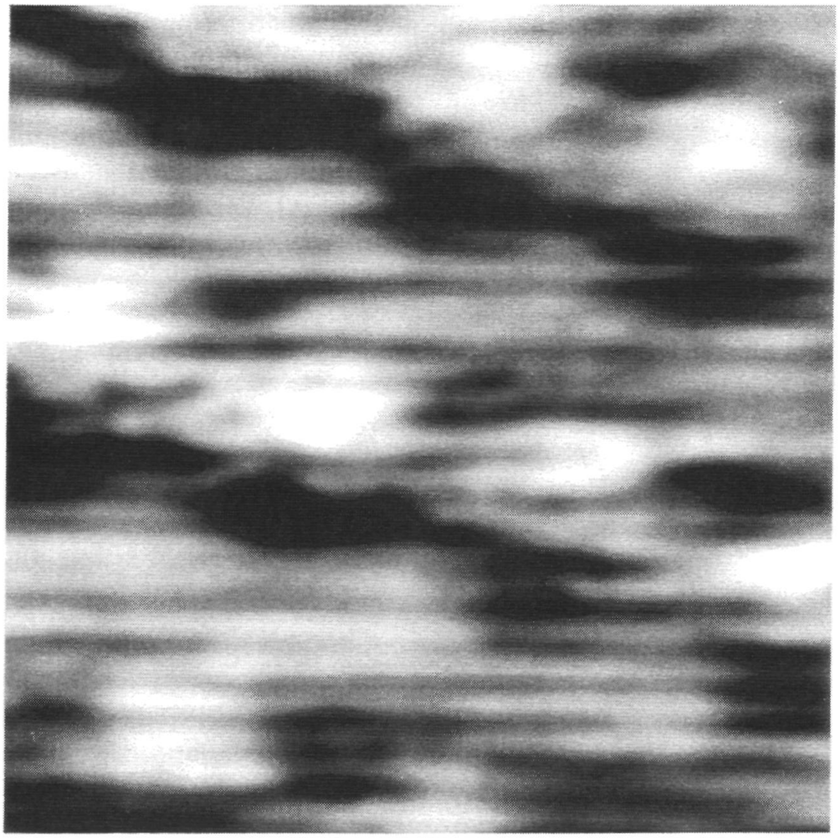

Fig. 4. STM solution image of n-$C_{27}H_{56}$ molecules. The zigzag of dots along the molecules are the individuals CH_2 groups. The scan size is 0.8 nm × 0.8 nm.

bate have been suggested (see Guckenberger *et al.* (1992) and references therein for a discussion on the imaging mechanisms of organic molecules).

New experiments are being prepared to study the effect of temperature in a specific n-alkane and to find a transition from an ordered to disordered arrangement. Controlling the temperature of the solution during the measurements will make it possible to find at which temperature the molecules can no longer be imaged.

4. Conclusion

It could be observed that temperature effects play an important role in the adsorption and ordering of n-alkane molecules on the HOPG surfaces, leading from a complete ordering of the molecules to a complete disordering.

5. Acknowledgements

One of the authors, M. S. Couto, is indebted to CAPES (Coordenação de aperfeiçoamento de Pessoal de Nível Superior), Brazil, for a scholarship making this research possible.

We want to thank Shell Netherlands B.V. for providing the n-alkanes used in this research program.

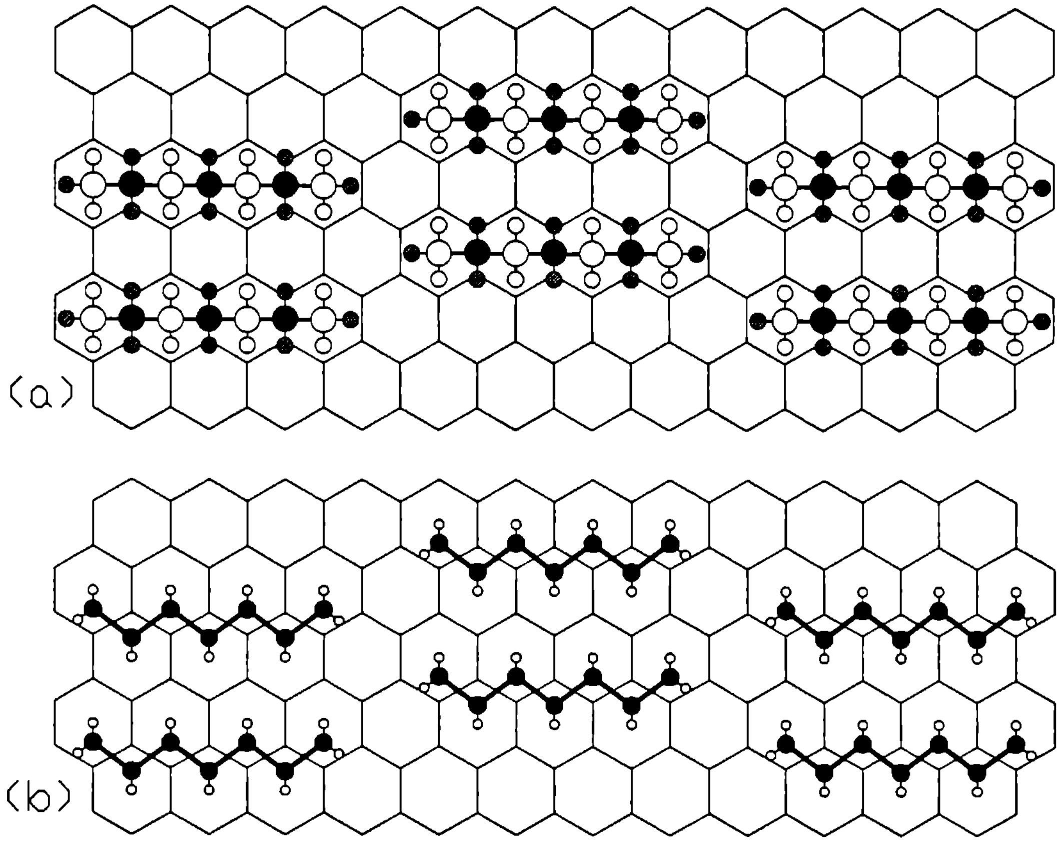

Fig. 5. Proposed models for the adsorbed layer. (*a*) The molecules are perpendicular to the HOPG surface. (*b*) The molecules are parallel to the HOPG surface. In both cases the spacing between to molecules in a row is 0.425 nm.

6. References

Brown, C. E., Everett, D. H., Powell, A. V., and Thorne, P. E., 1975, Faraday Diss. Chem. Soc., **59**, 97.

Bown, R., 1973, Ph.D. Thesis, Bristol.

Groszek, A. J., 1970, Proc. Roy. Soc. Lond. A, **314**, 473.

Guckenberger, R., Hartmann, T., Wiegräbe, W., and Baumeister, W.,1992, in *Scanning Tunneling Microscopy II*, edited by R. Wiesendanger and H. -J. Güntherodt, Springer Series in Surface Sciences 28.

Hottenhuis, M. H. J., Mickers, M. A. H., Gerritsen, J. W., and van der Eerden, J. P., 1988, Surf. Sci., **206**, 259.

Liu, X. Y., and Bennema, P., 1992, J. Chem. Phys., **97**, 3600.

Liu, X. Y., and Bennema, P., 1993, Phys. Rev. B, **48**, 1825.

McGonigal, G. C., Bernhardt, R. H., and Thomson, D. J., 1990, Appl. Phys. Lett., **57**, 28 .

McGonigal, G. C., Bernhardt, R. H., Yeo, Y. H., and. Thomson, D. J., 1991, J. Vac. Sci. Technol. B, **9**, 1107.

Rabe, J. P., and Buchholz, S., 1991a, Science, **253**, 424.

Rabe, J. P., and Buchholz, S., 1991b, Makromol. Chem., Macromol. Symp., **50**, 261.

Sumpter, B. G., Noid, D. W., and Wunderlich, B., 1992, Macromolecules, **25**, 7247.

Summary

In this thesis the results of a study of several types of crystal surfaces have been presented. The main techniques employed were scanning tunnelling microscopy (STM) and atomic force microscopy (AFM). Optical microscopy was also used for some of the crystals. A brief description of the STM and AFM techniques has been presented in the introduction of the thesis.

In the first part of the thesis (chapters 1 through 6) the polishing of diamond was studied in detail. The diamonds were polished in a standard way by pressing the crystals against a rapidly rotating cast iron wheel impregnated with a mixture of diamond powder and paraffin oil. Diamond shows a large anisotropy in the rate of material removal during polishing. The amount of material removed depends on the crystallographic orientation of the face being polished as well as on the direction of polishing along that face. The directions along which material is easily removed are known as 'soft' and those along which material removal is difficult are known as 'hard'.

The results of the experiments using STM and AFM showed that the faces polished along a hard direction were rough. Cracks could be seen along the intersection of the $\{111\}$ planes with the polished face. In some parts of the polished $\{111\}$ faces, triangular features, in accordance to the surface symmetry, were found. All this indicates that material removal along the hard directions is a mechanical process involving cleavage of small fragments from the surface.

For the faces polished along a soft direction the experiments showed a completely different surface topography. The faces were mostly covered by smooth grooves parallel to each other. Few grooves were rough and in some regions cracks could be seen. On a partially polished diamond surface, the examination of the boundary between as-grown and polished parts revealed the presence of isolated smooth grooves. This indicates that diamond polishing along the soft directions is also a mechanical process and involves the formation of nanogrooves, each in a single pass of the abrading particle. The morphology of the polished surface of a natural diamond containing 'naats' (micro twins) confirmed that material removal resulted from a mechanical interaction between the abrading particles and the diamond surface. A theory is put forward in which the formation of these grooves occurs by direct rupture of atomic bonds under the influence of high pressures induced by asperities on the tops of the abrading particles in contact with the surface.

An optical microscopic investigation of the iron wheel used for polishing revealed the presence of broad grooves. Raman spectroscopy indicated only the presence of diamond. Analyses of the black powder formed during polishing revealed iron in the form of carbides and oxides, diamond particles and probably amorphous carbon.

In an attempt to obtain a 'controlled polishing action', friction tracks were made along the soft directions on diamond surfaces, using a sliding diamond stylus. The AFM measurements showed that all tracks (even the ones produced by a single pass of the stylus) were composed of many individual smooth grooves. This confirms that for the soft directions the removal of material during polishing proceeds by the formation of nanogrooves. The fact that the grooves formed by the stylus were smooth, indicates that material is indeed removed through the disruption of atomic bonds under high pressures.

The second part of the thesis (chapters 7 through 9) deals with the surface morphology of different crystals.

The {100} and {111} surfaces of C_{70} crystals were studied *ex situ* at room temperature using AFM and optical microscopy. Attention was focused on the surface morphology resulting from the phase transition from the f.c.c. structure, at high temperatures, to the rhombohedral structure, at room temperature. A complex pattern of domain boundaries could be identified on both surfaces. For each of the surfaces the orientation of the domain boundaries could be determined, together with the orientation of the C_{70} molecules in each of the different domains. *In situ* studies of the phase transition using optical microscopy showed that the domains appear and disappear in groups on the surface but, unfortunately, the point of nucleation of the domain boundaries could not be identified. Another phase transition could be observed *in situ* at 303 K by optical polarization microscopy. It seems that this is a transition between the rhombohedral and the monoclinic structure, although in literature this transition has been reported to take place at lower temperatures.

The (001) face of potassium bichromate (KBC) crystals grown in aqueous solution was studied by using *in situ* and *ex situ* optical microscopy and *ex situ* AFM measurements. Examination of the growth spirals on the (001) and $(00\bar{1})$ faces showed that KBC crystallizes in a non-centrosymmetric space group. The propagation, bunching and blocking of the [100] steps on (001) were measured as a function of the supersaturation. For supersaturation values within the range -1.6% to 1.7% a 'dead' zone was observed in which the KBC crystals did not grow nor dissolved. *Ex situ* measurements using AFM showed the presence of steps of half, one or a few unit cells in height. For crystals separated from the solution while the supersaturation was inside the dead region, steps with cusps could be observed, in contrast with the straight steps found when the supersaturation was outside the dead region. The results obtained were discussed in terms of the existing models for step propagation and step bunching that take into account time dependent impurity adsorption.

Finally, the adsorption of n-alkanes on a (0001) graphite surface was studied *in situ* by STM. The ordered structure formed by these molecules on the surface of the graphite was studied as a function of the number of carbon atoms in the n-alkane molecule and the temperature. It could be observed that for a given temperature a minimum number of carbon atoms was necessary for the formation of ordered structures and that this number increased for increasing temperature. A model for the structure of the adsorbed layer and a possible explanation for the temperature effects are given.

Samenvatting

Dit proefschrift beschrijft de resultaten van de studie naar verschillende soorten kristaloppervlakken. De belangrijkste technieken, hierbij gebruikt, zijn 'scanning tunnelling microscopy' (STM), 'atomic force microscopy' (AFM) en, voor enkele kristallen, optische microscopie. In de inleiding van dit proefschrift wordt een korte beschrijving van de STM en AFM methoden gegeven.

In het eerste deel van dit proefschrift (hoofdstukken 1 tot en met 6) wordt het polijsten van diamanten bestudeerd. De diamanten zijn op een standaard wijze gepolijst door de kristallen tegen een ronddraaiende ijzeren schijf te drukken, welke geïmpregneerd is met diamantpoeder en paraffineolie. De diamanten vertonen een grote anisotropie in de hoeveelheid materiaal die verwijderd wordt tijdens het polijsten. Deze hoeveelheid is afhankelijk van de kristallografische orientatie van het gepolijste vlak alsmede van de polijstrichting op dit vlak. De richtingen waarlangs de diamant gemakkelijk afneemt staan bekend als 'zacht' en die waarlangs materiaal moeilijk verwijderd wordt als 'hard'.

De resultaten van STM en AFM waarnemingen laten zien dat vlakken die gepolijst zijn langs een 'harde' richting, ruw zijn. Barstjes evenwijdig met de snijlijn van een $\{111\}$ vlak met het gepolijste vlak waren waarneembaar. Op sommige plaatsen van de gepolijste $\{111\}$ vlakken waren driehoekige patronen zichtbaar, welke in overeenstemming zijn met de oppervlaktesymmetrie. Deze waarnemingen wijzen erop dat het verwijderen van materiaal langs een 'harde' richting een mechanisch proces is, waarbij kleine deeltjes van het oppervlak gekliefd worden.

De vlakken die gepolijst zijn langs een 'zachte' richting, laten een totaal verschillende oppervlakte topografie zien. Deze vlakken waren over het algemeen bedekt met gladde, parallelle groeven. Slechts enkele groeven waren ruw en slechts in enkele gebieden waren barstjes waarneembaar. Een studie van het grensgebied tussen een gepolijst deel van een diamantvlak en een origineel, ongepolijst deel toonde aldaar de aanwezigheid van geïsoleerde, gladde groeven aan. Dit wijst erop dat het polijsten van diamanten langs een 'zachte' richting ook een mechanisch proces is en dat de nano-groeven tijdens een enkelvoudige passage van een slijpkorrel gevormd worden. Dat het verwijderen van materiaal verloopt via een mechanische interactie tussen polijstkorrels en het diamantoppervlak wordt bevestigd door de morfologie van het gepolijste oppervlak van een natuurlijke diamant die naats (micro twins) bevat. Een hypothese is ontwikkeld waarin deze groeven ontstaan door verbreking van atoombindingen onder invloed van de hoge druk geïnduceerd door onregelmatigheden aan de punt van een polijstkorrel in contact met het te slijpen diamantoppervlak.

De ijzeren schijf, gebruikt voor het polijsten, is onderzocht met behulp van optische microscopie en Raman spectroscopie. Hieruit bleek dat hierop brede groeven aanwezig zijn en de op de schijf aanwezige deeltjes slechts uit diamant bestaan. Een analyse van het zwarte poeder dat ontstaat tijdens het polijsten, laat zien dat er ijzercarbides, ijzeroxides, diamantdeeltjes en waarschijnlijk amorf koolstof aanwezig zijn.

Om het polijsten op een gecontroleerde wijze na te bootsen, zijn er op diamantoppervlakken frictiesporen in een 'zachte' richting gemaakt met behulp van een diamantnaald. AFM metingen laten zien dat alle sporen (ook die welke gemaakt zijn tijdens één enkele passage) bestaan uit een groot aantal afzonderlijke groeven. Dit bevestigt dat voor de 'zachte' richtingen het materiaal verwijderd wordt door de vorming van nano-groeven. Het feit dat de door de naald gevormde groeven glad zijn, laat zien dat het materiaal inderdaad verwijderd is door de verbreking van atoombindingen onder hoge druk.

Het tweede deel van het proefschrift (hoofdstukken 7 tot en met 9) behandelt de oppervlaktemorfologiën van verschillende kristallen.

De {100} en {111} oppervlakken van C_{70} kristallen zijn ex-situ bestudeerd met behulp van AFM en optische microscopie bij kamertemperatuur. Aandacht is besteed aan de oppervlaktemorfologie die onstaat na de faseovergang van een f.c.c. structuur, bij hoge temperaturen, naar een rhombohedrische structuur, bij kamertemperatuur. Op beide oppervlakken kon een ingewikkeld patroon van domeingrenzen geïdentificeerd worden. Voor beide oppervlakken was het mogelijk om zowel de orientatie van de domeingrenzen als de orientatie van de C_{70} moleculen in de verschillende domeinen te bepalen. Uit in-situ metingen met behulp van optische microscopie aan de faseovergang, blijkt dat de domeinen in groepen verschijnen en verdwijnen. Helaas bleek het niet mogelijk het nucleatiepunt van de domeinvorming te bepalen. Een andere faseovergang, bij 303 K, is in-situ gezien met behulp van optische polarisatie microscopie. Dit is waarschijnlijk een faseovergang tussen een rhombohedrische en een monokliene fase, alhoewel in de literatuur hiervoor een lagere temperatuur wordt gegeven.

In-situ en ex-situ optische microscopie en ex-situ AFM zijn gebruikt om het (001) vlak van kaliumbichromaat (KBC) kristallen, groeiend of gegroeid vanuit een waterige oplossing, te bekijken. Vergelijking van de morfologie van groeispiralen op de (001) en de $(00\bar{1})$ vlakken liet zien dat KBC kristalliseert in een niet-centrosymmetrische ruimtegroep. De beweging, opeenhoping en blokkering van de [100] treden op (001) zijn gemeten als functie van de oververzadiging. Een dood gebied, waarin de kristallen niet groeien of oplossen, is gevonden voor oververzadigingen tussen -1.6% en 1.7%. Ex-situ AFM metingen laten zien dat er treden aanwezig zijn met een hoogte van een halve, één of een paar eenheidscellen. Kristallen die verwijderd zijn uit een oplossing met een oververzadiging die in het dode gebied lag, vertonen treden met 'cusps'. Dit in tegenstelling tot kristallen die verwijderd zijn uit een oplossing met een oververzadiging die buiten dit dode gebied lag. Het waargenomene is geïnterpreteerd aan de hand van bestaande modellen voor tredebeweging en tredeopeenhoping met inachtneming van tijdsafhankelijke adsorptie van onzuiverheden.

Tenslotte is de adsorptie van n-alkanen aan het (0001) oppervlak van grafiet met behulp van in-situ STM bestudeerd. De geordende structuur, gevormd door deze moleculen op het oppervlak, is bestudeerd als functie van het aantal koolstofatomen in de n-alkanen en de temperatuur. Het blijkt dat bij een gegeven temperatuur een minimum aantal koolstofatomen nodig is om een geordende structuur te vormen. Dit aantal neemt toe bij toenemende temperatuur. Er wordt een model voor de geadsorbeerde laag gegeven, alsmede een verklaring voor het temperatuureffect.

Sumário

Nesta tese os resultados das pesquisas realizadas nas superfícies de diversos tipos de cristais são apresentados. As principais técnicas utilizadas foram 'scanning tunnelling microscopy' (STM) e 'atomic force microscopy' (AFM), mas para alguns dos cristais microscopia óptica também foi usada. Breves descrições das técnicas de STM e AFM foram apresentadas na introdução da tese.

Na primeira parte da tese (capítulos 1 até 6) o polimento de diamantes foi estudado em detalhes. Os diamantes foram polidos na maneira usual, pressionando os cristais contra um disco de ferro, rodando a alta velocidade, impregnado com partículas abrasivas de diamante e parafina líquida. Diamantes apresentam uma alta anisotropia na taxa de remoção de material durante o polimento. A quantidade de material removido depende da orientação cristalográfica da face que está sendo polida e da direção de polimento ao longo da face. As direções nas quais o material é removido facilmente são conhecidas como 'macias' e aquelas nas quais o material é removido dificilmente são conhecidas como 'duras'.

Os resultados dos experimentos usando STM e AFM mostraram que as faces polidas ao longo das direções 'duras' eram rugosas. Fendas puderam ser vistas ao longo da interseção dos planos {111} com a face polida. Em algumas regiões das faces polidas {111}, foram encontradas partes com formato triangular (em acordo com a simetria da superfície). Todos esses fatos indicam que a remoção de material ao longo das direções 'duras' é um processo mecânico, envolvendo clivagem de pequenos fragmentos da superfície.

Para as faces polidas ao longo de uma direção 'macia' os experimentos mostraram uma topografia completamente diferente para as superfícies. As faces eram cobertas por ranhuras lisas e paralelas. Poucas ranhuras eram rugosas e somente em algumas regiões fendas foram encontradas. A superfície de um diamante sintético foi parcialmente polida e a interface entre a parte resultante do processo de crescimento e a parte polida foi examinada. Os resultados mostraram a presença de ranhuras isoladas. Isto indica que o polimento de diamantes ao longo das direções 'macias' também é um processo mecânico, envolvendo a formação de nano-ranhuras. Cada nano-ranhura é formada em uma única passagem de uma partícula abrasiva de diamante. A morfologia da superfície polida de um diamante natural contendo 'naats' (micro 'twins') confirmou que a remoção de material resultou de uma interação mecânica entre as partículas abrasivas de diamante e a superfície do diamante. Uma teoría é proposta na qual a formação das ranhuras ocorre através da ruptura direta de ligações atômicas sob a influência de altas pressões produzidas por asperidades no topo das partículas de diamante em contato com a superfície.

Investigação usando microscopia óptica no disco de ferro usado para o polimento dos diamantes revelou a presença de ranhuras largas. Espectroscopia Raman indicou somente a presença de diamante. A análise do pó preto formado durante o polimento revelou a presença de ferro na forma de carburetos e óxidos, partículas de diamante e, provavelmente, carbono amorfo.

Em uma tentativa de obter uma 'ação controlada de polimento', trilhas formadas pela fricção de uma agulha de diamante foram produzidas nas superfícies de alguns dos diamantes polidos. As medidas obtidas por AFM mostraram que todas as trilhas (mesmo as produzidas por uma única passagem da agulha de diamante) eram compostas de muitas ranhuras individuais. Isto confirma que para as direções 'macias' a remoção de material durante o polimento ocorre através da formação de nano-ranhuras. O fato que as ranhuras formadas pela agulha

de diamante eram lisas, indica que o material é realmente removido através da ruptura de ligações atômicas devido à altas pressões.

A segunda parte da tese (capítulos 7 a 9) trata da morfologia das superfícies de diferentes cristais.

As faces {100} e {111} de cristais de C_{70} foram estudados ex-situ à temperatura ambiente através de AFM e microscopia óptica. Atenção foi focalizada na morfologia resultante da transição de fase da estrutura fcc, a altas temperaturas, para a estrutura romboédrica, à temperatura ambiente. Um complexo padrão de domínios foi identificado em ambas as superfícies. Para cada uma das superfícies, tanto as orientações dos contornos dos domínios quanto a orientação das moléculas de C_{70} em cada domínio, puderam ser determinadas. Estudos in-situ da transição de fase usando microscopia óptica mostrou que os domínios aparecem e disaparecem em grupos na superfície, mas o ponto de nucleação dos domínios não pôde ser identificado. Uma outra transição de fase foi observada in-situ à 303 K através de microscopia óptica de polarização. Parece que esta é uma transição entre as estruturas romboédrica e monoclínica, embora esta transição tenha sido reportada à temperaturas mais baixas por outros pesquisadores.

A face (001) de cristais de bicromato de potássio (KBC) crescidos em solução aquosa foi estudada in-situ e ex-situ através de microscopia óptica e ex-situ através de AFM. Examinação do crescimento em espirais nas faces (001) e $(00\bar{1})$ mostrou que KBC cristaliza em um grupo espacial não-centrosimétrico. A propagação, 'bunching' e bloqueio de 'steps' na direção [100] das faces (001) foram medidos em função da supersaturação. Para valores de supersaturação entre -1.6% e 1.7% uma região 'morta' foi observada, na qual os cristais de KBC não crescem nem dissolvem. Medidas ex-situ usando AFM mostraram a presença de 'steps' medindo a metade, uma ou algumas células unitárias em altura. Em cristais retirados da solução com valores de supersaturação dentro da região 'morta', 'steps' com reetrâncias foram observados, em contraste com os 'steps' estreitos que foram encontrados para valores de supersaturação fora da região 'morta'. Os resultados obtidos foram discutidos em termos dos modelos existentes para propagação e 'bunching' de 'steps' que levam em conta a absorção temporal de impurezas.

Finalmente, a absorção de alcanos na face (0001) de grafite foi estudada in-situ através de STM. A estrutura ordenada formada pelas moléculas dos alcanos na superfície do grafite foi estudada em função do número de átomos de carbono na molécula e em função da temperatura. Pôde-se observar que para uma dada temperatura um número mínimo de átomos de carbono era necessário para a formação das estruturas ordenadas e que esse número aumentava para temperaturas mais altas. Um modelo foi apresentado para a estrutura da camada absorvida e uma possível explicação para os efeitos da temperatura foi dada.

Curriculum vitae

Marcos da Silva Couto
geboren op 10 mei 1966 te Santo Antônio do Monte,
Brazilië

Lagere School: Santo Antônio do Monte (1972 - 1979)

Middelbare School: Colégio Corália de Magalhães Brandão, Santo Antônio do Monte (1980 - 1983)

Universiteit: Bachelor in Natuurkunde aan de Universidade Federal de Minas Gerais, Belo Horizonte (1984 - 1987)
Master of Science in Natuurkunde, met de dissertatie ’Estudo do crescimento e agregação do ZnS coloidal’ aan de Universidade Federal de Minas Gerais, onder leiding van Dr. Oscar Nassif de Mesquita (1984 - 1987)

Promotie: Promotieonderzoek onder een braziliaanse beurs van CAPES op de afdeling Vaste Stof Chemie, onder leiding van Prof. Dr. P. Bennema, aan de Katholieke Universiteit Nijmegen (1990 - 1995)